# MULTISCALE METHOD FOR ELASTIC WAVE PROPAGATION IN THE HETEROGENEOUS, ANISOTROPIC MEDIA

A Dissertation

by

KAI GAO

Submitted to the Office of Graduate and Professional Studies of
Texas A&M University
in partial fulfillment of the requirements for the degree of

DOCTOR OF PHILOSOPHY

| | |
|---|---|
| Chair of Committee, | Richard Gibson Jr. |
| Co-Chair of Committee, | Yalchin Efendiev |
| Committee Members, | Mark Everett |
| | Benchun Duan |
| | Frederick Chester |
| Head of Department, | Rick Giardino |

August 2014

Major Subject: Geophysics

# ABSTRACT

Seismic wave simulation in realistic Earth media with full wavefield methods is a fundamental task in geophysical studies. Conventional approaches such as the finite-difference method and the finite-element method solve the wave equation in geological models represented with discrete grids and elements. When the Earth model includes complex heterogeneities at multiple spatial scales, the simulation requires fine discretization and therefore a system with many degrees of freedom, which often exceeds current computational abilities. In this dissertation, I address this problem by proposing new multiscale methods for simulating elastic wave propagation based on previously developed algorithms for solving the elliptic partial differential equations and the acoustic wave equation. The fundamental motivation for developing the multiscale method is that it can solve the wave equation on a coarsely discretized mesh by incorporating the effects of fine-scale medium properties using so-called multiscale basis functions. This can greatly reduce computation time and degrees of freedom compared with conventional methods. I first derive a numerical homogenization method for arbitrarily heterogeneous, anisotropic media that utilizes the multiscale basis functions determined from a local linear elasticity equation to compute effective, anisotropic properties, and these equivalent elastic medium parameters can be used directly in existing elastic modeling algorithms. Then I extend the approach by constructing multiple basis functions using two types of appropriately defined local spectral linear elasticity problems. Given the eigenfunctions determined from local spectral problems, I develop a generalized multiscale finite-element method (GMsFEM) for elastic wave propagation in heterogeneous, anisotropic media in both continuous Galerkin (CG) and discontinuous Galerkin (DG) formulations. The ad-

vantage of the multiscale basis functions is they are model-dependent, unlike the predefined polynomial basis functions applied in conventional finite-element methods. For this reason, the GMsFEM can effectively capture the influence of fine-scale variation of the media. I present results for several numerical experiments to verify the effectiveness of both the numerical homogenization method and GMsFEM. These tests show that the effectiveness of the multiscale method relies on the appropriate choice of boundary conditions that are applied for the local problem in numerical homogenization method and on the selection of basis functions from a large set of eigenfunctions contained in local spectral problems in GMsFEM. I develop methods for solving both these problems, and the results confirm that the multiscale method can be powerful tool for providing accurate full wavefield solutions in heterogeneous, anisotropic media, yet with reduced computation time and degrees of freedom compared with conventional full wavefield modeling methods. Specially, I applied the DG-GMsFEM to the Marmousi-2 elastic model, and find that DG-GMsFEM can greatly reduce the computation time compared with continuous Galerkin (CG) FEM.

To my parents and elder sister

# ACKNOWLEDGEMENTS

It is not a trivial way for me to arrive at this point. I recalled my first day in the U.S., when I got off the airplane in a humid Los Angles night, and struggled to find the terminal where the flight to Houston parked, but I got lost in the giant airport that I had never been before. I finally got to the correct terminal and boarding entrance, with the helps from nice passers-by and the airport securities. My life and study in A&M is somehow a longer version of that LAX night. I started from zero, experienced lost, panic, delight, successes as well as failures, and now have become a Ph.D. candidate "knowing something" about this field. But most importantly, I have been lucky enough to receive so many helps and inspirations from others.

I want to express my deepest appreciation to Dr. Rick Gibson, who guided me constantly, helped me generously, and supported me financially, through the five years. I must thank all the unique opportunities he provided me with, such as the AGU and SEG annual meetings, as well as all the careful and patient comments and revisions that he made word by word on my writings, regardless of abstract of only 150 words or article of 40 pages. I sincerely appreciate the opportunity that he included me in the project of developing multiscale method for wave propagation, through which I am able to learn a lot of this new field. Without him, this dissertation is not even possible, since even the text tool I adopt to write this dissertation, LaTeX, was first taught by him.

I am grateful to the professors, friends and colleagues in Department of Geology & Geophysics and Department of Mathematics: Dr. Yalchin Efendiev, Dr. Mark Everett, Dr. Benchun Duan, Dr. William Sager, Dr. Fred Chester, Dr. David Sparks, Dr. Yuefeng Sun, Jianchao Ge, Zaifeng Liu, Jingqian Kang, Dehan Zhu, Zhao Zhang,

Tingting Zhang, Liqin Sang, Bo Chen, Qifei Huang, Au Kim Vuong, Jungrak Son, Muhammad Sarwar, Haider Al Abdulaal, Sireesh Dadi, Ilaan Shtaygrud, Wing Tat Leung, Zhirui Zeng, Jian Gong, for many nice helps and simulating discussions. Specially, I want to thank Dr. Efendiev for providing me the opportunity of attending the Multiscale Wave Propagation Workshop in Saudi Arabia, and Dr. Sager for including me in the Shatsky Rise research cruise over the Northwestern Pacific, and Shubin Fu and Jianchao Ge for their generous helps that greatly promote the quality of my research. I intend to express great appreciation to Dr. Eric Chung in Department of Mathematics in Chinese University of Hong Kong (CUHK), who generously provided me the unique opportunity to visit CUHK for a week, shared ideas and simulated discussions, and also for the countless helps, reviews and comments during several manuscript writings and revisions.

I intend to thank Xiaoxi Zhang, Shuo Li, Jian Shen, Yue Deng, Chunyu Tian, Xin Liu, Danyu Shi, Xinyuan Yang, Zhou Wang, Shuo Feng, Xinyi Zhang, Xinyi Cai, Shiyu Hu, Ruoxi Lu, Cheng Wu, Xutong Li, Zhenggang Xu, Kai Tao, Jinchang Zhang, Zeyu Yang, Jingyi Li, Dr. Hongfeng Deng, Qiyuan Liu, Ruirui Wang, Jin Yang, Jie Cai and Lu Wang, and Rui Cai, Dr. Xin Huang and Dr. Boyi Ou in ION Geophysical, and Anbo Chen in CGG, for the nice memories. I also want to express my sincere thanks to Dr. Bingshou He and Dr. Anlong Li in Ocean University of China, for their consistent encouragements. Without you all, my life in the U.S. would be dull and gray.

Finally, I want to express my sincere and deep appreciation to Miss Ying Zhou, who constantly supports me, encourages me and accompanies me through this year, through the boring days of deriving equations, coding and debugging, and through the whole process of finishing this dissertation. Without her, this dissertation is impossible.

NOMENCLATURE

| | |
|---|---|
| $\mathbf{u}$ | displacement, $\mathbf{u} = \mathbf{u}(\mathbf{x}, t) = u_i$, $i = 1, 2, 3$ |
| $\mathbf{v}$ | particle velocity, $\mathbf{v} = \mathbf{v}(\mathbf{x}, t) = v_i$, $i = 1, 2, 3$ |
| $\boldsymbol{\sigma}$ | stress tensor, $\boldsymbol{\sigma} = \boldsymbol{\sigma}(\mathbf{x}, t) = \sigma_{ij}$, $i, j = 1, 2, 3$ |
| $\boldsymbol{\varepsilon}$ | strain tensor, $\boldsymbol{\varepsilon} = \boldsymbol{\varepsilon}(\mathbf{x}, t) = \varepsilon_{ij}$, $i, j = 1, 2, 3$ |
| $\mathbf{c}$ | fourth-order elasticity tensor, $\mathbf{c}(\mathbf{x}) = c_{ijkl}$, $i, j, k, l = 1, 2, 3$ |
| $\mathbf{C}$ | elasticity matrix in Voigt notation, $\mathbf{C}(\mathbf{x}) = C_{IJ}$, $I, J = 1, , 2, \cdots, 6$ |
| $\mathbf{S}$ | compliance matrix in Voigt notation, $\mathbf{S} = \mathbf{C}^{-1}$ |
| $\rho$ | mass density of medium, $\rho = \rho(\mathbf{x})$ |
| $\Omega$, $\partial\Omega$ | the whole computation domain and its boundary |
| $K$, $\partial K$ | a coarse block that may contain many finer elements and its boundary |
| $\{\!\{\boldsymbol{\sigma}\}\!\}$ | average of tensor $\boldsymbol{\sigma}$ at an edge |
| $[\![\mathbf{v}]\!]$ | jump of vector $\mathbf{v}$ at an edge |
| $\underline{[\![\mathbf{v}]\!]}$ | matrix jump of vector $\mathbf{v}$ at an edge |
| $\boldsymbol{\Phi}_i, \boldsymbol{\Psi}_i$ | multiscale basis functions for the $i$-th coarse block |
| $\boldsymbol{\phi}_j, \boldsymbol{\varphi}_j, \boldsymbol{\psi}_j$ | the $j$-th eigenfunction in a coarse block |
| $\mathbf{K}$ | stiffness matrix |
| $\mathbf{M}$ | mass matrix |
| $\mathbf{F}$ | force matrix |
| $\mathbf{E}$ | damping matrix |
| $\xi, \zeta$ | eigenvalues in the local spectral problems |
| $\mathbf{a} \cdot \mathbf{b}$ | dot product of two vectors $\mathbf{a}$ and $\mathbf{b}$ |
| $\mathbf{a} \otimes \mathbf{b}$ | outer product of two vectors $\mathbf{a}$ and $\mathbf{b}$ |

TABLE OF CONTENTS

Page

ABSTRACT . . . . . ii

DEDICATION . . . . . iv

ACKNOWLEDGEMENTS . . . . . v

NOMENCLATURE . . . . . vii

TABLE OF CONTENTS . . . . . viii

LIST OF FIGURES . . . . . x

LIST OF TABLES . . . . . xvi

1. INTRODUCTION . . . . . 1

    1.1 Motivation . . . . . 1
    1.2 Literature review . . . . . 7
    1.3 Outline . . . . . 15

2. NUMERICAL HOMOGENIZATION FOR HETEROGENEOUS, ANISOTROPIC ELASTIC MEDIA BASED ON MULTISCALE THEORY 17

    2.1 Introduction . . . . . 17
    2.2 Theory . . . . . 21
        2.2.1 Elastic wave equation . . . . . 21
        2.2.2 Multiscale basis function . . . . . 22
        2.2.3 Effective medium parameters . . . . . 25
    2.3 Numerical results . . . . . 32
        2.3.1 Horizontally layered medium . . . . . 32
        2.3.2 Arbitrarily heterogeneous medium . . . . . 35
    2.4 Discussion . . . . . 44
    2.5 Conclusions . . . . . 49

3. GENERALIZED MULTISCALE FINITE-ELEMENT METHOD FOR ELASTIC WAVE EQUATION . . . . . 50

    3.1 Introduction . . . . . 50
    3.2 Theory . . . . . 56
        3.2.1 Weak form of the elastic wave equation . . . . . 57
        3.2.2 Multiscale basis functions . . . . . 62

3.2.3 Stability condition and dispersion relation . . . . . 81
3.2.4 Implementation . . . . . 82
3.3 Numerical results . . . . . 89
3.3.1 Isotropic-TTI model . . . . . 89
3.3.2 Randomly heterogeneous anisotropic model with curved layers 94
3.3.3 Free surface problem . . . . . 98
3.3.4 Adaptive assignment of number of basis functions . . . . . 100
3.4 Conclusions . . . . . 105

4. APPLICATION OF GENERALIZED MULTISCALE FINITE-ELEMENT METHOD IN SIMULATING ELASTIC WAVE PROPAGATION IN MARMOUSI-2 ELASTIC MODEL . . . . . 109

4.1 Introduction . . . . . 109
4.2 Method . . . . . 112
4.3 Results and analysis . . . . . 116
4.3.1 Block I . . . . . 116
4.3.2 Block II . . . . . 122
4.3.3 Block III–VI . . . . . 133
4.4 Conclusions . . . . . 134

5. SUMMARY . . . . . 142

5.1 Conclusions . . . . . 142
5.2 Future work . . . . . 143

REFERENCES . . . . . 145

APPENDIX A. LOCAL STATIC LINEAR ELASTICITY PROBLEM SOLVED WITH 2ND-ORDER FINITE-ELEMENT . . . . . 161

APPENDIX B. NUMERICAL HOMOGENIZATION FOR 3-D HETEROGENEOUS, GENERALLY ANISOTROPIC MEDIA . . . . . 167

APPENDIX C. $2L$-TH ORDER ROTATED STAGGERED-GRID FINITE-DIFFERENCE SCHEME . . . . . 169

LIST OF FIGURES

FIGURE Page

1.1 An example of heterogeneities of the Earth medium in multiple spatial scales. (a) is the microscopic image of sandstone, (b) is the sandstone hand specimen, and (c) is the sandstone formation in the field. . . . 6

2.1 The mesh discretization of domain $\Omega$, ■ represents $\boldsymbol{\sigma} = (\sigma_{11}, \sigma_{33}, \sigma_{13})$, ● represents $\mathbf{v} = (v_1, v_3)$, black line rectangle $K_\sigma$ represents the support of stress components, black dashed line rectangle $K_v$ represents the support of velocity components. . . . . 22

2.2 Subgrid elasticity parameter models. (a)–(f) represent $C_{11}$, $C_{13}$, $C_{15}$, $C_{33}$, $C_{35}$ and $C_{55}$, respectively. The grid size is $1 \times 1$ m$^2$. . . . . 37

2.3 Comparisons of wavefields in fine grid medium and effective medium. (a) and (b) are $v_1$ and $v_3$ wavefields from fine grid model, respectively, and (c) and (d) are $v_1$ and $v_3$ wavefields from effective model, respectively. . . . . 39

2.4 Comparison of (a) $v_1$ and (b) $v_3$ wavefields along horizontal line at a depth of 2400 m of the snapshots 2.3(a)/2.3(c) and 2.3(b)/2.3(d). Blue lines are the fine grid solution, and red dots are solutions from effective medium. . . . . 40

2.5 Four-layer von Kármán correlation random medium model. (a)–(f) represent $C_{11}$, $C_{13}$, $C_{15}$, $C_{33}$, $C_{35}$ and $C_{55}$, respectively. The model contains 2000×2000 grids, each is 1 m × 1 m in size. . . . . 41

2.6 Comparisons of wavefield snapshots at 0.4 s in fine grid medium and effective medium. (a) and (b) are $v_1$ and $v_3$ wavefields from fine grid model, respectively, and (c) and (d) are $v_1$ and $v_3$ wavefields from effective model, respectively. . . . . 42

2.7 Comparison of (a) $v_1$ and (b) $v_3$ wavefields along horizontal line at a depth of 400 m of the snapshots 2.6(a)/2.6(c) and 2.6(b)/2.6(d). Blue lines are the fine grid solution, and red dots are solutions from effective medium. . . . . 43

2.8 Comparisons of seismograms between blue wiggles – original fine grid solution of $v_1$ component, and red wiggles – effective medium solution of $v_1$ component. The solution is without clipping, so that the waveforms of transmitted wavefields are integrated enough to be seen. 45

2.9 Comparisons of seismograms between blue wiggles – original fine grid solution of $v_3$ component, and red wiggles – effective medium solution of $v_3$ component. The solution is without clipping, so that the waveforms of transmitted wavefields are integrated enough to be seen. 46

2.10 Comparisons of seismograms between blue wiggles – original fine grid solution of $v_1$ component, and red wiggles – effective medium solution of $v_1$ component. Te solution is with clipping, so that the waveforms of reflections and scatterings are integrated enough to be seen. . . . 47

2.11 Comparisons of seismograms between blue wiggles – original fine grid solution of $v_3$ component, and red wiggles – effective medium solution of $v_3$ component. The solution is with clipping, so that the waveforms of reflections and scatterings are integrated enough to be seen. . . . 48

3.1 A sketch of the fine mesh $\mathcal{T}_h$, denoted by gray mesh, and coarse mesh $\mathcal{T}_H$, denoted by black mesh, in CG formulation of GMsFEM. Gray rectangle labeled $K$ represents the support of the $i$-the coarse node. $K$ contains many finer element which might have high contrasts in medium properties. . . . . 58

3.2 A sketch of the fine mesh $\mathcal{P}_h$, denoted by gray mesh, and coarse mesh $\mathcal{P}_H$, denoted by black mesh in DG formulation of GMsFEM. Gray rectangle labeled $K$ represents the $i$-th coarse element. Same with that in CG-GMsFEM, coarse block $K$ contains many finer element which might have high contrasts in medium properties. . . . . 60

3.3 (a)–(f) represent the $u_1$ component of the first 6 spectral basis functions corresponding with the first 6 smallest eigenvalues for an isotropic homogeneous subgrid model. . . . . 66

3.4 (a)–(f) represent the $u_3$ component of the first 6 spectral basis functions corresponding with the first 6 smallest eigenvalues for an isotropic homogeneous subgrid model. . . . . 67

3.5 (a)–(f) represent the $u_1$ component of the first 6 spectral basis functions corresponding with the first 6 smallest eigenvalues for an anisotropic homogeneous subgrid model. . . . . 69

3.6 (a)–(f) represent the $u_3$ component of the first 6 spectral basis functions corresponding with the first 6 smallest eigenvalues for an anisotropic homogeneous subgrid model. . . . . 70

3.7 Elasticity parameter variations within one coarse block. (a) and (b) represents $C_{11}$ and $C_{55}$, respectively. . . . . 71

3.8 (a)–(f) represent the $u_1$ component of the first 6 spectral basis functions corresponding with the first 6 smallest eigenvalues for an isotropic heterogeneous subgrid model in Figure 3.7(a) and 3.7(b). . . . . 72

3.9 (a)–(f) represent the $u_3$ component of the first 6 spectral basis functions corresponding with the first 6 smallest eigenvalues for an isotropic heterogeneous subgrid model in Figure 3.7(a) and 3.7(b). . . . . 73

3.10 (a)–(f) represent the $u_1$ component of the first 6 interior basis functions for the isotropic heterogeneous subgrid model in Figures 3.7(a) and 3.7(b). . . . . 77

3.11 (a)–(f) represent the $u_3$ component of the first 6 interior basis functions for the isotropic heterogeneous subgrid model in Figures 3.7(a) and 3.7(b). . . . . 78

3.12 (a)–(f) represent the $u_1$ component of the first 6 boundary basis functions for the isotropic heterogeneous subgrid model in Figures 3.7(a) and 3.7(b). . . . . 79

3.13 (a)–(f) represent the $u_3$ component of the first 6 boundary basis functions for the isotropic heterogeneous subgrid model in Figures 3.7(a) and 3.7(b). . . . . 80

3.14 A sketch of oversampling for DG formulation. $K$ is the coarse element where the corresponding problems needed to be solved, while $K'$ represented by gray dashed rectangle is the oversampled coarse element. After solving local problems in $K'$, we take the solutions corresponding with the nodes in $K$ as basis functions. For CG, a similar sketch can be got. . . . . 81

3.15 $u_1$ wavefield snapshots solved with (a) CG-FEM and (b)-(f) CG-GMsFEM. All the multiscale solutions have an upscaling ratio $r = 10$, and number of spectral basis functions $m$ =10, 20, 30, 40, 50 for (b)-(f), respectively. . . . . 92

3.16 $u_3$ wavefield snapshots solved with (a) CG-FEM and (b)-(f) CG-GMsFEM. All the multiscale solutions have an upscaling ratio $r = 10$, and number of spectral basis functions $m$ =10, 20, 30, 40, 50 for (b)-(f), respectively. . . . . 93

3.17 A heterogeneous, anisotropic elastic model. Parts (a)-(f) show $C_{11}$, $C_{13}$, $C_{15}$, $C_{33}$, $C_{35}$ and $C_{55}$, respectively. . . . . 95

3.18 $u_1$ wavefield snapshots of (a) fine grid solution and (b)-(f) multiscale solutions, with $(m_{\text{boundary}}, m_{\text{interior}}) = (10, 20)$, $(20, 20)$, $(20, 30)$, $(30, 30)$, $(20, 40)$, respectively. . . . . 96

3.19 $u_3$ wavefield snapshots of (a) fine grid solution and (b)-(f) multiscale solutions, with $(m_{\text{boundary}}, m_{\text{interior}}) = (10, 20)$, $(20, 20)$, $(20, 30)$, $(30, 30)$, $(20, 40)$, respectively. . . . . 97

3.20 Wavefield snapshots of (a) $u_1$ and (b) $u_3$ solved from CG-FEM on fine mesh, (c) $u_1$ and (d) $u_3$ solved with DG-GMsFEM on coarse mesh with $(m_{\text{boundary}}, m_{\text{interior}}) = (20, 30)$, (e) $u_1$ and (f) $u_3$ with $(20, 50)$, (g) $u_1$ and (h) $u_3$ with $(40, 30)$. Note the high-frequency resonance error at the top surface in the $(20, 30)$ DG-GMsFEM solution, which disappears in $(20, 50)$ and $(40, 30)$ solutions. . . . . 101

3.21 Comparisons of (a) $u_1$ seismogram and (b) $u_3$ seismogram solved from CG-FEM (blue curve), DG-GMsFEM with $(20, 30)$ basis functions (red curve), DG-GMsFEM with $(20, 50)$ basis functions (green curve), and DG-GMsFEM with $(40, 30)$ basis functions (yellow curve). . . . 102

3.22 The (a) P- and (b) S-wave velocity model, and (c) density model cropped from Marmousi 2 elastic model. . . . . 103

3.23 Number of (a) interior and (b) boundary basis functions calculated based on the S-wave velocity. . . . . 105

3.24 $u_1$ wavefield snapshots at 1.5 s from (a) conventional CG-FEM, (b) DG-GMsFEM with 70 type II basis functions total and (c) DG-GMsFEM with 170 type II basis functions total, and (d) with adaptive assignment of total number of type II basis functions from 70 to 170. . . . 106

3.25 $u_3$ wavefield snapshots at 1.5 s from (a) conventional CG-FEM, (b) DG-GMsFEM with 70 type II basis functions total and (c) DG-GMsFEM with 170 type II basis functions total, and (d) with adaptive assignment of total number of type II basis functions from 70 to 170. . . . 107

4.1 The original Marmousi-2 elastic model. (a)–(c) represent the P-wave velocity, S-wave velocity and density models, respectively. . . . . 117

4.2 Number of interior basis functions for six blocks from (a) top to (f) bottom. . . . . 118

4.3 Number of boundary basis functions for six blocks from (a) top to (f) bottom. . . . . 119

4.4 Wavefield comparisons between the $u_1$ wavefield with (a) CG-FEM and (b) DG-GMsFEM, and $u_3$ wavefield with (c) CG-FEM and (d) DG-GMsFEM. . . . . 121

4.5 $u_1$ wavefield seismogram calculated with CG-FEM. . . . . 123

4.6 $u_1$ wavefield seismogram calculated with DG-GMsFEM. . . . . 124

4.7 $u_1$ wavefield difference between the CG-FEM and DG-GMsFEM. . . 125

4.8 $u_3$ wavefield seismogram calculated with CG-FEM. . . . . 126

4.9 $u_3$ wavefield seismogram calculated with DG-GMsFEM. . . . . 127

4.10 $u_3$ wavefield difference between the CG-FEM and DG-GMsFEM. . . 128

4.11 Single trace seismogram comparison of the receiver at 8.125 km. (a) is the $u_1$ component, (b) is the $u_3$ component. . . . . 129

4.12 Single trace seismogram comparison of the receiver at 8.75 km. (a) is the $u_1$ component, (b) is the $u_3$ component. . . . . 130

4.13 Single trace seismogram comparison of the receiver at 9.375 km. (a) is the $u_1$ component, (b) is the $u_3$ component. . . . . 131

4.14 Single trace seismogram comparison of the receiver at 10 km. (a) is the $u_1$ component, (b) is the $u_3$ component. . . . . 132

4.15 Wavefield of (a) $u_1$ and (b) $u_3$ in block II calculated with DG-GMsFEM. 134

4.16 $u_1$ wavefield seismogram calculated with DG-GMsFEM for block II. . 135

4.17 $u_3$ wavefield seismogram calculated with DG-GMsFEM for block II. . 136

4.18 (a)$u_1$ and (b) $u_3$ wavefield seismograms calculated with DG-GMsFEM for block III. . . . . 137

4.19 (a)$u_1$ and (b) $u_3$ wavefield seismograms calculated with DG-GMsFEM for block IV. . . . . 138

4.20 (a)$u_1$ and (b) $u_3$ wavefield seismograms calculated with DG-GMsFEM for block V. . . . . 139

4.21 (a)$u_1$ and (b) $u_3$ wavefield seismograms calculated with DG-GMsFEM for block VI. . . . . 140

A.1 A sketch of the fine mesh discretization for the local problem. To solve the local problem with FEM, we compute displacement $\mathbf{u}$ at the locations ●, and after the calculation of $\mathbf{u}$, we can obtain the stress for a fine element at the center of a fine element at locations ▲. . . . 162

# LIST OF TABLES

TABLE Page

3.1 The relation between number of basis functions and the relative error, as well as the DOF and calculation time. $m$ is the number of type I spectral basis functions, DOF is the number of unknowns in the multiscale modeling system, $e(\mathbf{u})$ is the $L^2$-norm error of the displacement wavefield, $T_{\text{basis}}$ is the CPU time of calculating the multiscale basis functions, $T_{\text{inverse}}$ is the CPU time of calculating the Cholesky decomposition of the global mass matrix, and $T_{\text{modeling}}$ is the CPU of calculating the wavefield, i.e., all the time steps. The first row is the result from reference CG-FEM solution, therefore $m$, $e(\mathbf{u})$ and $T_{\text{basis}}$ are all left blank. . . . . 91

3.2 The relation between number of basis functions and the relative error, as well as the DOF and calculation time. $m_{\text{boundary}}$ is the number of boundary basis functions, $m_{\text{interior}}$ is the number of interior basis functions. The other quantities own same meaning as those in the first model example. The first row represents the calculation with CG-FEM. 99

C Coefficients of 20th order staggered-grid finite-difference scheme . . . 170

# 1. INTRODUCTION

## 1.1 Motivation

Numerical simulation of seismic waves through the Earth has long been an important field in geophysical studies. The solutions can provide insights not only into Earth structures on a global scale, but can also help image subsurface structures on the oil and gas exploration scale. There are two basic approaches to numerically simulate wave propagation in the Earth medium, approximation methods based on the high-frequency assumption of wave equation or certain simplifications of the Earth, and direct methods based on various techniques to solve wave equation without approximations. For the first category, we have, for example, the ray method (Červený and Hron, 1980; Beydoun and Keho, 1987; Gibson et al., 2005), the eikonal equation method (Vidale, 1988; Podvin and Lecomte, 1991; Sethian and Popovici, 1999), the Gaussian beam method (Hill, 1990; Gray and Bleistein, 2009), screen method (Wu, 1994), the one-way wave equation (OWWE) method (Claerbout, 1985; Zhang et al., 2005), the reflectivity method (Thomson, 1950; Haskell, 1953; Kennett, 1979, 1985), and so on.

However, simplification means loss of completeness, although they are highly developed and some of them have become standard tools for seismic imaging, seismic inversion, and velocity model build, etc.. For example, the ray tracing and eikonal equation methods are generally much faster than direct methods, and can help construct velocity models for either global seismology studies or reservoir explorations when combined with methods such as Kirchhoff migration (e.g., Zhu, 1988; Gray and May, 1994). OWWEs, for instance, are important and efficient tools for seismic imaging, providing more details and higher accuracy where the ray methods fails.

However, it is known that these approximation method may provide spurious, if not incomplete, information due to the intrinsic loss of completeness of these methods in simulating the seismic wavefield propagation in the complex geological models and structures (e.g., Leveille et al., 2011).

Direct methods, also known as the full wavefield methods, on the other hand, can be more accurate in describing the propagation of various seismic wavefields in complex structures and media, but can be much slower in terms of computational time and very expensive in terms of computation resources, such as memory. There are several essential reasons for such a situation. First, the computational requirements of the direct methods, such as finite-different method (FDM) (e.g., Virieux, 1986), finite-element method (FEM) (e.g., Marfurt, 1984), pseudo-spectral (PS) method (Fornberg, 1990), and so on, are directly proportional to the number of geometrical units, say, the discrete element or grid, that are required to represent the geological model adequately. Consider a naive example of a geological model discretized with quadrilateral (2-D) or hexahedral (3-D) elements. If it is necessary to double the number of elements in each direction to describe smaller heterogeneities or finer structures in the model, the result is an increase in computation cost of a factor of four in 2-D and eight in 3-D. Second, direct methods with explicit temporal discretization schemes are restricted by the so-called Courant-Friedrichs-Lewy (CFL) conditions to ensure numerical stability (e.g., Chu and Stoffa, 2012). When using elements of smaller size, the time step has to be tuned smaller accordingly, which means more time steps to simulate the wavefield for the same time period. Therefore, the description of finer structures or medium property heterogeneities of a large model usually results in much higher computational costs for large 2-D and 3-D geological models, costs that may exceed current computation ability.

One increasingly important application of full waveform simulation is seismic

imaging and inversion methods, such as reverse-time migration (RTM) (Baysal et al., 1983; McMechan, 1983; Chang and McMechan, 1987; Symes, 2007; Liu et al., 2011) and full-waveform inversion (FWI) (Tarantola, 1984; Mora, 1987; Singh et al., 1993; Shipp and Singh, 2002; Virieux and Operto, 2009). These approaches are rapidly becoming feasible tools for industrial seismic imaging and velocity model building, as well as for improving the quality of imaging and inversion in global scale seismology studies. These methods inherently depend on full wavefield solutions of the wave equations, and therefore the challenges of high computational costs are also the fundamental obstacles for them. Therefore, accurate and, more importantly, fast full wavefield methods to simulate seismic wave propagation in the Earth medium can be beneficial for both global seismology that aims to explain continental scale geological structures and petroleum seismology that aims to characterize reservoirs.

The design of accurate yet fast wave equation solvers should also include an important property of the Earth medium, that is, the Earth is heterogeneous at multiple spatial scales. Figures 1.1(a)–1.1(c) show examples of such heterogeneity.[1] On a scale of micrometers as shown in Figure 1.1(a), rocks are quite heterogeneous, where crystal fragments, pores, fluids and discontinuities are distributed in a highly random or a highly ordered structural geometry, resulting in different microscopic petrophysical characteristics of the rock. Heterogeneity of the rock, however, will also happen in a larger scale, say, millimeter scale or centimeter scale, as shown in Figure 1.1(b), where cross-bedding occurs, and the heterogeneity also becomes less random compared with that in Figure 1.1(a). On a meter scale or hundreds of meters scale as shown in Figure 1.1(c), we may encounter various kinds of layering,

[1] All photos are from Oxford Earth Sciences Image Store (OESIS), a website maintained by Dave Waters from Department of Earth Sciences, University of Oxford, and the collections of rock images have been permitted to be used for *bona fide* educational purposes, as stated on OESIS website `http://www.earth.ox.ac.uk/~oesis/index.html`.

faults and folds, which are usually important in exploration geophysics and reservoir characterization, but their origins and evolutions should be explained with quite different theories as those in Figure 1.1(a). Seismic wave propagation is a physical process that can happen at all these different scales, which can be described by exactly the same fundamental constitution relations, i.e., Hooke's law, and equations of motion, but with different frequencies of interest. For microscopic investigation, seismic waves in the order of kilohertz or megahertz might be helpful to reveal the petrophysical properties of rock. For exploration seismology, interested seismic waves are usually in the order of hertz, decahertz or at most hectohertz, due to attenuation of waves in the Earth medium. And in global scale seismology, we are only able to effectively analyze the seismic signals of decihertz or at most several hertz in frequency. This is simply due to the fact that seismic reflection, refraction, scattering and diffraction only become significant when the size of heterogeneities in the Earth medium is comparable with the dominant wavelength of the seismic wave. Therefore, people tend to simplify the heterogeneities on finer scale with some approximation method when investigating the seismic wave propagation on coarse scales, which is also partly due to the high computational costs we mentioned earlier in modeling the full wavefield with much finer discretization of the model. For example, the effective medium theory (Backus, 1962; Schoenberg and Muir, 1989; Carcione et al., 2012) is a widely applied tool in oil and gas exploration, which replaces the heterogeneities on fine scale with some equivalent yet spatial homogeneous parameters on coarse scale. It is obvious that the effective medium theory will immediately fail when the seismic wavelength of interest is at the same scale with the geological heterogeneities. Besides, the effective medium cannot be always accurate due to its fundamental assumptions, e.g., the Earth medium is composed of horizontal layers with thickness much smaller than the dominant wavelength of seismic wavefield. When the error

introduced by homogenizing the important heterogeneities with the effective medium theory exceeds the error of modeling method itself, the effective medium will not be useful for relating seismic data to material properties. Discretization of geological models in current exploration seismology usually adopts grid size in the order of 5 m to 20 m, therefore it is difficult to consider much finer, arbitrary heterogeneities below this scale, either with effective medium theory or using finer discretization due to the considerations mentioned above. This is an important motivation for finding a consistent way to simulate the seismic wave propagation on the coarse scale with the fine-scale information incorporated into the modeling system, so that the numerical simulation can obtain affordable computational costs with minimal error.

These difficulties will become even more serious in full wavefield modeling for elastic, visco-elastic and poro-elastic media, since the constitutive relations and equations of motion are substantially more complicated than the acoustic wave equation (e.g., Carcione, 2007). Nevertheless, it is more appropriate to consider the Earth media as elastic, visco-elastic or poro-elastic rather than simple acoustic media, since true Earth media include features such as anisotropy due to layering (Carcione et al., 2012) and fracturing (Sayers, 2002), which can make important differences in seismic data analysis and subsurface imaging, and further, seismic interpretation. The elastic behavior is also the foundation of multicomponent seismics developed in recent decade (Davis, 2001; Yan and Sava, 2008; Etgen et al., 2009; Kamath and Tsvankin, 2013; Vigh et al., 2014), which records both the compressional and shear wave signals, and can enhance the interpretation of subsurface structures and reservoir properties. The full wavefield method for elastic wave equation, as a result, has become a necessary tool for elastic imaging and inversion methods (Virieux et al., 2011). This is another important motivation for developing fast and accurate numerical simulation methods for elastic wave propagation based on the multiscale theory.

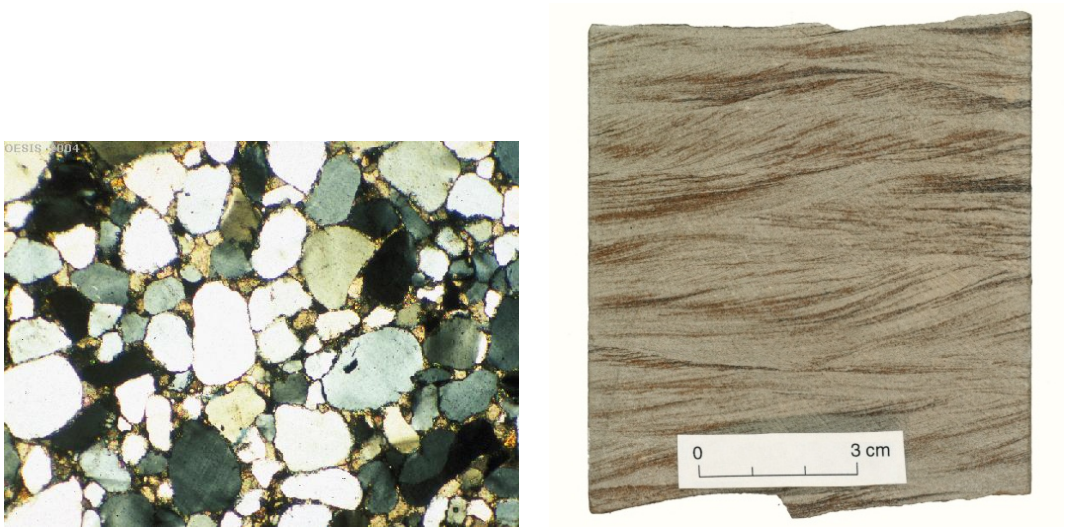


(a) (b)

(c)

Figure 1.1: An example of heterogeneities of the Earth medium in multiple spatial scales. (a) is the microscopic image of sandstone, (b) is the sandstone hand specimen, and (c) is the sandstone formation in the field.

## 1.2 Literature review

The full wavefield solution of the wave equation requires direct discretization of the wave equation. Early attempts focused on solving the acoustic wave equation with the finite-difference method (FDM) and its high-order formulation (Alterman and Karal, 1968; Alford et al., 1974; Kelly et al., 1976; Dablain, 1986), which represent the computation domain with a set of uniformly discrete grids, and discretize the temporal and spatial partial derivatives with the difference of the values on the grids. The application of finite-difference solutions of the wave equation allows the direct and accurate modeling of complex subsurface structures. Since then, FDM has gained long history of development in both theory and applications in realistic geophysical exploration, and many efforts are devoted to improve the accuracy the finite-difference discretization. For example, Virieux (1986) introduced the staggered-grid finite-difference scheme for the first-order velocity-stress elastic wave equation, which can better handle solid-fluid interface compared with conventional central-difference FDM. The staggered-grid finite-difference method was later improved by Levander (1988). Conventional FDM and staggered-grid FDM have been extended to address more kinds of wave equations in later developments, including the visco-elastic wave equation (Robertsson et al., 1994) and the poro-elastic wave equation (Özdenvar and McMechan, 1997; Masson et al., 2006).

The FDM is easy to implement, and error and dispersion analyses are relatively simple as well, and therefore it has gained wide application in practice. However, FDM is not flexible when an unstructured mesh is required to correctly represent the geological structures. The situation is especially urgent when there are faults or steep dips in the model, where the structured mesh will inevitably introduce stair-like boundaries and interfaces, and therefore introduce error in the modeling with FDM.

The finite-element method (FEM), on the other hand, is designed to solve partial differential equations on an unstructured mesh and can naturally handle curved interfaces, and it was introduced to solve acoustic and elastic wave equations (Bolt and Smith, 1976; Marfurt, 1984; Drake and Bolt, 1989). FEM has a more complex implementation, partly due to the computation of assembling the global matrices for the modeling system (Hughes, 1987; Larson and Bengzon, 2013). Specifically, the linear system for wave equation modeling, which is a time-dependent system, can generally be written as

$$\mathbf{M}\ddot{\mathbf{U}} + \mathbf{E}\dot{\mathbf{U}} + \mathbf{K}\mathbf{U} + \mathbf{F} = \mathbf{0}, \tag{1.1}$$

where $\mathbf{M}$ is the global mass matrix, $\mathbf{E}$ is the global damping matrix, $\mathbf{K}$ is the global stiffness matrix, and $\mathbf{F}$ is the global force vector, $\mathbf{U}$ is the wavefield displacement (e.g., Marfurt, 1984; Virieux et al., 2011). With second-order central finite-difference discretization of the time derivatives, i.e.,

$$\ddot{\mathbf{U}} = \frac{\mathbf{U}^{t+\Delta t} - 2\mathbf{U}^{t} + \mathbf{U}^{t-\Delta t}}{\Delta t^2}, \tag{1.2}$$

we clearly need the inverse of global mass matrix $\mathbf{M}$ to get $\mathbf{U}^{t+\Delta t}$ from $\mathbf{U}^{t}$ and $\mathbf{U}^{t+\Delta t}$. For models with a large number of degrees of freedom, this is often quite inefficient, although LU decomposition can be applied (Marfurt, 1984). While mass lumping, i.e., creating a diagonal mass matrix with diagonal elements equal to the sum of all elements in a row, reduces this cost, it can also reduce the accuracy of the solution or even lead to instability when using high-order finite element basis functions (Grote et al., 2006).

The problem is solved by choosing appropriate integration points when calculat-

ing the local mass and stiffness matrices on the elements, i.e., the Gauss-Lobatto-Legendre (GLL) integration points, which can result in strictly diagonal global mass matrix, and this method is called spectral-element method (SEM). SEM was first introduced to the field of computational fluid dynamics (Patera, 1984), and later was applied in computational seismology (Seriani and Priolo, 1994; Komatitsch and Vilotte, 1998; Komatitsch et al., 1999, 2000a,b; Komatitsch and Tromp, 2003; Komatitsch and Martin, 2007). SEM is also advantageous in terms of dispersion behavior, which has spectral convergence (De Basabe and Sen, 2007; Virieux et al., 2011). SEM was later extended to handle triangular element and mixed formulation of acoustic and elastic wave equations (Cohen, 2002; Cohen and Fauqueux, 2005), which allows an easier implementation of perfectly matched layers (PML) to absorb the outgoing waves at the boundaries.

The above methods belong to the continuous Galerkin (CG) formulations of FEM, i.e., the basis functions are piecewise continuous within the support of field variable nodes, and are continuous at boundaries of elements as well, therefore the wavefield solutions are supposed to be continuous and smooth globally. However, the efficiency of CG-FEM is limited by the continuity requirements at areas where high contrasts in medium properties exist. Besides, CG-FEM is difficult to apply with a mesh discretization that includes various types of elements, such as a nonconforming mesh and hanging nodes. Another main drawback of CG-FEM is that due to the overlapping in the supports of the nodes, direct parallelization of the computation is quite difficult. These problems are naturally addressed with the discontinuous Galerkin (DG) FEM, which allows for solutions to be discontinuous across cell boundaries. DG-FEM was first proposed for the neutron transport equation by Reed and Hill (1973), and later applied in various different kinds of partial differential equations (e.g., Wheeler, 1978; Rivière et al., 1999). The application of DG-FEM to the wave propagation problem

started with the acoustic wave equation (Rivière et al., 2001; Grote et al., 2006) and elastic wave equations (Grote et al., 2006; De Basabe et al., 2008), and later poro-elastic wave equation (de la Puente et al., 2008; Dupuy et al., 2011), and a hybrid DG method was proposed for acoustic wave equation based on the mixed formulation of acoustic wave equation (Chung and Engquist, 2006, 2009). The DG method with higher-order time accuracy was also realized with so-called arbitrary high order derivatives (ADER) time integration (Käser and Dumbser, 2006; Dumbser and Käser, 2006; Käser et al., 2007; Dumbser et al., 2007; Käser and Dumbser, 2008). Wilcox et al. (2010) also proposed a DG scheme for elastic-acoustic coupled medium with high-order accuracy. DG schemes share the advantages that the global mass matrix is block diagonal, and therefore can dramatically reduce the computational cost compared with CG-FEM. Besides, since different elements are strictly distinct, the parallelization of the algorithm is much easier, and the efficiency of seismic wave equation modeling is much higher than CG-FEM as a result. Nevertheless, it is necessary to tune an important penalty parameter in DG-FEM, a parameter that is required for stability and convergence in this formulation.

Both the CG and DG formulations of the FEM can be powerful tools for seismic wave equation modeling (Virieux et al., 2011), both on the global scale or exploration scale seismic wave simulations. However, the various schemes of CG- and DG-FEM have not yet overcome the difficulties of large computational costs for large geological models, even with parallelization of the algorithm, especially when considering the multiscale nature of the Earth medium we have mentioned above.

The multiscale method developed in recent decades is an important potential solution to the multiscale problem. Hou and Wu (1997) proposed the pioneered

work for solving the elliptic partial differential equation

$$-\nabla \cdot (a\nabla u) = \mathbf{f}, \tag{1.3}$$

in $\Omega$, where $a = a(\mathbf{x}) = a_{ij}(\mathbf{x})$ is the conductivity that may be highly heterogeneous in space and $u = u(\mathbf{x})$ is the scalar field variable, with the multiscale finite-element method (MsFEM). In their approach, the elliptic problem is solved on a coarse mesh that may contain heterogeneities of the medium properties on a finer scale, and they determined the so-called multiscale basis functions $\phi_i$ solved from local problem

$$-\nabla \cdot (a\nabla \phi_i) = \mathbf{0}, \tag{1.4}$$

in each of the coarse node support $K_i \in \Omega$. The advantage of such basis functions is that $\phi$ depends on the local heterogeneities of $a(\mathbf{x})$, therefore can "store" the fine-scale information, which can finally help solve equation 1.3 more accurately on coarse mesh, while is less expensive in terms of computational memory.

The idea of multiscale basis function was later adopted in Chung et al. (2011a,b) and Gibson et al. (2014), where a multiscale method based on mixed formulation, i.e., pressure-velocity formulation, of the acoustic wave equation is designed to reduce the computational cost of full wavefield simulation. Gao et al. (2013) proposed an extension based on Chung et al. (2011a,b) for elastic wave equation.

The accuracy of MsFEM can be improved by capturing the fine-scale information with several multiscale basis functions solved from local spectral problem defined in each $K_i \in \Omega$ (Efendiev et al., 2011), which is

$$-\nabla \cdot (a\nabla \phi_i) = \lambda a \phi_i, \tag{1.5}$$

where $\lambda$ represent the eigenvalues. The improvement in the accuracy of multiscale solution relies on appropriate selection of eigenfunctions solved from 1.5, and mathematical analyses show that it is adequate to select the first several eigenfunctions $\phi_{i,1}, \phi_{i,2}, \cdots, \phi_{i,m}$, corresponding to the first several smallest eigenvalues $0 \leq \lambda_1 \leq \lambda_2 \leq \cdots \leq \lambda_m$, to achieve convergence of the multiscale solution. Efendiev et al. (2013) and Efendiev et al. (2013) constructed a different type of local spectral problem that is related to the solutions of equation 1.3 equipped with a set of carefully designed boundary conditions, and such improvement results in the so-called generalized multiscale finite-element method (GMsFEM). Chung et al. (2013b) and Chung et al. (2013a) applied this idea in acoustic wave propagation problem, and gave a rigorous proof of the stability and convergence of GMsFEM for acoustic wave equation. The basic assumption of applying such local spectral problem is that these eigenfunctions which corresponds with the smallest eigenvalues are physically the eigenmodes in the local support with lowest frequencies, and the multiscale basis functions that are built directly from these eigenfunctions can effectively relate the wavefield on the coarse scale to the wavefield on the finer scale.

While the numerical homogenization and GMsFEM for elastic wave equation are constructed based on the extensions of the above mentioned works, there are other previous investigations that are also entitled "multiscale" method, yet were constructed on different philosophies and methodologies, by recognizing the multiple-scale nature of the realistic medium.

One of these multiscale methods for wave propagation problem is operator-based upscaling of the wave equation (Arbogast et al., 1998; Vdovina et al., 2005). In this approach, the acoustic wave equation is solved with a two-stage upscaling procedure, where first in each coarse element the acoustic wave equation is solved on the fine scale, and in the second stage the particle acceleration wavefield, which is the gra-

dient of the pressure wavefield, is solved with the fine scale solution in each coarse element. Korostyshevskaya and Minkoff (2006) and Vdovina and Minkoff (2008) also gave an error and convergence analysis for this upscaling method and found that this multiscale method is equivalent to adding a new mixed derivative term to the wave equation, which is non-physical. The approach was also extended to solve the elastic wave equation (Vdovina et al., 2009). A clear difference between this operator-based upscaling and our own method is that we never need to solve the local problem, or the fine scale problem, in each time step. Instead, the only time where we need to solve fine scale problem is the once, in a preliminary offline stage before online time stepping, and the result, i.e., the eigenfunctions, are only related to the spatial variations of the medium, rather than the coarse wavefield. Vdovina et al. (2005) and Vdovina et al. (2009) also presented some examples of applying their multiscale method for seismic wave propagation. Owhadi and Zhang (2008) proposed another multiscale method based on the global change of coordinates technique (Owhadi and Zhang, 2005, 2007). However, the numerical approximation of the coordinates change is not trivial and requires rather expensive computation costs. Another multiscale method, the heterogeneous multiscale method (HMM) was proposed in E and Engquist (2002) and E and Engquist (2005), and later was investigated in finite-difference (Engquist et al., 2007, 2011) and finite-element implementations (Abdulle and Grote, 2011) for the acoustic wave equation. However, implementation of HMM requires the evaluation of a fine-scale local problem in each time step and therefore cannot be quite efficient as our multiscale basis function approach, which requires only a one-time solution of local problems before the time stepping. Capdeville et al. (2010) proposed a numerical homogenization method for non-periodic generally heterogeneous medium, which extracts the microscopic, or the fast part, of the medium properties, and then did a homogenization expansion in a way that is similar to conventional

numerical homogenization. However, this method requires the scale-separation of the medium, which may reduce the effectiveness in practical applications.

Given the above challenges in full wavefield modeling of wave equations, I develop new multiscale methods for simulating elastic wave propagation. Specifically, I propose a numerical homogenization for elastic media based on the multiscale basis function determined from local linear elasticity problem, which is an elastic extension of Hou and Wu (1997) and Chung et al. (2011a). This basis function performs as a spatial weight and enables us to get a set of effective elastic parameters, which can be utilized in any current elastic wave equation modeling algorithms and codes without many modifications of the algorithms and codes themselves, and can dramatically reduce the computational time and memory requirements. The most important feature of this numerical homogenization approach is that it can naturally handle arbitrarily heterogeneous media with general anisotropy, without concerning any simplifications or approximations of the Earth media, such as layering and fracturing. Also, I develop a GMsFEM both in CG and DG formulations for elastic wave propagation, which is an elastic extension of the GMsFEM proposed for the elliptic PDEs developed in Efendiev et al. (2011) and acoustic wave equation developed in Chung et al. (2013b) and Chung et al. (2013a). The core of the GMsFEM is the construction of two types of multiscale basis function based on some local linear elasticity spectral problems. Compared with the polynomial basis functions in conventional FEMs, the proposed multiscale basis functions depend on the fine-scale heterogeneity information of the media and are closely related to the low-frequency eigenmodes of the local coarse blocks. They are therefore more physically meaningful. Besides, the calculation of these multiscale basis functions is done one-time before simulation of propagation in the time stepping, and this enables the GMsFEM to simulate the elastic wave propagation only on a coarse scale grid. This one-time offline calculation

of local problems is the most important feature that distinguish the GMsFEM from those previously mentioned multiscale approaches (E and Engquist, 2002; Engquist et al., 2007; Vdovina et al., 2005, 2009; Abdulle and Grote, 2011) that need solutions of local problems at each time step, and therefore makes GMsFEM more effective in reducing the time and memory cost of full wavefield simulation of elastic wave equation.

## 1.3 Outline

In this dissertation, I construct new multiscale methods for elastic wave propagation in heterogeneous, anisotropic media with three sections.

In Section 2, I will first define the local linear elasticity problem with some proper boundary conditions to calculate the multiscale basis function. With the multiscale basis function, I derive a finite-difference scheme for stress-velocity mixed form elastic wave equation, and in this process, I obtain some coefficients before the difference terms that are equivalent to the effective medium parameters of the elastic wave equation. I use two examples and some comparisons between the multiscale approach and the conventional approaches including the Backus method Backus (1962) and the Schoenberg-Muir theory (Schoenberg and Muir, 1989) to verify the effectiveness of the homogenization method.

In Section 3, I first introduce the concept of a coarse mesh discretization overlaid by a fine mesh, and present weak forms of the second-order displacement form elastic wave equation. Then I introduce two methods to calculate the multiscale basis functions from two types of related yet different local linear elasticity spectral problems. I also introduce the damping boundary conditions used to reduce the spurious reflections of outgoing waves at the boundaries, and discuss a tentative approach based on solving eikonal equation to adaptively assign different numbers of basis functions

to different coarse blocks. Using four numerical examples, I verify the effectiveness of the proposed CG- and DG-GMsFEM, and compare the results with that from conventional CG-FEM. Also, I verify the idea of adaptive assignment of number of basis functions to different coarse blocks with a subset of Marmousi-2 elastic model.

In Section 4, I apply the DG-GMsFEM method to simulate the elastic wave propagation in the Marmousi-2 elastic model, as a demonstration of the multiscale for realistic examples. The Marmousi-2 model is large and at same time very finely discretized, and contains abundant of faults, steep dips and heterogeneities, which is a suitable model to test the effectiveness of the DG-GMsFEM. I summarize the methodology of DG-GMsFEM in the Method section, and give a detailed analysis of the modeling results in the Results and analysis part, including the error and the computational time.

In Conclusions, I will summarize the multiscale numerical homogenization and the GMsFEM, and also propose some possible improvements based on the current work.

# 2. NUMERICAL HOMOGENIZATION FOR HETEROGENEOUS, ANISOTROPIC ELASTIC MEDIA BASED ON MULTISCALE THEORY

## 2.1 Introduction

Earth models for applications in seismic modeling or imaging in oil and gas exploration are often simplified to media representing complex heterogeneity with smoothly changing physical properties, or sometimes layered media. A specific example in reservoir characterization is the representation of fractured media as a combination of an unfractured rock matrix and randomly or preferentially oriented fractures. Such approximations and simplifications can provide a means of representing the micro-scale petrophysical properties of the real medium, while still incorporating the influence of the micro-scale heterogeneity in analysis of the macro-scale Earth medium. One of the fundamental problems is then how to define a set of equivalent medium parameters that can accurately reproduce the macro-scale behavior of the real rocks, including properties such as seismic velocity, density, and anisotropy, for instance.

There have been many methods to address this problem, most of which are based on a horizontal layering approximation of the Earth. Backus (1962) proposed an averaging method ("Backus averaging") that averages the stress and displacement components in the vertical direction for equivalent elastic medium that is composed of horizontally aligned isotropic or transversely isotropic layers. This method has become the most widely applied method in practice. Their method, however, considers only anisotropy up to transversely isotropy with vertical axis (VTI), or horizontal axis (HTI), while in real geology, layers may exhibit lower-symmetry anisotropy, such as transversely isotropy with titled axis (TTI), or monoclinic anisotropy (Tsvankin

et al., 2010). The Backus averaging method has been extended to include the lower-symmetry anisotropy in Helbig and Schoenberg (1987). Later, by applying matrix and group theory, Schoenberg and Muir (1989) proposed a more general effective medium theory for horizontally aligned elastic layers, with general anisotropy where all the 21 independent elasticity constants might be nonzero in the elasticity matrix (we will refer to this as "Schoenberg-Muir theory"). Carcione et al. (2012) verified the Schoenberg-Muir theory, and by comparing the elastic wave equation modeling results they found that it can accurately solves the effective elasticity parameters for elastic medium composed of VTI, HTI, and TTI as well.

A limitation of the Backus averaging and Schoenberg-Muir theory is that the fine-scale medium must be horizontally layered. Researchers have made some attempts to extend such upscaling for media with general heterogeneities in fine scale. For example, Rijpsma and Zijl (1998) and Zijl et al. (2002) proposed a numerical homogenization procedure for Hooke's law based on several preservation principles, and they proposed that the upscaling can be implemented by displacement-stress averaging, displacement-energy averaging or stress-energy averaging. Grechka (2003) demonstrated another numerical-oriented method, but with some more straightforward boundary conditions to solve the local problem. In both of these two methods, they solve some appropriately defined local problem, which is either static or frequency-dependent equation of motion in elastic medium, and with the solution of the local problem, the displacement, strain, or stress can be averaged, and further the effective elasticity tensor can be defined by assuming the elastic wave equation has the same formulation in the coarse scale with that in the fine scale. Such kind of numerical or upscaling procedure is similar to Backus averaging, except that they are numerical-based, i.e., some local problem has to be solved numerically before the averaging.

Elastic properties such as anisotropy of the Earth can also come from the preferentially aligned fractures, and there have been corresponding theories to describe the effective medium approximated from the fractured rocks (e.g., Sayers and Kachanov, 1991; Sayers, 1996, 2002; Grechka and Kachanov, 2006; Schoenberg and Sayers, 1995; Tsvankin and Grechka, 2011). Besides, the problem of overall properties of cracked solid has also been studied by assuming circular or elliptic cracks (e.g., Budiansky and O'Connell, 1976; Hudson, 1980; Kachanov, 1980, 1992). These effective medium theories require certain parameterization of the fractures or cracks, while in this paper we concentrate on the media that use none of these parameterizations other than the elasticity constants and density. Therefore, there are fundamental differences between these types of effective medium theories and the numerical approach we investigate in this paper.

From the aspect of numerical simulation of seismic wave propagation, the effective medium theory can be viewed as an approach to reduce the computational costs for wave equation modeling, since the computational costs of various numerical methods for full wavefield modeling, such as the finite-difference method (e.g., Dablain, 1986; Virieux, 1986) and the finite-element method (e.g., Marfurt, 1984; Komatitsch et al., 1999; Käser and Dumbser, 2008), etc., are directly proportional with the element number in the geological models, and effective medium theory can provide a set of equivalent parameters that enables the simulations to be implemented with coarser element. This task has also been attacked by the so-called multiscale method for wave equations (Vdovina et al., 2005; Korostyshevskaya and Minkoff, 2006; Vdovina and Minkoff, 2008; Engquist et al., 2007, 2011; Owhadi and Zhang, 2008; Abdulle and Grote, 2011; Chung et al., 2011b, 2013a; Fu et al., 2013; Gao et al., 2013; Gibson et al., 2014). These various approaches to the multiscale problem can be quite different in their underlying principles, but tend to reach one specific goal, that

is to solve the wave equations on a set of coarsely discretized mesh to approximate the solutions of the wave equations on the finely discretized mesh, and each coarse element may contain finer elements with highly heterogeneous medium properties in space. Compared with the effective medium theories that are derived with certain assumptions (e.g., Backus, 1962), there are no restrictions on the subgrid medium parameter variations in the multiscale method, which means the subgrid media can be arbitrarily heterogeneous.

In this paper we investigate a numerical homogenization approach to derive the effective medium for arbitrarily heterogeneous elastic media with general anisotropy based on the multiscale method for wave equations (Chung et al., 2011a,b; Gao et al., 2013; Gibson et al., 2014). We first define a local problem to solve the multiscale basis function, with the boundary conditions that favors the derivations of rotated staggered-grid (RSG) finite-difference-like scheme (Saenger et al., 2000; Saenger and Bohlen, 2004), and finally we calculate the effective elasticity parameters by using the solved multiscale basis function. This approach (we will call it the "multiscale method" in the text), which is essentially a numerical approach, allows for arbitrary subgrid medium parameter variations. We remark that the local problem we solve to determine basis functions is essentially the same as that applied by Zijl et al. (2002) and Grechka (2003). However, they apply different boundary conditions, and their numerical procedures are designed to compute parameters based on average stresses and strains in a coarse block. In contrast, our method is based on a rotated, staggered-grid finite-difference approach, and the boundary conditions are designed to be consistent with this algorithm. Furthermore, instead of computing average stress and strain, we compute multiscale basis functions, and the effective parameters are based on appropriate summations of these bases.

Our paper will be organized as follows. In the following part, we will start

from the elastic wave equation in stress-velocity form, define the appropriate local problem and boundary conditions and solve the multiscale basis function, and then apply these results to calculate the effective elasticity constants. In the third part, we designed several numerical experiments to verify the effectiveness of our method, and give a discussion of a possible improvement of our method in a following section. An appendix shows the possibility of three-dimensional extensions of our method.

## 2.2 Theory

### *2.2.1 Elastic wave equation*

We start from the 2-D elastic wave equation expressed in the stress-velocity form as (e.g., Carcione, 2007)

$$\partial_t \boldsymbol{\sigma} = \mathbf{C}\boldsymbol{\Lambda}^{\mathrm{T}}\mathbf{v}, \tag{2.1a}$$

$$\rho\partial_t \mathbf{v} = \nabla \cdot \boldsymbol{\sigma} + \mathbf{f}, \tag{2.1b}$$

where $\mathbf{v} = \mathbf{v}(\mathbf{x}, t) = (v_1, v_3)^{\mathrm{T}}$ is the particle velocity vector, $\boldsymbol{\sigma} = \boldsymbol{\sigma}(\mathbf{x}, t) = (\sigma_{11}, \sigma_{33}, \sigma_{13})^{\mathrm{T}}$ is the stress tensor, $\mathbf{f} = \mathbf{f}(\mathbf{x}, t) = (f_1, f_3)^{\mathrm{T}}$ is the external source term, and

$$\mathbf{C} = \begin{pmatrix} C_{11} & C_{13} & C_{15} \\ C_{13} & C_{33} & C_{35} \\ C_{15} & C_{35} & C_{55} \end{pmatrix} \tag{2.2}$$

is the elasticity matrix in Voigt notation, and

$$\boldsymbol{\Lambda} = \begin{pmatrix} \partial_1 & 0 & \partial_3 \\ 0 & \partial_3 & \partial_1 \end{pmatrix}. \tag{2.3}$$

Equation 2.1 can describe the wave propagation in anisotropic elastic media with symmetry up to hexagonal anisotropy with titled symmetry axis in the $x_1 - x_3$ plane, i.e., transversely isotropy with titled axis (TTI), and monoclinic anisotropy (assuming the symmetry plane is the $x_1 - x_3$ plane), where $C_{15}$ and $C_{35}$ are possibly nonzero. In the following analysis, we will omit the source term $\mathbf{f}$ for convenience.

### *2.2.2 Multiscale basis function*

We discretize the computation domain $\Omega$ with a set of coarse mesh cells $\mathcal{Q}_H$ indicated by black lines and black dashed lines in Figure 2.1. The support of $\boldsymbol{\sigma}$ is denoted by $K_\sigma$, and the support of $\mathbf{v}$ is denoted by $K_v$. Each coarse element $K_\sigma$ or $K_v$ in $\mathcal{Q}_H$ may contain finer elements, consisting of a finer discretization of $\Omega$, say, $\mathcal{Q}_h$, indicated by gray lines in Figure 2.1.

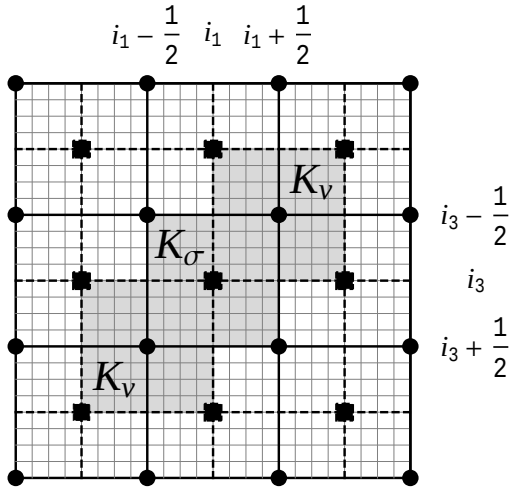


Figure 2.1: The mesh discretization of domain $\Omega$, ■ represents $\boldsymbol{\sigma} = (\sigma_{11}, \sigma_{33}, \sigma_{13})$, ● represents $\mathbf{v} = (v_1, v_3)$, black line rectangle $K_\sigma$ represents the support of stress components, black dashed line rectangle $K_v$ represents the support of velocity components.

The goal of our multiscale approach to solve the numerical homogenization prob-

lem for arbitrary heterogeneous media is to derive a finite-difference-like scheme that can solve the wave equation 2.1 on the coarse mesh $\mathcal{Q}_H$. This allows us to get a set of coefficients for the finite-difference terms that are equivalent to the effective elastic parameters of the coarse elements.

We first express the stress wavefield on $\mathcal{Q}_H$ as

$$\begin{aligned}\boldsymbol{\sigma}(\mathbf{x},t) &= \sum_i \mathbf{p}_i(t)\boldsymbol{\phi}_i(\mathbf{x}) \\ &= \sum_i (p_{11,i}(t)\phi_{11,i}(\mathbf{x}), p_{33,i}(t)\phi_{33,i}(\mathbf{x}), p_{13,i}(t)\phi_{13,i}(\mathbf{x})),\end{aligned} \tag{2.4}$$

where $i$ represent the $i$-th coarse cell, $\boldsymbol{\phi}_i(\mathbf{x})$ is the spatial multiscale basis function, and $\mathbf{p}_i(t)$ is the temporal part of $\boldsymbol{\sigma}_i$ . Rather than the conventional polynomial basis functions defined for FEM (e.g., Hughes, 1987; Hansbo and Larson, 2011), the multiscale basis functions here are determined through an appropriately defined local problem, which we will discuss later.

We also define the particle velocity wavefield on $\mathcal{Q}_H$ as

$$\begin{aligned}\mathbf{v}(\mathbf{x},t) &= \sum_i \mathbf{q}_i(t)\boldsymbol{\psi}_i(\mathbf{x}) \\ &= \sum_i (q_{1,i}(t)\psi_{1,i}(\mathbf{x}), q_{3,i}(t)\psi_{3,i}(\mathbf{x})),\end{aligned} \tag{2.5}$$

where we assume constant basis functions within each coarse cell, i.e., $\boldsymbol{\psi}_i = (\psi_{1,i}, \psi_{3,i}) = (1,1)$, for the velocity components, and $\mathbf{q}_i(t)$ is the temporal part of $\mathbf{v}_i$.

This mesh $\mathcal{Q}_H$ is similar to grid point positions in the rotated staggered grid (RSG) finite-difference scheme (Saenger et al., 2000; Saenger and Bohlen, 2004), where the stress components are placed in the center of a grid, occupying integer-grid position along both axes, and the velocity components are placed on the corners

of a grid, occupying half-grid positions along both axes.

Now we define a local problem to calculate the multiscale basis functions $\boldsymbol{\phi}_i(\mathbf{x})$, which is the linear elasticity extension of the multiscale basis functions in so-called multiscale finite-element method (MsFEM) developed for acoustic case (Efendiev and Hou, 2009; Chung et al., 2011a,b; Gibson et al., 2014).

We know that $K_\sigma = [i_1 - \frac{1}{2}, i_1 + \frac{1}{2}] \times [i_3 - \frac{1}{2}, i_3 + \frac{1}{2}]$ for stress $\boldsymbol{\sigma}(i_1, i_3)$ is in fact also composed of four sub-rectangles, which are parts of the supports of $\mathbf{v}(i_1 - \frac{1}{2}, i_3 - \frac{1}{2})$, $\mathbf{v}(i_1 + \frac{1}{2}, i_3 - \frac{1}{2})$, $\mathbf{v}(i_1 - \frac{1}{2}, i_3 + \frac{1}{2})$ and $\mathbf{v}(i_1 + \frac{1}{2}, i_3 + \frac{1}{2})$, as indicated in Figure 2.1. When determining the multiscale basis functions for $\boldsymbol{\sigma}(i_1, i_3)$, we solve the following local static linear elasticity problem in each of these four sub-rectangles:

$$\boldsymbol{\sigma} = \mathbf{C}\boldsymbol{\Lambda}^{\mathrm{T}}\mathbf{u}, \tag{2.6a}$$

$$-\nabla \cdot \boldsymbol{\sigma} = \mathbf{0}, \tag{2.6b}$$

under the boundary conditions

$$\sigma_{11} = 1, \qquad \text{on } \mathcal{E}_1, \tag{2.7a}$$

$$\sigma_{33} = 1, \qquad \text{on } \mathcal{E}_3, \tag{2.7b}$$

$$\sigma_{13} = 1, \qquad \text{on } \mathcal{E}_1 \text{ and } \mathcal{E}_3, \tag{2.7c}$$

where $\mathcal{E}_1$ and $\mathcal{E}_3$ are the two vertical and horizontal edges of each of the four sub-rectangles, respectively, and $\mathbf{u}$ is the displacement. The local problem 2.6 along with boundary conditions 2.7 can be solved with second-order finite-element method for linear elasticity (e.g., Larson and Bengzon, 2013). We present necessary details of how to solve local problem in Appendix A. Solutions of $\sigma_{11}$, $\sigma_{33}$ and $\sigma_{13}$, which are denoted as $\phi_{11}$, $\phi_{33}$ and $\phi_{13}$, in all these four rectangles, are joined in $K_\sigma$ and taken

as the multiscale basis functions of $\sigma_{11}(i_1, i_3)$, $\sigma_{33}(i_1, i_3)$ and $\sigma_{13}(i_1, i_3)$, respectively.

### *2.2.3 Effective medium parameters*

We then transform equation 2.1a into an equivalent form as

$$\mathbf{S}\partial_t \boldsymbol{\sigma} = \boldsymbol{\Lambda}^{\mathrm{T}}\mathbf{v}, \tag{2.8}$$

where $\mathbf{S} = \mathbf{C}^{-1}$. Explicitly, it is,

$$\begin{pmatrix} S_{11} & S_{13} & S_{15} \\ S_{13} & S_{33} & S_{35} \\ S_{15} & S_{35} & S_{55} \end{pmatrix} \partial_t \begin{pmatrix} \sigma_{11} \\ \sigma_{33} \\ \sigma_{13} \end{pmatrix} = \begin{pmatrix} \partial_1 v_1 \\ \partial_3 v_3 \\ \partial_1 v_3 + \partial_3 v_1 \end{pmatrix}. \tag{2.9}$$

Beginning with the first equation in 2.9, we write the stress as spatial basis function and temporal part as defined in equation 2.4, multiply both sides by a test function $\phi_{11}$, integrate over the support $K_\sigma$ of stress components $\boldsymbol{\sigma}(i_1, i_3)$, and get

$$\begin{aligned} &\begin{pmatrix} \int_{K_\sigma} S_{11}\phi_{11}\phi_{11}d\mathbf{x} & \int_{K_\sigma} S_{13}\phi_{33}\phi_{11}d\mathbf{x} & \int_{K_\sigma} S_{15}\phi_{13}\phi_{11}d\mathbf{x} \end{pmatrix} \begin{pmatrix} \dot{p}_{11} \\ \dot{p}_{33} \\ \dot{p}_{13} \end{pmatrix} \\ &= \int_{K_\sigma} \phi_{11}\partial_1 v_1 d\mathbf{x}, \end{aligned} \tag{2.10}$$

where $\dot{p}_{ij} = dp_{ij}/dt$. To get the effective medium parameters for $K_\sigma$, we need to eliminate the integral on both sides of the above equation. For the RHS of equation 2.10, we can integrate by parts, and get

$$\int_{K_\sigma} \phi_{11}\partial_1 v_1 d\mathbf{x}$$

$$= \int_{i_3-1/2}^{i_3+1/2} \int_{i_1-1/2}^{i_1+1/2} \phi_{11} \partial_1 v_1 dx_1 dx_3$$
$$= \left( \int_{i_3-1/2}^{i_3+1/2} v_1 \phi_{11} dx_3 \right) \Bigg|_{i_1-1/2}^{i_1+1/2} - \int_{i_3-1/2}^{i_3+1/2} \int_{i_1-1/2}^{i_1+1/2} v_1 \partial_1 \phi_{11} dx_1 dx_3. \tag{2.11}$$

First we simplify the second part in RHS of equation 2.11. Recall that the velocity component $v_1$ is constant in each of the four rectangles composing of $K_\sigma(i_1, i_3)$. Therefore,

$$\begin{aligned}
&\int_{i_3-1/2}^{i_3+1/2} \int_{i_1-1/2}^{i_1+1/2} v_1 \partial_1 \phi_{11} dx_1 dx_3 \\
&= \int_{i_3-1/2}^{i_3} \int_{i_1-1/2}^{i_1} v_1 \partial_1 \phi_{11} dx_1 dx_3 + \int_{i_3-1/2}^{i_3} \int_{i_1}^{i_1+1/2} v_1 \partial_1 \phi_{11} dx_1 dx_3 \\
&+ \int_{i_3}^{i_3+1/2} \int_{i_1-1/2}^{i_1} v_1 \partial_1 \phi_{11} dx_1 dx_3 + \int_{i_3}^{i_3+1/2} \int_{i_1}^{i_1+1/2} v_1 \partial_1 \phi_{11} dx_1 dx_3.
\end{aligned} \tag{2.12}$$

Then for each of the four rectangles, e.g., $K_{\sigma,1} = [i_1 - \frac{1}{2}, i_1] \times [i_3 - \frac{1}{2}, i_3]$, since $v_1$ is constant and $\phi_{11} = 1$ on two vertical edges of $K_{\sigma,1}$, we have

$$\begin{aligned}
&\int_{i_3-1/2}^{i_3} \int_{i_1-1/2}^{i_1} v_1 \partial_1 \phi_{11} dx_1 dx_3 \\
&= v_1 \left( i_1 - \frac{1}{2}, i_3 - \frac{1}{2} \right) \int_{i_3-1/2}^{i_3} \int_{i_1-1/2}^{i_1} \partial_1 \phi_{11} dx_1 dx_3 \\
&= v_1 \left( i_1 - \frac{1}{2}, i_3 - \frac{1}{2} \right) \int_{i_3-1/2}^{i_3} \int_{1}^{1} d\phi_{11} dx_3 \\
&= v_1 \left( i_1 - \frac{1}{2}, i_3 - \frac{1}{2} \right) \times 0 \\
&= 0.
\end{aligned} \tag{2.13}$$

For the rest of three integrals in equation 2.12, we have same result, and therefore

$$\int_{i_3-1/2}^{i_3+1/2} \int_{i_1-1/2}^{i_1+1/2} v_1 \partial_1 \phi_{11} dx_1 dx_3 = 0. \tag{2.14}$$

For the first part in equation 2.11, we have

$$
\begin{aligned}
&\left(\int_{i_3-1/2}^{i_3+1/2} v_1\phi_{11}dx_3\right)\Bigg|_{i_1-1/2}^{i_1+1/2} \\
&= \left(\int_{i_3-1/2}^{i_3} v_1\phi_{11}dx_3 + \int_{i_3}^{i_3+1/2} v_1\phi_{11}dx_3\right)\Bigg|_{i_1-1/2}^{i_1+1/2} \\
&= \int_{i_3-1/2}^{i_3}\left[v_1\left(i_1+\frac{1}{2},x_3\right) - v_1\left(i_1-\frac{1}{2},x_3\right)\right]\phi_{11}dx_3 \\
&+ \int_{i_3}^{i_3+1/2}\left[v_1\left(i_1+\frac{1}{2},x_3\right) - v_1\left(i_1-\frac{1}{2},x_3\right)\right]\phi_{11}dx_3 \\
&= \frac{\Delta x_3}{2}\left[v_1\left(i_1+\frac{1}{2},i_3+\frac{1}{2}\right) + v_1\left(i_1+\frac{1}{2},i_3-\frac{1}{2}\right)\right. \\
&\qquad \left. -v_1\left(i_1-\frac{1}{2},i_3+\frac{1}{2}\right) - v_1\left(i_1-\frac{1}{2},i_3-\frac{1}{2}\right)\right] \\
&= \frac{\Delta r}{2\Delta x_1}\frac{1}{\Delta r}\left\{\left[v_1\left(i_1+\frac{1}{2},i_3+\frac{1}{2}\right) - v_1\left(i_1-\frac{1}{2},i_3-\frac{1}{2}\right)\right]\right. \\
&\qquad \left. + \left[v_1\left(i_1+\frac{1}{2},i_3-\frac{1}{2}\right) - v_1\left(i_1-\frac{1}{2},i_3+\frac{1}{2}\right)\right]\right\}\Delta x_1\Delta x_3 \\
&\approx \frac{\Delta r}{2\Delta x_1}(D_3v_1 + D_1v_1)\Delta x_1\Delta x_3, \qquad (2.15)
\end{aligned}
$$

where $\Delta r = \sqrt{\Delta x_1^2 + \Delta x_3^2}$, $D_1$ and $D_3$ are the partial derivatives along the rotated axes, as defined in the rotated staggered-grid finite-difference method (Saenger et al., 2000; Saenger and Bohlen, 2004; Saenger et al., 2007), and the last step in equation 2.15 uses the discrete finite-difference term to approximate the continuous partial derivatives, and therefore

$$
\int_{K_\sigma} \phi_{11}\partial_1 v_1 d\Omega \approx \Delta x_1\Delta x_3\partial_1 v_1 = S_{K_\sigma}\partial_1 v_1, \qquad (2.16)
$$

where $S_{K_\sigma} = \Delta x_1\Delta x_3$ is the area of $K_\sigma$.

Meanwhile, for the LHS of equation 2.10, since both $S_{ij}$ and $\phi_{st}$ are discrete values

on each fine grid within $K_\sigma$, we then have, for example,

$$\int_{K_\sigma} S_{11}\phi_{11}\phi_{11}d\mathbf{x} \approx \frac{S_{K_\sigma}}{n_1 n_3}\sum_{j_1=1}^{n_1}\sum_{j_3=1}^{n_3} S_{11}(j_1,j_3)\phi_{11}(j_1,j_3)\phi_{11}(j_1,j_3) = S_{K_\sigma}\tilde{S}_{11}, \quad (2.17)$$

where $n_1$ and $n_3$ represent the grid number in $x_1$ and $x_3$ direction within $K_\sigma$, respectively.

With the above results, for the first equation we finally have

$$\begin{pmatrix} \tilde{S}_{11} & \tilde{S}_{33} & \tilde{S}_{13} \end{pmatrix} \begin{pmatrix} \dot{p}_{11} \\ \dot{p}_{33} \\ \dot{p}_{13} \end{pmatrix} = \partial_1 v_1, \quad (2.18)$$

where $\tilde{S}_{ij}$ represents the effective compliance in $K_\sigma$, and can be calculated similarly as in equation 2.17. Clearly, equation 2.18 is defined on coarse mesh $\mathcal{Q}_H$ with "effective" elasticity parameters $\tilde{S}_{ij}$.

We can repeat the same manipulation for the second equation in equation 2.9. Based on the boundary conditions we prescribe for $\phi_{33}$, i.e., $\phi_{33} = 1$ on two horizontal edges of each of the four sub-rectangles, we integrate both sides with a test function $\phi_{33}$ on both sides, and then for the RHS we have

$$\begin{aligned} &\int_{K_\sigma} \phi_{33}\partial_3 v_3 d\mathbf{x} \\ &= \int_{i_3-1/2}^{i_3+1/2}\int_{i_1-1/2}^{i_1+1/2} \phi_{33}\partial_3 v_3 dx_1 dx_3 \\ &= \left(\int_{i_1-1/2}^{i_1+1/2} v_3\phi_{33}dx_1\right)\Bigg|_{i_3-1/2}^{i_3+1/2} - \int_{i_3-1/2}^{i_3+1/2}\int_{i_1-1/2}^{i_1+1/2} v_3\partial_3\phi_{33}dx_1dx_3 \\ &\approx S_{K_\sigma}\partial_3 v_3. \end{aligned} \quad (2.19)$$

Again, the terms on the LHS can be calculated similar with that in equation 2.17.

And finally, for the third equation in equation 2.9, we integrate both sides with a test function $\phi_{13}$ in $K_\sigma$, and get the RHS as

$$
\begin{aligned}
&\int_{K_\sigma} \phi_{13}(\partial_1 v_3 + \partial_3 v_1) d\mathbf{x} \\
&= \int_{i_3-1/2}^{i_3+1/2} \int_{i_1-1/2}^{i_1+1/2} (\phi_{13}\partial_1 v_3 + \phi_{13}\partial_3 v_1) dx_1 dx_3 \\
&= \left( \int_{i_3-1/2}^{i_3+1/2} v_3 \phi_{13} dx_3 \right) \Bigg|_{i_1-1/2}^{i_1+1/2} - \int_{i_3-1/2}^{i_3+1/2} \int_{i_1-1/2}^{i_1+1/2} v_3 \partial_1 \phi_{13} dx_1 dx_3 \\
&+ \left( \int_{i_1-1/2}^{i_1+1/2} v_1 \phi_{13} dx_1 \right) \Bigg|_{i_3-1/2}^{i_3+1/2} - \int_{i_3-1/2}^{i_3+1/2} \int_{i_1-1/2}^{i_1+1/2} v_1 \partial_3 \phi_{13} dx_1 dx_3 \\
&\approx S_{K_\sigma}(\partial_1 v_3 + \partial_3 v_1),
\end{aligned} \tag{2.20}
$$

and the LHS can be got in a similar way with that in equation 2.17.

Now we look at the equation 2.1b. We integrate the first equation within 2.1b in, e.g., the support of $\mathbf{v}(i_1 + \frac{1}{2}, i_3 + \frac{1}{2})$, and get

$$
\begin{aligned}
&\int_{i_3}^{i_3+1} \int_{i_1}^{i_1+1} \rho \partial_t v_1 dx_1 dx_3 \\
&= \int_{i_3}^{i_3+1} \int_{i_1}^{i_1+1} \partial_1 \sigma_{11} dx_1 dx_3 + \int_{i_3}^{i_3+1} \int_{i_1}^{i_1+1} \partial_3 \sigma_{13} dx_1 dx_3 \\
&= \int_{i_3}^{i_3+1} \int_{\sigma_{11}(i_1,x_3)}^{\sigma_{11}(i_1+1,x_3)} d\sigma_{11} dx_3 + \int_{i_1}^{i_1+1} \int_{\sigma_{13}(x_1,i_3)}^{\sigma_{13}(x_1,i_3+1)} d\sigma_{13} dx_1 \\
&= \int_{i_3}^{i_3+1} [\sigma_{11}(i_1+1, x_3) - \sigma_{11}(i_1, x_3)] dx_3 \\
&+ \int_{i_1}^{i_1+1} [\sigma_{13}(x_1, i_3+1) - \sigma_{13}(x_1, i_3)] dx_1 \\
&= \left[ \int_{i_3}^{i_3+1/2} \sigma_{11}(i_1+1, x_3) dx_3 + \int_{i_3+1/2}^{i_3+1} \sigma_{11}(i_1+1, x_3) dx_3 \right]
\end{aligned}
$$

$$
\begin{aligned}
&- \left[ \int_{i_3}^{i_3+1/2} \sigma_{11}(i_1, x_3) dx_3 + \int_{i_3+1/2}^{i_3+1} \sigma_{11}(i_1, x_3) dx_3 \right] \\
&+ \left[ \int_{i_1}^{i_1+1/2} \sigma_{13}(x_1, i_3+1) dx_1 + \int_{i_1+1/2}^{i_1+1} \sigma_{13}(x_1, i_3+1) dx_1 \right] \\
&- \left[ \int_{i_1}^{i_1+1/2} \sigma_{13}(x_1, i_3) dx_1 + \int_{i_1+1/2}^{i_1+1} \sigma_{13}(x_1, i_3) dx_1 \right] \\
&= \frac{\Delta x_3}{2} [\sigma_{11}(i_1+1, i_3) + \sigma_{11}(i_1+1, i_3+1) - \sigma_{11}(i_1, i_3) - \sigma_{11}(i_1, i_3+1)] \\
&+ \frac{\Delta x_1}{2} [\sigma_{13}(i_1, i_3+1) + \sigma_{13}(i_1+1, i_3+1) - \sigma_{13}(i_1, i_3) - \sigma_{13}(i_1+1, i_3)]. \qquad (2.21)
\end{aligned}
$$

Recall the manipulations in the last step of equation 2.15, it is trivial to find that

$$
\begin{aligned}
&\int_{i_3}^{i_3+1} \int_{i_1}^{i_1+1} \rho \partial_t v_1 dx_1 dx_3 \\
&\approx \frac{\Delta r}{2\Delta x_1} (D_3\sigma_{11} + D_1\sigma_{11}) \Delta x_1 \Delta x_3 + \frac{\Delta r}{2\Delta x_3} (D_3\sigma_{13} - D_1\sigma_{13}) \Delta x_1 \Delta x_3 \\
&= S_{K_v} (\partial_1\sigma_{11} + \partial_3\sigma_{13}), \qquad (2.22)
\end{aligned}
$$

where $S_{K_v}$ is the area of the support of $\mathbf{v}(i_1 + \frac{1}{2}, i_3 + \frac{1}{2})$. Further, for the LHS of equation 2.22, since $v_1$ is constant in $K_v$, we then have

$$
\begin{aligned}
\int_{i_3}^{i_3+1} \int_{i_1}^{i_1+1} \rho \partial_t v_1 dx_1 dx_3 &= \partial_t v_1 \int_{i_3}^{i_3+1} \int_{i_1}^{i_1+1} \rho dx_1 dx_3 \\
&\approx \partial_t v_1 \tilde{\rho} S_{K_v}, \qquad (2.23)
\end{aligned}
$$

with

$$
\tilde{\rho} = \frac{1}{m_1} \frac{1}{m_3} \sum_{j_1=1}^{m_1} \sum_{j_3=1}^{m_3} \rho(j_1, j_3). \qquad (2.24)
$$

Therefore,

$$
\tilde{\rho} \partial_t v_1 = \partial_1\sigma_{11} + \partial_3\sigma_{13}. \qquad (2.25)
$$

Similarly, for the second equation in 2.1b, we have

$$\tilde{\rho}\partial_t v_3 = \partial_1 \sigma_{13} + \partial_3 \sigma_{33}, \tag{2.26}$$

with $\tilde{\rho}$ have exactly the same definition as that in equation 2.24.

We then arrive at the effective elastic wave equation on the coarse mesh $\mathcal{Q}_H$ as

$$\partial_t \boldsymbol{\sigma} = \tilde{\mathbf{C}} \boldsymbol{\Lambda}^{\mathrm{T}} \mathbf{v}, \tag{2.27}$$

$$\tilde{\rho}\partial_t \mathbf{v} = \nabla \cdot \boldsymbol{\sigma} + \mathbf{f}, \tag{2.28}$$

where the effective elasticity matrix $\tilde{\mathbf{C}} = \tilde{\mathbf{S}}^{-1}$, and

$$\tilde{\mathbf{S}} = \begin{pmatrix} S_{11}\phi_{11}\phi_{11} & S_{13}\phi_{33}\phi_{11} & S_{15}\phi_{13}\phi_{11} \\ S_{13}\phi_{11}\phi_{33} & S_{33}\phi_{33}\phi_{33} & S_{35}\phi_{13}\phi_{33} \\ S_{15}\phi_{11}\phi_{13} & S_{35}\phi_{33}\phi_{13} & S_{55}\phi_{13}\phi_{13} \end{pmatrix}, \tag{2.29}$$

where each of the element in $\tilde{\mathbf{S}}$ is a summation of the product of compliances and basis functions of all the fine elements within $K_\sigma$:

$$S_{ij}\phi_{st}\phi_{pq} = \frac{1}{n_1 n_3} \sum_{j_1=1}^{n_1} \sum_{j_3=1}^{n_3} S_{ij}(j_1, j_3)\phi_{st}(j_1, j_3)\phi_{pq}(j_1, j_3), \tag{2.30}$$

The effective density is simply computed with equation 2.24.

Since each $\tilde{\mathbf{C}}$ is computed as a weighted average of compliances, it can be interpreted as an effective property that is in some ways analogous to Backus averaging. In our case, however, the weight terms in the averaging are the basis function terms computed numerically from the solution of the local elasticity problem.

This approach does not impose and restrictions on the geometry or magnitude

of subgrid medium variations, which therefore can be arbitrary. In such cases, even for simple layered subgrid medium property variations, there are no analytic results for $\phi_{11}$, $\phi_{33}$ or $\phi_{13}$, i.e., they can be only determined numerically, and this is quite different from previous theories such as Backus averaging or Schoenberg-Muir theory. Also, this method can be straightforwardly extended to 3-D (see Appendix B) where general anisotropy with all 21 independent elasticity constants is addressed, and, again, the subgrid medium can be arbitrarily heterogeneous.

## 2.3 Numerical results

We apply three kinds of numerical tests to verify the effectiveness of our proposed method. These tests are mainly for the first category of effective medium theory, i.e., the Backus averaging and the Schoenberg-Muir theory.

### *2.3.1 Horizontally layered medium*

In the first set of tests, we compare the results from Backus averaging, the Schoenberg-Muir theory and the multiscale method for horizontally layered isotopic and anisotropic elastic media. It is important to note that the original version of Backus averaging method is valid for describing the effective properties of media composed of isotropic elastic layers, or elastic layers with anisotropy up to vertical transverse isotropy (VTI) and horizontal transverse isotropy (HTI), i.e., $C_{15} = C_{35} = 0$. Schoenberg-Muir theory can describe the effective properties of medium composed of layers with generally anisotropic elastic properties, including titled transverse isotropy (TTI) or triclinic anisotropy where all 21 independent elasticity constants nonzero. To keep appropriate length of our text, in the test we restrict our attention on anisotropy up to two-dimensional TTI, i.e., medium properties can be described by elasticity matrix 2.2.

For simplicity, we take the two sets of test parameters presented by Carcione et al.

(2012). In their tests, they have used Schoenberg-Muir theory to derive the effective medium parameters, and verified the accuracy by comparing the spatial wavefields calculated by Fourier pseudospectral method for original layered medium and the effective medium.

The first test is for a medium composed of VTI layers and HTI layers, with elastic constants $C_{11} = 46.00$, $C_{13} = 18.00$, $C_{15} = 0.00$, $C_{33} = 30.00$, $C_{35} = 0.00$, $C_{55} = 7.00$ for VTI layer, and $C_{11} = 30.00$, $C_{13} = 18.00$, $C_{15} = 0.00$, $C_{33} = 46.00$, $C_{35} = 0.00$, $C_{55} = 7.00$ for HTI layer. We assume fine grid model contains $1000 \times 1000$ grids, and we set the coarsening to be $10 \times 10$, which means that in each coarse grid block, there are $10 \times 10$ fine grids. Besides, the size of fine grid is 1 m in each direction, and in our test, we set the layer thickness is 1 m as well.

The effective elasticity constants from Backus averaging or Schoenberg-Muir theory are (Carcione et al., 2012)

$$\mathbf{C}_{\text{Backus}} = \mathbf{C}_{\text{Schoenberg-Muir}} = \begin{pmatrix} 38.00 & 18.00 & 0 \\ & 36.30 & 0 \\ & & 7.00 \end{pmatrix} \quad \text{GPa}, \tag{2.31}$$

and by our method,

$$\mathbf{C}_{\text{Multiscale}} = \begin{pmatrix} 37.78 & 17.89 & 0 \\ & 36.24 & 0 \\ & & 7.00 \end{pmatrix} \quad \text{GPa}. \tag{2.32}$$

Since Carcione et al. (2012) verified the results of the Schoenberg-Muir theory by means of wave equation modeling, we take the results from Schoenberg-Muir theory to be the true solution. We compared the results from Backus averaging, Schoenberg-

Muir theory and our method, and we see that for such a layer composition, Backus averaging and Schoenberg-Muir theory give exactly the same result, and due to the numerical solution nature of our method, we give almost equivalent results but with tiny deviations. In fact, the relative differences of the elasticity constants from our calculated constants are

$$\text{relative difference} = -\begin{pmatrix} 0.57\% & 0.62\% & 0 \\ & 0.15\% & 0 \\ & & 0 \end{pmatrix} \tag{2.33}$$

In the second test, the medium is composed of VTI and TTI layers, and the layer thickness is again 1 m, and the elasticity constants are $C_{11} = 46.00$, $C_{13} = 18.00$, $C_{15} = 0.00$, $C_{33} = 30.00$, $C_{35} = 0.00$, $C_{55} = 7.00$ for the VTI medium, and $C_{11} = 35.00$, $C_{13} = 21.00$, $C_{15} = -4.00$, $C_{33} = 35.00$, $C_{35} = -4.00$, $C_{55} = 10.00$ for the TTI material. Under such composition, we could only use only Schoenberg-Muir theory and our method for the comparison. The Shoenberg-Muir solution is

$$\mathbf{C}_{\text{Schoenberg-Muir}} = \begin{pmatrix} 40.00 & 19 & -1.6 \\ & 31.90 & -1.5 \\ & & 8.1 \end{pmatrix} \quad \text{GPa}, \tag{2.34}$$

and our solution is

$$\mathbf{C}_{\text{Multiscale}} = \begin{pmatrix} 39.83 & 18.85 & -1.58 \\ & 31.50 & -1.43 \\ & & 8.11 \end{pmatrix} \quad \text{GPa}, \tag{2.35}$$

with relative errors

$$\text{relative difference} = -\begin{pmatrix} 0.42\% & 0.80\% & 1.44\% \\ & 1.26\% & 4.64\% \\ & & -0.20\% \end{pmatrix}. \tag{2.36}$$

And we can see that except $C_{15}$, $C_{33}$ and $C_{35}$, the other parameters are deviated with less than 1% relative error. The difference for $C_{35}$ between our approach and analytical result is relatively large compared with that of the other elasticity constants, and it is not obvious why this constant is special. This might be due to numerical errors introduced when we solve the local problem, since we have used only second-order FEM. By improving the accuracy of the scheme of solving the local problem, this difference might be reduced.

### *2.3.2 Arbitrarily heterogeneous medium*

In the proceeding section, we have compared our method with Backus averaging and Schoenberg-Muir theory and sees that our method can be accurate. However, as we have discussed before, neither Backus method nor Schoenberg-Muir theory is directly applicable to medium which is arbitrarily heterogeneous, while there are no such difficulties by applying our method. In the following we will apply our method to such a model, and since there is no independent solution in this situation, we will compare the wave equation modeling results from the fine grid model and from the effective medium. For both cases, we use 20th-order RSG finite-difference method (see Appendix C), with multi-axial perfectly matched layers (M-PML) (Meza-Fajardo and Papageorgiou, 2008) to absorb the outgoing wavefield at the four boundaries.

The first model is composed of $200 \times 200$ coarse elements, each of which is composed of $20 \times 20$ fine elements, and each of the fine element has a size of 1 m $\times$ 1 m.

Figures 2.2(a)–2.2(f) show the elasticity parameter variations within each coarse element. All elasticity constants show some heterogeneities, including horizontal layering, elliptic inclusions with different orientations, and random heterogeneities as well. Clearly, such a subgrid model cannot be simply treated as finely layered model, and therefore Backus averaging or Schoenberg-Muir theory cannot be directly utilized here. The elasticity constants of the equivalent homogeneous effective medium, which can be computed using equation 2.29, are

$$\mathbf{C}_{\text{Multiscale}} = \begin{pmatrix} 38.96 & 20.40 & -1.21 \\ & 34.52 & -0.96 \\ & & 8.92 \end{pmatrix} \quad \text{GPa}, \tag{2.37}$$

which represents monoclinic anisotropy. We assume constant density for the model, i.e., $\rho = 2500$ kg·m$^{-3}$.

The forward modeling in both the original model and the effective model utilizes a 7.5 Hz Ricker wavelet for the source located in the center of the model. For the coarse grid model, this corresponds to about 12 grid cells per qS-wavelength and 26 grid cells for the qP-wavelength. Given that the fine grid is sampled 20 times more finely, these ratios are about 20 times larger for the fine model.

Figure 2.3(a)–2.3(d) compares the wave equation forward modeling wavefields at 0.5 s from the two models. We see that the wavefields in the effective medium can well approximate the wavefields in the fine grid model. Furthermore, we compare directly the two wave fields at this same time at a depth of 2400 m in the model. We plot the fine grid wavefield as blue curve and plot the coarse grid wavefield with red dots, and we see that they are in good agreement (Figure 2.4), and we can expect similar accurate approximation of seismograms from the receivers placed in

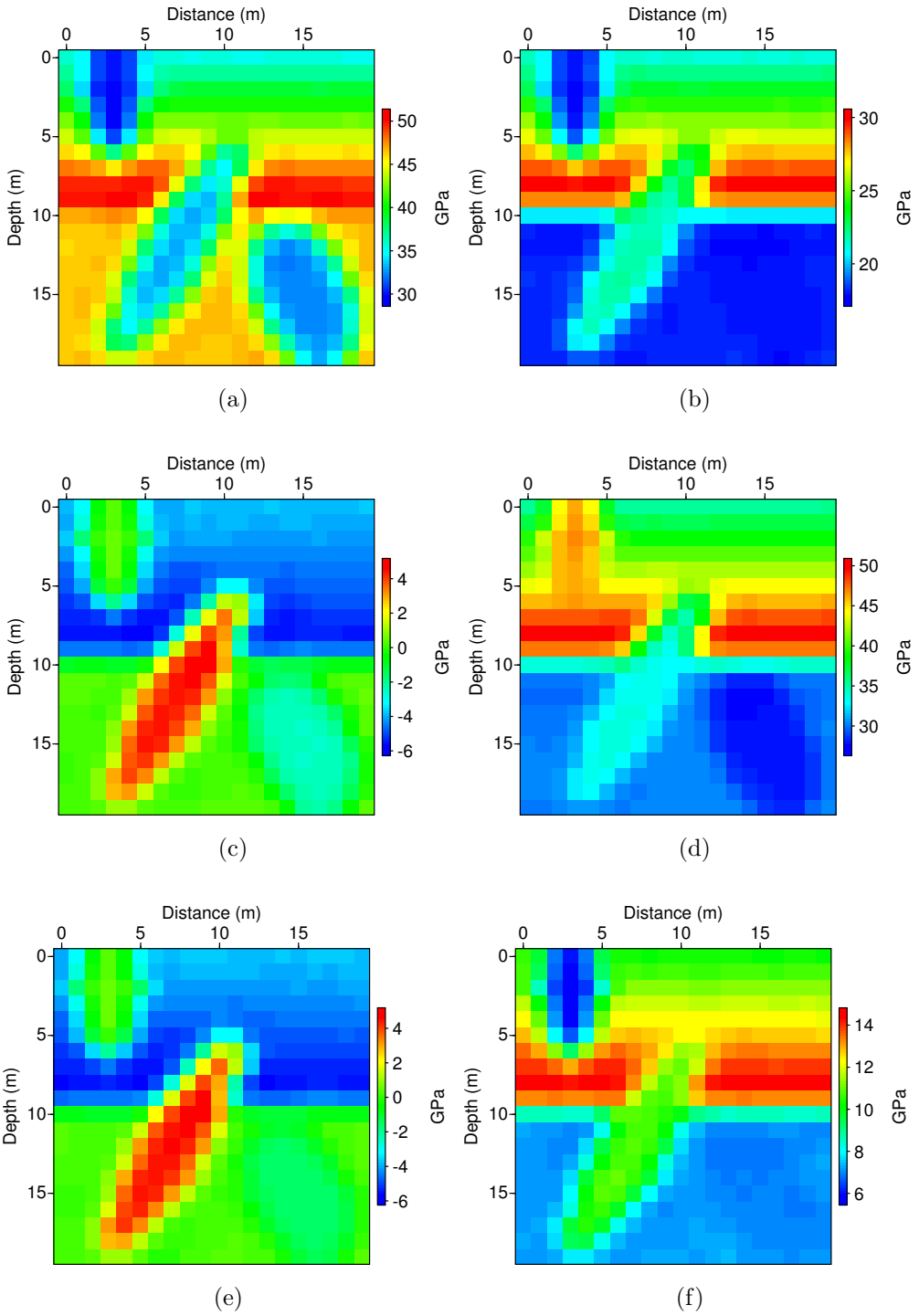


Figure 2.2: Subgrid elasticity parameter models. (a)–(f) represent $C_{11}$, $C_{13}$, $C_{15}$, $C_{33}$, $C_{35}$ and $C_{55}$, respectively. The grid size is $1 \times 1$ m$^2$.

same positions in two models, given the accuracy in space. Because of the small grid size of the fine model, the modeling time step has to be quite small to ensure stability, 0.1 ms in our modeling, while for the effective medium we can safely use 1.0 ms. This makes the ratio of computation time of fine grid modeling and effective medium modeling to be about 93303 s : 9.13 s, i.e., $10^5$, for the same total wave propagation time (0.5 s in our numerical experiments).

The second model is an random medium model, generated with the von Kármán correlation function (Goff and Jordan, 1988; Klimeš, 2002), with correlation lengths 30 m in horizontal direction and 5 m in vertical direction, respectively, and there are three horizontal reflectors within the model. The original model contains 2000×2000 grids, each is 1 m×1 m in size. Figure 2.5(a)–2.5(f) show the elasticity constants variations of this model. Besides, we assume constant density (1000 kg/m$^3$ for convenience) for our model. As in the previous example, such a model does not satisfy the basic assumptions of Backus averaging or Schoenberg-Muir theory.

We compute effective moduli and density models using a coarse grid with 200×200 cells, each of which is 10 m×10 m, i.e., each coarse grid contains 10×10 fine cells from the original model. The source placed at (1000 m, 40 m) is a Ricker wavelet with central frequency 15 Hz, and the receivers are at a depth of 40 m, ranging from 0 to 2000 m, with a interval of 10 m. We compare the wavefield snapshots and the seismograms calculated using the 20-th order RSG. Figure 2.6(a)–2.6(d) are the wavefield snapshots of $v_1$ and $v_3$ components at 0.4 s. This visual comparison shows that the wavefields in the effective medium can well approximate the wavefield in the original random medium.

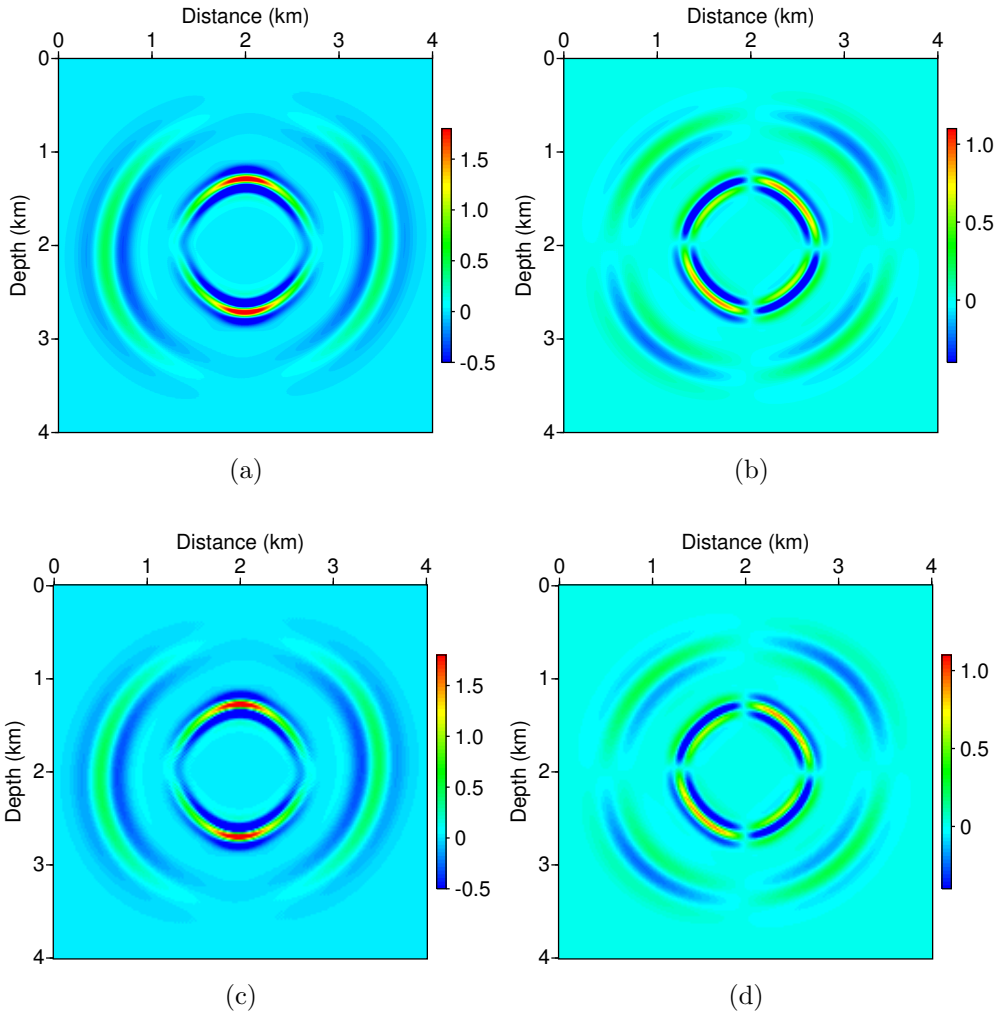


Figure 2.3: Comparisons of wavefields in fine grid medium and effective medium. (a) and (b) are $v_1$ and $v_3$ wavefields from fine grid model, respectively, and (c) and (d) are $v_1$ and $v_3$ wavefields from effective model, respectively.

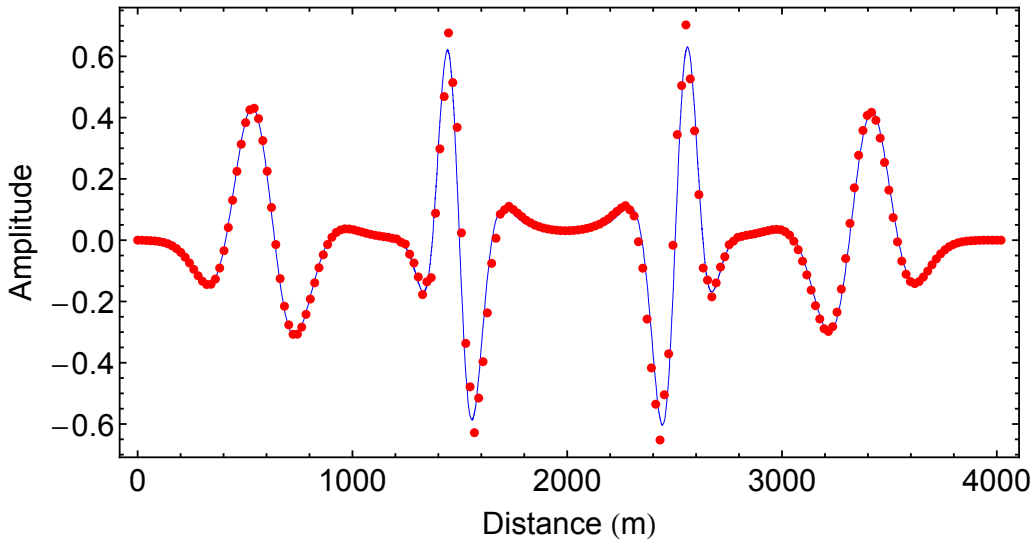


(a)

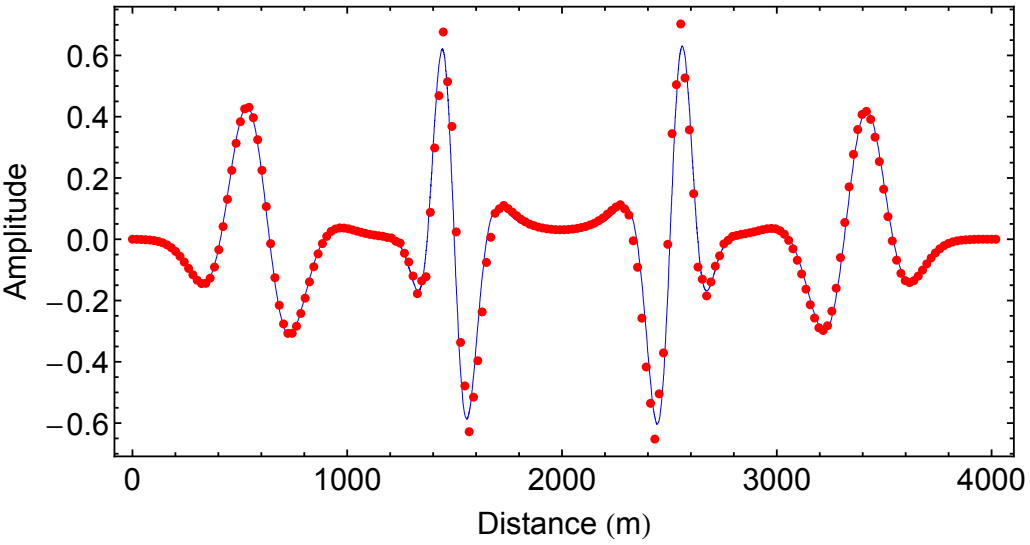


(b)

Figure 2.4: Comparison of (a) $v_1$ and (b) $v_3$ wavefields along horizontal line at a depth of 2400 m of the snapshots 2.3(a)/2.3(c) and 2.3(b)/2.3(d). Blue lines are the fine grid solution, and red dots are solutions from effective medium.

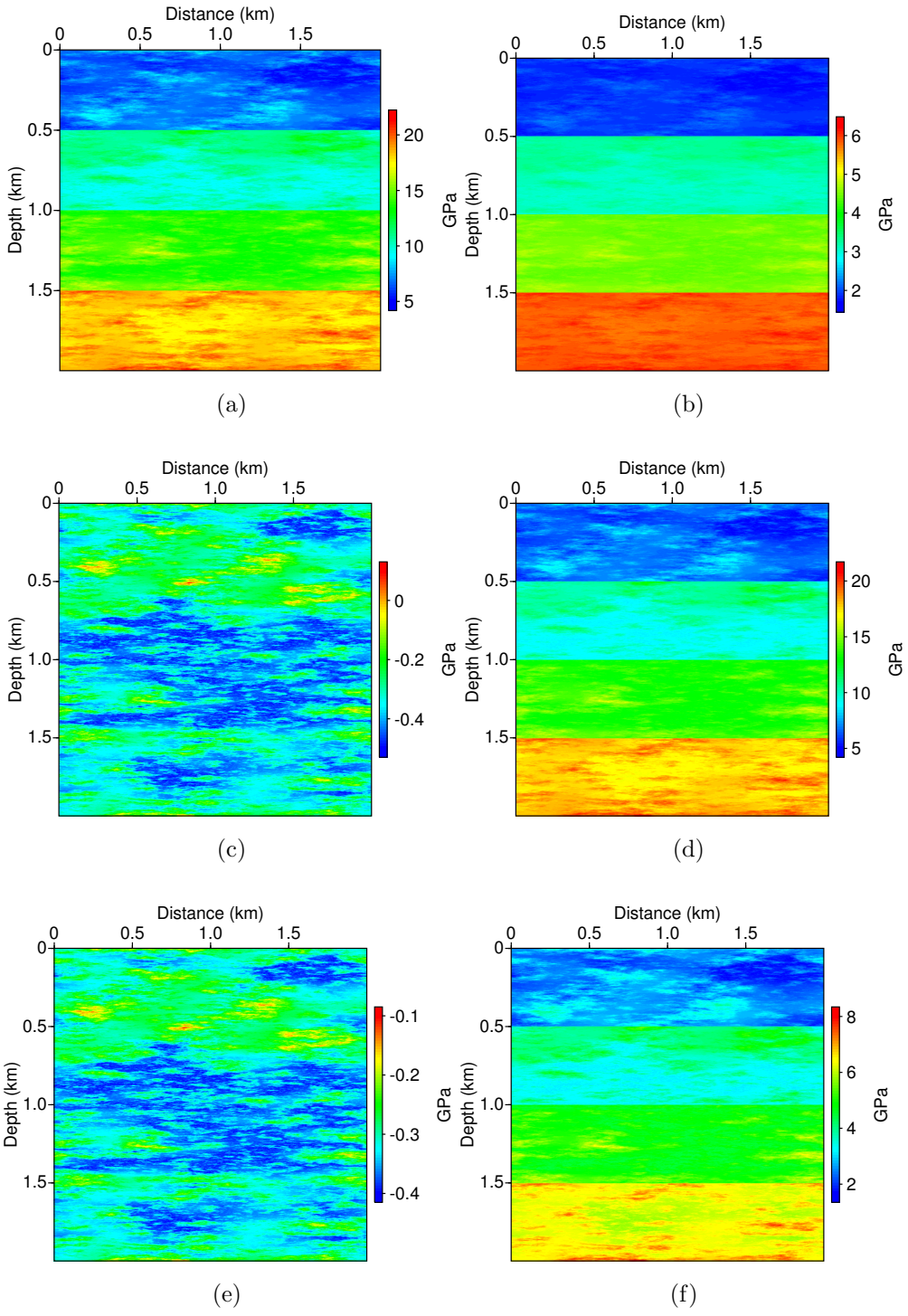


Figure 2.5: Four-layer von Kármán correlation random medium model. (a)–(f) represent $C_{11}$, $C_{13}$, $C_{15}$, $C_{33}$, $C_{35}$ and $C_{55}$, respectively. The model contains 2000×2000 grids, each is 1 m × 1 m in size.

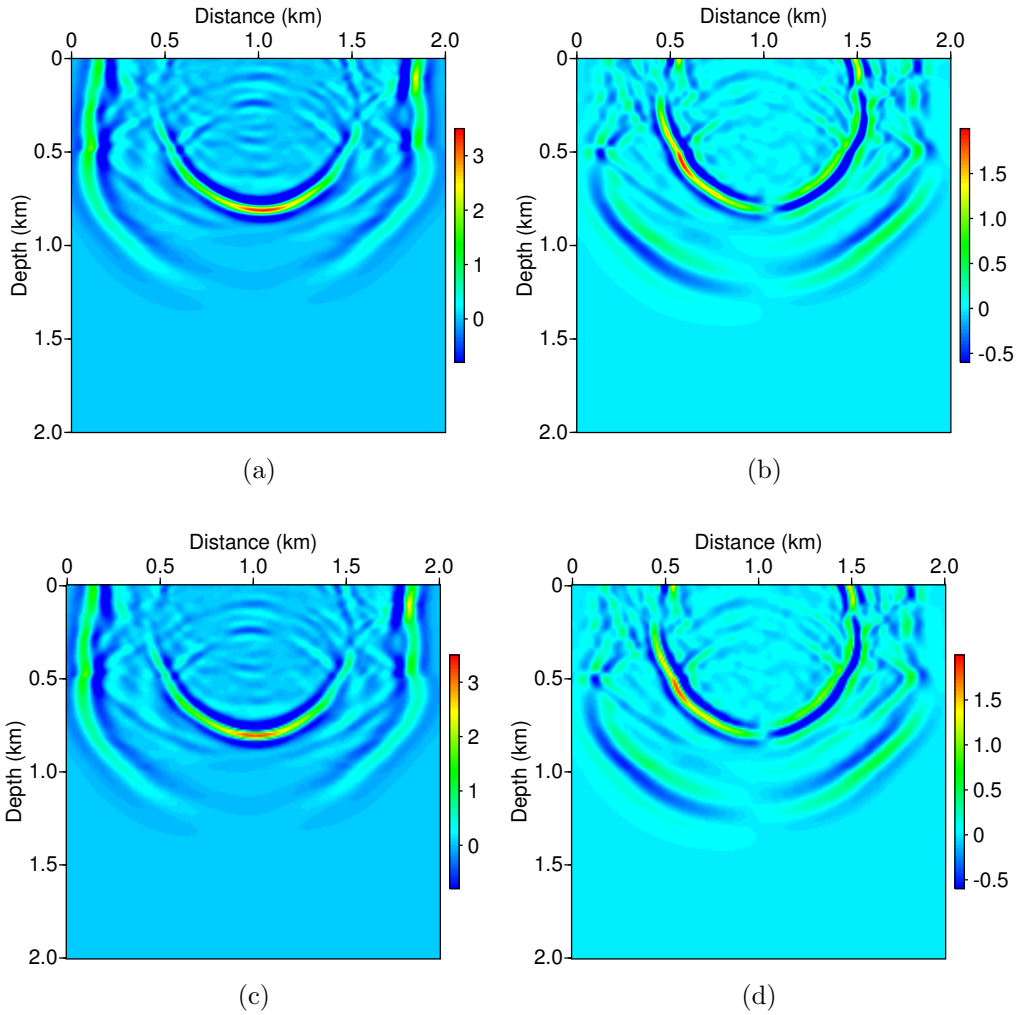


Figure 2.6: Comparisons of wavefield snapshots at 0.4 s in fine grid medium and effective medium. (a) and (b) are $v_1$ and $v_3$ wavefields from fine grid model, respectively, and (c) and (d) are $v_1$ and $v_3$ wavefields from effective model, respectively.

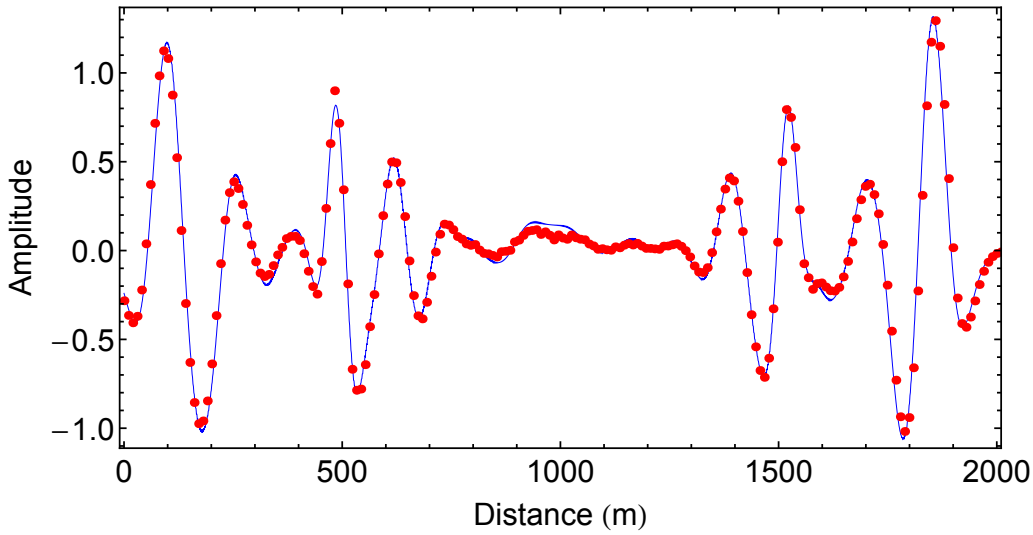


(a)

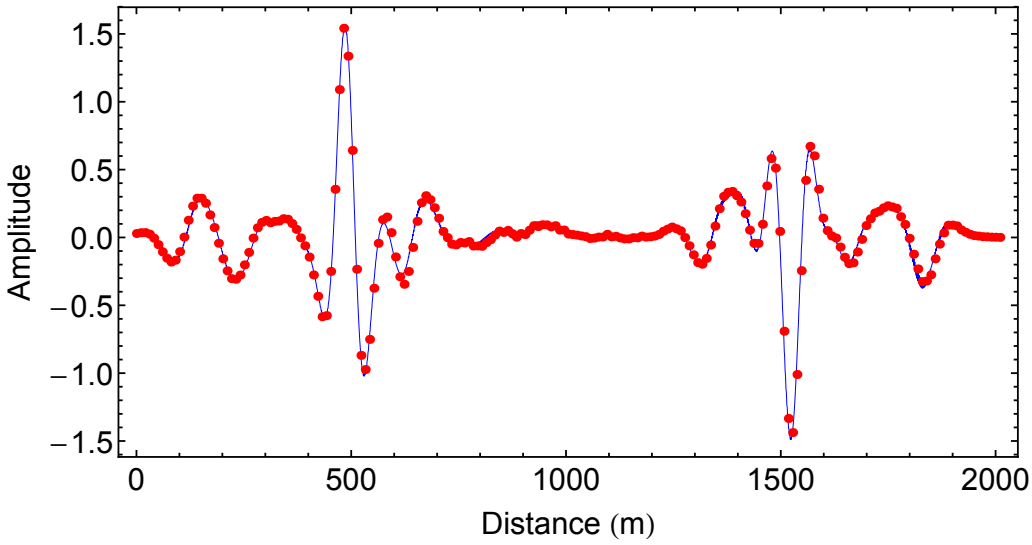


(b)

Figure 2.7: Comparison of (a) $v_1$ and (b) $v_3$ wavefields along horizontal line at a depth of 400 m of the snapshots 2.6(a)/2.6(c) and 2.6(b)/2.6(d). Blue lines are the fine grid solution, and red dots are solutions from effective medium.

Furthermore, Figures 2.8 and 2.9 show the seismograms from the two models, and Figures 2.10 and 2.11 show the seismograms that are clipped to exaggerate the reflections and scattered wavefields from the reflectors and heterogeneities in the model. There are only some inconsistencies in the seismogram at about 0.7 s in $v_1$ seismogram and at about 0.4 to 0.5 s in $v_3$ seismogram. For the other parts, the effective medium solution is a satisfactory approximation of the original solution.

## 2.4 Discussion

The numerical homogenization method we develop here has a similar local problem compared with the work in Grechka (2003). However, we remark they have different underlying assumptions, i.e., we solve local problem for multiscale basis functions, while Grechka (2003) solve the local problem for local stress and strain, and the effective medium parameters are solved with these local solutions by further solving a linear algebraic system. Besides, due to these different starting points, we have applied different boundary conditions for the local problem. While in Grechka (2003) several different boundary conditions should be set and the local problem has to be solved several times, we set only one boundary conditions and solve the local problem only once, which is a little more efficient. We also notice that in Grechka (2003), the fracture (discontinuity) can be included in a representative volume, which normally requires discontinuous Galerkin finite-element method to address to our knowledge. At present, we apply only continuous Galerkin finite-element method to solve local problem, and therefore the fracture cannot be accurately treated. However, implementing the basis function calculation using discontinuous Galerkin finite-element method will make the incorporation of fractures in the media straightforward for our method as well.

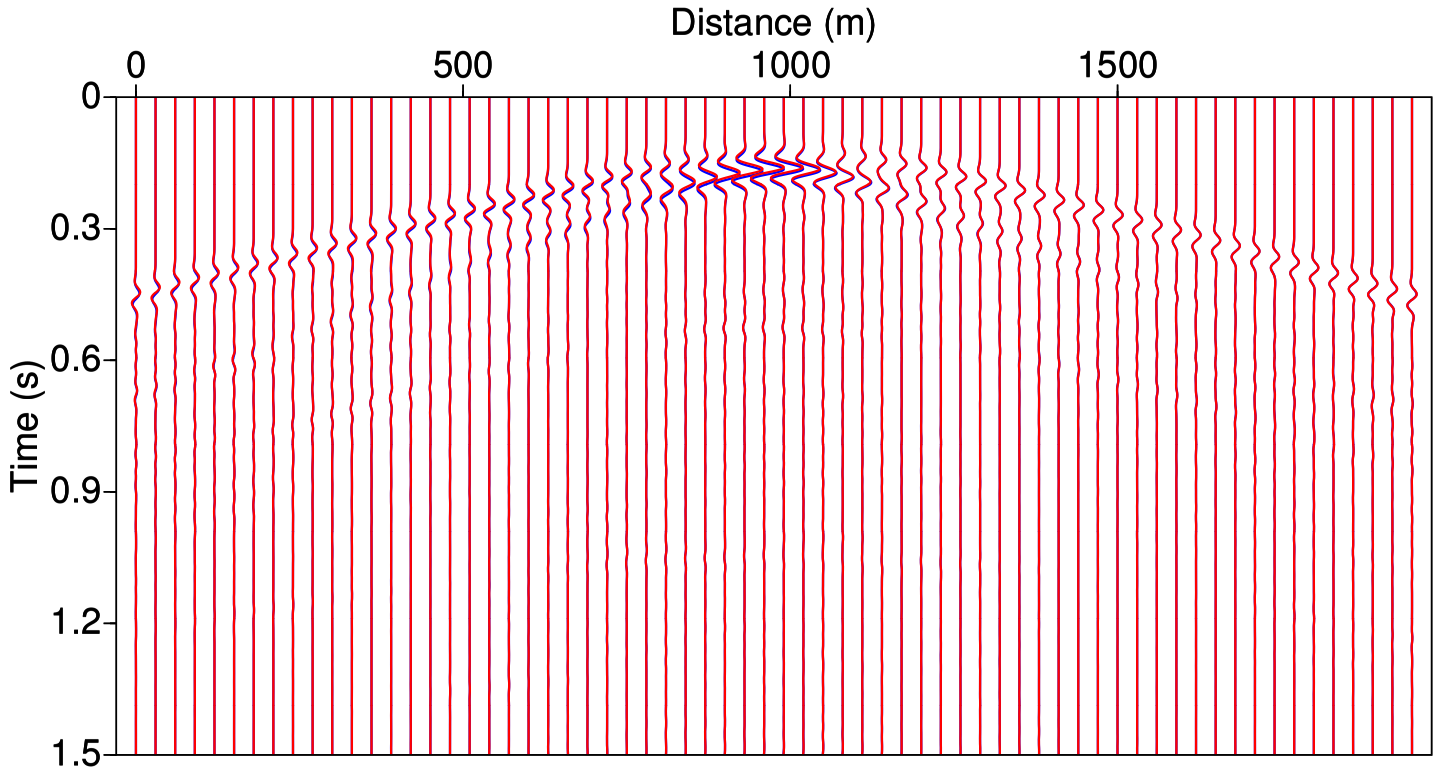


Figure 2.8: Comparisons of seismograms between blue wiggles – original fine grid solution of $v_1$ component, and red wiggles – effective medium solution of $v_1$ component. The solution is without clipping, so that the waveforms of transmitted wavefields are integrated enough to be seen.

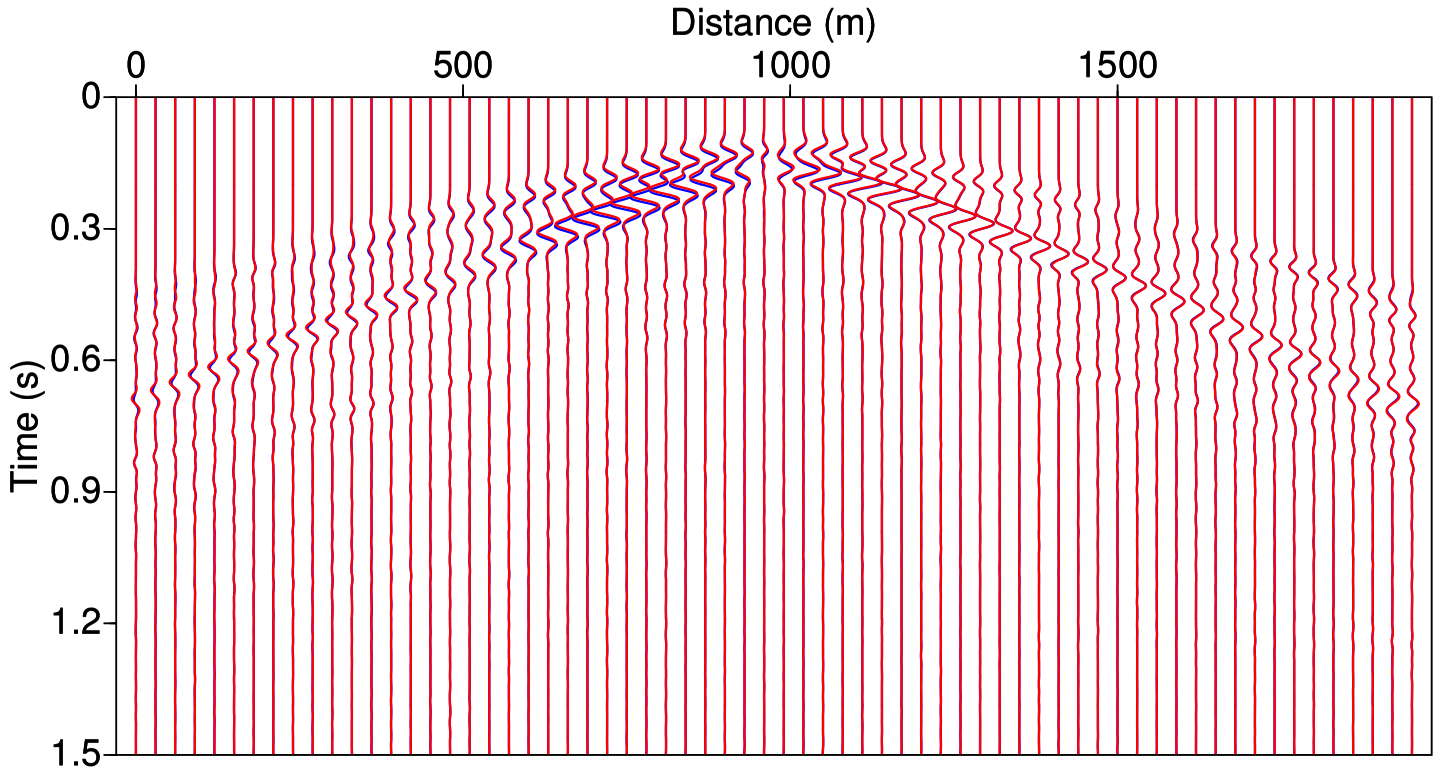


Figure 2.9: Comparisons of seismograms between blue wiggles – original fine grid solution of $v_3$ component, and red wiggles – effective medium solution of $v_3$ component. The solution is without clipping, so that the waveforms of transmitted wavefields are integrated enough to be seen.

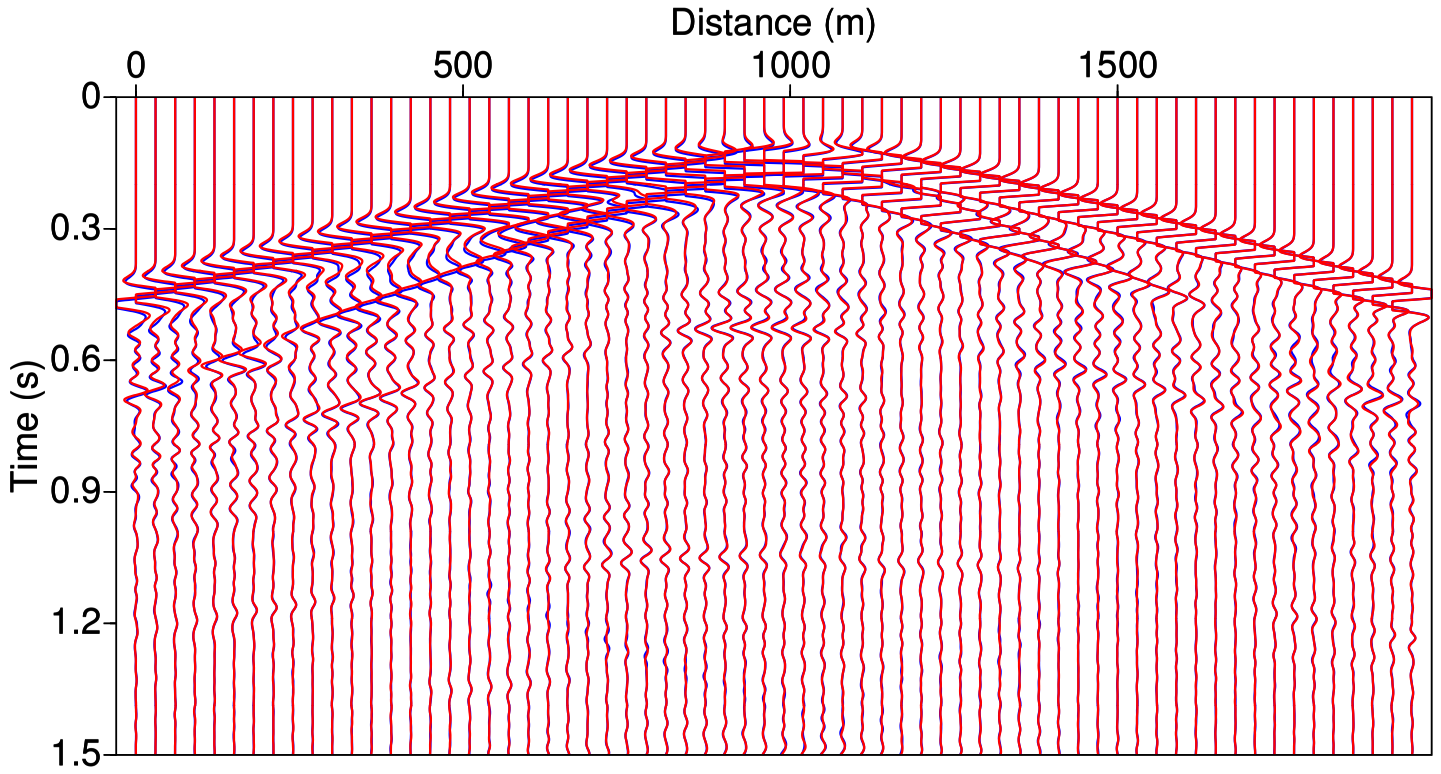


Figure 2.10: Comparisons of seismograms between blue wiggles – original fine grid solution of $v_1$ component, and red wiggles – effective medium solution of $v_1$ component. Te solution is with clipping, so that the waveforms of reflections and scatterings are integrated enough to be seen.

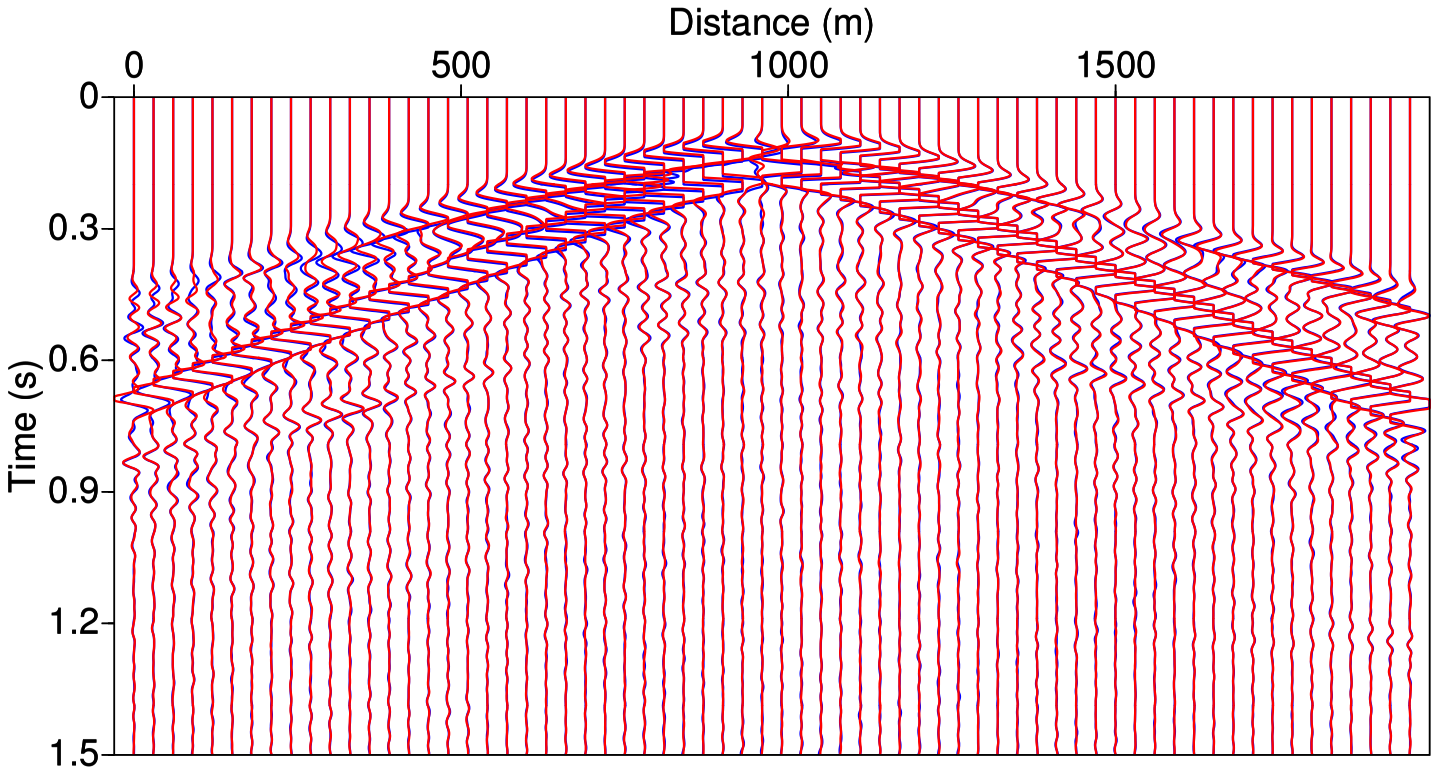


Figure 2.11: Comparisons of seismograms between blue wiggles – original fine grid solution of $v_3$ component, and red wiggles – effective medium solution of $v_3$ component. The solution is with clipping, so that the waveforms of reflections and scatterings are integrated enough to be seen.

## 2.5 Conclusions

We have provided a numerical upscaling method for anisotropic elastic medium. This method is constructed based on the multiscale theory previous developed for wave equation modeling. Specifically, we have defined local linear elasticity problem with appropriate boundary conditions, from which we can get the multiscale basis functions for stress components. The coefficients for the finite-difference-like terms based on these multiscale basis functions can be considered as the effective medium parameters. Our method is applicable to calculate effective medium parameters for arbitrary subgrid medium property variations. We have used several numerical examples, including horizontally layered medium and medium with general heterogeneous subgrid variations, to demonstrate the effectiveness of our method.

# 3. GENERALIZED MULTISCALE FINITE-ELEMENT METHOD FOR ELASTIC WAVE EQUATION

## 3.1 Introduction

Seismic wave propagation has long been a fundamental research field both in global scale seismology and reservoir exploration scale seismics. There are two basic categories of methods to investigate the propagation of waves through the Earth media, the approximation methods and the full wavefield methods. Approximation methods rely on either the simplification of the Earth media, or the approximation of the wave equation, which include, for instance, the ray tracing method (Červený and Hron, 1980; Beydoun and Keho, 1987; Gibson et al., 2005), the Gaussian beam method (Hill, 1990; Gray and Bleistein, 2009), the one-way wave equation approach (Claerbout, 1985; Zhang et al., 2005), the reflectivity method (Kennett, 1985), etc.. These methods are generally fast and computationally affordable. However, they are intrinsically incomplete and therefore may fail in complex geology, where steep dips, faults, salt bodies, irregular interfaces, fractures exist. The direct methods on the other hand, consist of many different numerical methods to solve various kinds of wave equations directly without approximations and simplifications, including, for example, the finite-difference method (Dablain, 1986; Virieux, 1986; Saenger et al., 2000), the finite-element method (Marfurt, 1984; Drake and Bolt, 1989; Komatitsch and Tromp, 2002; Chung and Engquist, 2006), the pseudo-spectral method (Fornberg, 1990), and so on, and are essential fundamentals of full-wavefield based seismic imaging and inversion methods, such as reverse-time migration (McMechan, 1983; Symes, 2007) and full waveform inversion (Tarantola, 1984; Virieux and Operto, 2009; Shipp and Singh, 2002). However, the applications of full wavefield methods are also

computational expensive, where the computation costs are directly proportional to the number of discrete elements that are required to represent the geological model, and this makes the wide applications of full-wavefield based imaging and inversion methods infeasible for realistic large 2-D and 3-D geological models. Moreover, the Earth medium should be considered as a complex system that is heterogeneous at different spatial scales. To include the influences of heterogeneities at finer scales when simulating the wave propagation on coarser scale, people tend to apply various effective medium theories (Backus, 1962; Schoenberg and Muir, 1989; Sayers, 2002) to get a set of equivalent parameters that is supposed to best approximate the properties of the heterogeneous media. However, all of these effective medium theories rely on long wavelength assumption, i.e., size of the heterogeneities is much smaller than the dominant wavelength of the wavelet, and when such assumptions fail, the reflections and scatterings become important, which cannot be correctly modeled by the effective medium approach.

In this paper, we are interested in developing fast yet accurate full wavefield modeling method for elastic wave propagation in heterogeneous, anisotropic media. The most straightforward way to model various types of wave equations is the finite-difference method due to its simplicity in implementation, where we have the conventional central finite-difference method (FDM) (Alterman and Karal, 1968; Alford et al., 1974; Kelly et al., 1976; Dablain, 1986; Liu, 2013), the staggered-grid finite-difference method (Virieux, 1986; Levander, 1988), the rotated staggered-grid method (Saenger et al., 2000; Saenger and Bohlen, 2004), etc.. However, FDM enjoys less flexibility in handling unstructured meshes, hanging nodes, and non-conforming meshes, and free surface topography problem, and only recently, the mimetic finite-difference method (Lipnikov and Huang, 2008; de la Puente et al., 2014) claims be able to achieve this goal, yet there are corresponding increase in

computational costs and the decrease in allowed time step size due to the distortion of grids. The finite-element methods (FEM), on the other hand, compose an effective solution to deal with the unstructured mesh of the geological model, which can honor the curved interfaces of the geological bodies, or the complex fault systems. The FEM also brings great benefits for dealing with free surface topography that can be naturally satisfied through the weak formulation of the FEM. Various FEM techniques have been developed. Some of the earliest efforts to solve the wave equation with the FEM are conventional continuous Galerkin (CG) FEMs (Bolt and Smith, 1976; Marfurt, 1984; Hughes, 1987; Drake and Bolt, 1989). However, CG-FEM can be quite computationally expensive due to the requirement of inverting the global mass matrix, which is not diagonal or block diagonal without mass lumping. This problem is removed with the spectral-element method (SEM) (Patera, 1984; Komatitsch and Vilotte, 1998; Komatitsch et al., 1999; Komatitsch and Tromp, 1999, 2002; Komatitsch et al., 2010; Cohen, 2002; Cohen and Fauqueux, 2005), which adopts Gauss-Lobatto-Legendre (GLL) integration points to obtain a strictly diagonal global mass matrix. Nevertheless, CG-FEM requires the continuity of wavefield solutions at the edges of elements, and is therefore less accurate when describing the wave propagation across high-contrast interfaces or discontinuities in the model. Besides, CG-FEM is unable to handle mesh discretization that is composed of different types of elements, non-conforming mesh or hanging nodes. These problems are naturally solved with the discontinuous Galerkin (DG) FEM initially developed for the transport equation (Reed and Hill, 1973) and elliptic partial differential equations (Wheeler, 1978; Rivière et al., 1999; Arnold et al., 2002). The DG-FEM has gradually gained broader application to time-dependent problems such as the wave equations (Grote et al., 2006; Chung and Engquist, 2006, 2009; Käser and Dumbser, 2006; Dumbser and Käser, 2006; De Basabe et al., 2008; de la Puente et al., 2008;

Dupuy et al., 2011; Wilcox et al., 2010). Importantly, DG-FEM has the advantage over CG-FEM that the global mass matrix is block diagonal, and the support of elements is distinct, a feature that favors straightforward parallel implementation, and this is quite important for large models. However, DG-FEM also suffers from some drawbacks, such as more complicated error and dispersion analyses and the requirement of tuning penalty parameters and more degrees of freedom.

Regardless of the implementation complexity, neither FDMs nor FEMs solved the common issue of high computational costs when solving the wave equations in large models. One approach to reduce such costs is the so-called multiscale method. The multiscale method was originally designed for elliptic partial differential equations (Hou and Wu, 1997). Unlike all the above mentioned FEMs, the multiscale FEM (MsFEM) seeks special basis functions, i.e., the multiscale basis functions, to include the influence of fine-scale heterogeneity when solving the PDEs on the coarse scale, and the usage of the multiscale basis functions enables the FEM to consider high contrasts in the medium properties that may vary by several orders of magnitudes spatially. These multiscale basis functions are not predefined polynomials like those in conventional FEMs (e.g., Larson and Bengzon, 2013). Instead, they are solved from appropriately defined local problems (Hou and Wu, 1997; Efendiev and Hou, 2009; Jiang et al., 2009). Chung et al. (2011a,b) and Gibson et al. (2014) applied the idea of multiscale basis functions and designed a multiscale method for mixed-form acoustic wave equation. To improve the accuracy of the MsFEM, Efendiev et al. (2011) and Efendiev et al. (2013) proposed to utilize multiple multiscale basis functions solved from local spectral problem, which is the generalized multiscale finite-element method (GMsFEM). These basis functions are constructed from the eigenfunctions that correspond to the first several smallest eigenvalues of the local spectral problem, and are therefore correspond to the local eigenmodes with lowest

frequencies. Chung et al. (2013b) proposed a discontinuous Galerkin (DG) GMsFEM for the second-order acoustic wave equation, where they constructed so-called interior basis and boundary basis functions to capture fine-scale media heterogeneity information for the wavefield simulation on coarse scale. This DG-GMsFEM was also strictly analyzed in Chung et al. (2013a). There are other methods titled "multiscale", yet they begin with different assumptions and methodologies, for instance, the operator-based upscaling for the acoustic wave equation (Arbogast et al., 1998; Vdovina et al., 2005). Korostyshevskaya and Minkoff (2006) and Vdovina and Minkoff (2008) analyzed the error and convergence characteristics of this approach. However, in their approach, local problems have to be solved at each time step, whereas in the multiscale approach by Chung et al. (2011b) and Chung et al. (2013a), the local problems only need to be solved once before the time stepping, to get the multiscale basis functions. Vdovina et al. (2009) developed a similar operator-based upscaling approach for elastic wave equation. Owhadi and Zhang (2005, 2007, 2008) proposed the multiscale method for the wave equation based on the global change of coordinates. E and Engquist (2002, 2005) proposed the heterogeneous multiscale method (HMM), and later was developed in finite-difference and finite-element formulations (Engquist et al., 2007, 2011; Abdulle and Grote, 2011). The HMM also requires evaluations of local problem in each time step, which is time expensive. Capdeville et al. (2010) proposed a numerical homogenization method for non-periodic heterogeneous elastic media, which extracts the microscopic part of medium properties, followed by a homogenization expansion. However, this method assumes scale separation of the media, which cannot always be satisfied in practice.

Based on previous works for the elliptic partial differential equations and the acoustic wave equation (Efendiev et al., 2011, 2013; Efendiev et al., 2013; Chung et al., 2013b,a; Gibson et al., 2014), we propose a GMsFEM to simulate the wave

propagation in heterogeneous, anisotropic elastic media on the coarse mesh. The essence of our GMsFEM is to construct multiscale basis functions with appropriately defined local problems, which will be used in both CG and DG formulation of the GMsFEM. We investigated two types of related yet different multiscale basis functions. For the first type of multiscale basis function, we solve a linear elasticity eigenvalue problem in the support of a node on the coarse mesh, or in the region of a coarse element. By selecting the eigenfunctions correspond to the first several smallest eigenvalues, we construct a finite-dimensional basis function space for CG- and DG-GMsFEM. For the second type of multiscale basis function, we construct a basis space which is composed of two orthogonal subspaces, and these two subspaces are consisted of multiscale functions defined with different local spectral problems. The first subspace is spanned by the basis functions that are solved directly from the local eigenvalue problem of linear elasticity for the interior nodes of the coarse node support or coarse element, while the second subspace consists of the basis functions solved from a local spectral problem which is related to the boundaries of the coarse node support or coarse element. For both of these spaces, we select the eigenfunctions that correspond to the first several smallest eigenvalues. These basis functions correspond to the local eigenmodes with lowest frequencies. The resulting GMsFEM allows us to utilize these multiscale basis functions to capture the fine scale information of the heterogeneous media, while effectively reducing the degrees of freedom that are required to implement the modeling compared with conventional method such like CG-FEM. For DG-GMsFEM, the computational time will also be reduced, compared with conventional CG-FEM.

Our paper is organized as follows. We first introduce the CG and DG formulations of GMsFEM for the elastic wave equation in heterogeneous, anisotropic media. Specifically, we define the appropriate bilinear forms for the elastic wave equation,

then we introduce two approaches to construct the multiscale basis functions with appropriately defined local problems, as well as the oversampling technique to reduce the influence of prescribed boundary conditions, and an adaptive way to assign different numbers of basis functions for coarse elements in DG-GMsFEM. We then present four numerical results to verify the effectiveness of our multiscale method, including a heterogeneous model composed of isotropic and TTI half spaces, a heterogeneous model generated with von Kármán correlation function. We also investigate the free surface Rayleigh wave problem, and the last numerical example is devoted to verify the adaptive assignment of number of basis functions. Finally, we give a brief discussion of limitations of our current work and propose some possible improvements.

## 3.2 Theory

We will develop both the CG- and DG-GMsFEM in this section. We will first give the weak forms of the elastic wave equation in CG and DG formulations, then we will show how to construct the multiscale basis functions using appropriately defined local spectral problems. Although the formulations of CG- and DG-GMsFEM are different, the multiscale basis functions for these two formulations can be constructed in the same way.

We remark that we present the definitions, equations and derivations in this part in a general style, and therefore they are valid for both 2-D and 3-D cases. However, we will present only 2-D examples in this part, as well as the next part of numerical results.

### *3.2.1 Weak form of the elastic wave equation*

#### *3.2.1.1 Elastic wave equation*

We begin with the elastic wave equation in the form (e.g., Carcione, 2007)

$$\rho\partial_t^2\mathbf{u} = \nabla\cdot\boldsymbol{\sigma} + \mathbf{f}, \tag{3.1a}$$

$$\boldsymbol{\sigma} = \mathbf{c} : \boldsymbol{\varepsilon}, \tag{3.1b}$$

$$\boldsymbol{\varepsilon} = \frac{1}{2}[\nabla\mathbf{u} + (\nabla\mathbf{u})^{\mathrm{T}}] \tag{3.1c}$$

where $\mathbf{u} = \mathbf{u}(\mathbf{x}, t)$ is the displacement wavefield we aim to solve with our multiscale method in the spatial domain $\Omega$, which could be 2-D or 3-D in general, and temporal domain $[0, T]$. Also $\boldsymbol{\sigma} = \boldsymbol{\sigma}(\mathbf{u})$ is the stress tensor, $\boldsymbol{\varepsilon} = \boldsymbol{\varepsilon}(\mathbf{u})$ is the strain tensor, $\mathbf{f}$ is the external source term, $\mathbf{c} = \mathbf{c}(\mathbf{x})$ is the fourth-rank elasticity tensor and $\rho = \rho(\mathbf{x})$ is the density of the medium.

In our theory, the elasticity tensor $\mathbf{c}$ can be generally anisotropic, i.e., all the 21 independent elasticity parameters in $\mathbf{c}$ can be non-zero, in 3-D case. However, since we will present only 2-D results in this paper, we will express the elasticity tensor $\mathbf{c}$ in the following Voigt notation:

$$\mathbf{C} = \begin{pmatrix} C_{11} & C_{13} & C_{15} \\ C_{13} & C_{33} & C_{35} \\ C_{15} & C_{35} & C_{55} \end{pmatrix}, \tag{3.2}$$

which can describe the elastic wave propagation in anisotropic media with symmetry up to hexagonal anisotropy with titled symmetry axis in the $x_1 - x_3$ plane, i.e., transversely isotropy with titled axis (TTI), and monoclinic anisotropy (assuming the symmetry plane is the $x_1 - x_3$ plane), where $C_{15}$ and $C_{35}$ are possibly nonzero.

#### *3.2.1.2 CG formulation*

We first formulate the multiscale method in the CG framework for 2-D simulations with applications to higher-order cases of anisotropy. For the CG formulation, we first discretize the whole computational domain $\Omega$ with a coarse mesh $\mathcal{T}_H$ overlying a finer mesh $\mathcal{T}_h$. Figure 3.1 illustrates this mesh design, where we use the black lines to represent the coarse mesh, and gray lines to represent the finer mesh. The support of a coarse node can be denoted as $K$, which contains many finer elements. The mesh can be unstructured, though we assume structured elements in the theory development to develop the current results. Nevertheless, the following derivations are equally valid for an unstructured mesh.

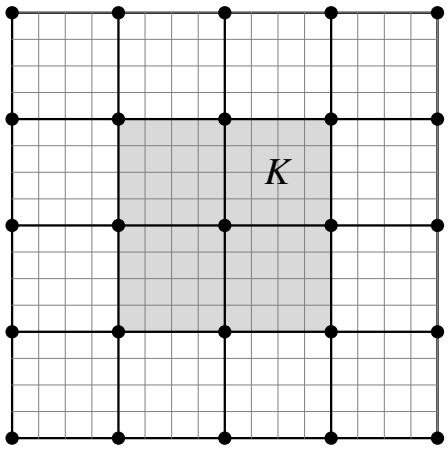


Figure 3.1: A sketch of the fine mesh $\mathcal{T}_h$, denoted by gray mesh, and coarse mesh $\mathcal{T}_H$, denoted by black mesh, in CG formulation of GMsFEM. Gray rectangle labeled $K$ represents the support of the $i$-the coarse node. $K$ contains many finer element which might have high contrasts in medium properties.

We express the displacement wavefield $\mathbf{u}$ on the coarse mesh $\mathcal{T}_H$ as

$$\mathbf{u}_H(\mathbf{x},t) = \sum_{i=1}^{N} \mathbf{d}_i(t)\mathbf{\Phi}_i(\mathbf{x}), \tag{3.3}$$

where $\mathbf{\Phi}_i(\mathbf{x})$ are the spatial basis functions of $\mathbf{u}_H(\mathbf{x},t)$, and $\mathbf{\Phi}_i$ belong to the finite-dimensional function space $V_H = \{\mathbf{\Phi}_i\}_{i=1}^N$. Note that each $\mathbf{\Phi}_i$ is piecewise continuous in $\Omega$. Space $V_H$ is our multiscale basis function space, which will be defined in the next section. We multiply the elastic wave equation 3.1 with a test function $\mathbf{v} \in V_H$, integrate over $\Omega$, apply Gauss's theorem, and get the weak form of the elastic wave equation as

$$\int_\Omega \rho \partial_t^2 \mathbf{u}_H \cdot \mathbf{v} d\mathbf{x} + a_{\mathrm{CG}}(\mathbf{u}_H, \mathbf{v}) = \int_\Omega \mathbf{f} \cdot \mathbf{v} d\mathbf{x}, \tag{3.4}$$

where the bilinear form $a_{\mathrm{CG}}$ is

$$a_{\mathrm{CG}}(\mathbf{u},\mathbf{v}) = \int_\Omega \boldsymbol{\sigma}(\mathbf{u}) : \boldsymbol{\varepsilon}(\mathbf{v}) d\mathbf{x} + \int_{\partial\Omega} [\boldsymbol{\sigma}(\mathbf{u}) \cdot \mathbf{n}] \cdot \mathbf{v} ds. \tag{3.5}$$

Also, $\mathbf{n}$ is the outward pointed normal of $\partial\Omega$. We have set homogeneous Neumann boundary condition, i.e., $\boldsymbol{\sigma}(\mathbf{u}) \cdot \mathbf{n} = \mathbf{0}$, for simplicity.

#### *3.2.1.3 DG formulation*

The discontinuous Galerkin formulation of our multiscale method is a natural choice if a non-conformal mesh is taken into consideration. For DG formulation, we discretize $\Omega$ with a set of coarse mesh cells $\mathcal{P}_H$, each coarse element containing more finely discretized elements in the finer mesh $\mathcal{P}_h$, as is shown in Figure 3.2 for a 2-D meshing case. Again, the solution of the wave equation 3.1 can be expressed as

$$\mathbf{u}_H(\mathbf{x},t) = \sum_{i=1}^{N} \mathbf{d}_i(t)\mathbf{\Psi}_i(\mathbf{x}), \tag{3.6}$$

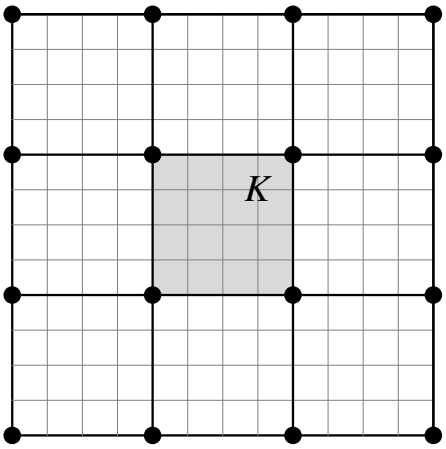


Figure 3.2: A sketch of the fine mesh $\mathcal{P}_h$, denoted by gray mesh, and coarse mesh $\mathcal{P}_H$, denoted by black mesh in DG formulation of GMsFEM. Gray rectangle labeled $K$ represents the $i$-th coarse element. Same with that in CG-GMsFEM, coarse block $K$ contains many finer element which might have high contrasts in medium properties.

where the basis functions $\boldsymbol{\Psi}_i \in W_H$. The multiscale basis function space $W_H$ will be defined in the next section. We assume that the basis functions $\boldsymbol{\Psi}_i$ are continuous within each coarse element $K$, but generally discontinuous at the coarse element boundaries $\partial K$.

As is true in general for discontinuous Galerkin finite-element methods (e.g., Grote et al., 2006; Arnold et al., 2002; Wihler, 2006), we define some terms related to the boundaries of the coarse element.

Letting $\mathcal{E}_H$ be the set of all interior coarse element edges in the 2-D case (the set of all interior coarse element faces in 3-D), then we define the average of a tensor $\boldsymbol{\sigma}$ on $E \in \mathcal{E}_H$ as

$$\{\!\{\boldsymbol{\sigma}\}\!\} = \frac{1}{2}(\boldsymbol{\sigma}^+ + \boldsymbol{\sigma}^-) \tag{3.7}$$

where $\boldsymbol{\sigma}^{\pm} = \boldsymbol{\sigma}|_{K^{\pm}}$, and $K^{\pm}$ are the two coarse elements having the common $E$.

Meanwhile, the jump of a vector $\mathbf{v}$ on $E \in \mathcal{E}_H$ is given by:

$$[\![\mathbf{v}]\!] = \mathbf{v}^+ \cdot \mathbf{n}^+ + \mathbf{v}^- \cdot \mathbf{n}^-, \tag{3.8}$$

where $\mathbf{n}^\pm$ is the unit outward normal vector on the boundary of $K^\pm$. We also have a matrix jump term resulting from the outer product of vector with edge or face normals, which is defined as

$$\underline{[\![\mathbf{v}]\!]} = \mathbf{v}^+ \otimes \mathbf{n}^+ + \mathbf{v}^- \otimes \mathbf{n}^-. \tag{3.9}$$

Also, for the edges on the computation domain boundary $\partial\Omega$, the above average and jump terms can be defined as

$$\{\!\{\boldsymbol{\sigma}\}\!\} = \boldsymbol{\sigma}, \quad [\![\mathbf{v}]\!] = \mathbf{v} \cdot \mathbf{n}, \quad \underline{[\![\mathbf{v}]\!]} = \mathbf{v} \otimes \mathbf{n}, \tag{3.10}$$

where $\mathbf{n}$ is the outward pointed normal of coarse element $K$.

We multiply the elastic wave equation 3.1 with some arbitrary test function $\mathbf{v} \in W_H$, and get the weak form

$$\int_\Omega \rho \partial_t^2 \mathbf{u}_H \cdot \mathbf{v} d\mathbf{x} + a_{\mathrm{DG}}(\mathbf{u}_H, \mathbf{v}) = \int_\Omega \mathbf{f} \cdot \mathbf{v} d\mathbf{x}, \tag{3.11}$$

where the bilinear form $a_{\mathrm{DG}}(\mathbf{u}, \mathbf{v})$ is defined as

$$\begin{aligned} a_{\mathrm{DG}}(\mathbf{u}, \mathbf{v}) = & \sum_{K \in \mathcal{P}_H} \int_K \boldsymbol{\sigma}(\mathbf{u}) : \boldsymbol{\varepsilon}(\mathbf{v}) d\mathbf{x} \\ & - \sum_{E \in \mathcal{E}_H} \int_E (\{\!\{\boldsymbol{\sigma}(\mathbf{u})\}\!\} : \underline{[\![\mathbf{v}]\!]} + \eta \underline{[\![\mathbf{u}]\!]} : \{\!\{\boldsymbol{\sigma}(\mathbf{v})\}\!\}) ds \\ & + \sum_{E \in \mathcal{E}_H} \frac{\gamma}{|E|} \int_E (\underline{[\![\mathbf{u}]\!]} : \{\!\{\mathbf{c}\}\!\} : \underline{[\![\mathbf{v}]\!]} + [\![\mathbf{u}]\!] \cdot \{\!\{\mathbf{D}\}\!\} \cdot [\![\mathbf{v}]\!]) ds, \end{aligned} \tag{3.12}$$

with $\mathbf{D} = \text{diag}(C_{11}, C_{22}, C_{33})$, $C_{IJ}$ are components of the four-order elasticity tensor $\mathbf{c}$ in Voigt notation (e.g., Carcione, 2007). $\eta$ is a parameter that takes values $-1$, 0 or 1, and we choose $\eta = 1$, which makes our method the classical symmetric interior penalty Galerkin (SIPG) method (Arnold et al., 2002; Chung et al., 2013a; De Basabe et al., 2008). $\gamma$ is the penalty parameter, and we set $\gamma > 0$. We have omitted the terms related to the boundary edges, since we assume homogeneous Neumann boundary condition. This bilinear form is inspired by those defined for linear elasticity problem (Wihler, 2006) and isotropic elastic wave equation (De Basabe et al., 2008), however, we have used non-constant matrix penalty parameters and two different penalty terms, i.e., $\{\!\{\mathbf{c}\}\!\} = \{\!\{\mathbf{c}(\mathbf{x})\}\!\}$ and $\{\!\{\mathbf{D}\}\!\} = \{\!\{\mathbf{D}(\mathbf{x})\}\!\}$. We find that such penalty terms can better guarantee the stability of the DG scheme. Meanwhile, we use a fixed $\gamma$ for all boundaries for convenience, which can alternatively vary from edge to edge. It should be remarked that the bilinear form 3.12, which is essentially the time-independent part of the elastic wave equation 3.1, is not unique, and there are some other similar choices which may be equally good (e.g., Rivière, 2008; Kaufmann et al., 2008; Hansbo and Larson, 2011).

### *3.2.2 Multiscale basis functions*

The key task in our multiscale method, given the above weak forms of elastic wave equation, is to construct appropriate multiscale basis functions $\mathbf{\Phi}_i$ or $\mathbf{\Psi}_i$ to form the function space $V_H$ or $W_H$ for CG- or DG-GMsFEM. In this section, we will introduce two methods to construct the multiscale basis functions, both are solved from appropriately defined local problems, and both can be taken to form the basis function space for the wave equation.

#### *3.2.2.1 Type I*

The first way to define a set of multiscale basis functions is by solving local linear elasticity eigenvalue problem. Specifically, suppose $K$ is the support of a coarse node in CG formulation, or the coarse element in DG formulation, then we solve the following eigenvalue problem in $K$:

$$-\nabla \cdot \boldsymbol{\sigma} = \zeta \rho \mathbf{u}, \tag{3.13a}$$

$$\boldsymbol{\sigma} = \mathbf{c} : \boldsymbol{\varepsilon}, \tag{3.13b}$$

$$\boldsymbol{\varepsilon} = \frac{1}{2}[\nabla \mathbf{u} + (\nabla \mathbf{u})^{\mathrm{T}}], \tag{3.13c}$$

with zero Neumann boundary condition $\boldsymbol{\sigma} \cdot \mathbf{n} = 0$ on $\partial K$, where $\zeta$ is the eigenvalue, and $\mathbf{n}$ is the outward pointed normal of $K$. The elasticity tensor $\mathbf{c}$ can be spatially heterogeneous. This local problem corresponds to the following discrete system:

$$\mathbf{AU} = \zeta \mathbf{MU}, \tag{3.14}$$

where the global stiffness and global mass matrices $\mathbf{A}$ and $\mathbf{M}$ are computed from

$$\mathbf{A} = \int_K \boldsymbol{\sigma}(\boldsymbol{\gamma}) : \boldsymbol{\varepsilon}(\boldsymbol{\eta}) d\mathbf{x}, \tag{3.15}$$

$$\mathbf{M} = \int_K \rho \boldsymbol{\gamma} \cdot \boldsymbol{\eta} d\mathbf{x}, \tag{3.16}$$

for the coarse node support or coarse element $K$, with $\boldsymbol{\gamma}, \boldsymbol{\eta} \in V_h$, and they can be discretized and calculated with appropriate quadrature and integration rules (e.g., Hughes, 1987; Larson and Bengzon, 2013) for calculation of eigenvectors.

The above linear elasticity eigenvalue problem can be solved with a conventional solver without difficulties, since normally the dimension of the above system is not

large due to the limited size of a coarse element. To ensure stability, we would add to $\mathbf{A}$ a $10^{-8}$ to $10^{-9}$ of the maximum value of the diagonal element of $\mathbf{A}$. Solutions of the eigenvalue problem for the displacement $\mathbf{u}$ are labeled as $\boldsymbol{\psi}_k$, denoting the $k$-th eigen-displacement in the coarse block $K$. Physically, they are the standing modes in $K$ with frequencies $\omega_k = \sqrt{\zeta_k}$.

Depending on the dimension of the coarse block $K$, there can be many eigenfunctions associated with the local problem 3.13. The analyses for elliptic partial differential equation (Efendiev et al., 2013) and for acoustic wave equation (Chung et al., 2013b,a) tell us that it is adequate to select only a few of the eigenfunctions as the basis functions for $\mathbf{u}_H$. The criterion for selecting eigenfunctions is to chose those representing most of the energy in the eigenmodes $\boldsymbol{\psi}_k$. Correspondingly, the sum of the inverse of selected eigenvalues $\sum_{l=1}^{m} \zeta_l^{-1}$ should be a large portion of the sum of all the inverse of eigenvalues $\sum_{l=1}^{L} \zeta_l^{-1}$ ($L$ is the number of eigenfunctions). Therefore, for DG formulation, we can select the first $m$ eigenfunctions $\boldsymbol{\psi}_1, \boldsymbol{\psi}_2, \cdots, \boldsymbol{\psi}_m$ corresponding to the $m$ smallest eigenvalues $0 \leq \zeta_1 \leq \zeta_2 \leq \cdots \leq \zeta_m$ of the above local problem, and construct the multiscale basis function space as

$$W_H(K) = \text{span}\{\boldsymbol{\psi}_1, \boldsymbol{\psi}_2, \cdots, \boldsymbol{\psi}_m\}. \tag{3.17}$$

This choice applies the bases corresponding to= the most dominant wave modes, i.e., the wave modes with the lowest several frequencies. Due to the limited resolution of the coarse block $K$, higher frequencies cannot be accurately represented.

In the DG formulation, $\boldsymbol{\psi}_k$ can be utilized directly to represent the wavefield in equation 3.6, as defined in equation 3.17. However, in the CG formulation, we need to multiply these eigenfunctions by a partition of unity, $\boldsymbol{\chi}_i$, to form the multiscale

basis functions in equation 3.3 (Efendiev and Hou, 2009; Fu et al., 2013),

$$V_H(K) = \text{span}\{\boldsymbol{\chi}_K\boldsymbol{\psi}_1, \boldsymbol{\chi}_K\boldsymbol{\psi}_2, \cdots, \boldsymbol{\chi}_K\boldsymbol{\psi}_m\}. \tag{3.18}$$

The partition of unity is defined as a collection of smooth and nonnegative functions in the appropriate space $M$ that satisfy $\sum_K \chi_K(\mathbf{x}) = 1$ for any $\mathbf{x} \in M$. Thus $\chi_K$ could be understood as the standard FEM basis functions that are defined for various kinds of elements and various orders. For example, in one dimension, $\chi_K$ are the standard linear basis functions, i.e., $\chi_K = \{1 - x, x\}$, in the lowest order case.

It is clear that the basis functions solved from the local eigenvalue problem 3.13 are influenced by the anisotropic and heterogeneous properties in the region $K$, and they are different for different local $\mathbf{c}(\mathbf{x})$ and $\rho(\mathbf{x})$. This is the most distinct difference between our multiscale basis functions and the high order basis functions in various finite-element methods (Marfurt, 1984; Hughes, 1987; Komatitsch et al., 1999), where the basis functions are predefined polynomials and are independent of the earth model.

Three examples help to illustrate the behavior of these basis functions. Figures 3.3(a)–3.3(f) and 3.4(a)–3.4(f) represent the $u_1$ and $u_3$ component of the first 6 eigenfunctions corresponding to the first 6 smallest eigenvalues obtained by solving the local eigenvalue problem for an isotropic homogeneous subgrid model, with elastic parameters $C_{11}$=10.0 GPa and $C_{55}$=4.0 GPa, $C_{33} = C_{11}$, $C_{13} = C_{11} - 2C_{55}$, $C_{13} = C_{15} = 0$, and density $\rho$=1000 kg/m$^3$. Note that the first eigenfunction in Figures 3.3(a) and 3.4(a) is constant, corresponding to the constant solution that satisfies local problem 3.13 by default.

In contrast, Figures 3.5(a)–3.5(f) and 3.6(a)–3.6(f) show an example of selecting the first 6 eigenfunctions for a 2-D TTI homogeneous subgrid model, with elasticity

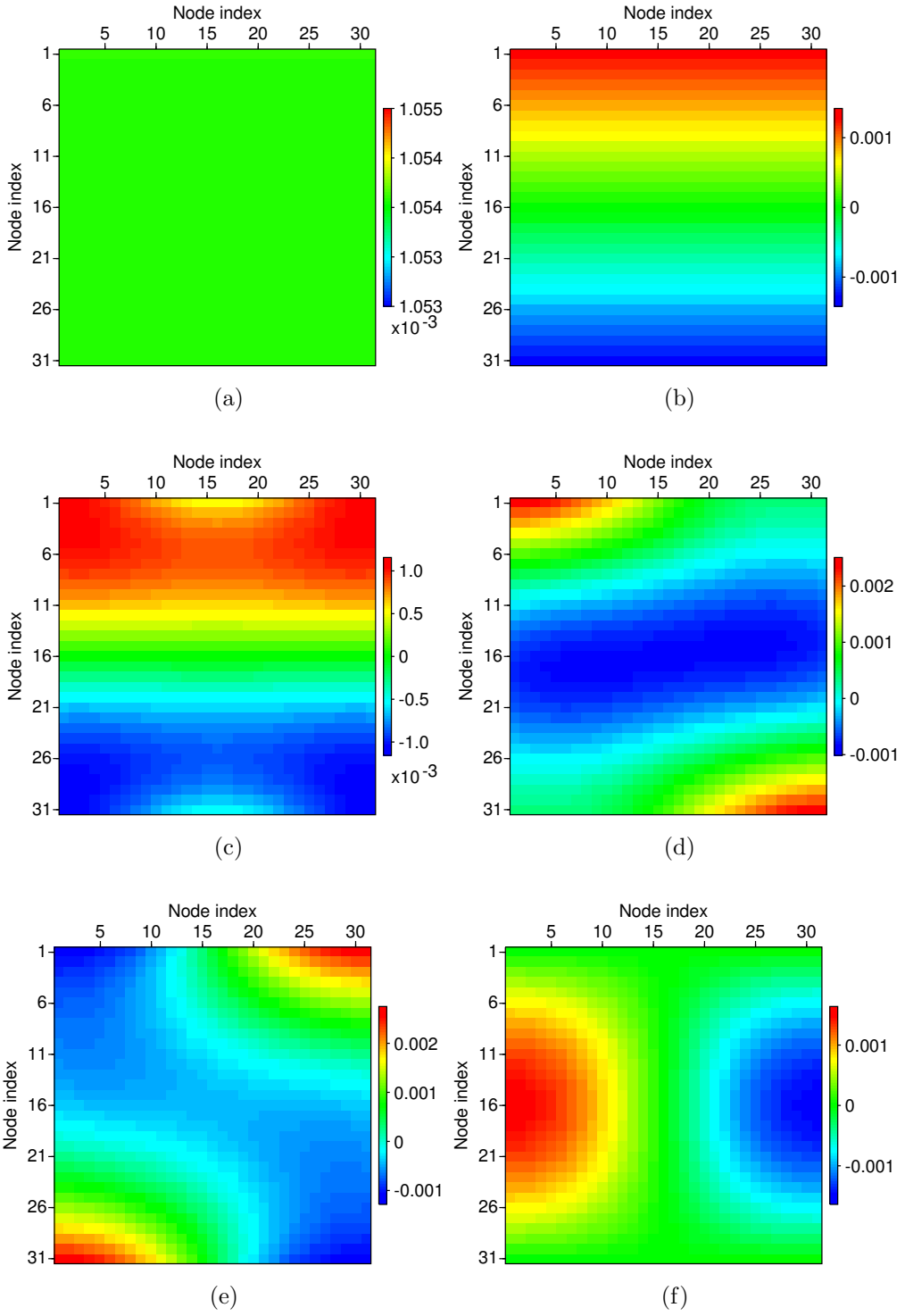


Figure 3.3: (a)–(f) represent the $u_1$ component of the first 6 spectral basis functions corresponding with the first 6 smallest eigenvalues for an isotropic homogeneous subgrid model.

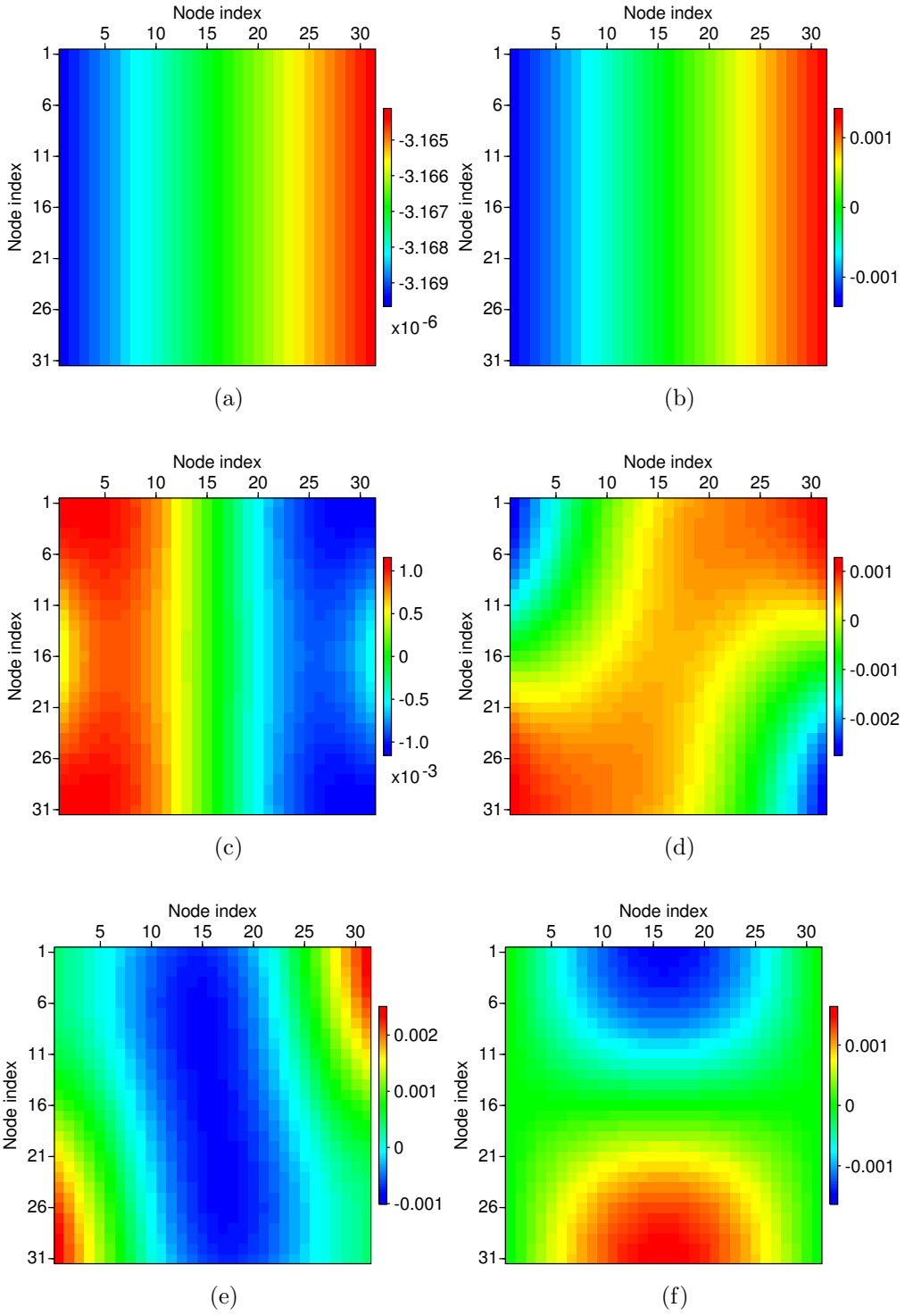


Figure 3.4: (a)–(f) represent the $u_3$ component of the first 6 spectral basis functions corresponding with the first 6 smallest eigenvalues for an isotropic homogeneous subgrid model.

constants $C_{11}$=10.5 GPa, $C_{13}$=3.25 GPa, $C_{15}$=-0.65 GPa, $C_{33}$=13.0 GPa, $C_{35}$=-1.52 GPa and $C_{55}$=4.75 GPa, and density $\rho$=1000 kg/m$^3$. The spectral basis functions clearly have different patterns than those in isotropic homogeneous medium, and it is this difference that results in the different kinetic, dynamic and anisotropy patterns in the seismic wavefields.

Complex heterogeneities will also introduce variations in the local spectral basis functions. Figures 3.7(a) and 3.7(b) show a subgrid model that contains several elliptic inclusions and some random heterogeneities on an homogeneous isotropic elastic background. Figures 3.8(a)–3.8(f) and 3.9(a)–3.9(f) show the first 6 eigenfunctions for this subgrid model. Patterns of the eigenfunctions in this model are no long symmetric as in Figures 3.3(a)–3.3(f) and 3.4(a)–3.4(f), but contain spatial variations that are related to the shape and elastic properties of the heterogeneous inclusions.

#### *3.2.2.2 Type II*

Another way to construct the multiscale basis functions is to decompose the basis function space into two parts, $W_H = W_H^1 \cup W_H^2$, which is an elastic extension of the acoustic wave equation case (Chung et al., 2013b,a).

The space $W_H^1$ is defined to capture the interior eigenmodes for $K$. Consider the local eigenvalue problem in $K$: find the pair $(\mathbf{u}, \zeta)$ such that

$$\begin{aligned} -\nabla \cdot \boldsymbol{\sigma} &= \zeta \rho \mathbf{u}, \\ \boldsymbol{\sigma} &= \mathbf{c} : \boldsymbol{\varepsilon}, \\ \boldsymbol{\varepsilon} &= \frac{1}{2}[\nabla \mathbf{u} + (\nabla \mathbf{u})^{\mathrm{T}}], \end{aligned} \tag{3.19}$$

where we set zero Dirichlet boundary condition, i.e., $\mathbf{u} = \mathbf{0}$ on $\partial K$. The above local

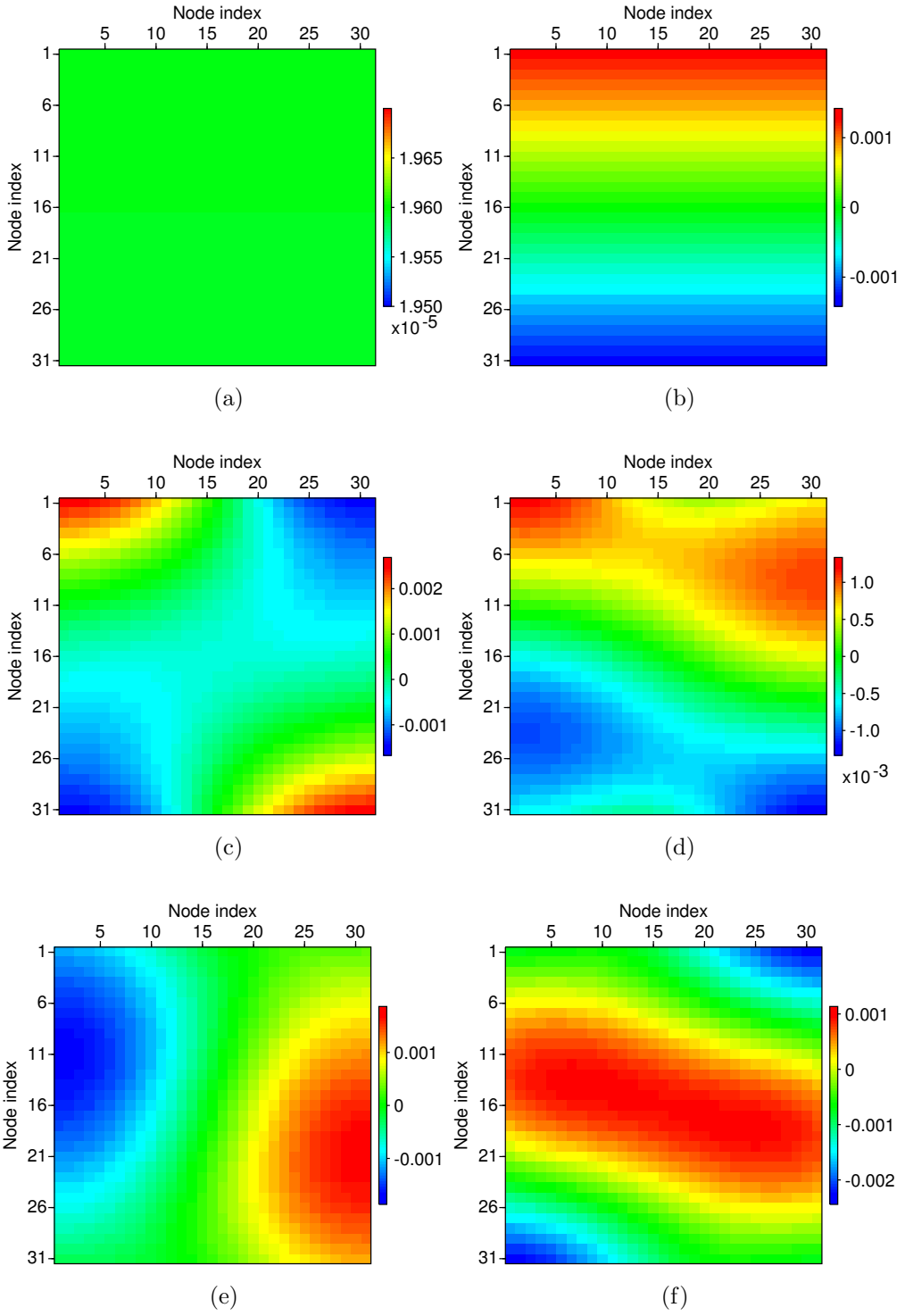


Figure 3.5: (a)–(f) represent the $u_1$ component of the first 6 spectral basis functions corresponding with the first 6 smallest eigenvalues for an anisotropic homogeneous subgrid model.

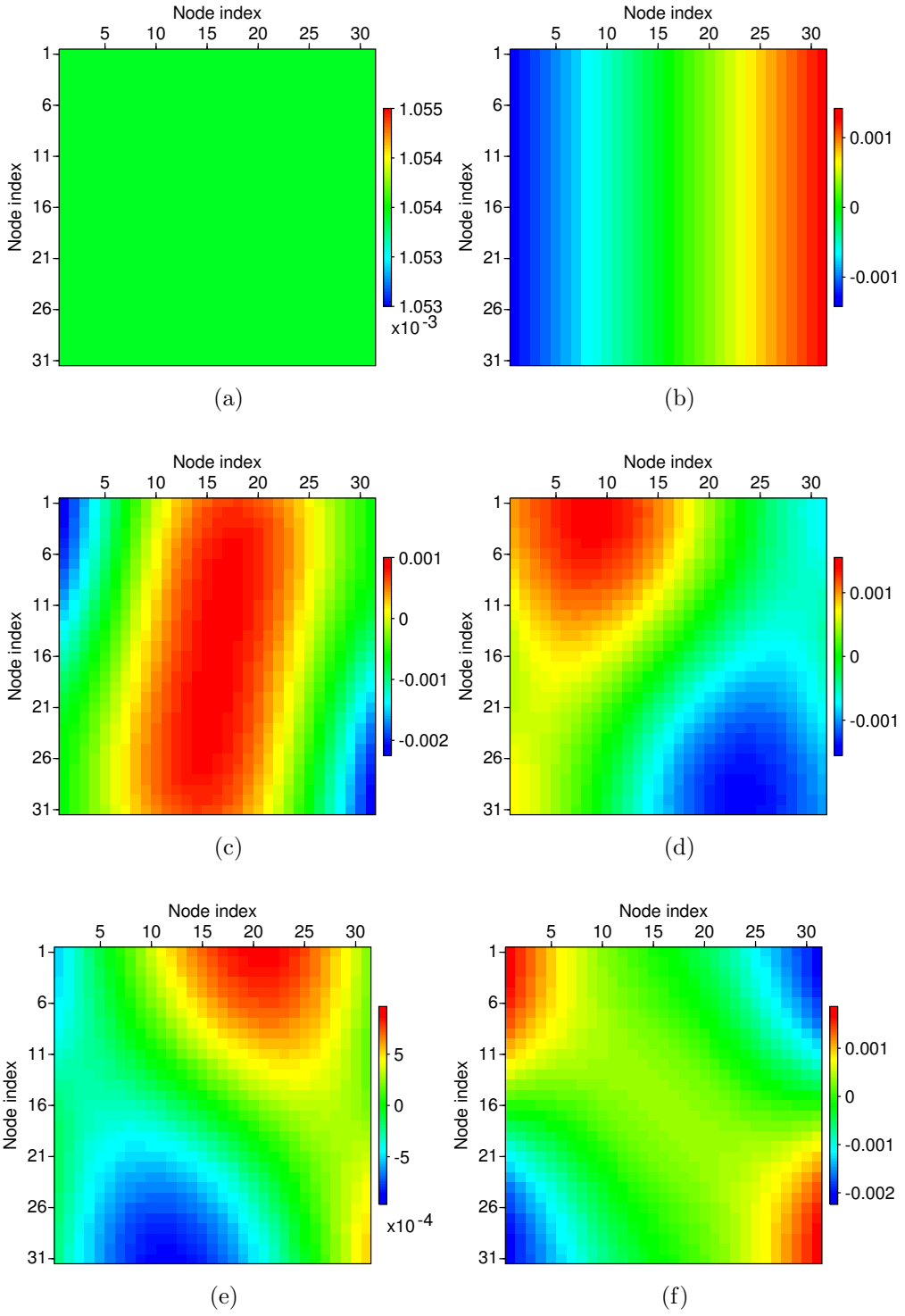


Figure 3.6: (a)–(f) represent the $u_3$ component of the first 6 spectral basis functions corresponding with the first 6 smallest eigenvalues for an anisotropic homogeneous subgrid model.

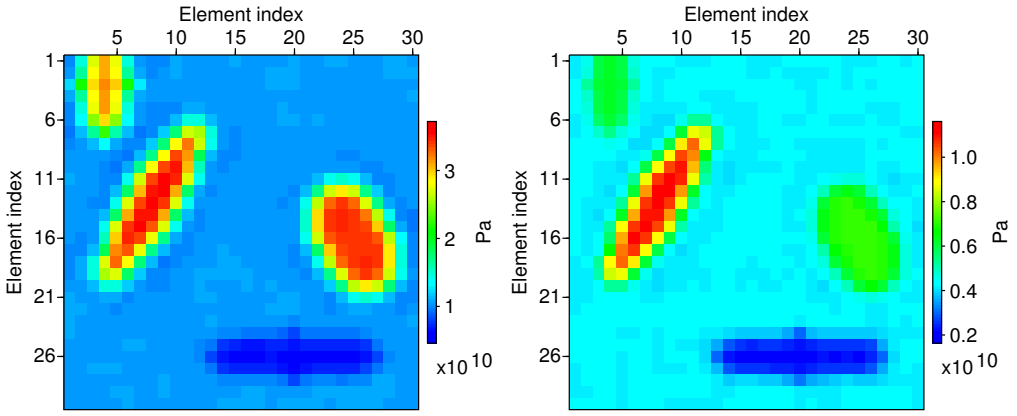


(a) (b)

Figure 3.7: Elasticity parameter variations within one coarse block. (a) and (b) represents $C_{11}$ and $C_{55}$, respectively.

problem corresponds with the following system:

$$\mathbf{A}_{\text{interior}}\mathbf{U} = \zeta\mathbf{M}_{\text{interior}}\mathbf{U}, \tag{3.20}$$

with $\mathbf{A}$ and $\mathbf{M}$ defined in equation 3.15 and 3.16, respectively, and the subscript "interior" represents the nodes that are not on $\partial K$. This local problem is quite similar in form with that defined in equation 3.13, but the solutions will be fundamentally different due to different boundary conditions in these two problems. In a similar way of previous local problems, we will select the first $m_1$ eigenfunctions $\boldsymbol{\phi}_1, \boldsymbol{\phi}_2, \cdots, \boldsymbol{\phi}_{m_1}$ corresponding to the first $m_1$ smallest eigenvalues $0 \leq \zeta_1 \leq \zeta_2 \leq \cdots \leq \zeta_{m_1}$ of the above problem, and then the space $W_H^1$ is defined as

$$W_H^1(K) = \text{span}\{\boldsymbol{\phi}_1, \boldsymbol{\phi}_2, \cdots, \boldsymbol{\phi}_{m_1}\}. \tag{3.21}$$

The multiscale basis functions from $W_H^1$ are called interior basis functions.

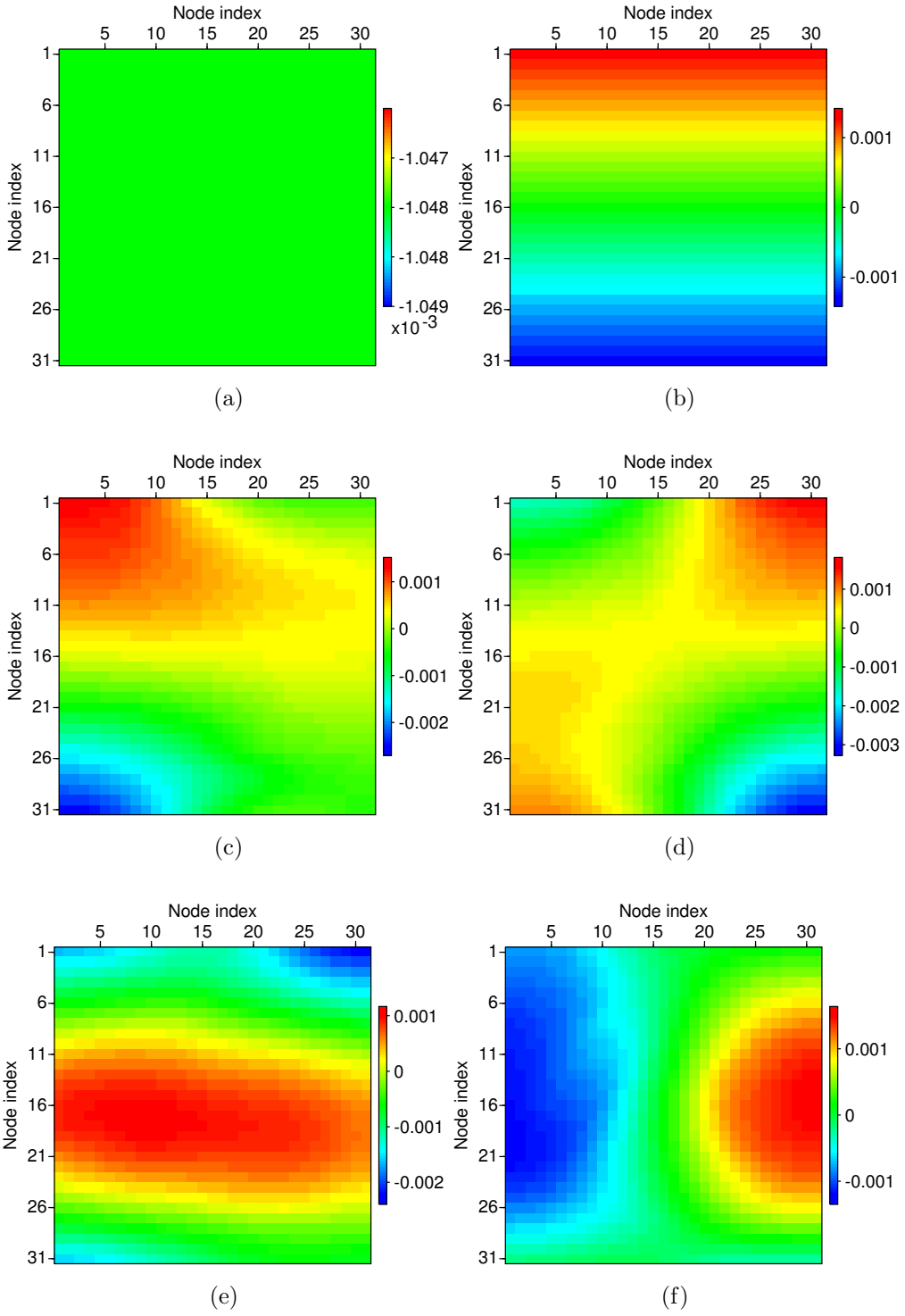


Figure 3.8: (a)–(f) represent the $u_1$ component of the first 6 spectral basis functions corresponding with the first 6 smallest eigenvalues for an isotropic heterogeneous subgrid model in Figure 3.7(a) and 3.7(b).

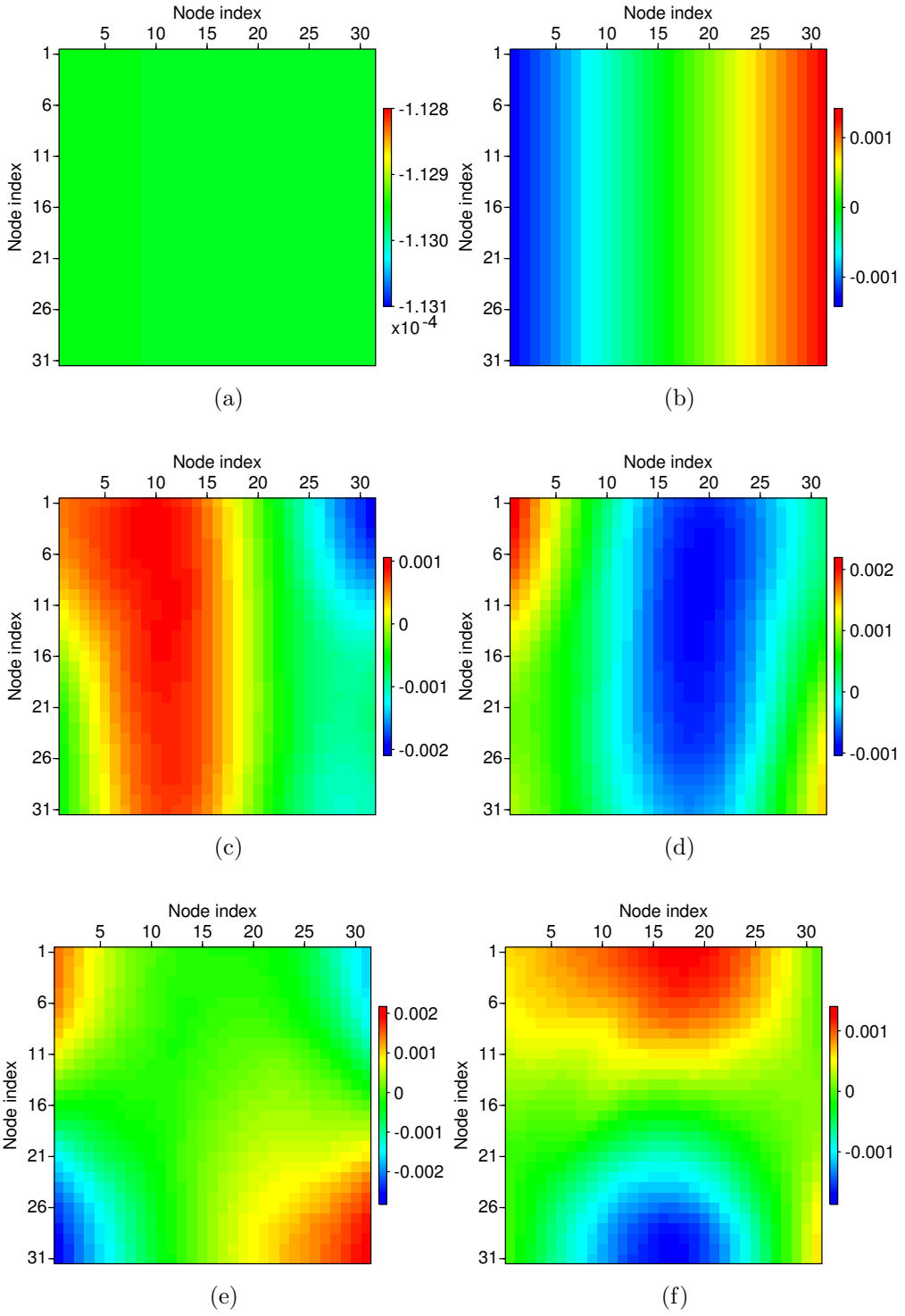


Figure 3.9: (a)–(f) represent the $u_3$ component of the first 6 spectral basis functions corresponding with the first 6 smallest eigenvalues for an isotropic heterogeneous subgrid model in Figure 3.7(a) and 3.7(b).

In the above definition for interior basis functions, we have set $\mathbf{u} = \mathbf{0}$ on $\partial K$. Consequently, the wavefield cannot represent a wavefield propagating across grid cells and their boundaries $\partial K$. We therefore define the space $W_H^2$ which takes care of the contribution of the boundaries of $K$. For a domain $K$, we first solve the local linear elasticity problem

$$-\nabla \cdot \boldsymbol{\sigma} = \mathbf{0}, \tag{3.22a}$$

$$\boldsymbol{\sigma} = \mathbf{c} : \boldsymbol{\varepsilon}, \tag{3.22b}$$

$$\boldsymbol{\varepsilon} = \frac{1}{2}[\nabla \mathbf{u} + (\nabla \mathbf{u})^{\mathrm{T}}], \tag{3.22c}$$

with Dirichlet boundary conditions $\mathbf{u} = \boldsymbol{\delta}_j$, where $j$ indexes boundary nodes on $\partial K$. For example, in 2-D, we can set $\mathbf{u} = (\delta_j, 0)$ or $\mathbf{u} = (0, \delta_j)$ at the $j$-th boundary node of $K$, where $\delta_j$ is the delta function and $j = 1, 2, \cdots, p$, with $p$ being the total number of boundary nodes. We denote the solutions as $\mathbf{u}_1, \mathbf{u}_2, \cdots, \mathbf{u}_{dp}$, where $d = 1$, 2, or 3 is the number of spatial dimensions, and then a trial basis function space $\tilde{W}_H^2$ is defined as

$$\tilde{W}_H^2(K) = \mathrm{span}\{\mathbf{u}_1, \mathbf{u}_2, \cdots, \mathbf{u}_{dp}\}, \tag{3.23}$$

For a rectangular $K$ that is composed of $30 \times 30$ finer elements, for instance, a total of 240 solutions will be calculated with the two source conditions on each boundary node, and these solutions can effectively reflect the medium property variations within $K$ associated with varying values on the boundaries. In practice, we select only a few important modes from $\tilde{W}_H^2$ to form a basis function space $W_H^2$, and the important modes are obtained from the following local spectral problem defined in

the trial basis function space $\tilde{W}_H^2$:

$$\mathbf{A}\tilde{\mathbf{U}} = \xi \mathbf{N}\tilde{\mathbf{U}}, \tag{3.24}$$

where

$$\mathbf{A} = \int_K \boldsymbol{\sigma}(\tilde{\boldsymbol{\gamma}}) : \boldsymbol{\varepsilon}(\tilde{\boldsymbol{\eta}}) d\mathbf{x}, \tag{3.25}$$

$$\mathbf{N} = \int_{\partial K} \rho \tilde{\boldsymbol{\gamma}} \cdot \tilde{\boldsymbol{\eta}} ds, \tag{3.26}$$

with $\tilde{\boldsymbol{\gamma}}, \tilde{\boldsymbol{\eta}} \in \tilde{W}_H^2$. Note that $\mathbf{N}$ is a mass matrix that is related to the edge of $K$, distinct from the mass matrix $\mathbf{M}$ in equation 3.16.

The space $\tilde{W}_H^2(K)$ contains a large number of eigenvector solution when the dimension of $K$ is large, and to construct a reduced space $W_H^2(K)$, we select the first $m_2$ eigenvectors $\tilde{\mathbf{u}}_1, \tilde{\mathbf{u}}_2, \cdots, \tilde{\mathbf{u}}_{m_2}$ corresponding to the first $m_2$ smallest eigenvalues, $0 \leq \xi_1 \leq \xi_2 \leq \cdots \xi_{m_2}$, and define the space $W_H^2$ by

$$W_H^2(K) = \text{span}\{\boldsymbol{\varphi}_1, \boldsymbol{\varphi}_2, \cdots, \boldsymbol{\varphi}_{m_2}\}, \tag{3.27}$$

with the basis

$$\boldsymbol{\varphi}_{i,l} = \sum_{j=1}^{dp} (\tilde{\mathbf{u}}^{\mathrm{T}})_{i,j} \mathbf{u}_{j,l}, \tag{3.28}$$

where in each terms of the above equation, $(i, j)$ represents the $j$-th node in the $i$-th vector.

These multiscale basis functions from $W_H^1$ are called boundary basis functions. Figures 3.10(a)–3.10(f) and 3.11(a)–3.11(f) show the corresponding first 6 interior basis functions solved from local spectral problem 3.20 for the isotropic heterogeneous model mentioned in the example for type I basis function, and it should be

noted that the interior basis functions are different from those defined through local spectral problem in equation 3.13. Figures 3.12(a)–3.12(f) and 3.13(a)–3.13(f) show the first 6 boundary basis functions solved from local spectral problem 3.24, with snapshot solutions solved with local linear elasticity problem 3.22 for the isotropic heterogeneous model. Clearly, both the interior and boundary basis functions can capture fine scale information since they are model-dependent, as for the type I basis function.

The above discussions are valid for the DG formulation. For CG, the type II basis functions can be constructed in exactly the same way, except that the calculated eigenfunctions should be multiplied with partition of unity $\chi_K$, as is in equation 3.18, i.e.,

$$V_H^1(K) = \text{span}\{\boldsymbol{\chi}_K\boldsymbol{\phi}_1, \boldsymbol{\chi}_K\boldsymbol{\phi}_2, \cdots, \boldsymbol{\chi}_K\boldsymbol{\phi}_{m_1}\}, \tag{3.29}$$

$$V_H^2(K) = \text{span}\{\boldsymbol{\chi}_K\boldsymbol{\varphi}_1, \boldsymbol{\chi}_K\boldsymbol{\varphi}_2, \cdots, \boldsymbol{\chi}_K\boldsymbol{\varphi}_{m_2}\}, \tag{3.30}$$

with eigenfunctions $\boldsymbol{\phi}_i$ and $\boldsymbol{\varphi}_i$ same with those in equations 3.21 and 3.27, respectively.

#### *3.2.2.3 Oversampling*

The oversampling method is a way to reduce the influence of fixed boundary conditions that are prescribed on $K$ when solving local problems (Hou and Wu, 1997; Efendiev et al., 2013). The concept of oversampling is shown by Figure 3.14. When solving for the two types of basis functions, we solve the local problems on a larger region $K'$ that includes a region outside $K$, as indicated by the dashed black rectangle in Figure 3.14. We still apply the boundary conditions and local problems that are defined in equations 3.13, 3.24 and 3.20, where the boundary conditions are

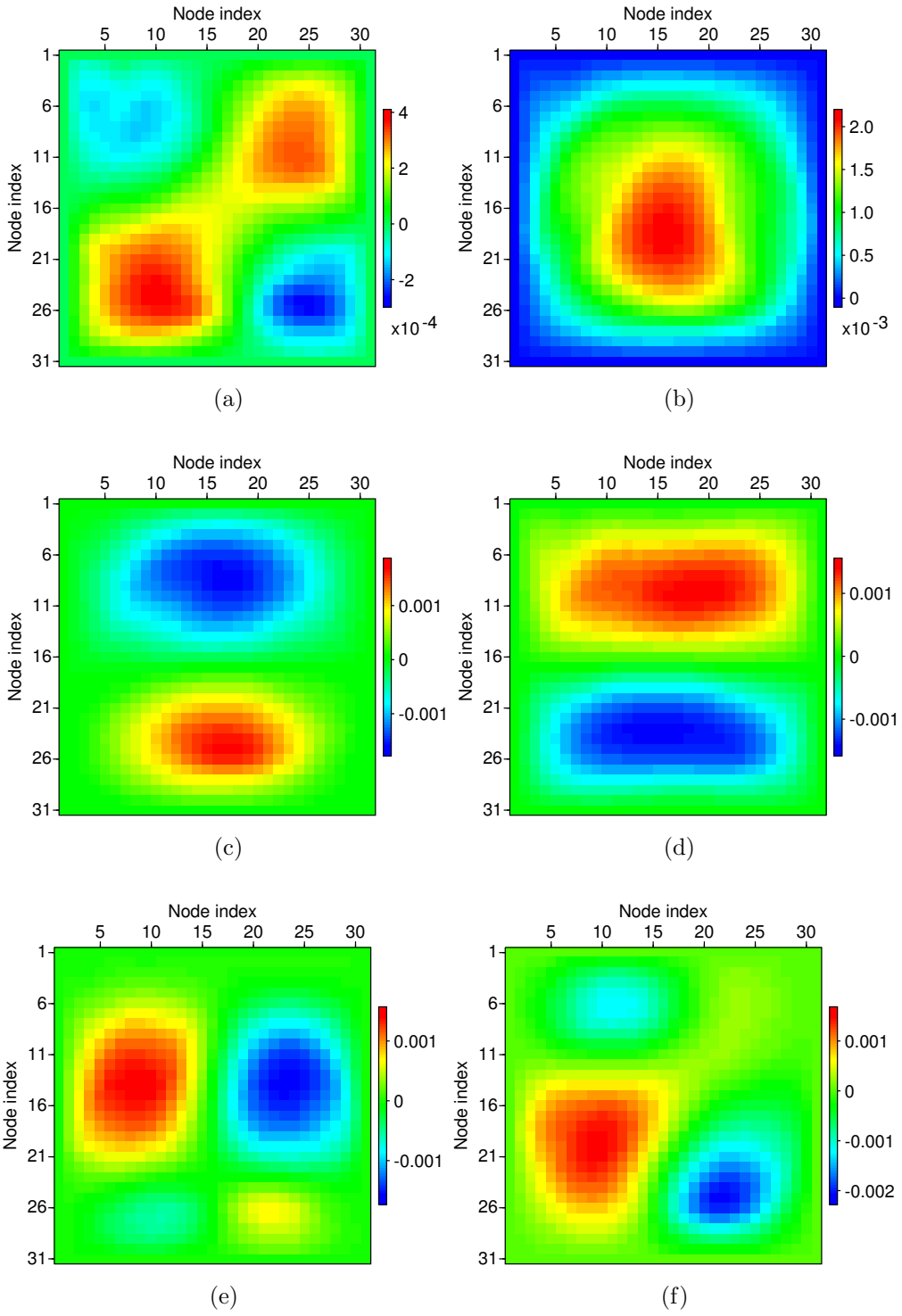


Figure 3.10: (a)–(f) represent the $u_1$ component of the first 6 interior basis functions for the isotropic heterogeneous subgrid model in Figures 3.7(a) and 3.7(b).

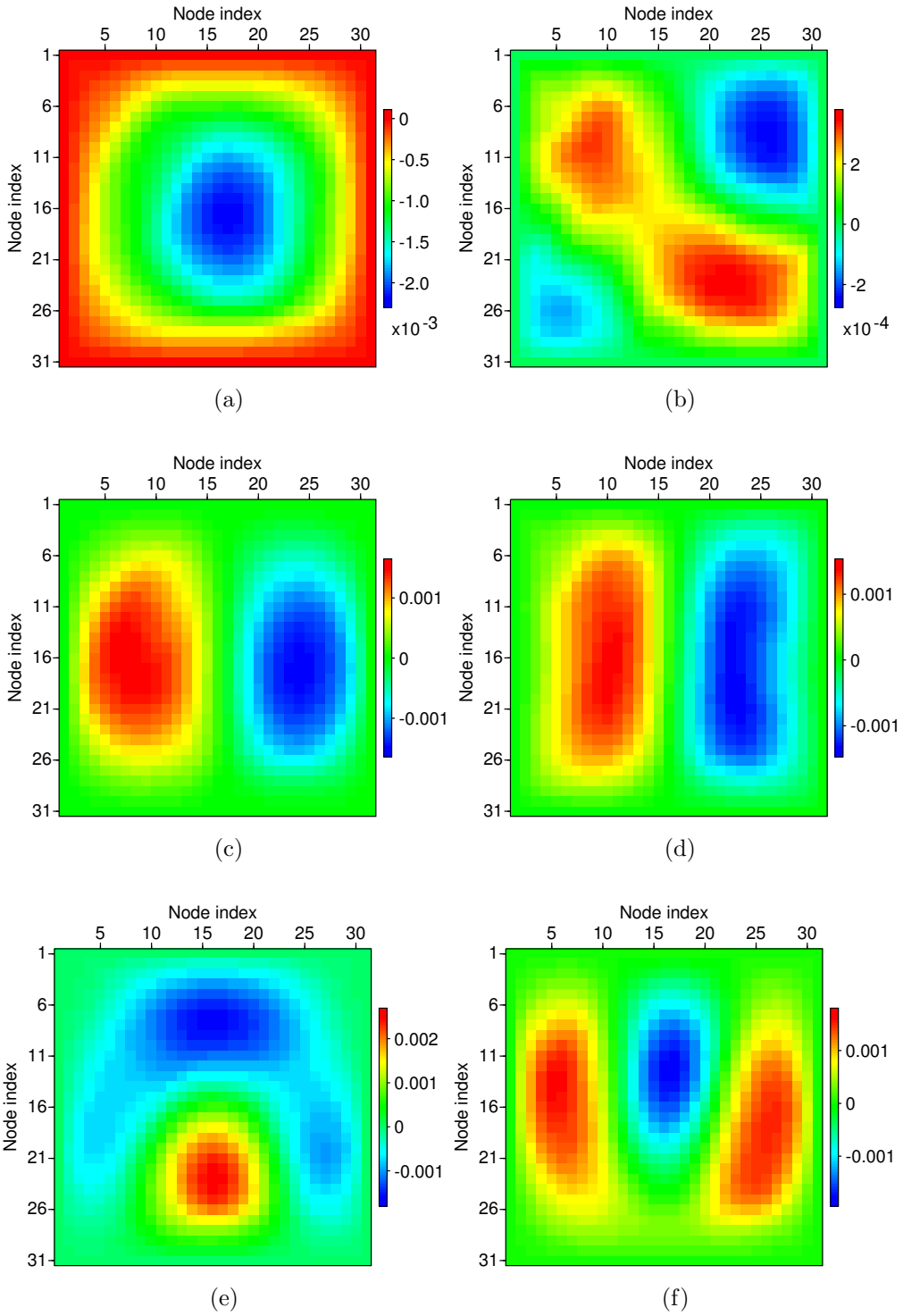


Figure 3.11: (a)–(f) represent the $u_3$ component of the first 6 interior basis functions for the isotropic heterogeneous subgrid model in Figures 3.7(a) and 3.7(b).

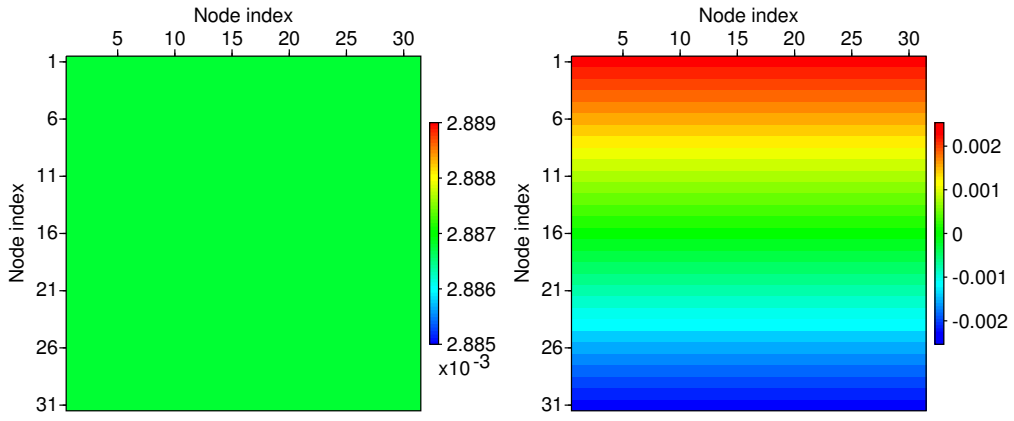


(a)




(b)

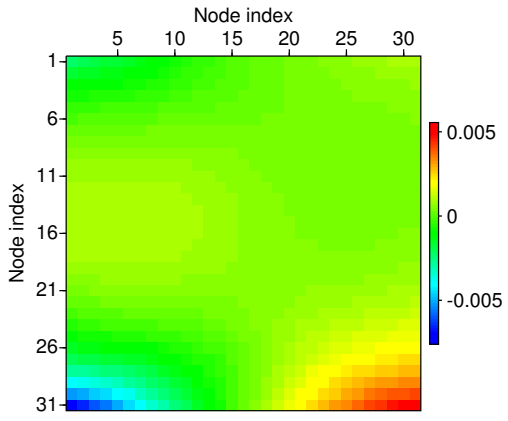


(c)

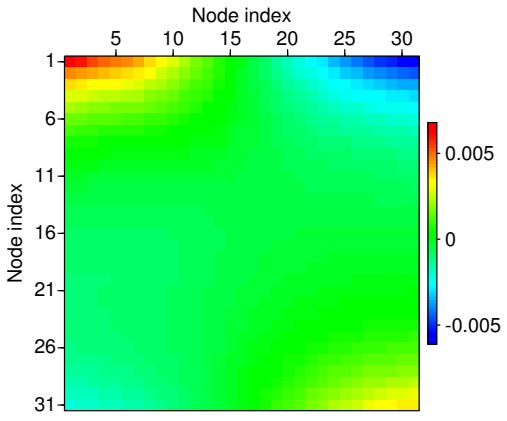


(d)

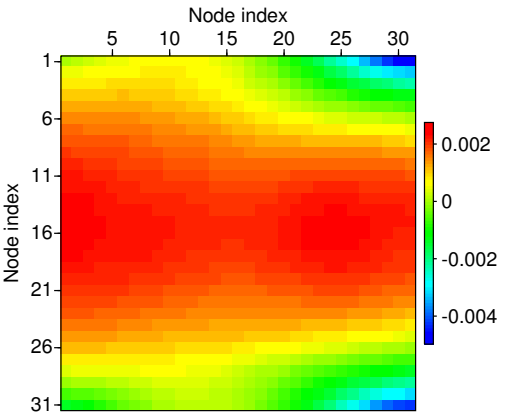


(e)

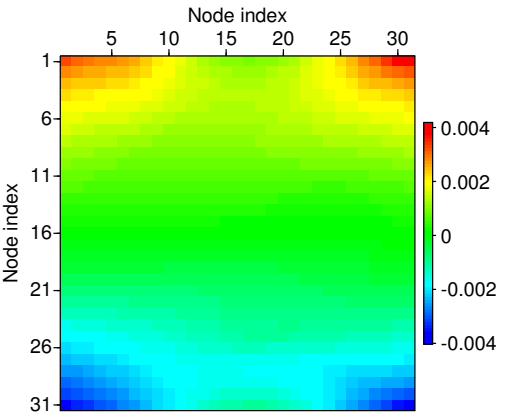


(f)

Figure 3.12: (a)–(f) represent the $u_1$ component of the first 6 boundary basis functions for the isotropic heterogeneous subgrid model in Figures 3.7(a) and 3.7(b).

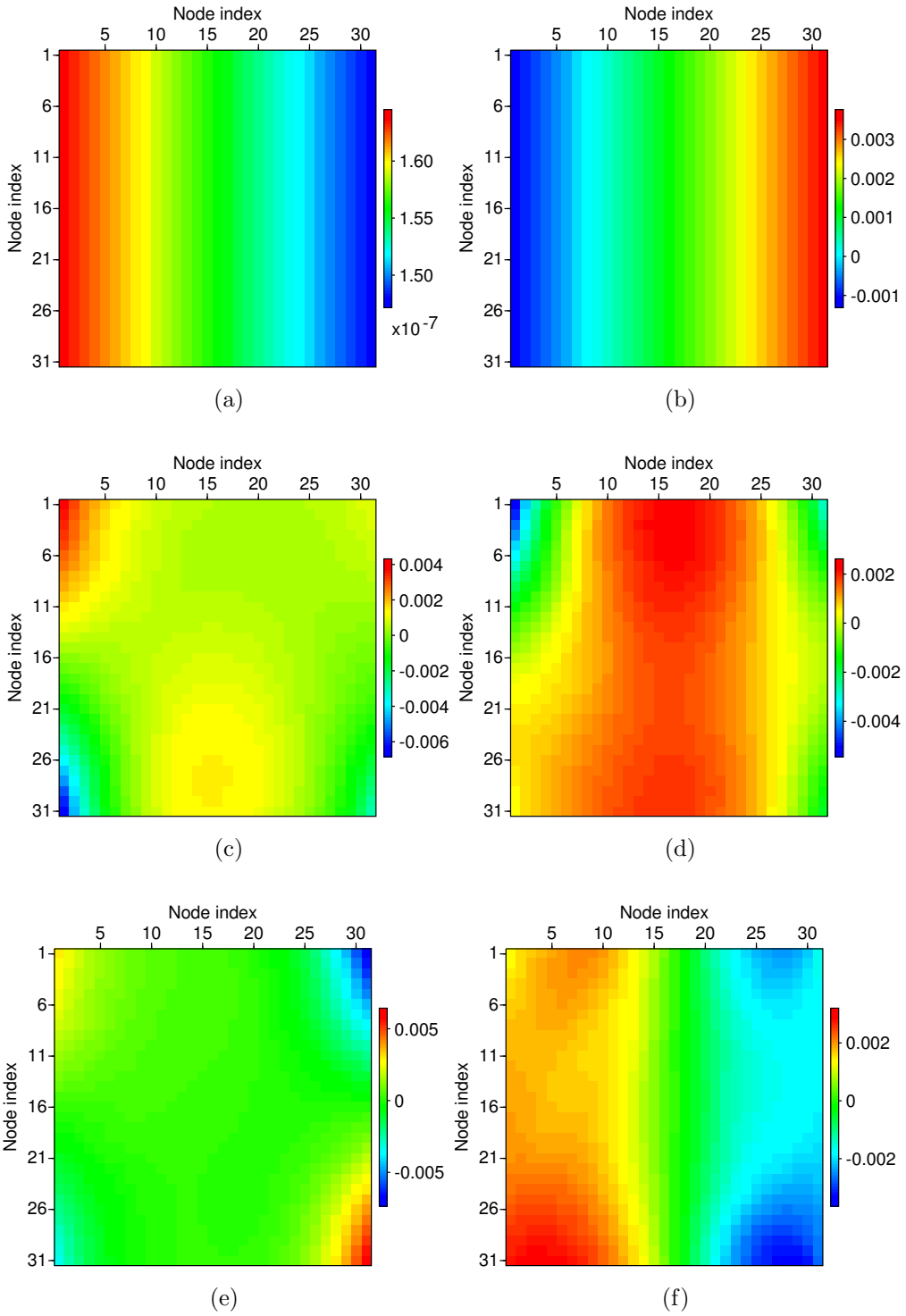


Figure 3.13: (a)–(f) represent the $u_3$ component of the first 6 boundary basis functions for the isotropic heterogeneous subgrid model in Figures 3.7(a) and 3.7(b).

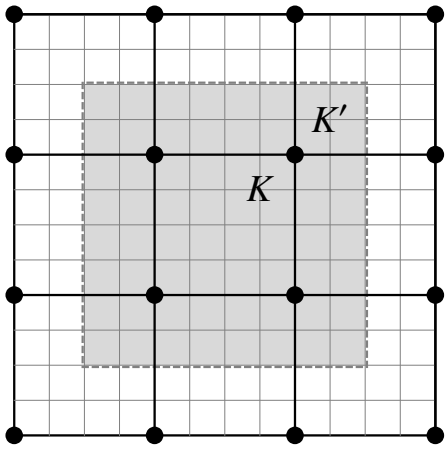


Figure 3.14: A sketch of oversampling for DG formulation. $K$ is the coarse element where the corresponding problems needed to be solved, while $K'$ represented by gray dashed rectangle is the oversampled coarse element. After solving local problems in $K'$, we take the solutions corresponding with the nodes in $K$ as basis functions. For CG, a similar sketch can be got.

prescribed on $\partial K'$, rather than $\partial K$. After we obtains the solutions on $K'$, we select values on the interior region corresponding to $K$ and take them as the oversampling multiscale basis functions. In this way, the boundary nodes on $\partial K$, which are the interior nodes of $K'$, are less affected by the prescribed boundary conditions of various local problem and therefore can better represent the local properties of the elastic wave equation.

### *3.2.3 Stability condition and dispersion relation*

A rigorous proof of the stability condition as well as the dispersion relation of the multiscale method would be beyond the scope of this paper. We will present these relations in future work. For a reference purpose, we would recommend Chung et al. (2013a) for a complete and rigorous proof of the stability and convergence of the similar multiscale method for acoustic wave equation case. Also, we would recommend to use some standard results of stability condition for conventional continuous and

discontinuous Galerkin finite-element method (De Basabe and Sen, 2007; De Basabe et al., 2008; Cockburn, 2003) in our multiscale method at present. In the Numerical Results part, we will present some comparisons between the conventional CG/DG with our multiscale CG/DG method, and in both modelings with explicit scheme, we use $\Delta t$ that can ensure the long time stability of conventional CG/DG method, since our tests suggest such $\Delta t$ can be adequate to ensure the stability of multiscale CG/DG method as well.

### *3.2.4 Implementation*

#### *3.2.4.1 Semi-discrete form of the GMsFEM*

With the basis functions we have introduced above, the semi-discrete system of the GMsFEM can be expressed as

$$\mathbf{M}\ddot{\mathbf{d}}_H + \mathbf{K}\mathbf{d}_H + \mathbf{F} = \mathbf{0}, \tag{3.31}$$

where $\mathbf{M}$, $\mathbf{K}$ and $\mathbf{F}$ is the global mass matrix, stiffness matrix and force vector, respectively. For example, for CG-GMsFEM,

$$M_{ij} = \int_\Omega \mathbf{\Phi}_i^{\mathrm{T}} \cdot \mathbf{\Phi}_j d\mathbf{x}, \tag{3.32}$$

$$K_{ij} = a_{\mathrm{CG}}(\mathbf{\Phi}_i, \mathbf{\Phi}_j), \tag{3.33}$$

$$F_i = \int_\Omega \mathbf{f} \cdot \mathbf{\Phi}_i d\mathbf{x}, \tag{3.34}$$

which can be calculated by matrix multiplication (Kaufmann et al., 2008; Larson and Bengzon, 2013).

For the DG formulation, all the expressions are the same, except that the basis functions are $\mathbf{\Psi}_i$, and $a_{\mathrm{CG}}(\mathbf{\Phi}_i, \mathbf{\Phi}_j)$ is replaced with $a_{\mathrm{DG}}(\mathbf{\Psi}_i, \mathbf{\Psi}_j)$.

#### *3.2.4.2 Absorbing boundary conditions*

In any practical applications of wave equation modeling, it is necessary to set appropriate boundary conditions at the computation domain boundaries, including a free surface boundary condition and absorbing boundary condition (ABC). Since the free surface boundary conditions can be naturally satisfied by setting $\boldsymbol{\sigma} \cdot \mathbf{n} = \mathbf{0}$ (Larson and Bengzon, 2013; Komatitsch et al., 1999), we focus on choosing appropriate boundary conditions that can damp or absorb outgoing waves at the boundaries.

There have been many different approaches that can achieve this goal, e.g., one-way wave equation based ABC (Engquist and Majda, 1977; Higdon, 1991; Givoli et al., 2006; Hagstrom et al., 2008; Liu and Sen, 2010, 2012), attenuation-based approach (Cerjan et al., 1985; Kosloff and Kosloff, 1986; Sarma et al., 1998), and perfectly matched layers (Bérenger, 1994; Collino and Tsogka, 2001; Gao and Zhang, 2008; Komatitsch and Martin, 2007; Meza-Fajardo and Papageorgiou, 2008; Ping et al., 2014). Here, we adopt the Rayleigh damping (e.g., Sarma et al., 1998), or so-called proportional damping, to reduce the amplitude of outgoing waves at the boundaries. Nevertheless, we also set a non-constant damping zone for Rayleigh damping by changing the spatial weight from the inner to the outer nodes, and the weight profile in the $i$-th axis direction we have chosen is a power-law curve, i.e.,

$$w_{i,j}(x_i) = \left( \frac{j-1}{L_i} \right)^{b_i}, \tag{3.35}$$

where $j$ is the $j$-th node counting from the common boundary of computation domain and the attenuating zone, $L_i$ is the total number of nodes in the attenuating zone in the $i$-th direction, $b_i$ is the power-law exponent for the damping zone. The reason for choosing such a varying weight is to avoid sudden medium properties, since by adding Rayleigh damping the medium has changed to viscous medium, which will

cause reflections at the boundary of damping zone and central computational domain. The weight in equation 3.35 is similar with the idea in Liu and Sen (2010), yet they applied a linear weight where $b_i = 1$. Combining the weights in all directions, we get

$$w(\mathbf{x}) = \sum_{i=1}^{3} w_i(x_i). \tag{3.36}$$

By introducing the proportional damping boundary condition, the modeling system 3.31 will become

$$\mathbf{M}\ddot{\mathbf{d}}_H + \mathbf{E}\dot{\mathbf{d}}_H + \mathbf{K}\mathbf{d}_H + \mathbf{F} = \mathbf{0}, \tag{3.37}$$

where $\mathbf{E}$ is the global damping matrix that are only non-zero on the damping boundary zone. For each element $K$ in the damping boundary zone, the damping matrix can be written as the sum of mass matrix and stiffness matrix with some coefficients as

$$\mathbf{E}_K = \alpha_1 \mathbf{M}_K + \alpha_2 \mathbf{K}_K, \tag{3.38}$$

where the damping coefficients satisfy

$$2\omega_i \xi_i = \alpha_1 + \alpha_2 \omega_i^2, \tag{3.39}$$

the parameters $\omega_i$ are related the frequencies of the source wavelet (Sarma et al., 1998), and the $\xi_i$ are the damping ratio with respect to the critical damping ratio related to the medium properties and to the width of the damping zone around the computation zone. The coefficients can be solved directly from equation 3.39 by choosing two distinct frequencies $\omega_1$ and $\omega_2$, and two different damping ratios $\xi_1$ and $\xi_2$:

$$\alpha_1 = \frac{2\omega_1\omega_2(\xi_2\omega_1 - \xi_1\omega_2)}{\omega_1^2 - \omega_2^2}, \tag{3.40}$$

$$\alpha_2 = \frac{2(\xi_1\omega_1 - \xi_2\omega_2)}{\omega_1^2 - \omega_2^2}. \tag{3.41}$$

We remark that the choice of two different $\xi_i$ is different from that in Sarma et al. (1998), where the two damping ratios are set to be the same, i.e., $\xi_1 = \xi_2$.

#### *3.2.4.3 Adaptability in choosing the number of basis functions*

The accuracy of the multiscale solution is closely related to the number of basis functions in the coarse elements. In principle, for a fixed ratio of coarse to fine element dimensions, the shorter the wavelength of the wavefield traveling through the coarse element, the more basis functions are required to represent the wavefield in this coarse element. This is a natural conclusion from the physical meaning of the multiscale basis functions, since in the last section, we have known that the multiscale basis functions are solved from local spectral problems, and the selection of first eigenfunctions corresponds with selecting the eigenmodes with lowest frequencies. Therefore, to represent the shorter wavelength portion of a wavefield, more eigenfunctions, i.e., more multiscale basis functions are required.

However, in a certain model, the elasticity parameters and density may be spatially heterogeneous, and in some circumstances we may encounter highly heterogeneous media. When we solve the wave equation with GMsFEM on the coarse mesh, in some coarse elements we may need greater number of basis functions than the others. Low velocity portions of the model will require more basis functions, but this will be too many for regions with larger velocities. We therefore propose an adaptive way to quantify and set the number of basis functions in each coarse element.

In a particular model, for each coarse element, say, $K_j$, we calculate the harmonic

average of S-wave velocity, i.e.,

$$v_{\text{S,Harmonic}} = n_1 n_3 \left( \sum_{i_1=1}^{n_1} \sum_{i_3=1}^{n_3} \sqrt{\frac{\rho(i_1, i_3)}{C_{55}(i_1, i_3)}} \right)^{-1}, \tag{3.42}$$

and then a time duration $\delta t_j$, which characterizes the average time for a plane wave propagating through the coarse element $K_j$, can be calculated as

$$\delta t_j = \frac{1}{v_{\text{S,Harmounic}}}, \tag{3.43}$$

from which we can know the maximum and minimum time differences in the model:

$$\delta t_{\max} = \max_{\cup K_j} \delta t_j, \tag{3.44}$$

$$\delta t_{\min} = \min_{\cup K_j} \delta t_j, \tag{3.45}$$

where $K_j$ denotes in the coarse block $K_j$, and $\cup K_j$ means the set of all coarse blocks.

Assume the maximum and minimum number of basis functions we assign to the coarse element are $n_{\max}$ and $n_{\min}$, respectively, then for some coarse element $K_j$ the number of basis functions we assign satisfies

$$\frac{n_{\max} - n_j}{n_{\max} - n_{\min}} = \frac{\delta t_{\max} - \delta t_j}{\delta t_{\max} - \delta t_{\min}}, \tag{3.46}$$

where we take the integer part of $n_j$, if necessary. In this way, the coarse elements where the wave velocity is slower, i.e., the wavelength is shorter, will be assigned with greater number of basis functions, and vice versa.

It should be noted that this method determining the number of basis functions can only give a relative indication of which cells need more or fewer bases. We

still need to set minimum and maximum numbers of basis functions $n_{\min}$ and $n_{\min}$ beforehand, which requires test evaluations.

#### *3.2.4.4 A global projection approach*

The global matrices can be calculated by projecting the global matrices of the corresponding fine mesh problem onto the coarse mesh with a global projection matrix assembled from the calculated multiscale basis functions. Assume we can first assemble the global matrices $\mathbf{M}_h$, $\mathbf{K}_h$ and $\mathbf{F}_h$ on the fine mesh with traditional finite-element assembly methods (e.g., Rivière, 2008; Kaufmann et al., 2008; Larson and Bengzon, 2013), then for CG formulation, we form a global projection matrix $\mathbf{R}$ with the multiscale basis functions as

$$\mathbf{R} = (R_1, R_2, \cdots, R_N)^{\mathrm{T}}, \tag{3.47}$$

where

$$R_i = [\mathbf{\Phi}_{i,1}, \mathbf{\Phi}_{i,2}, \cdots, \mathbf{\Phi}_{i,m_i}], \tag{3.48}$$

with $\mathbf{\Phi}_{i,j}$ being the $j$-th multiscale basis function of the $i$-th coarse node, which follows the definition 3.18 of type I basis function, or 3.30 and 3.29 of type II basis function, $m_i$ is the total number of basis functions of the $i$-th coarse node. For DG formulation, $\mathbf{R}$ can be constructed in the same way.

The global projection matrix $\mathbf{R}$ therefore has the dimension $(\sum_{i=1}^{N} m_i) \times n$, where $N$ is the number of coarse nodes in CG formulation, and coarse elements in DG formulation, and $m_i$ is the number of basis functions in $K_i$, and $n$ is the number of degrees of freedom of fine mesh $\mathcal{T}_h$ or $\mathcal{P}_h$. With $\mathbf{R}$, the semi-discrete system 3.37 can

be written as

$$\mathbf{R}\mathbf{M}_h\mathbf{R}^{\mathrm{T}}\ddot{\mathbf{d}}_H + \mathbf{R}\mathbf{E}_h\mathbf{R}^{\mathrm{T}}\dot{\mathbf{d}}_H + \mathbf{R}\mathbf{K}_h\mathbf{R}^{\mathrm{T}}\mathbf{d}_H + \mathbf{R}\mathbf{F}_h = \mathbf{0}. \tag{3.49}$$

Clearly, $\mathbf{d}_H$ has the length of $\sum_{i=1}^{N} m_i$, compared with $n$ of $\mathbf{d}_h$ in the corresponding finie mesh problem. Importantly, the expected wavefield on the fine mesh can be recovered through

$$\mathbf{d}_h = \mathbf{R}\mathbf{d}_H, \tag{3.50}$$

which means that the degrees of freedom that are required to save and recover the complete wavefield can be greatly reduced, given that normally the ratio between $n$ and $\sum_{i=1}^{N} m_i$ is large. For example, assume there is an equal number of basis functions in all $K_i$, say, $m$, then for a rectangular domain $\Omega$ with rectangular elements $K$ in 2-D, this ratio is $2(n_1+1)(n_2+1)/[(n_1/r_1+1)(n_2/r_2+1)m]$ for the CG formulation, and $2(r_1+1)(r_2+1)/m$ for the DG formulation. Here $n_i$ is the number of element in $i$-th direction on fine mesh and $r_i$ is the number of element contained in $i$-th direction in $K$. This ratio can be large if $r_i$ is large.

#### *3.2.4.5 Time stepping*

For temporal discretization, we simply use a second-order central finite difference, i.e.,

$$\ddot{\mathbf{d}}_H = \frac{\mathbf{d}_H^{t+\Delta t} - 2\mathbf{d}_H^{t} + \mathbf{d}_H^{t+\Delta t}}{\Delta t^2}, \tag{3.51}$$

$$\dot{\mathbf{d}}_H = \frac{\mathbf{d}_H^{t+\Delta t} - \mathbf{d}_H^{t-\Delta t}}{2\Delta t} \tag{3.52}$$

which has second-order accuracy. More complicated time stepping schemes, e.g., the Newwark scheme (e.g., Marfurt, 1984; Hughes, 1987) could be adopted for the

temporal discretization.

#### *3.2.4.6 Source term*

We have set the source as a force vector $\mathbf{f} = \mathbf{f}(\mathbf{x}, \theta, t) = (f_1, f_3)$ with Ricker wavelet signature in time and a Gaussian smoothing zone around the source position in space,

$$\mathbf{f}(\mathbf{x}, \theta, t) = G(\mathbf{x})\mathbf{P}(\theta)R(t), \tag{3.53}$$

where

$$G(\mathbf{x}) = \exp\left[-\left(\frac{\mathbf{x} - \mathbf{x}_0}{b}\right)^2\right], \tag{3.54}$$

$$\mathbf{P}(\theta) = (\cos\theta, \sin\theta)^{\mathrm{T}}, \tag{3.55}$$

$$R(t) = [1 - 2\pi^2 f_0^2 (t - t_0)^2] \exp[-\pi^2 f_0^2 (t - t_0)^2]. \tag{3.56}$$

Here $\mathbf{x}_0$ is the source position, $b$ is the correlation length in space with $b = 7h$, where $h$ being the element size on the fine mesh, $\theta$ is the polar angle of the source force vector with $\theta = 0$ being the force points along $x_1$ axis, $f_0$ is the central frequency of the wavelet, $t_0 = 1/f_0$. This source function will be used in all the following numerical examples, except that the central frequency $f_0$ may vary example from example.

## 3.3 Numerical results

We verify the effectiveness of our GMsFEM with four different examples.

### *3.3.1 Isotropic-TTI model*

In the first example, we test the CG multiscale approach using a model composed of isotropic and TTI materials to verify the effectiveness of our method for numerical modeling on the coarse mesh. The whole model is 4000 m in horizontal direction

and 4000 m in depth, and at the depth of 1800 m, there is an interface, above which is a homogeneous isotropic medium with elastic parameters $C_{11} = 10$ GPa, $C_{55} = 4$ GPa. Below the interface is homogeneous TTI medium with elasticity constants $C_{11} = 10.8125$ GPa, $C_{13} = 4.1875$ GPa, $C_{15} = -1.1908$ GPa, $C_{33} = 15.8125$ GPa, $C_{35} = -3.1393$ GPa, $C_{55} = 5.6875$ GPa, and the whole model has density of 1000 kg/m$^3$. We discretize the model with 400×400 fine elements, so that each element is 10 m in horizontal direction and 10 m in depth. For the multiscale modeling, we discretize the model the 40×40 coarse elements, so that the size of coarse element is 100 m in each direction. We have set $\theta = \pi/2$, i.e., a vertical force vector, as the source. In this example, we set $f_0$ to be 20 Hz. We also used a 1 ms time interval for both conventional CG-FEM and our CG-GMsFEM. We have adopted type I basis functions for the CG-GMsFEM, without oversampling.

Tests compare the vertical component displacement ($u_3$) wavefield snapshots at 0.5 s of the CG-FEM and CG-GMsFEM, which are are calculated with equation 3.47. Figure 3.16(a) is the $u_3$ wavefield snapshot solved from conventional CG-FEM method, and Figures 3.16(b)-3.16(f) are solutions from CG-GMsFEM, with the number of spectral basis functions $m$ =10, 20, 30, 40, and 50, respectively. Multiscale solution with 10 spectral basis functions has large obvious errors, since we can clearly see numerical dispersion in the snapshot. We define the $L^2$-norm error of the wavefield as

$$e(\mathbf{u}) = \frac{\|\mathbf{u}_h - \mathbf{R}\mathbf{u}_H\|}{\|\mathbf{u}_h\|}, \tag{3.57}$$

and then we can see in Table 3.3.1 that the error decreases from 108% to 0.691% by increasing from 10 to 50 basis functions. Meanwhile, the degrees of freedom increases from 1.681e4 to 8.405e4. In comparison, the corresponding degrees of freedom in CG-FEM is 3.21602e5. Also, the CPU time for calculating the multiscale basis

functions and the preprocessing of global matrices increases with the use of more basis functions. However, this calculation is one-time, and the resulting matrices can be used in the same model for different source positions and receiver positions, which is critically important for full-wavefield based imaging methods, such as reverse time migration.

The CG-GMsFEM is not advantageous in terms of computation time compared with conventional method, as can be seen from Table 3.1. Nevertheless, the construction of CG-GMsFEM is important, since it can provide important insights of the relation between the accuracy and the number of basis functions.

| $m$ | DOF | $e(\mathbf{u})$ | $T_{\text{basis}} + T_{\text{inverse}}$ | $T_{\text{modeling}}$ |
|---|---|---|---|---|
| - | 3.216e5 | - | - + 12.91 | 132.77 |
| 10 | 1.681e4 | 1.08e0 | 422.86+5.41 | 24.36 |
| 20 | 3.362e4 | 2.87e-1 | 520.73+17.47 | 97.45 |
| 30 | 5.043e4 | 7.89e-2 | 597.33+41.61 | 208.11 |
| 40 | 6.724e4 | 2.74e-2 | 673.02+71.24 | 380.81 |
| 50 | 8.405e4 | 6.91e-3 | 1010.47+123.31 | 701.86 |

Table 3.1: The relation between number of basis functions and the relative error, as well as the DOF and calculation time. $m$ is the number of type I spectral basis functions, DOF is the number of unknowns in the multiscale modeling system, $e(\mathbf{u})$ is the $L^2$-norm error of the displacement wavefield, $T_{\text{basis}}$ is the CPU time of calculating the multiscale basis functions, $T_{\text{inverse}}$ is the CPU time of calculating the Cholesky decomposition of the global mass matrix, and $T_{\text{modeling}}$ is the CPU of calculating the wavefield, i.e., all the time steps. The first row is the result from reference CG-FEM solution, therefore $m$, $e(\mathbf{u})$ and $T_{\text{basis}}$ are all left blank.

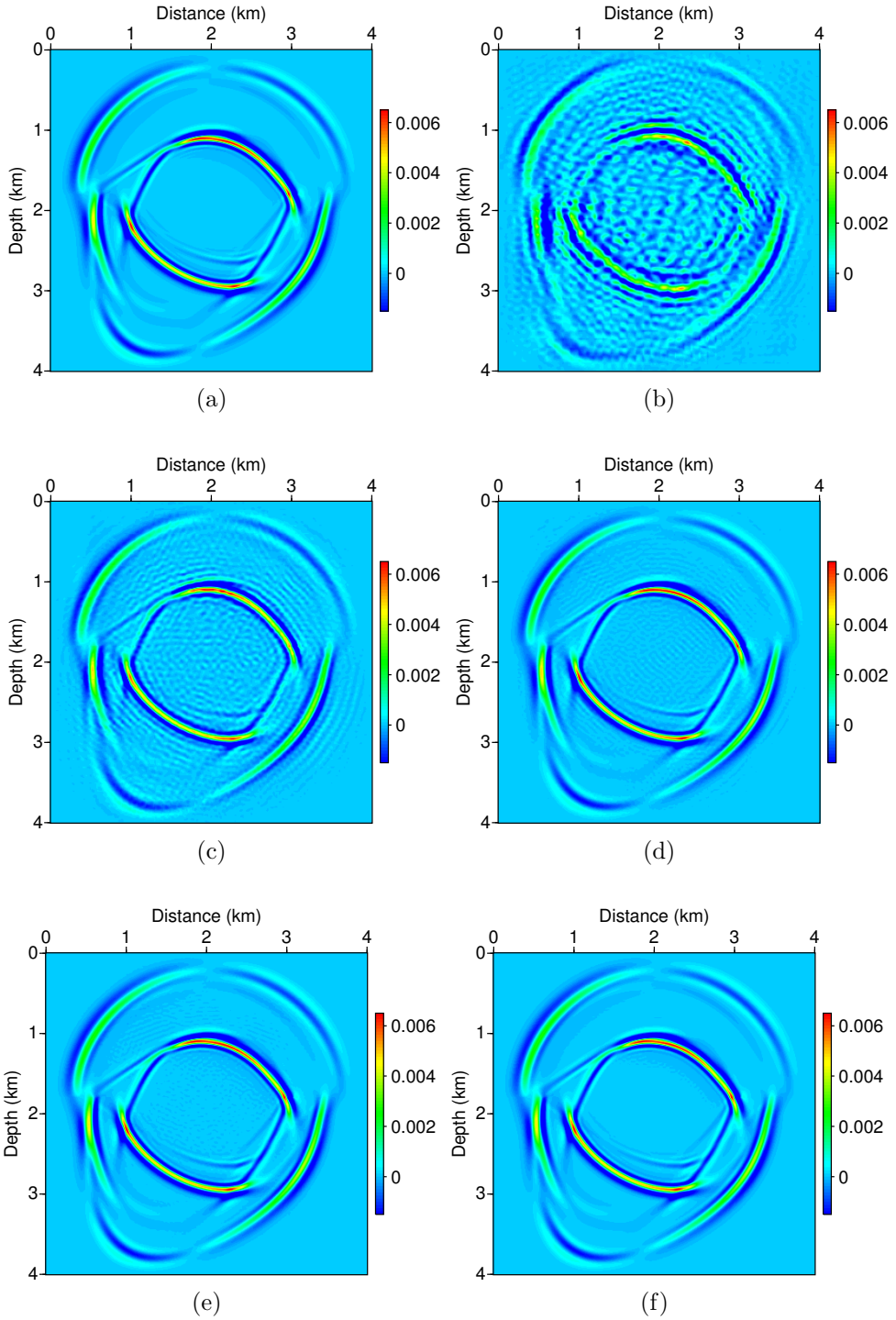


Figure 3.15: $u_1$ wavefield snapshots solved with (a) CG-FEM and (b)-(f) CG-GMsFEM. All the multiscale solutions have an upscaling ratio $r = 10$, and number of spectral basis functions $m$ =10, 20, 30, 40, 50 for (b)-(f), respectively.

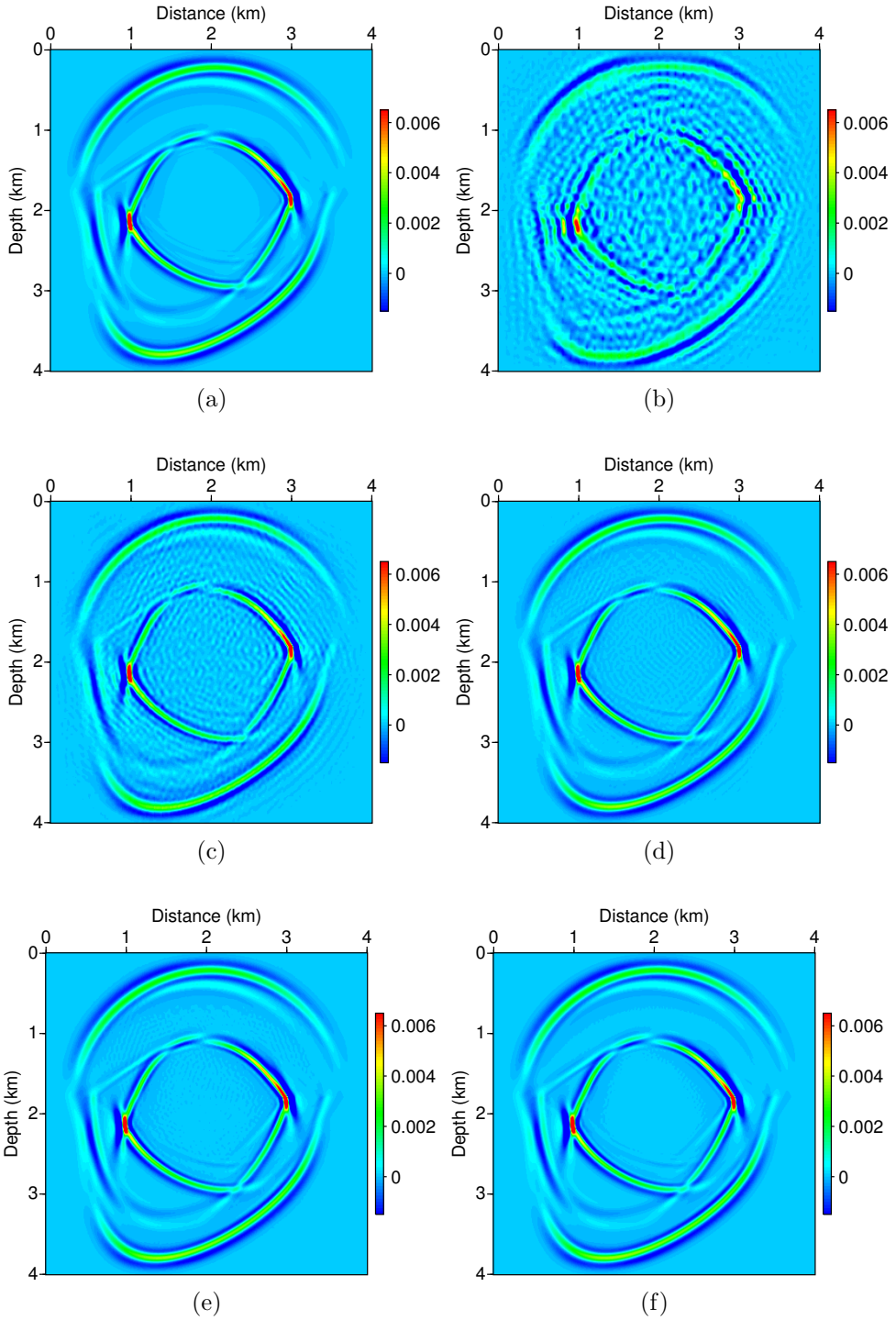


Figure 3.16: $u_3$ wavefield snapshots solved with (a) CG-FEM and (b)-(f) CG-GMsFEM. All the multiscale solutions have an upscaling ratio $r = 10$, and number of spectral basis functions $m$ =10, 20, 30, 40, 50 for (b)-(f), respectively.

### *3.3.2 Randomly heterogeneous anisotropic model with curved layers*

We verify the effectiveness of the DG formulation of our GMsFEM in a heterogeneous anisotropic elastic model, with elasticity parameters shown in Figures 3.17(a)-3.17(f). The density is set to be homogeneous with the value 1000 kg/m$^3$. This heterogeneous model is 6000 m in depth and 6000 m in horizontal distance, and consists of 600×600 fine elementss. For multiscale modeling, we discretize the model with 60×60 coarse elements, and therefore the coarse element is 100 m in each direction, containing 10×10 fine elements. There are three curved reflectors as well as random heterogeneities generated from a von Kármán correlation function (Klimeš, 2002). The correlation length is 30 m in horizontal direction and 5 m in vertical direction. The source is placed at (3000 m, 2500 m), and we apply a Ricker wavelet with 15 Hz central frequency. The time sampling interval is 0.5 ms. We have adopted type II basis functions for our DG-GMsFEM, with 5 element oversampling, i.e., on each of the four boundaries of coarse element $K$, we oversample $K$ with 5 more fine elements. We adopt a penalty parameter $\gamma = 5.0$ for the modeling.

Figures 3.18(a) and 3.19(a) are the $u_1$ and $u_3$ wavefield snapshot obtained by a conventional continuous Galerkin finite-element method (CG-FEM) on the fine mesh, respectively, and Figures 3.18(b)–3.18(f) and 3.19(b)–3.19(f) are solutions from DG-GMsFEM. The number of boundary and interior basis functions range from 10 to 40, respectively, indicated by $(m_{\text{boundary}}, m_{\text{interior}})$. The wavefield contains complicated direct and reflected waves from curved reflectors, as well as waves scattered from the random heterogeneities. Visual inspection shows that the wavefield with $(10, 20)$ basis functions is contains numerical dispersion due to the large element size. However, wavefields with $(30, 30)$ and $(20, 40)$ basis functions are almost the same as that in Figure 3.18(a), i.e., the CG-FEM solution.

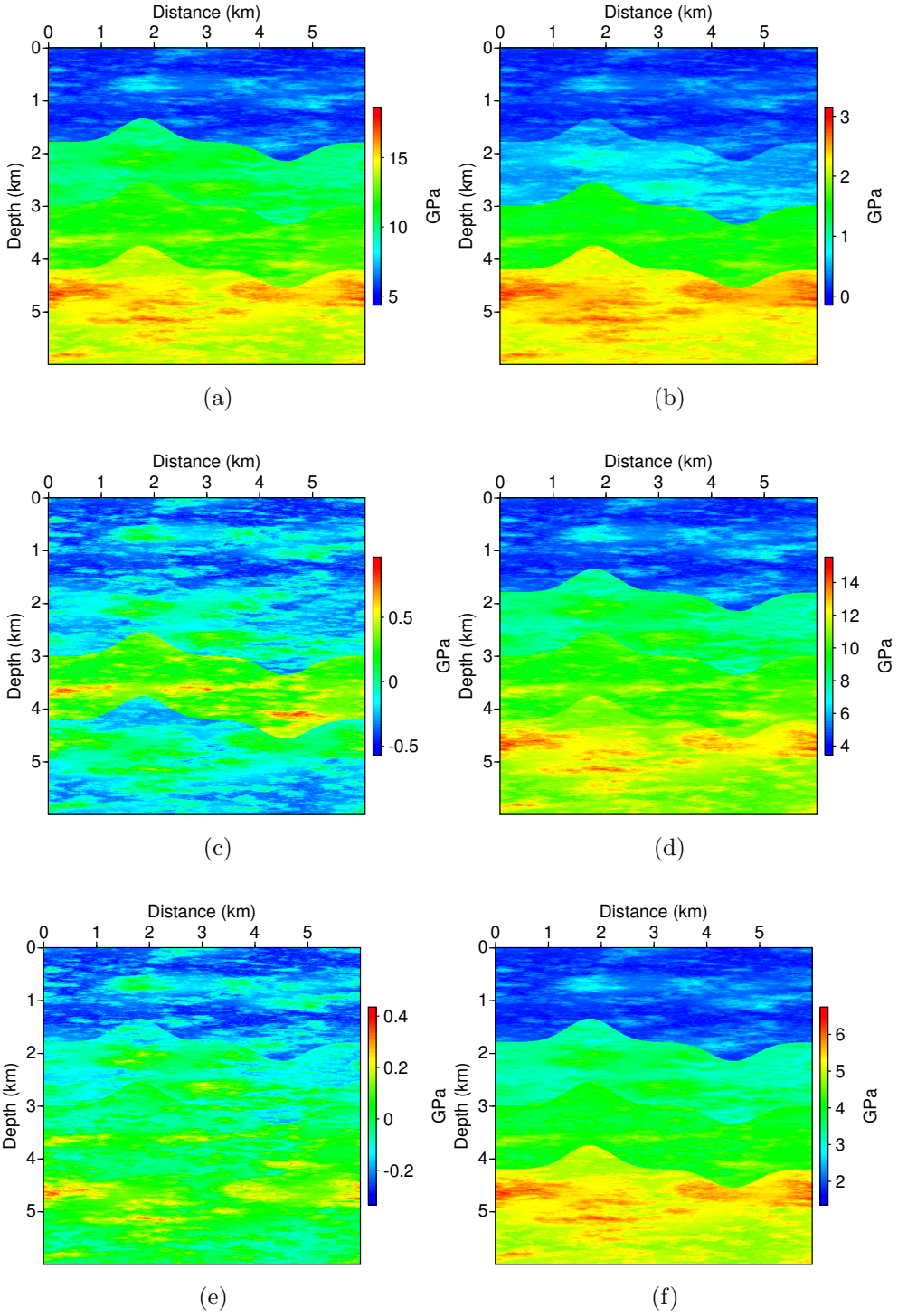


Figure 3.17: A heterogeneous, anisotropic elastic model. Parts (a)-(f) show $C_{11}$, $C_{13}$, $C_{15}$, $C_{33}$, $C_{35}$ and $C_{55}$, respectively.

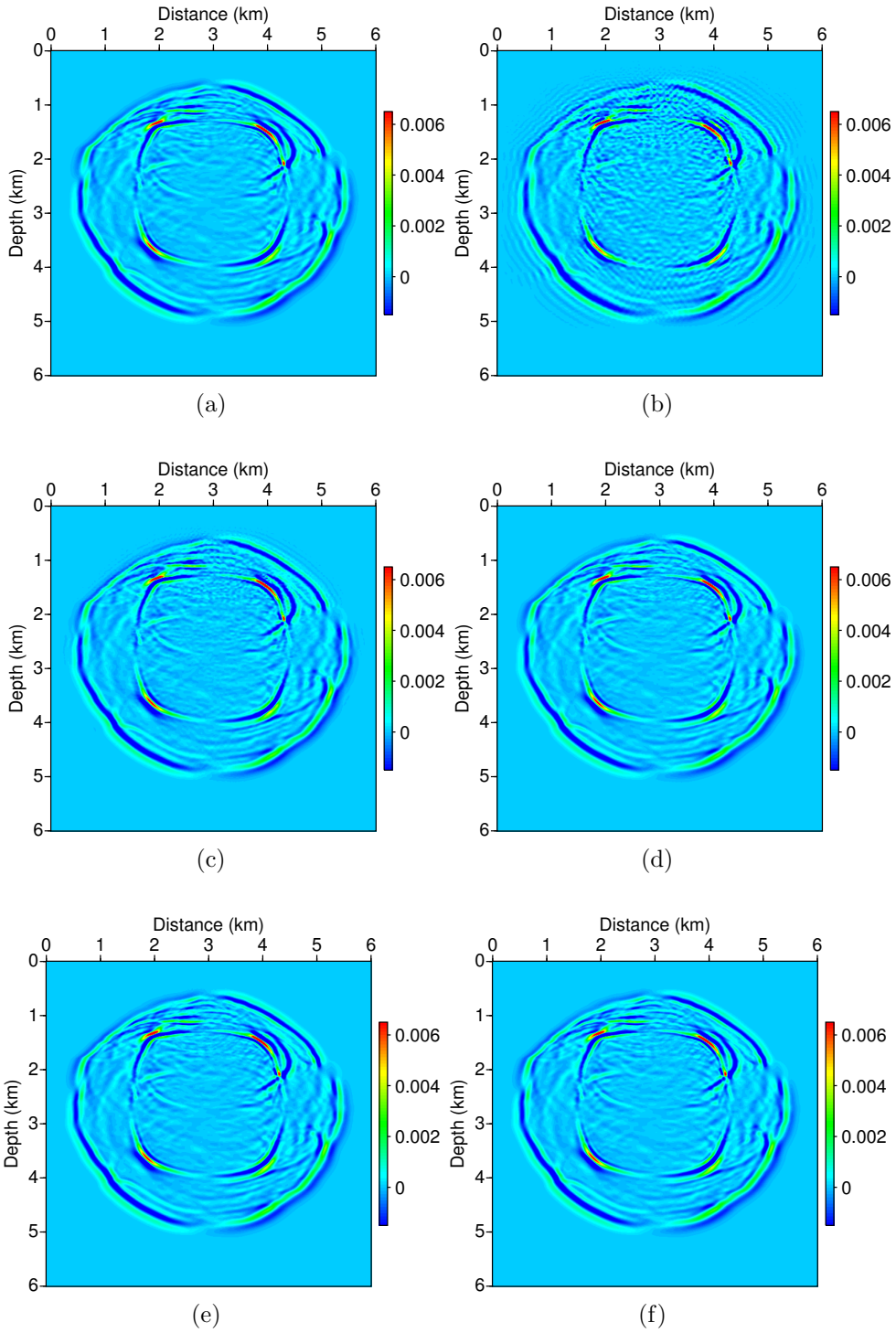


Figure 3.18: $u_1$ wavefield snapshots of (a) fine grid solution and (b)-(f) multiscale solutions, with $(m_{\text{boundary}}, m_{\text{interior}}) = (10, 20)$, $(20, 20)$, $(20, 30)$, $(30, 30)$, $(20, 40)$, respectively.

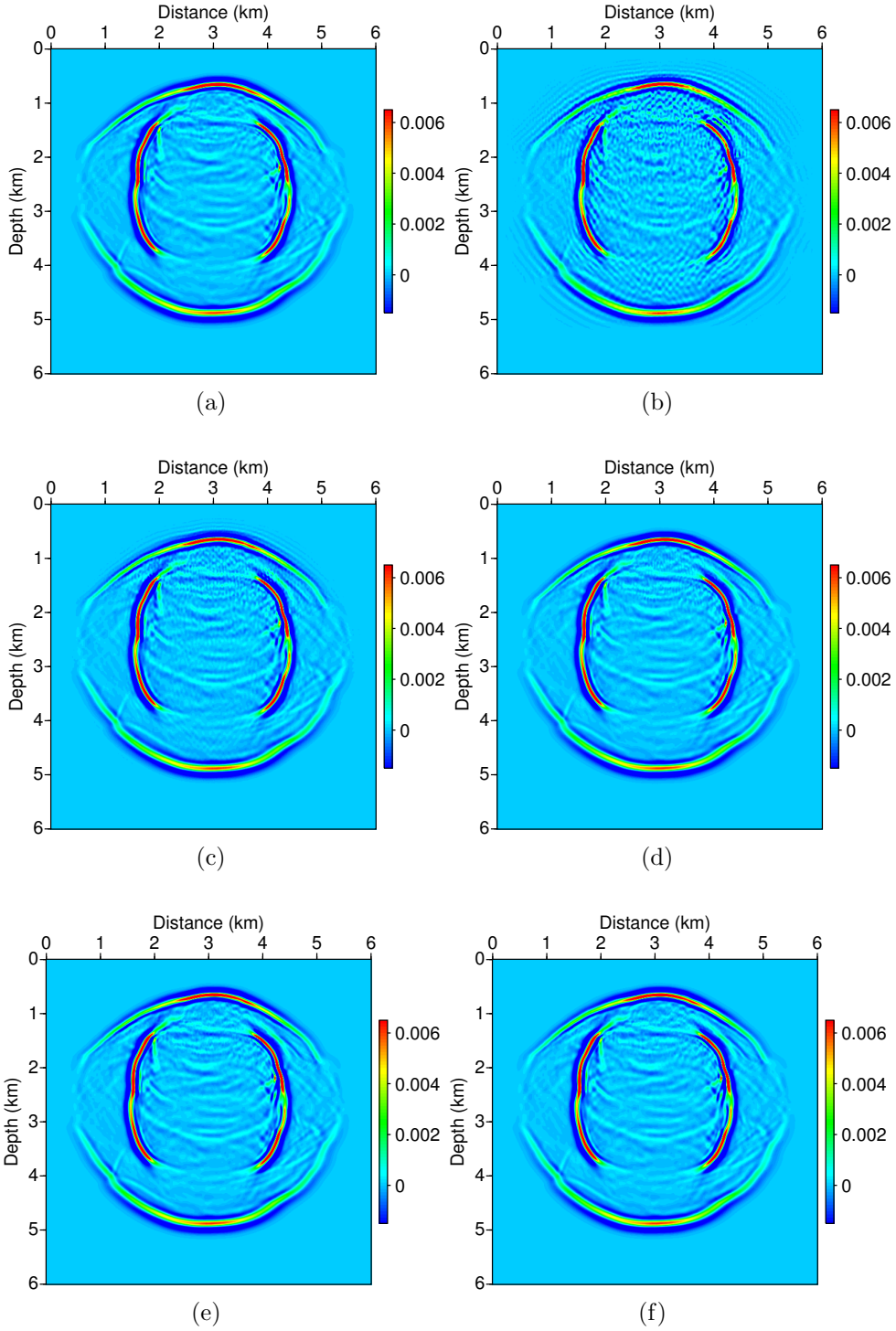


Figure 3.19: $u_3$ wavefield snapshots of (a) fine grid solution and (b)-(f) multiscale solutions, with $(m_{\text{boundary}}, m_{\text{interior}}) = (10, 20)$, $(20, 20)$, $(20, 30)$, $(30, 30)$, $(20, 40)$, respectively.

We only show 5 different combinations of boundary and interior basis in the wavefield snapshots. However, to further quantify the relation between the number of basis functions with the relative error as well as other quantities, we summarize more results in Table 3.3.2. In our test, the case with fewest basis functions, i.e., $(10, 10)$, which also has maximum relative error, 109%. With more and more basis functions, this error reduces to 1.88% when using 30 boundary basis functions and 40 interior basis functions. At the same time, the degrees of freedom increases to 7.2e4 to 2.52e5, which is still much fewer than that in corresponding fine mesh problem with degrees of freedom 8.712e5. Meanwhile, we could see that the interior basis function is more useful in reducing the erorrs. For example, the combination of $(20, 30)$ is more accurate than the combination of $(30, 20)$, although they both have 10 more basis functions totally than the combination $(20, 20)$. The same situation happens for the combinations $(30, 40)$ and $(40, 30)$ as well. The CPU time of calculating more basis functions and preprocessing the global matrices is longer naturally. However, we have to remark that this calculation is one-time, as is the case in the first model.

### *3.3.3 Free surface problem*

Practical applications of any seismic modeling methods would require a formal treatment of the free surface of the Earth, which otherwise will be replaced with some ABCs (Robertsson, 1996; Mittet, 2002). Accurate modeling of the seismic wavefield at the free surface is especially important when the seismic scenario takes place in areas with rugged topography, such as mountains, and can also help us to understand the characteristics of various surface waves, such as Rayleigh wave, which can further help infer the shallow velocity structures (Xia et al., 1999). Bohlen and Saenger (2006) presented a detailed discussion of the free surface problem based on the rotated staggered-grid (RSG) finite difference method (Saenger et al., 2000;

| $m_{\text{boundary}}$ | $m_{\text{interior}}$ | DOF | $e(\mathbf{u})$ | $T_{\text{basis}} + T_{\text{inverse}}$ (s) | $T_{\text{modeling}}$ (s) |
|---|---|---|---|---|---|
| - | - | 7.22e5 | - | - + 68.81 | 1220.07 |
| 10 | 10 | 7.20e4 | 1.09e0 | 2542.13 + 11.46 | 59.5 |
| 10 | 20 | 1.08e5 | 4.45e-1 | 2795.81 + 15.70 | 115.7 |
| 20 | 10 | 1.08e5 | 4.98e-1 | 2585.41 + 15.74 | 139.54 |
| 20 | 20 | 1.44e5 | 1.66e-1 | 3023.63 + 30.59 | 235.1 |
| 20 | 30 | 1.80e5 | 5.58e-2 | 3543.56 + 46.37 | 319.61 |
| 20 | 40 | 2.16e5 | 2.01e-2 | 3666.00 + 51.95 | 430.76 |
| 30 | 20 | 1.80e5 | 9.84e-2 | 3626.55 + 44.66 | 321.68 |
| 30 | 30 | 2.16e5 | 4.14e-2 | 3242.50 + 56.38 | 448.28 |
| 30 | 40 | 2.52e6 | 1.88e-2 | 3984.56 + 70.88 | 583.62 |
| 40 | 30 | 2.52e5 | 3.89e-2 | 3577.49 + 73.04 | 596.98 |

Table 3.2: The relation between number of basis functions and the relative error, as well as the DOF and calculation time. $m_{\text{boundary}}$ is the number of boundary basis functions, $m_{\text{interior}}$ is the number of interior basis functions. The other quantities own same meaning as those in the first model example. The first row represents the calculation with CG-FEM.

Saenger and Bohlen, 2004) and found that free surface requires finer discretization to obtain accuracy. Since the accuracy of our method is controlled by the number of basis functions we have used to represent the wavefield, we will examine the effectiveness of the GMsFEM for a simple free surface problem.

We take an isotropic homogeneous model for the test. The model is 4 km in horizontal direction and 2 km in depth, and is discretized with 40×20 rectangular elements, and each of coarse elements contains 10×10 finer elements. Elastic constants of the model are $C_{11} = 10.0$ GPa and $C_{55} = 4.0$ GPa, with density $\rho = 1000$ kg/m$^3$. The source is a Ricker wavelet with 15 Hz central frequency and is placed at 2 km in the horizontal direction, 10 m in depth. The receivers extend from 0 m to the end of the model, with a spacing of 10 m. We set free surface boundary condition for the top surface and damping boundary conditions as we have discussed in last section for all other boundaries. Since the free surface boundary condition, i.e., $\boldsymbol{\sigma} \cdot \mathbf{n} = \mathbf{0}$, can

$\boldsymbol{\sigma} \cdot \mathbf{n} = \mathbf{0}$, can be naturally satisfied in CG-FEM (e.g., Larson and Bengzon, 2013), we then compare the modeling results from CG-FEM and DG-GMsFEM. We apply the penalty parameter $\gamma = 9.0$.

Figures 3.20(a) and 3.20(b) show the $u_1$ and $u_3$ wavefield snapshots at 0.75 s, where we can see the Rayleigh wave near the surface. Also, the outgoing waves have been damped, which verifies the effectiveness of the damping boundary conditions we have set. We also show the DG-GMsFEM solutions with 20 boundary basis functions and 30 interior basis functions in Figures 3.20(c) and 3.20(d). There are errors in the solution, which appears as high-frequency resonance near the top surface within the wavefront of the shear wave. The high-frequency resonance is especially strong in the $u_3$ wavefield in Figure 3.20(d). However, these resonances do not appear after other parts of the S-wave wavefronts, e.g., in the depth of 1 km on the $u_3$ wavefield. On the other hand, the high-frequency resonance error disappears in the DG-GMsFEM solutions with 20 boundary basis functions and 50 interior basis functions, or with 40 boundary basis functions and 30 interior basis functions, as shown in Figures 3.20(e) and 3.20(f), and 3.20(g) and 3.20(h), respectively. This comparison shows that the free surface boundary condition needs a larger number of basis functions to be accurately modeled compared to other parts where body waves dominate.

### *3.3.4 Adaptive assignment of number of basis functions*

We take an example the illustrate the process of calculating the number of basis functions for each coarse element. Figures 3.22(a), 3.22(b) and 3.22(c) show the P- and S-wave velocity, and density of part of Marmousi 2 elastic model (Martin et al., 2006). However, to better present the wavefield snapshots, we change the element size from 1.25 m to 10 m. The element number in each direction is 600, and we intend to solve the elastic wave equation in this model with a coarse mesh composed

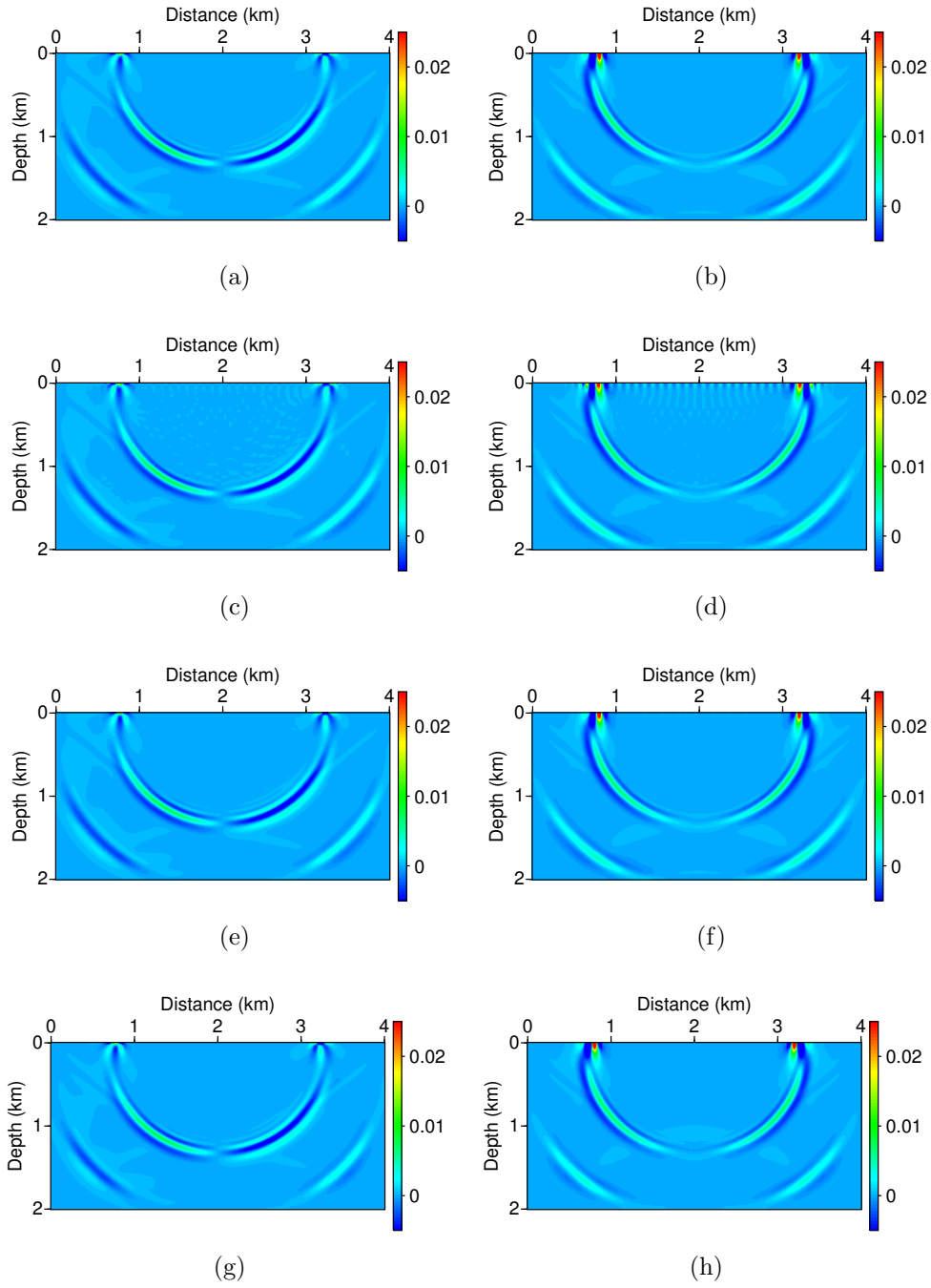


Figure 3.20: Wavefield snapshots of (a) $u_1$ and (b) $u_3$ solved from CG-FEM on fine mesh, (c) $u_1$ and (d) $u_3$ solved with DG-GMsFEM on coarse mesh with $(m_{\text{boundary}}, m_{\text{interior}}) = (20, 30)$, (e) $u_1$ and (f) $u_3$ with $(20, 50)$, (g) $u_1$ and (h) $u_3$ with $(40, 30)$. Note the high-frequency resonance error at the top surface in the $(20, 30)$ DG-GMsFEM solution, which disappears in $(20, 50)$ and $(40, 30)$ solutions.

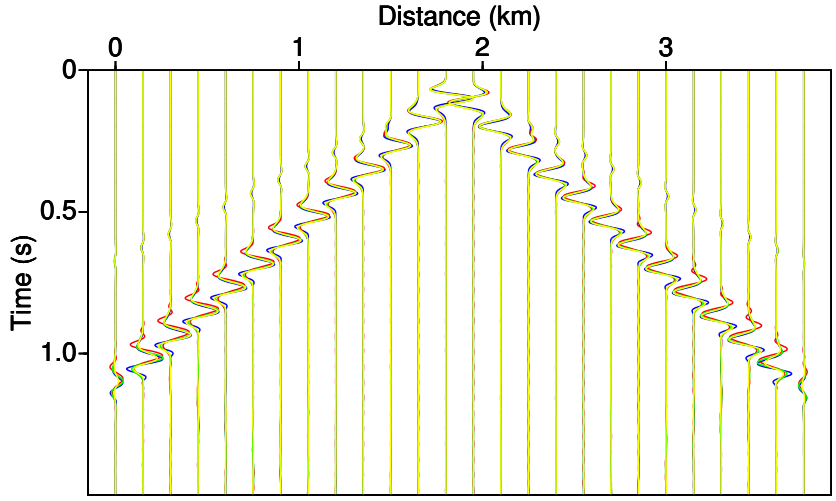


(a)

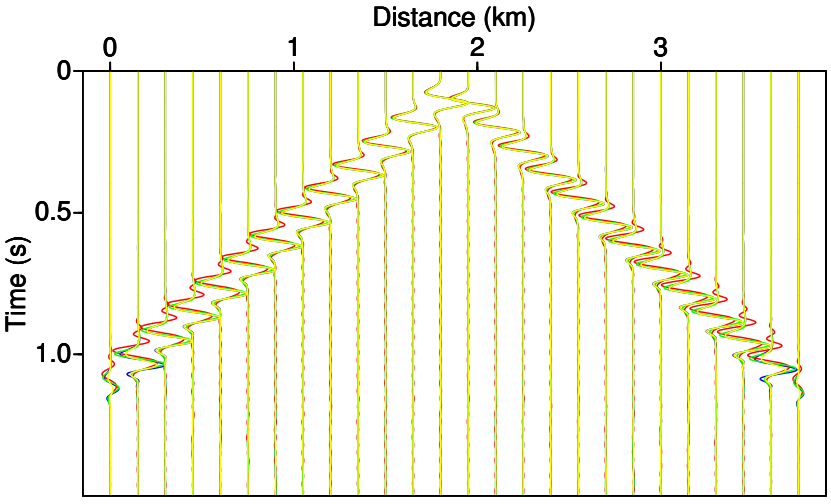


(b)

Figure 3.21: Comparisons of (a) $u_1$ seismogram and (b) $u_3$ seismogram solved from CG-FEM (blue curve), DG-GMsFEM with $(20, 30)$ basis functions (red curve), DG-GMsFEM with $(20, 50)$ basis functions (green curve), and DG-GMsFEM with $(40, 30)$ basis functions (yellow curve).

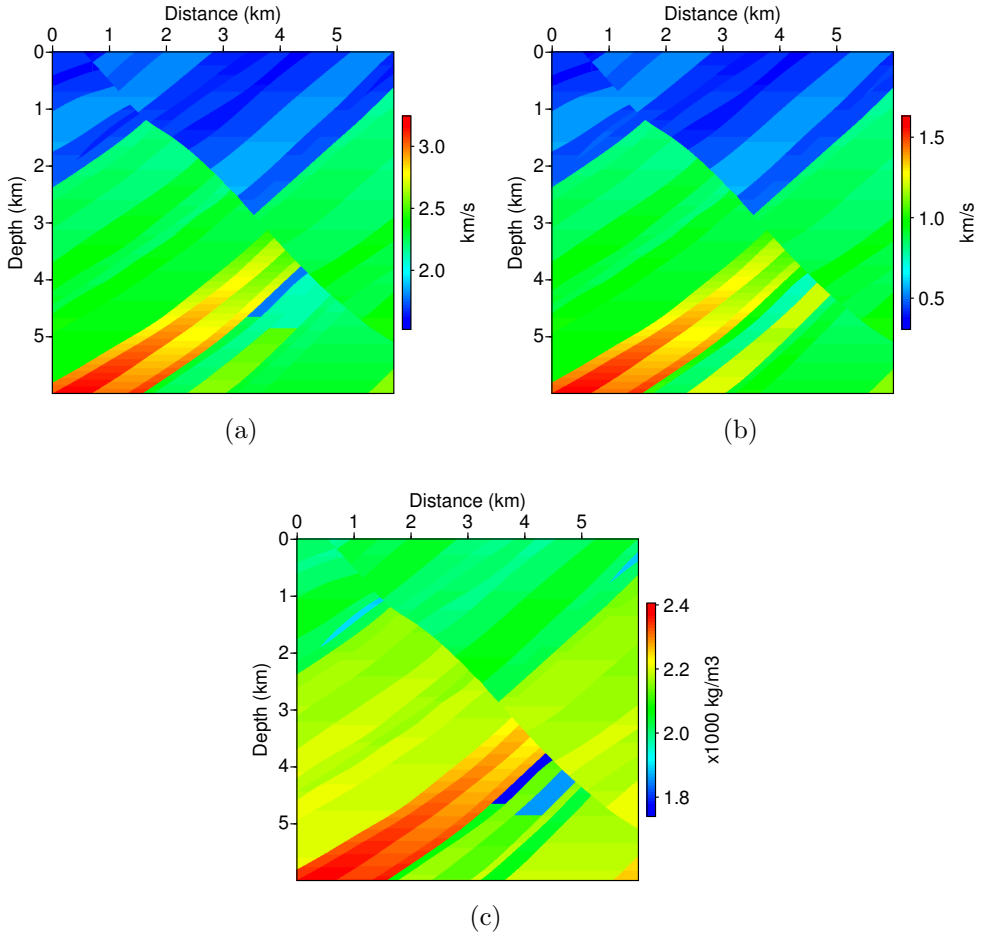


Figure 3.22: The (a) P- and (b) S-wave velocity model, and (c) density model cropped from Marmousi 2 elastic model.

of $30 \times 30$ coarse elements, which means that each coarse element contains $20 \times 20$ fine elements, and the coarse element size is 200 m in each direction. The velocity in the upper part of the model is clearly slower than that in the lower part, and therefore we want to assign more basis functions for the upper part. We also set damping boundary conditions at all the four boundaries. The source is a Ricker wavelet with central frequency 5 Hz, placed at $(3, 2)$ km. We have used a penalty parameter $\gamma = 100.0$ in all the following DG simulations.

We first calculate the number of multiscale basis functions based on the method we introduced in the Implementation part. The number of interior and boundary basis functions are shown in Figures 3.23(a) and 3.23(b). We can see that this map is consistent with our expectation that the near surface part, where the velocity is slower, needs more basis functions, and the very lower part of the model requires much less number of basis functions.

We now compare the wavefield solutions. As in previous examples, we set the CG-FEM solution as the reference solution, and the $u_1$ and $u_3$ wavefield snapshots at 1.5 s are shown in Figures 3.24(a) and 3.25(a), respectively. The P-wave are not so strong compared with the S-wave, because the the P-waves have already propagated out of model at the recording time. The computation time of the CG-FEM solution is 1659.38 s. This computation time is longer than that in the second example, since we have used thicker damping layers to absorb the outgoing waves at the boundaries. Meanwhile, Figures 3.24(b) and 3.25(b) show the $u_1$ and $u_3$ wavefield snapshots solved from DG-GMsFEM with total 70 type II basis functions, respectively. There are obvious dispersions of S-wave, due to the lack of adequate basis functions in these coarse blocks. The computation time is 167.14 s, and the $L^2$-norm error of this multiscale solution with respect to CG-FEM solution is 52.2%. We further adopt total 170 basis functions in Figures 3.24(c) and 3.25(c), which takes 906.78 s to

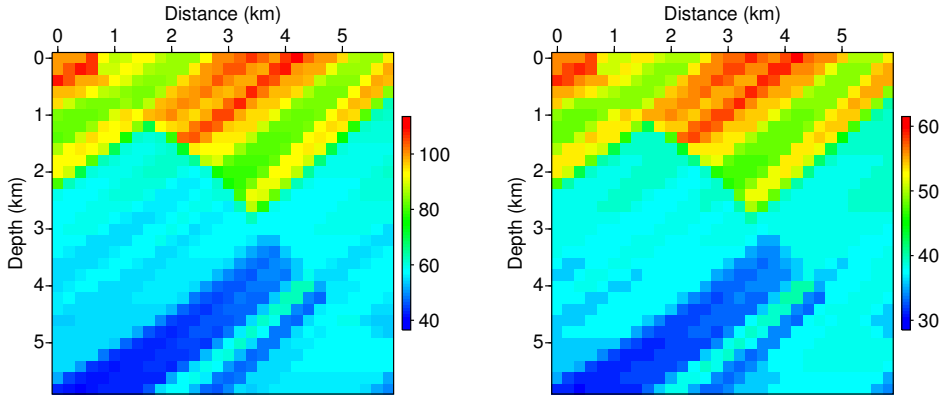


(a) (b)

Figure 3.23: Number of (a) interior and (b) boundary basis functions calculated based on the S-wave velocity.

finish all the time steps in the modeling, with 0.76 % $L^2$-norm error. This solution is more accurate than the multiscale solution with total 70 basis functions, due to the removal of S-wave dispersions with more basis functions. We now implement the DG-GMsFEM with different numbers of basis functions in each coarse element according to the result shown in Figures 3.23(a) and 3.23(b), which takes 412.5 s, with $L^2$-norm error 2.58 %. The error is larger than that using total 170 basis functions in all coarse elements, but still in the same level, and uses only about half of the computation time. We then know that by assigning different numbers of basis functions for each coarse element according to the magnitude of eikonal time difference in the coarse block can help to reduce the computation time.

## 3.4 Conclusions

We have developed a generalized multiscale finite-element method for elastic wave propagation in inhomogeneous, anisotropic media, both in continuous Galerkin and discontinuous Galerkin formulations. This method is a significant extension of the

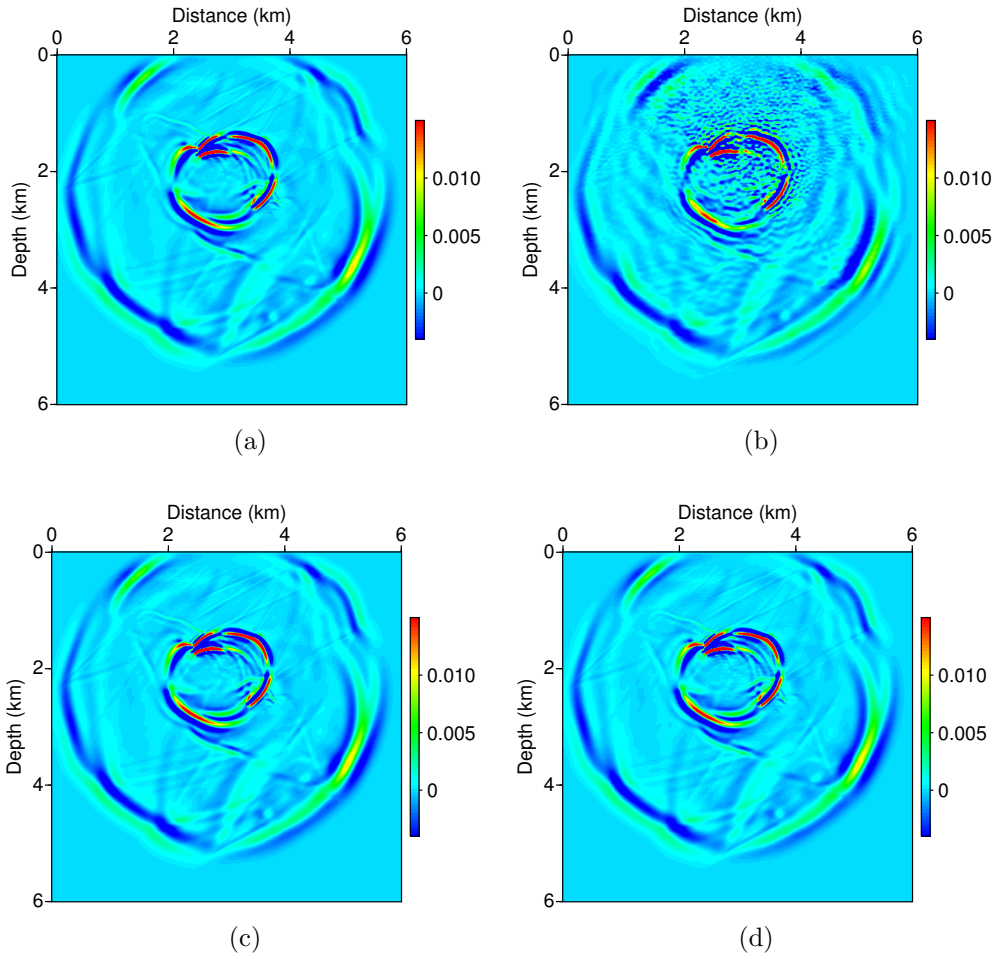


Figure 3.24: $u_1$ wavefield snapshots at 1.5 s from (a) conventional CG-FEM, (b) DG-GMsFEM with 70 type II basis functions total and (c) DG-GMsFEM with 170 type II basis functions total, and (d) with adaptive assignment of total number of type II basis functions from 70 to 170.

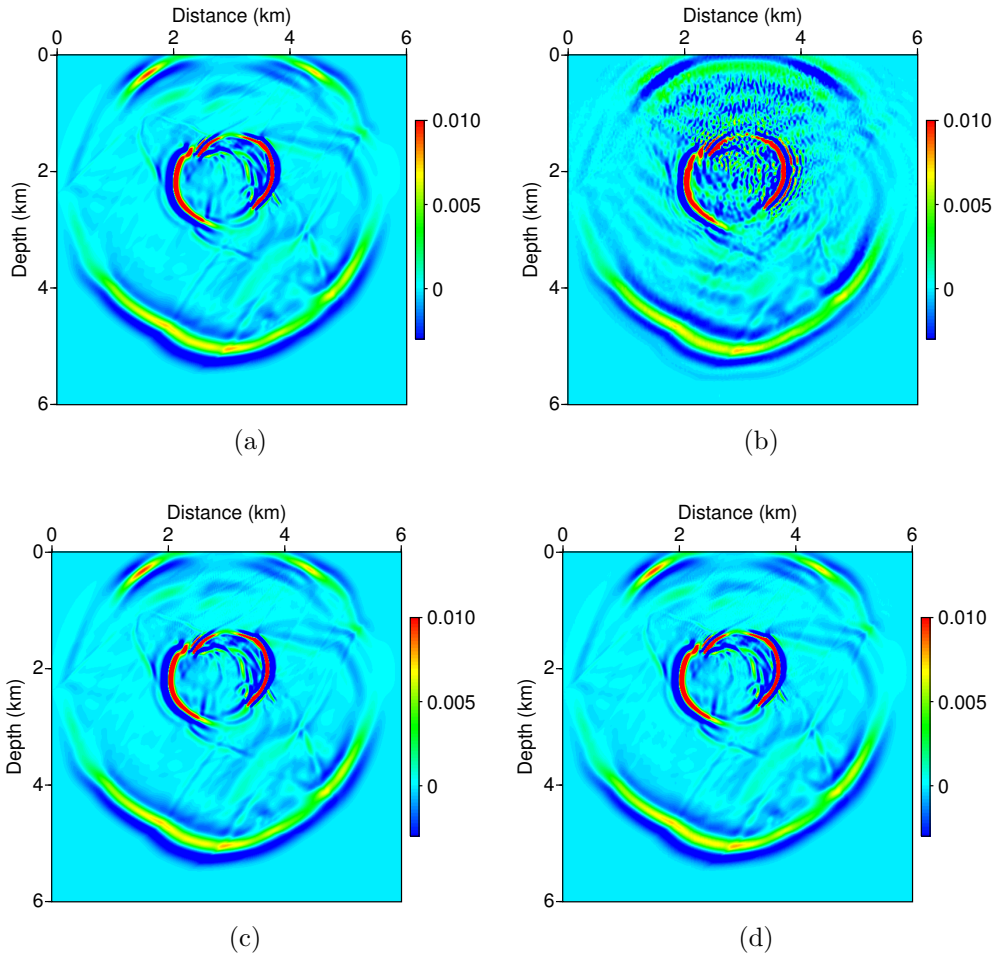


Figure 3.25: $u_3$ wavefield snapshots at 1.5 s from (a) conventional CG-FEM, (b) DG-GMsFEM with 70 type II basis functions total and (c) DG-GMsFEM with 170 type II basis functions total, and (d) with adaptive assignment of total number of type II basis functions from 70 to 170.

similar methodology for acoustic wave equation. We explore two ways to compute the multiscale basis functions, one from linear elasticity eigenvalue problem, the other from two separate local spectral problems that are related to the boundary and the interior of coarse blocks. These multiscale basis functions can effectively capture the finer scale information of the model, and allow us to use much fewer degrees of freedom than the corresponding system of the modeling problem using conventional finite-element methods, to implement the seismic wave simulation. We designed four examples to verify the effectiveness of our method, and find that the accuracy of the multiscale solution is closely related to the number of bases used in modeling. The level of accuracy can be controlled by varying this number, which can be important in applications where a more approximate result is acceptable.

# 4. APPLICATION OF GENERALIZED MULTISCALE FINITE-ELEMENT METHOD IN SIMULATING ELASTIC WAVE PROPAGATION IN MARMOUSI-2 ELASTIC MODEL

## 4.1 Introduction

Full wavefield solution of seismic wave equations are an important tool in both global seismological studies and reservoir explorations (Komatitsch et al., 2010; Virieux et al., 2011). Specifically, with increasing needs to apply full-wavefield based imaging and inversion methods such as reverse-time migration (e.g., Baysal et al., 1983; McMechan, 1983) and full-waveform inversion (e.g., Tarantola, 1984; Mora, 1987) to characterize complex geological structures, full wavefield modeling methods begin to play an essential role in industry. The motivation for applying full-wavefield imaging and inversion methods is that they can provide more accurate and complete information than conventional approximation methods, such as ray method and the one-way wave equation method (Červený and Hron, 1980; Claerbout, 1985; Zhang et al., 2005; Gibson et al., 2005). However, the application of full-wavefield based methods is often limited by the expensive cost of calculating the full wavefield solution of seismic wave equations, which is often accomplished by approaches such as finite-difference method (e.g., Dablain, 1986; Virieux, 1986), finite-element method (e.g., Marfurt, 1984; Komatitsch and Vilotte, 1998; Käser and Dumbser, 2006; Chung and Engquist, 2009; Wilcox et al., 2010), pseudospectral method (e.g., Kosloff and Baysal, 1982; Fornberg, 1990), and so on. These can become prohibitively expensive for large models in 2-D or 3-D, since the computation costs of these "grid-based" methods are directly proportional with the number of element or grids that are required to correctly represent the geological model. It is also important to realize

the fact that current computational power can support full wavefield simulation of seismic wave equations on meshes with about 10 to 20 m in element size, however, the heterogeneities of the Earth medium may happen at multiple spatial scales, and these heterogeneities, e.g., fractures, cavities, discontinuities, etc., on the finer scale which may be 1 m or even smaller, can have great influences on the wavefield propagation in the media. Conventionally, such fine scale heterogeneities can be homogenized with homogenization methods, such as the effective medium theory (e.g., Backus, 1962; Schoenberg and Muir, 1989), and the effective compliance theories for fractured rocks (Sayers and Kachanov, 1991; Sayers, 1999, 2002). Since there are always heterogeneities that are much complicated than these effective theories that can correctly represent, such homogenizations are not always accurate or correct.

We therefore developed the Generalized Multiscale Finite-Element Method (GMsFEM) for linear elastic wave equations in Section 3. The GMsFEM allows us to solve the elastic wave equation on the coarse grid, where each of the grid may be spatial heterogeneous, including but not limiting to the high contrasts in the medium properties, fractures, cavities, and discontinuities, etc.. The effectiveness of GMsFEM relies on the so-called multiscale basis functions which are solved from appropriately defined local spectral problems, which are discussed in Section 3. These basis functions can capture the fine-scale information of the media, and can be used to recover the fine-scale wavefield after solving the wave equation modeling system on the coarse scale. The GMsFEM for elastic wave equation is the natural extension of the GMsFEM for elliptic problem (Efendiev et al., 2011, 2013; Fu et al., 2013) and acoustic wave equation (Chung et al., 2013b,a).

In Section 2, we have used several simple numerical examples to verify the effectiveness of the GMsFEM in reducing the degrees of freedom of the system and the computation time of the field wavefield simulation. We now apply the DG-GMsFEM

on a more realistic geological model, the Marmousi-2 elastic model (Martin et al., 2006), to test the capability of GMsFEM in accelerating the full wavefield modeling of the elastic wave equation. Marmousi-2 elastic model is an upgrade of the acoustic Marmousi model (Versteeg, 1993) that designed for testing various seismic imaging and inversion algorithms. The model is 17 km in horizontal direction and 3.5 km in depth, and contains 199 horizons, and layers with several different lithologies, including water, sand, shale, salt and limestone. The P-wave velocities of these layers are directly adopted from the original acoustic Marmousi model, while the S-wave velocities are calculated from the P-S wave velocity relation suggested in Greenberg and Castagna (1992), and the density parameter is also calculated based semi-empirical relations. The Marmousi-2 model has been substantially rediscretized with finer elements, with a grid size 1.25 m by 1.25 m, a size that is much finer than those adopted in most industrial applications, and such discretization also makes the model contains many grid cells, making it difficult to implement the full wavefield simulation on simple PCs. Our current prototype implementation of the GMsFEM in MATLAB makes it difficult to assess very large models. Nevertheless, we will select some strongly heterogeneous parts from the Marmousi-2 model and evaluate the simulations.

Our paper is organized as follows. In the Method part, we will briefly introduce the formulation of the DG-GMsFEM, including the computation of the multiscale basis functions that enable us to capture the fine-scale information of the media. In the Results and analysis part, we will show various comparisons of wavefield snapshot and seismogram between our DG-GMsFEM solution and the reference continuous Galerkin (CG) FEM solution, and give a brief analysis on the error. We conclude the paper in the Conclusions part.

## 4.2 Method

Throughout our theory development, we have adopted the second-order elastic wave equation in the displacement form which is expressed as

$$\rho\partial_t^2\mathbf{u} = \frac{1}{2}\nabla\cdot\{\mathbf{c}:[\nabla\mathbf{u}+(\nabla\mathbf{u})^{\mathrm{T}}]\}+\mathbf{f}, \tag{4.1}$$

where $\mathbf{u}=\mathbf{u}(\mathbf{x},t)$ is the displacement wavefield in the domain $\Omega\times T\subset\mathbb{R}^d\times\mathbb{R}$, with $d=1,2,3$, $\mathbf{f}=\mathbf{f}(\mathbf{x},t)$ is the external source term, $\mathbf{c}=\mathbf{c}(\mathbf{x})$ is the fourth-rank elasticity tensor and $\rho=\rho(\mathbf{x})$ is the density of the medium.

To solve equation 4.1, we discretize $\Omega$ with a set of coarse mesh, $\mathcal{P}_H$, each coarse element in $\mathcal{P}_H$ may contain many finer elements. The solution of the wave equation 4.1 on $\mathcal{P}_H$ can be expressed as

$$\mathbf{u}_H(\mathbf{x},t)=\sum_{i=1}^{N}\mathbf{d}_i(t)\boldsymbol{\Psi}_i(\mathbf{x}), \tag{4.2}$$

where the basis functions $\boldsymbol{\Psi}_i\in W_H$, and $W_H$ is a finite dimensional space that is consisted of basis functions $\boldsymbol{\Psi}_i$ which are continuous within each coarse element $K$, but discontinuous at the coarse element boundaries $\partial K$, and $N$ is the number of coarse elements.

We then can obtain the weak form of equation 4.1 by multiplying by some arbitrary test function $\mathbf{v}\in W_H$, which is

$$\int_\Omega \rho\partial_t^2\mathbf{u}_H\cdot\mathbf{v}d\mathbf{x}+a(\mathbf{u}_H,\mathbf{v})=\int_\Omega\mathbf{f}\cdot\mathbf{v}d\mathbf{x}, \tag{4.3}$$

where

$$
\begin{aligned}
a(\mathbf{u},\mathbf{v}) = & \sum_{K\in\mathcal{P}_H}\int_K \boldsymbol{\sigma}(\mathbf{u}):\boldsymbol{\varepsilon}(\mathbf{v})d\mathbf{x} \\
& - \sum_{E\in\mathcal{E}_H}\int_E (\{\!\{\boldsymbol{\sigma}(\mathbf{u})\}\!\}:\underline{[\![\mathbf{v}]\!]} + \underline{[\![\mathbf{u}]\!]}:\{\!\{\boldsymbol{\sigma}(\mathbf{v})\}\!\})ds \\
& + \sum_{E\in\mathcal{E}_H}\frac{\gamma}{|E|}\int_E (\underline{[\![\mathbf{u}]\!]}:\{\!\{\mathbf{c}\}\!\}:\underline{[\![\mathbf{v}]\!]} + [\![\mathbf{u}]\!]\cdot\{\!\{\mathbf{D}\}\!\}\cdot[\![\mathbf{v}]\!])ds, \qquad (4.4)
\end{aligned}
$$

with $\boldsymbol{\sigma}(\mathbf{u}) = \mathbf{c}:\boldsymbol{\varepsilon}(\mathbf{u})$ is the stress tensor, $\boldsymbol{\varepsilon}(\mathbf{u}) = [\nabla\mathbf{u}+(\nabla\mathbf{u})^{\mathrm{T}}]/2$ is the strain tensor, $\mathbf{D} = \mathrm{diag}(C_{11}, C_{22}, C_{33})$, $C_{IJ}$ are components of the four-order elasticity tensor $\mathbf{c}$ in Voigt notation (e.g., Carcione, 2007), and $\gamma > 0$ is the penalty parameter. Also, $\mathcal{E}_H$ is the set of all interior coarse element edges in 2-D case, or the set of all interior coarse element faces in 3-D case, and the average and jump terms on $E \in \mathcal{E}_H$ are defined as (e.g., Grote et al., 2006; Arnold et al., 2002; Wihler, 2006)

$$\{\!\{\boldsymbol{\sigma}\}\!\} = (\boldsymbol{\sigma}^+ + \boldsymbol{\sigma}^-)/2, \qquad (4.5)$$

$$[\![\mathbf{v}]\!] = \mathbf{v}^+\cdot\mathbf{n}^+ + \mathbf{v}^-\cdot\mathbf{n}^-, \qquad (4.6)$$

$$\underline{[\![\mathbf{v}]\!]} = \mathbf{v}^+\otimes\mathbf{n}^+ + \mathbf{v}^-\otimes\mathbf{n}^-, \qquad (4.7)$$

where $\boldsymbol{\sigma}^\pm = \boldsymbol{\sigma}|_{K^\pm}$, and $K^\pm$ are the two coarse elements having the common $E$, $\mathbf{n}^\pm$ is the unit outward normal on $\partial K^\pm$.

We now define the basis function space $W_H$, which is decomposed into two parts, $W_H = W_H^1 \cup W_H^2$.

Space $W_H^1$ includes interior modes for $K$, and it is constructed through solving

$$\int_K \boldsymbol{\sigma}(\mathbf{u}):\boldsymbol{\varepsilon}(\mathbf{v})d\mathbf{x} = \zeta\int_K \rho\mathbf{u}\cdot\mathbf{v}ds, \qquad (4.8)$$

where $\mathbf{u} = \mathbf{0}$ on $\partial K$. This local problem is defined for the interior of $K$ only. We then select the first $m_1$ eigenfunctions $\boldsymbol{\phi}_1, \boldsymbol{\phi}_2, \cdots, \boldsymbol{\phi}_{m_1}$ corresponding to the $m_1$ smallest eigenvalues $0 \leq \zeta_1 \leq \zeta_2 \leq \cdots \leq \zeta_{m_1}$ of the above problem, and then the basis space $W_H^1$ on $K$ is defined as $W_H^1(K) = \text{span}\{\boldsymbol{\phi}_1, \boldsymbol{\phi}_2, \cdots, \boldsymbol{\phi}_{m_1}\}$. The multiscale basis functions from $W_H^1$ are called interior basis functions.

The space $W_H^2$ represents strong variations on the boundaries of a coarse block. For a coarse block $K$, we first solve the local linear elasticity problem

$$\int_K \boldsymbol{\sigma}(\mathbf{u}) : \boldsymbol{\varepsilon}(\mathbf{v}) d\mathbf{x} = \mathbf{0}, \tag{4.9}$$

with Dirichlet boundary conditions $\mathbf{u} = \boldsymbol{\delta}_j$. In 2-D, we can set $\mathbf{u} = (\delta_j, 0)$ or $\mathbf{u} = (0, \delta_j)$ at the $j$-th boundary node of $K$, where $\delta_j$ is the delta function and $j = 1, 2, \cdots, p$, with $p$ being the total number of boundary nodes. We denote the solutions as $\mathbf{u}_1, \mathbf{u}_2, \cdots, \mathbf{u}_{dp}$, where $d$ is the number of dimension, and then a trial basis function space $\tilde{W}_H^2$ is defined as $\tilde{W}_H^2 = \text{span}\{\mathbf{u}_1, \mathbf{u}_2, \cdots, \mathbf{u}_{dp}\}$. We then solve local spectral problem

$$\int_K \boldsymbol{\sigma}(\tilde{\boldsymbol{\gamma}}) : \boldsymbol{\varepsilon}(\tilde{\boldsymbol{\eta}}) d\mathbf{x} = \xi \int_{\partial K} \rho \tilde{\boldsymbol{\gamma}} \cdot \tilde{\boldsymbol{\eta}} ds, \tag{4.10}$$

with $\tilde{\boldsymbol{\gamma}}, \tilde{\boldsymbol{\eta}} \in \tilde{W}_H^2$. We select the first $m_2$ eigenvectors $\tilde{\mathbf{u}}_1, \tilde{\mathbf{u}}_2, \cdots, \tilde{\mathbf{u}}_{m_2}$ corresponding to the first $m_2$ smallest eigenvalues, $0 \leq \xi_1 \leq \xi_2 \leq \cdots \xi_{m_2}$, and define the space $W_H^2$ as $W_H^2 = \text{span}\{\boldsymbol{\varphi}_1, \boldsymbol{\varphi}_2, \cdots, \boldsymbol{\varphi}_{m_2}\}$, with the basis $\boldsymbol{\varphi}_{i,l} = \sum_{j=1}^{dp} (\tilde{\mathbf{u}}^{\mathrm{T}})_{i,j} \mathbf{u}_{j,l}$, where $(i, j)$ represents the $j$-th node in the $i$-th vector. The multiscale basis functions from $W_H^2$ are called boundary basis functions.

The number of basis functions in each coarse element can be different, and we calculate the number of basis functions according to the harmonic average of S-wave

velocity in each coarse element: the coarse element which has large S-wave velocity will be assigned fewer number of multiscale basis functions, and vice versa.

We have also added Rayleigh damping boundary conditions for the modeling, and finally, the semi-discrete form for the wave equation can be written as

$$\mathbf{M}\ddot{\mathbf{d}}_H + \mathbf{E}\dot{\mathbf{d}}_H + \mathbf{K}\mathbf{d}_H + \mathbf{F} = \mathbf{0}, \tag{4.11}$$

where $\mathbf{M}$ is the global mass matrix, $\mathbf{K}$ is the global stiffness matrix, $\mathbf{F}$ is the global force vector:

$$M_{ij} = \int_\Omega \mathbf{\Phi}_i^{\mathrm{T}} \cdot \mathbf{\Phi}_j d\mathbf{x}, \qquad K_{ij} = a(\mathbf{\Phi}_i, \mathbf{\Phi}_j), \qquad F_i = \int_\Omega \mathbf{f} \cdot \mathbf{\Phi}_i d\mathbf{x}. \tag{4.12}$$

Also, $\mathbf{E}$ is the global damping matrix for the damping boundaries, which is assembled from the damping matrix of element $K$:

$$\mathbf{E}_K = w_K(\alpha_1 \mathbf{M}_K + \alpha_2 \mathbf{K}_K), \tag{4.13}$$

where the damping coefficients $\alpha_1$ and $\alpha_2$ satisfy $2\omega_i\xi_i = \alpha_1 + \alpha_2\omega_i^2$, and the parameters $\omega_i$ are related the frequencies of the source wavelet (Sarma et al., 1998), $\xi_i$ are damping ratios with respect to the critical damping ratio related to the medium properties, as well as the width of the damping zone around the computation zone, and $w_K$ is the spatial varying weight which is 0 at the boundary of computational domain and damping zone, and 1 at the outer most nodes of the damping zone. $\mathbf{M}_K$ and $\mathbf{K}_K$ are the mass and stiffness matrix assembled on $K$, respectively.

## 4.3 Results and analysis

The original Marmousi-2 elastic model is large and the full wavefield modeling on the whole model is beyond the ability of our current unoptimized MATLAB code implementation. Figures 4.1(a)–4.1(c) show the P-wave velocity, S-wave velocity and density models of the Marmousi-2 elastic model, and we first convert them to elasticity models with $C_{11} = \rho v_{\mathrm{P}}^2$, $C_{55} = \rho v_{\mathrm{S}}^2$, and $C_{13} = C_{11} - 2C_{55}$, $C_{15} = C_{35} = 0$. We implement the modeling in the region of 7.5 km to 10.5 km in the horizontal direction, and 0.5 km to 3.5 km in depth, and decompose this area with six equal blocks divided in depth, so each block is 0.5 km in depth and 2.0 km in the horizontal direction. Modeling was applied separately in these six blocks.

We first assign the number of basis functions with our proposed approach based on the harmonic average of the S-wave velocity in each coarse element, and the number of interior and boundary basis functions for the six smaller blocks are shown in Figures 4.2(a)–4.2(f) and Figures 4.3(a)–4.3(f), respectively.

### *4.3.1 Block I*

For the first block, we placed the source, which is a Ricker wavelet with central frequency 30 Hz, at $(1500, 10)$ m, and placed the receiver at upper surface. The total simulation was carried out for a total propagation time of 4.625 s, with a 0.185 ms time step. To apply DG-GMsFEM for this model, we discretize the block with $20 \times 120$ coarse elements, which makes the coarse element 25 m in each direction, containing $20 \times 20$ fine elements. We adopt a penalty parameter $\gamma = 16.0$ in the modeling, and this value has also been used in the modeling in other blocks. We have applied the free boundary condition for the top boundary, and damping boundary conditions for all other three boundaries. We remark that the S-wave velocity is especially low in block I, which is about 0.3 km/s, and with 30 Hz wavelet the

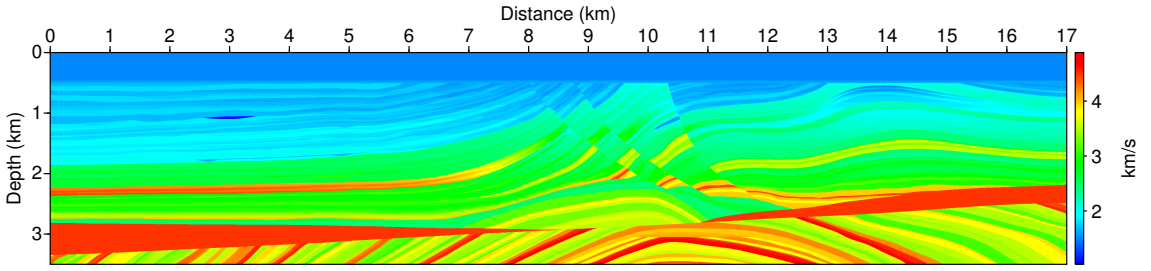


(a)

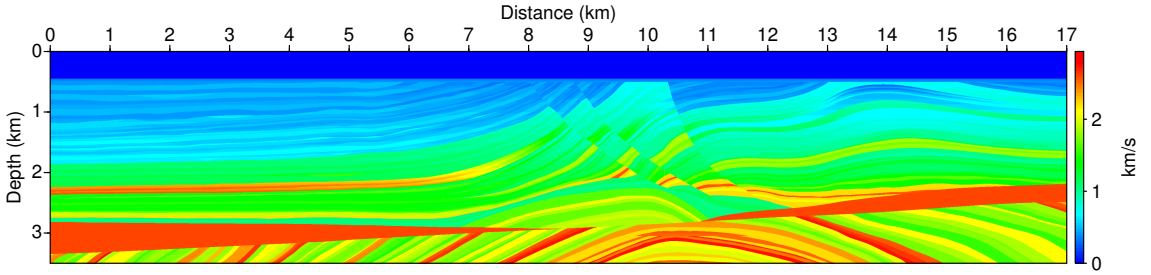


(b)

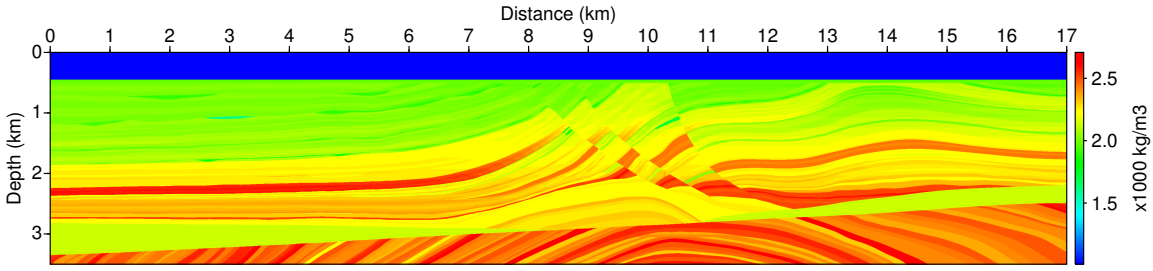


(c)

Figure 4.1: The original Marmousi-2 elastic model. (a)–(c) represent the P-wave velocity, S-wave velocity and density models, respectively.

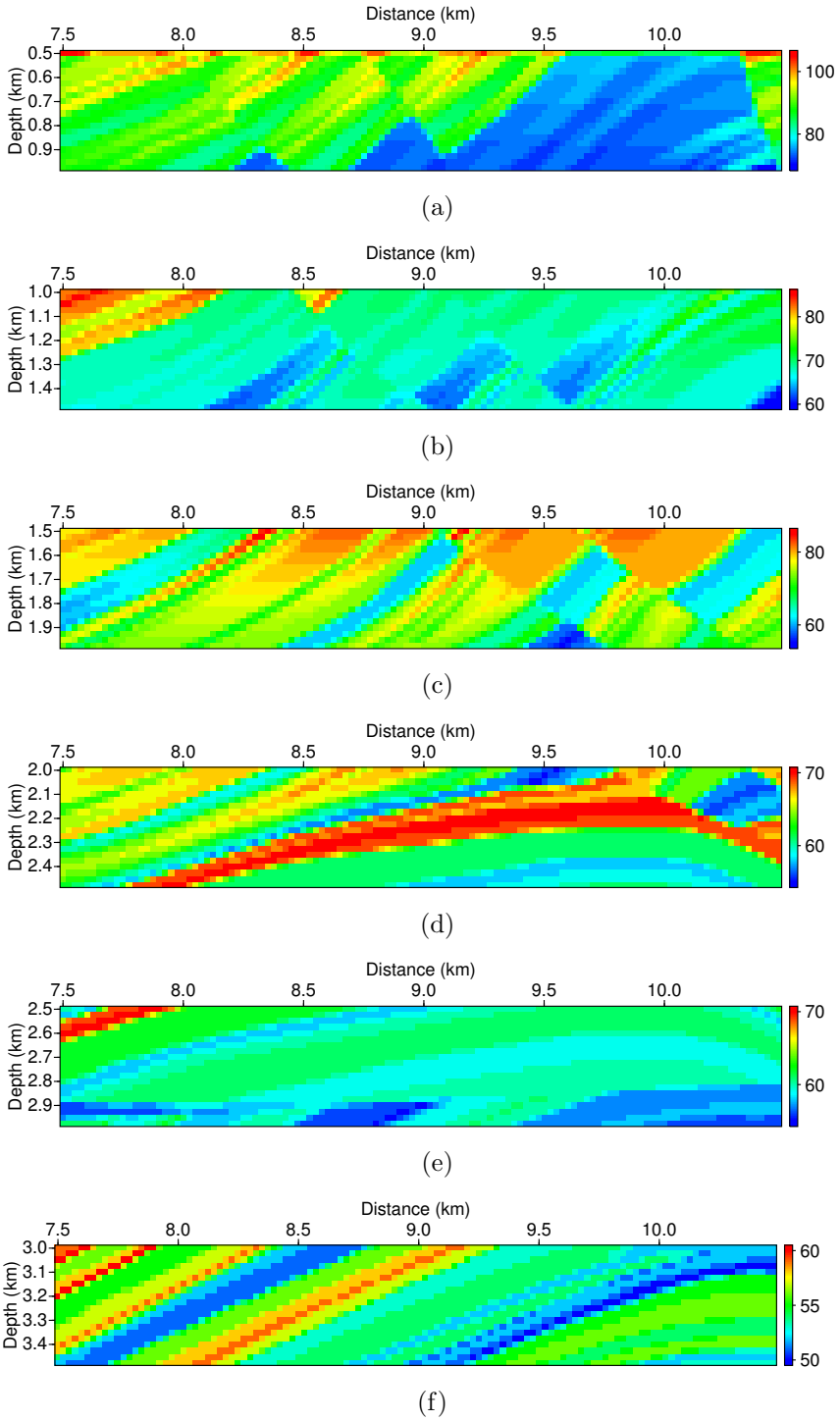


Figure 4.2: Number of interior basis functions for six blocks from (a) top to (f) bottom.

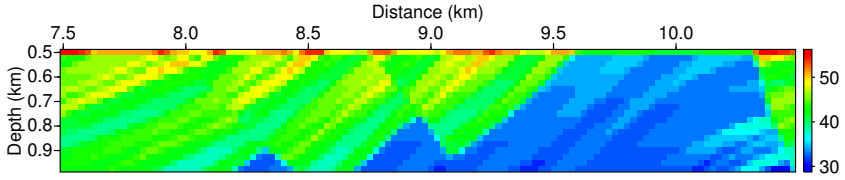


(a)

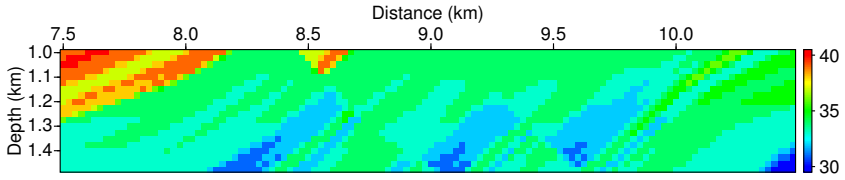


(b)

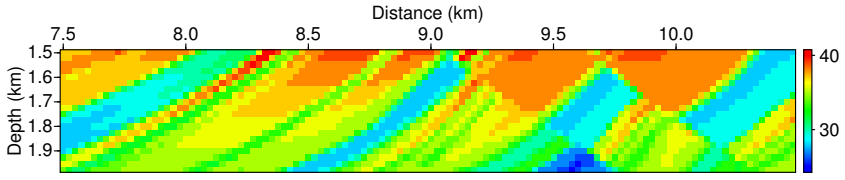


(c)

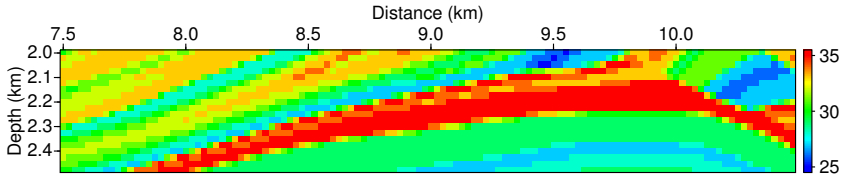


(d)

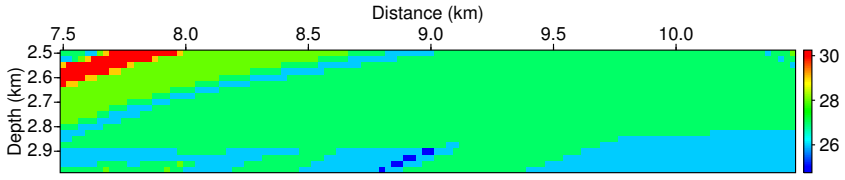


(e)

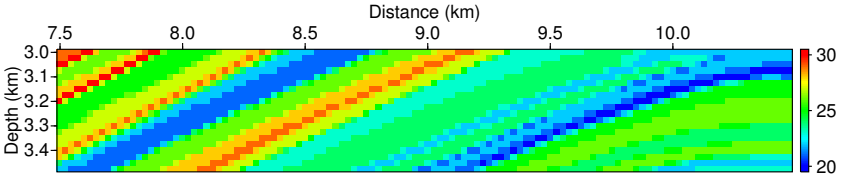


(f)

Figure 4.3: Number of boundary basis functions for six blocks from (a) top to (f) bottom.

average wavelength is about 10 m, shorter than the coarse element size. Such a wavelength-element size relation makes wavefield simulation impossible even with the pseudospectral method, which requires at least two grids in a wavelength. Nevertheless, with the multiscale basis functions, we are able to model the wavefield accurately. In Figures 4.4(a)–4.4(d), we compared our DG-GMsFEM solution with CG-FEM solution. Figure 4.4(a) and 4.4(c) show the $u_1$ and $u_3$ wavefield snapshots at 0.555 s, while the corresponding DG-GMsFEM solutions are shown in 4.4(b) and 4.4(d). It can be seen that our DG-GMsFEM can correctly model the wavefronts of both P- and S-wave, as well as the reflections. In fact, the $L^2$-norm error of the wavefield, which is calculated with $e(\mathbf{u}) = \|\mathbf{u}_{\text{ref}} - \mathbf{u}_{\text{GMsFEM}}\|/\|\mathbf{u}_{\text{ref}}\|$, is 2.83%, where $\mathbf{u}_{\text{ref}}$ is the reference solution, which is calculated by CG-FEM in this example. Meanwhile, the total online computation time for the CG-FEM is about 4.0e5 s, while our DG-GMsFEM takes only about 1.1e5 s, which is about 25% of the CG-FEM. We also remark that we only used the lowest order finite-element polynomial basis functions in CG-FEM, along with mass lumping for the mass matrix.

In addition to the spatial snapshots we have already presented, direct comparisons of the time history of the wavefields in the form of seismograms also provide important measures of the accuracy of the DG-GMsFEM. Figures 4.5 and 4.6 show the seismogram calculated with CG-FEM and DG-GMsFEM, respectively, and Figure 4.7 shows the absolute difference between these two solutions. Since we have set free surface boundary condition for the top surface, and the receiver is located at the free surface, the S-wave contributes most of the errors, as indicated by the S-wave direct arrivals in 4.7, which also causes noticeable error of reflections and scatterings at about 1.75 s, at 9.6 km position. For the reflections from layers below the surface, the DG-GMsFEM can be considered as a satisfactory solution, given the fact that DG-GMsFEM only uses 25% computation time. The same error characteristics

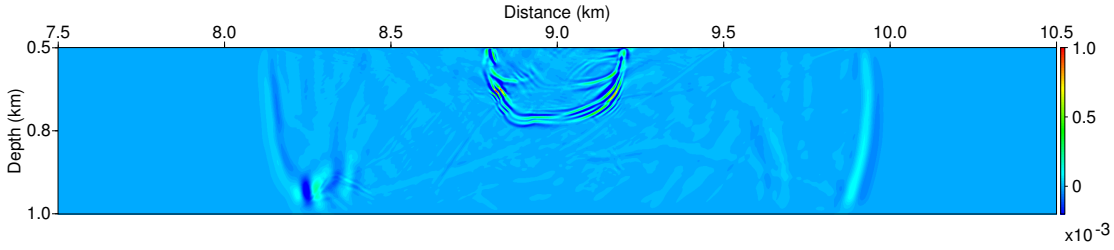


(a)

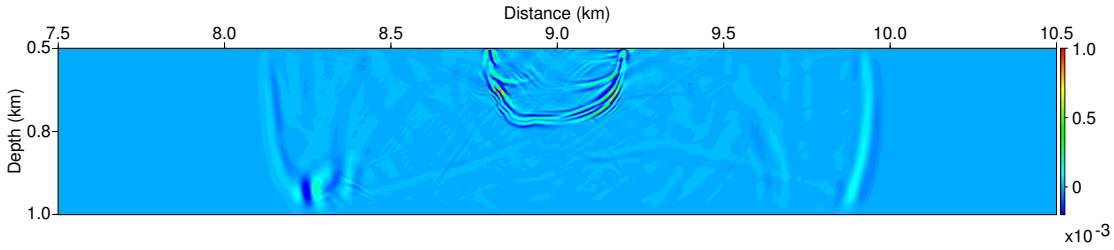


(b)

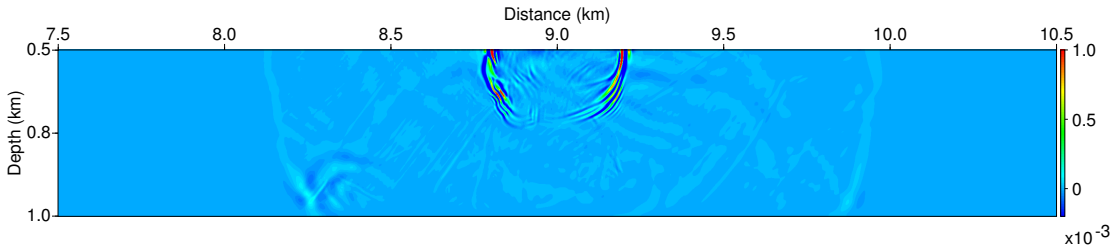


(c)

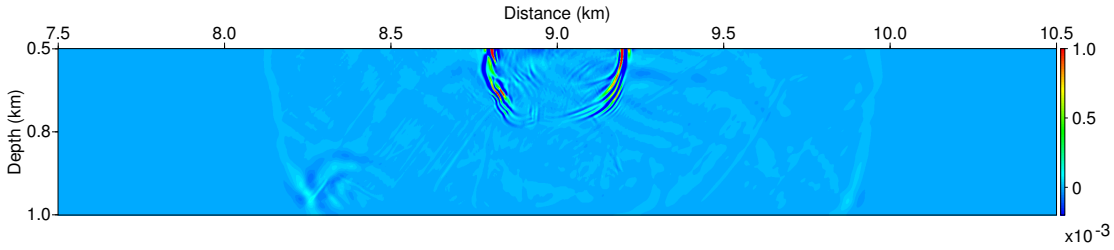


(d)

Figure 4.4: Wavefield comparisons between the $u_1$ wavefield with (a) CG-FEM and (b) DG-GMsFEM, and $u_3$ wavefield with (c) CG-FEM and (d) DG-GMsFEM.

also occur in the $u_3$ component seismograms in Figures 4.8 for CG-FEM and 4.9 for DG-GMsFEM, and the error between these two solutions in Figure 4.10.

A more detailed investigation of the seismic solutions is presented with a comparison of single traces. Figures 4.11(a)/4.11(b), 4.12(a)/4.12(b), 4.13(a)/4.13(b) and 4.14(a)/4.14(b) show the comparisons of the single trace $u_1$ and $u_3$ component seismograms of the receiver at 8.125 km, 8.75 km, 9.375 km and 10 km, respectively. Consistent with the complete seismogram shown in Figures 4.7 and 4.10, the $u_3$ component has smaller error at all these four traces, indicated by the good consistency between blue curve (CG-FEM solution) and red curve (DG-GMsFEM solution). Meanwhile, the consistency on $u_1$ component is worse, differing in the amplitude of direct S-wave.

### *4.3.2 Block II*

For the second block which ranges from 1.0 km to 1.5 km in depth and 7.5 km to 10.5 km with the first block, we placed the 30 Hz Ricker wavelet in the center of the model, and set all four boundaries to be damping boundary conditions as described in the Method part. The receivers are located in 1.1 km in depth, ranging from 7.5 km to 10.5 km. Since both the P- and S-wave velocities in this block are larger compared with those in the block I, we would expect that the relative error between the reference CG-FEM solution and our DG-GMsFEM solution will be smaller, both in wavefield snapshots and in seismograms. Nevertheless, to avoid duplication, we will not repeat the comparisons as those for Block I, but only show wavefield snapshot and seismogram with DG-GMsFEM to qualitatively check if there are obvious numerical dispersion in the solution, so that we can know if the number of basis functions we have set for the coarse elements in this block is appropriate.

The simulation of total 25000 time steps using 0.185 ms time interval, with the

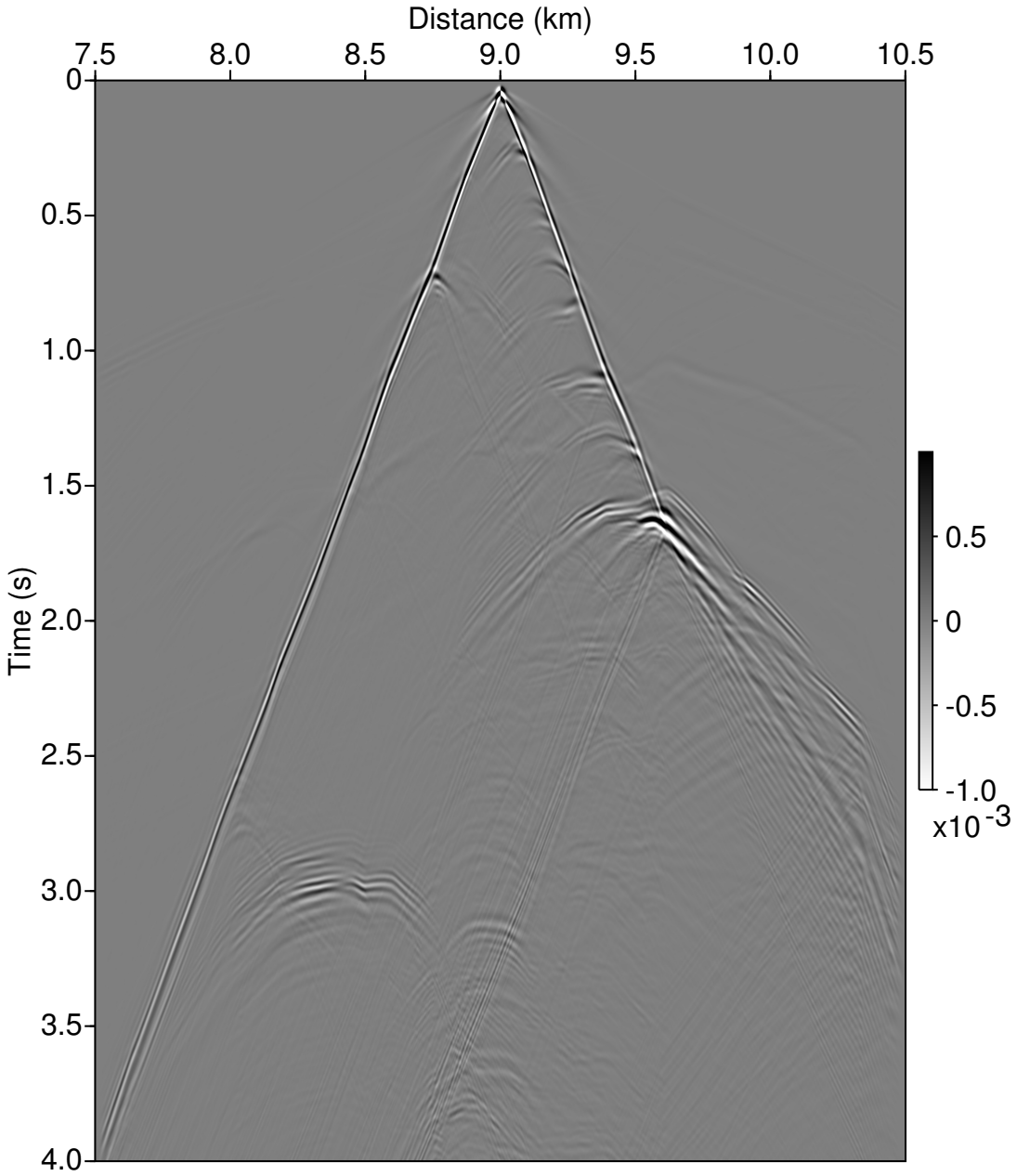


Figure 4.5: $u_1$ wavefield seismogram calculated with CG-FEM.

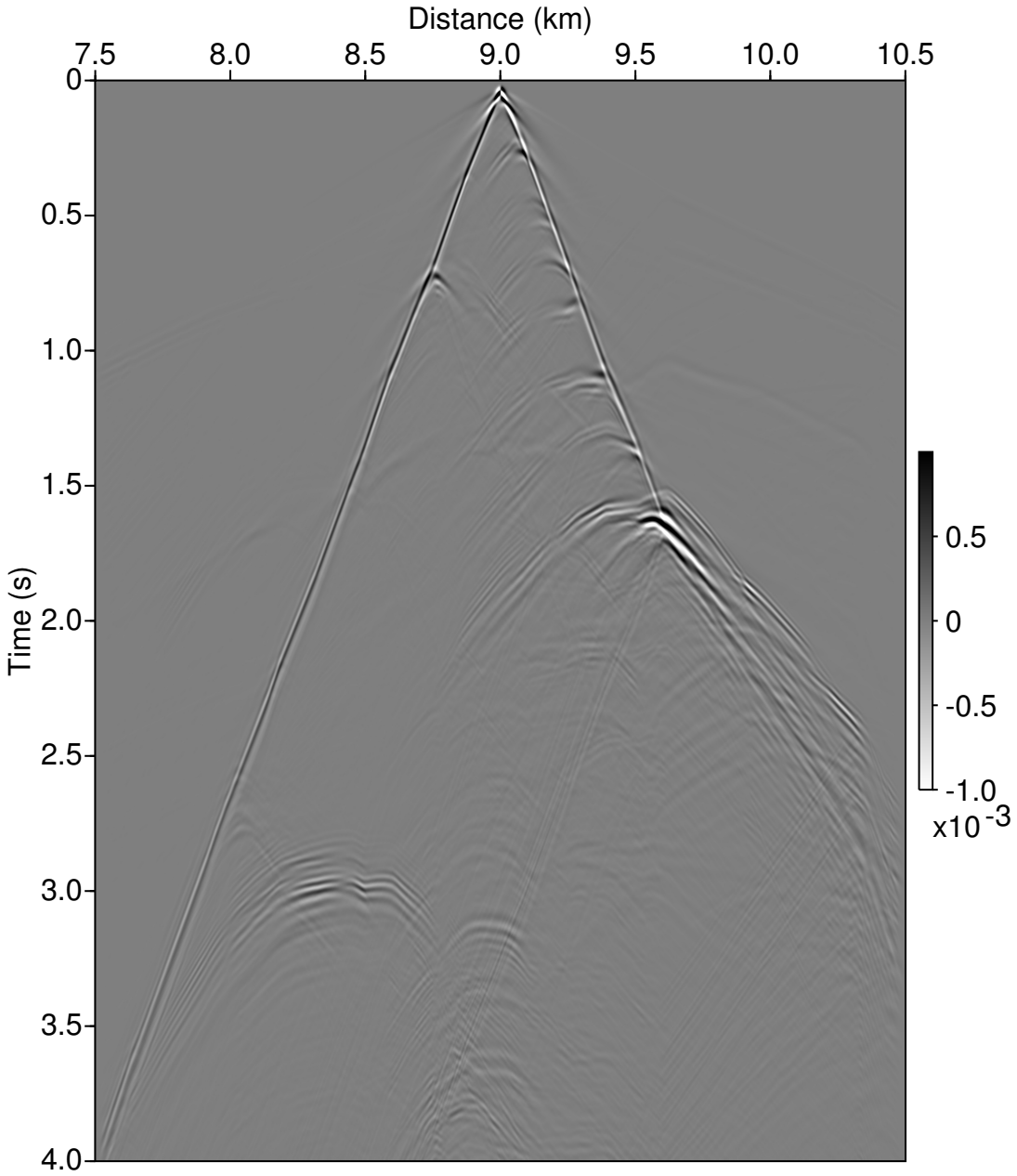


Figure 4.6: $u_1$ wavefield seismogram calculated with DG-GMsFEM.

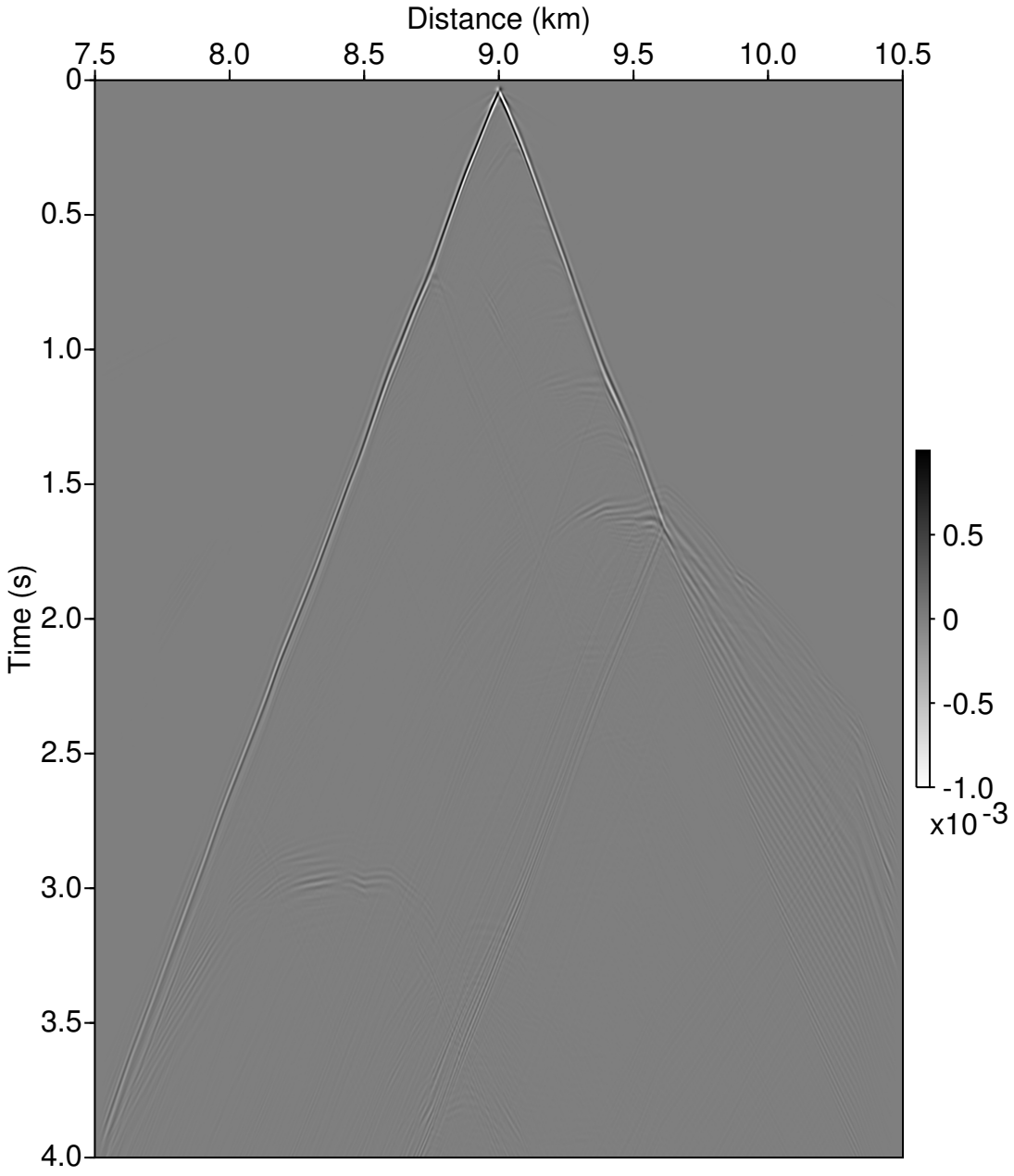


Figure 4.7: $u_1$ wavefield difference between the CG-FEM and DG-GMsFEM.

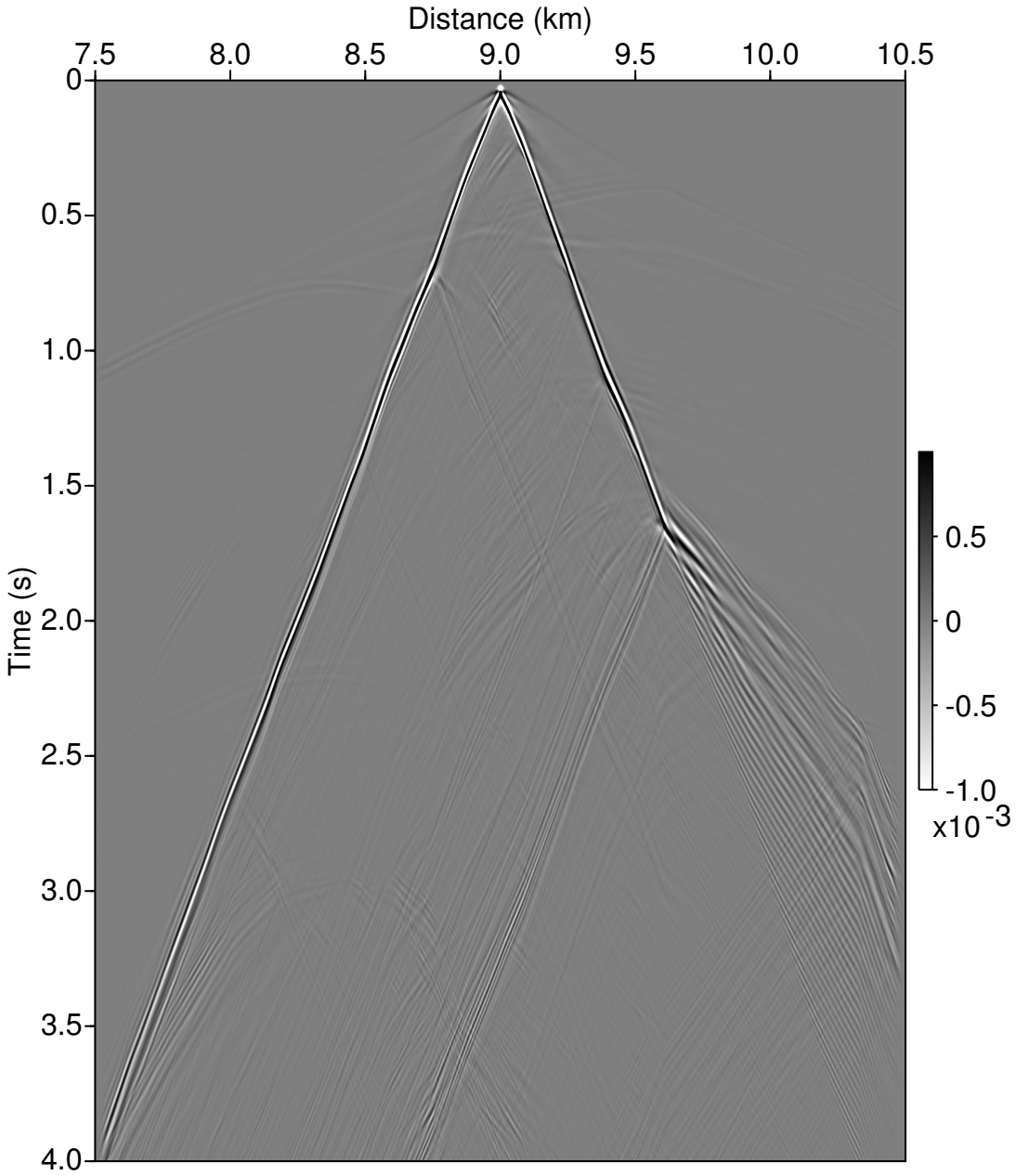


Figure 4.8: $u_3$ wavefield seismogram calculated with CG-FEM.

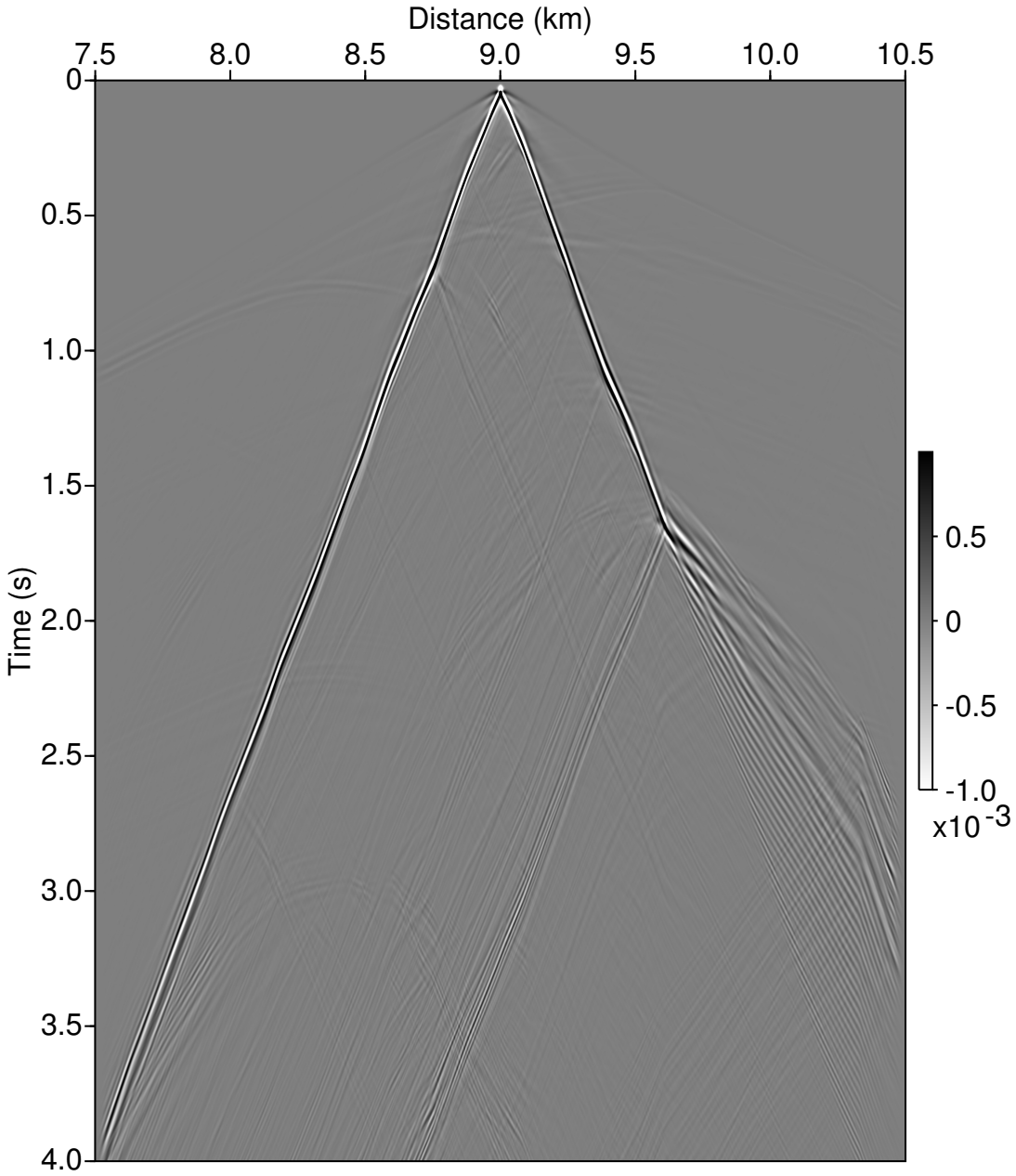


Figure 4.9: $u_3$ wavefield seismogram calculated with DG-GMsFEM.

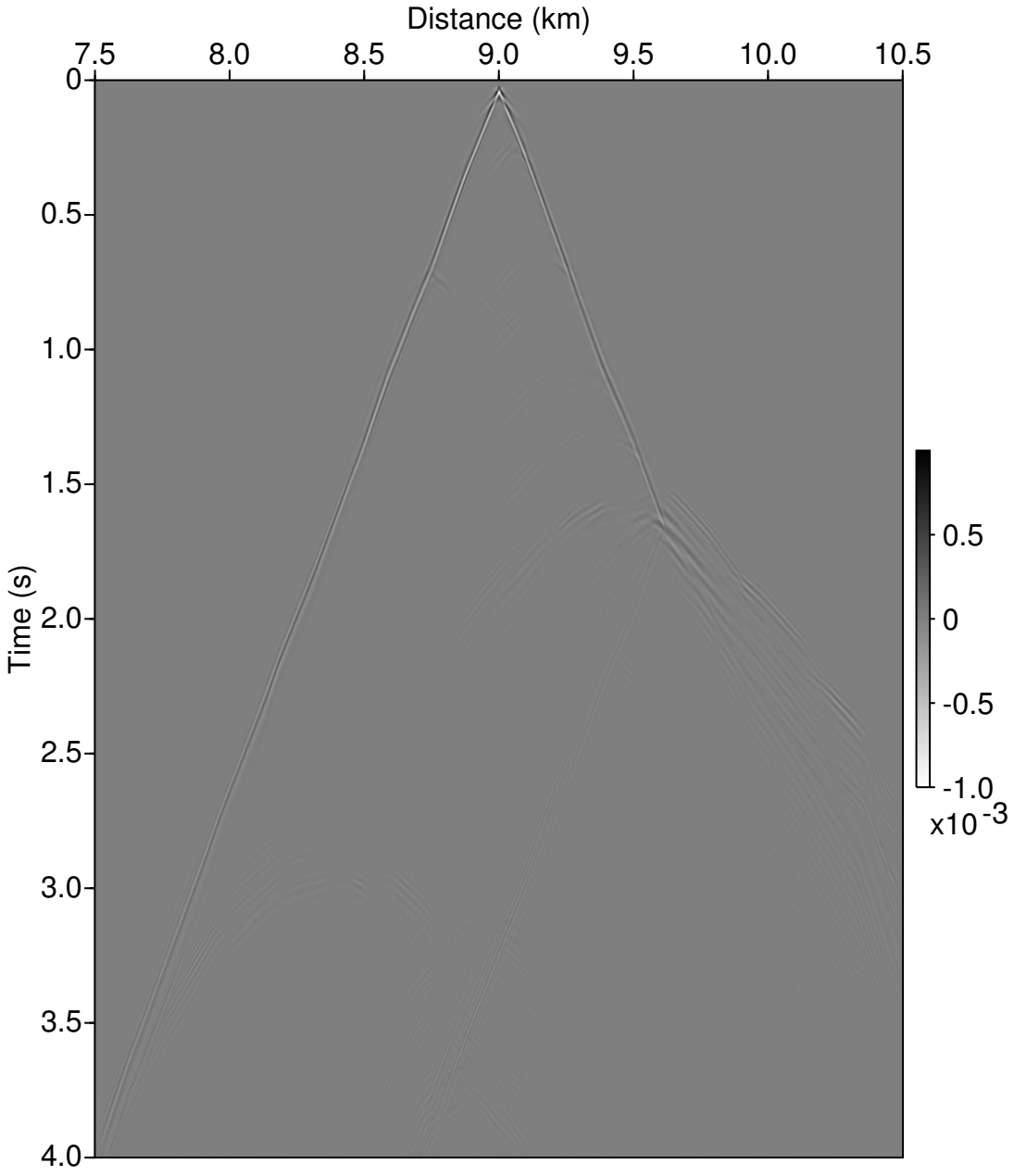


Figure 4.10: $u_3$ wavefield difference between the CG-FEM and DG-GMsFEM.

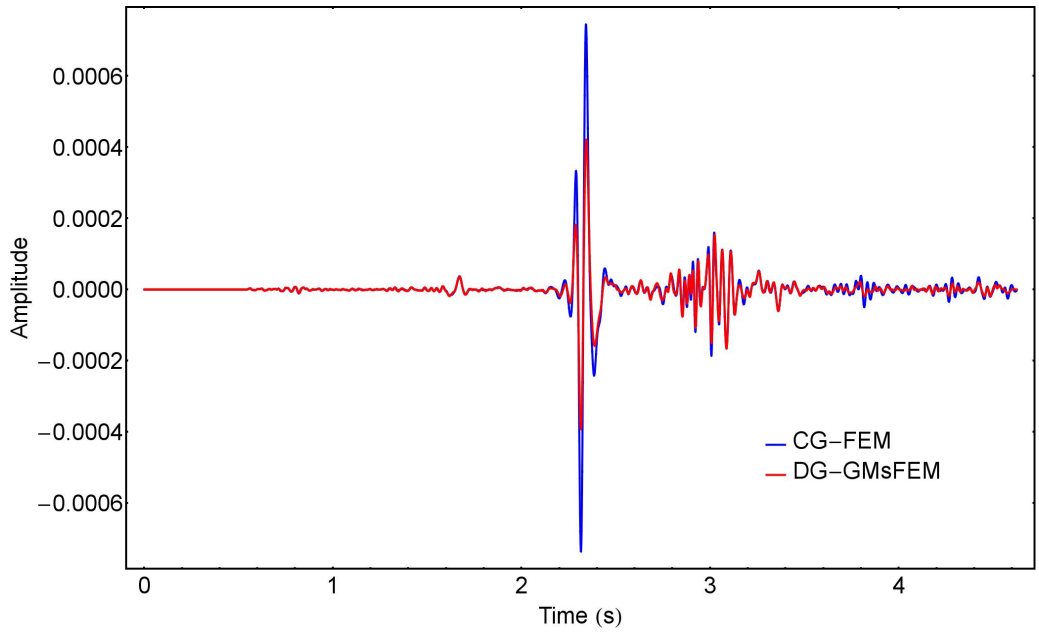


(a)

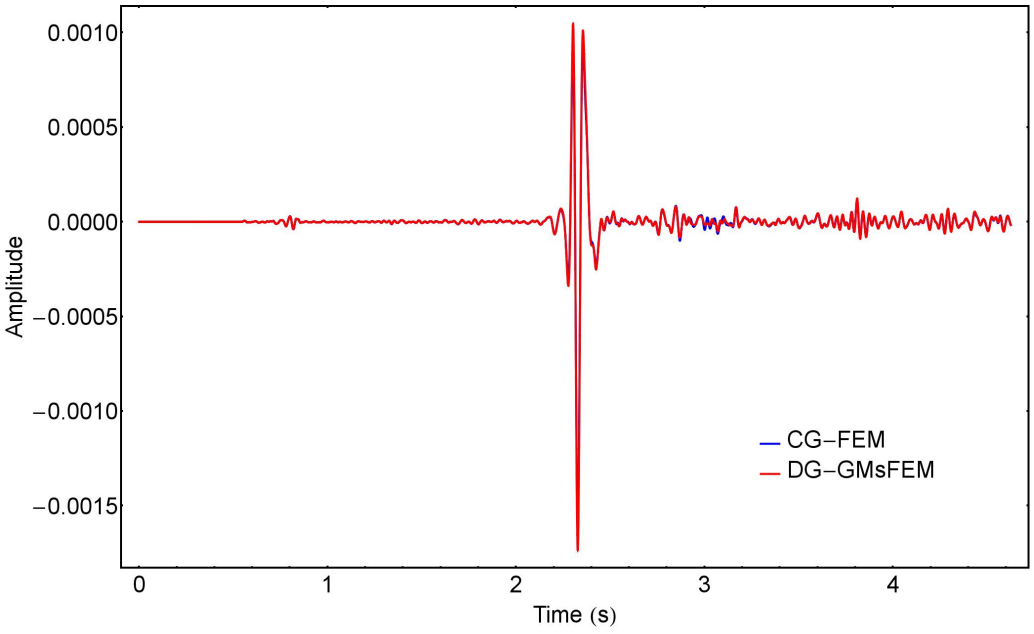


(b)

Figure 4.11: Single trace seismogram comparison of the receiver at 8.125 km. (a) is the $u_1$ component, (b) is the $u_3$ component.

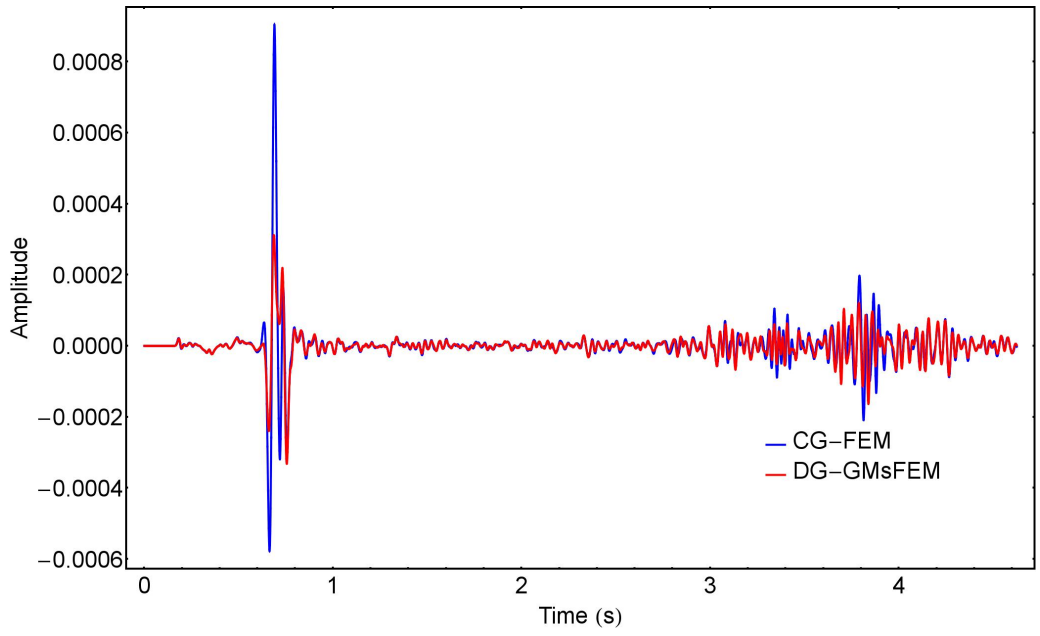


(a)

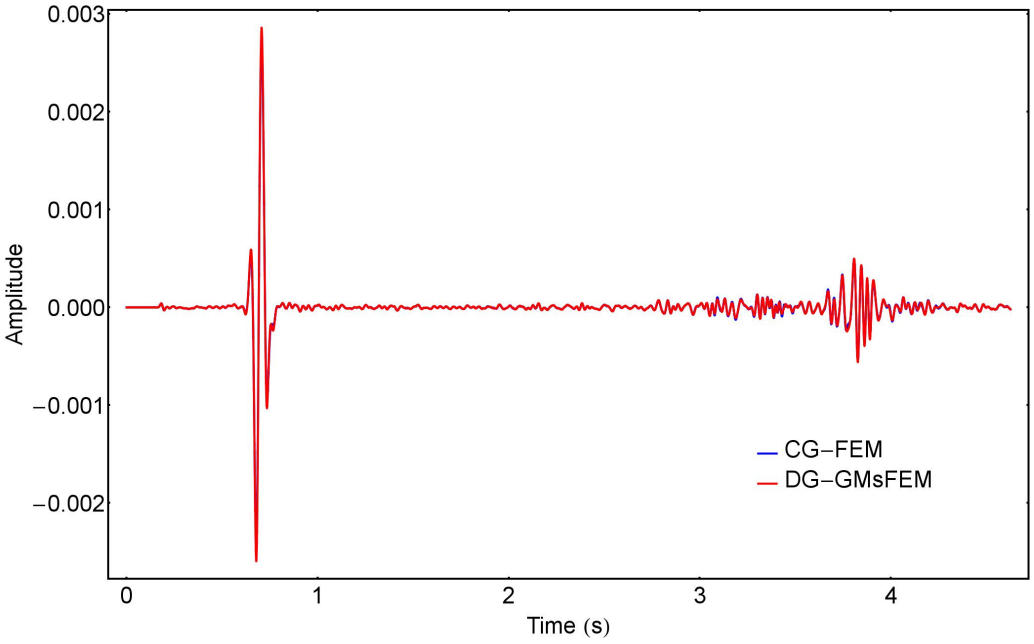


(b)

Figure 4.12: Single trace seismogram comparison of the receiver at 8.75 km. (a) is the $u_1$ component, (b) is the $u_3$ component.

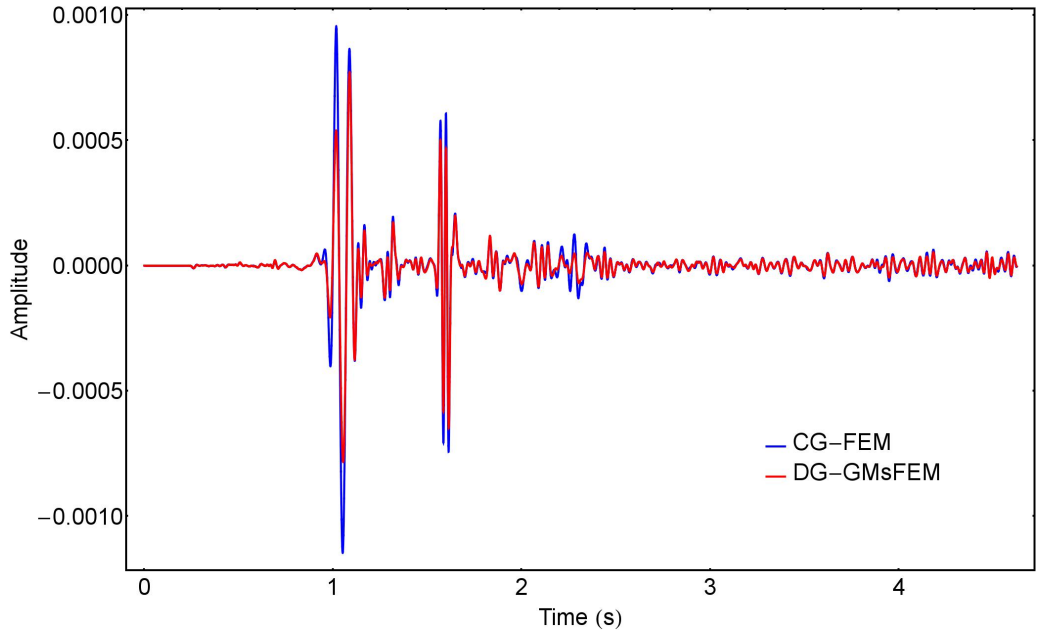


(a)

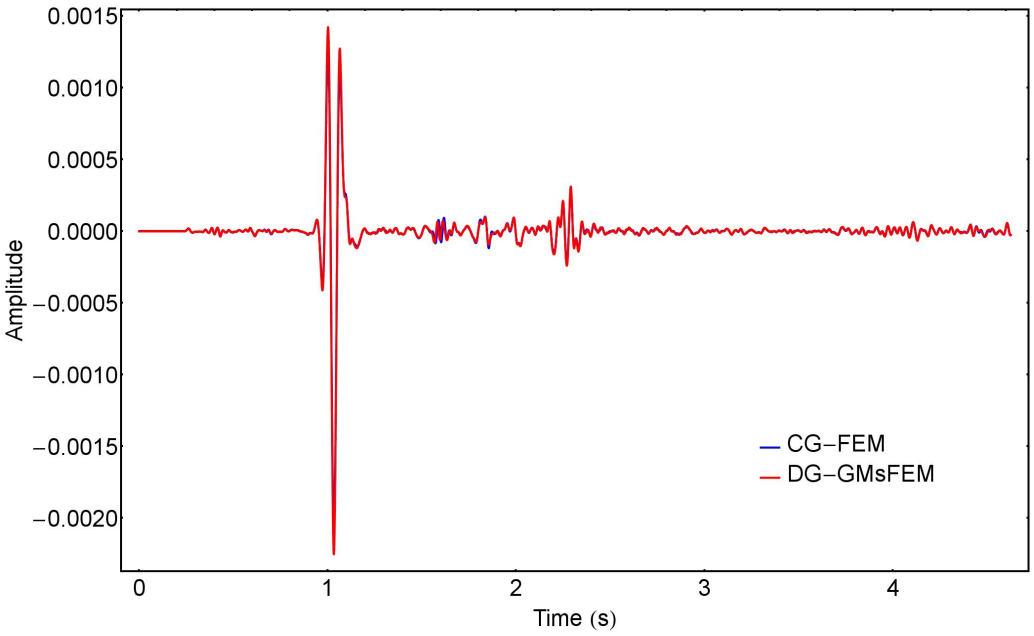


(b)

Figure 4.13: Single trace seismogram comparison of the receiver at 9.375 km. (a) is the $u_1$ component, (b) is the $u_3$ component.

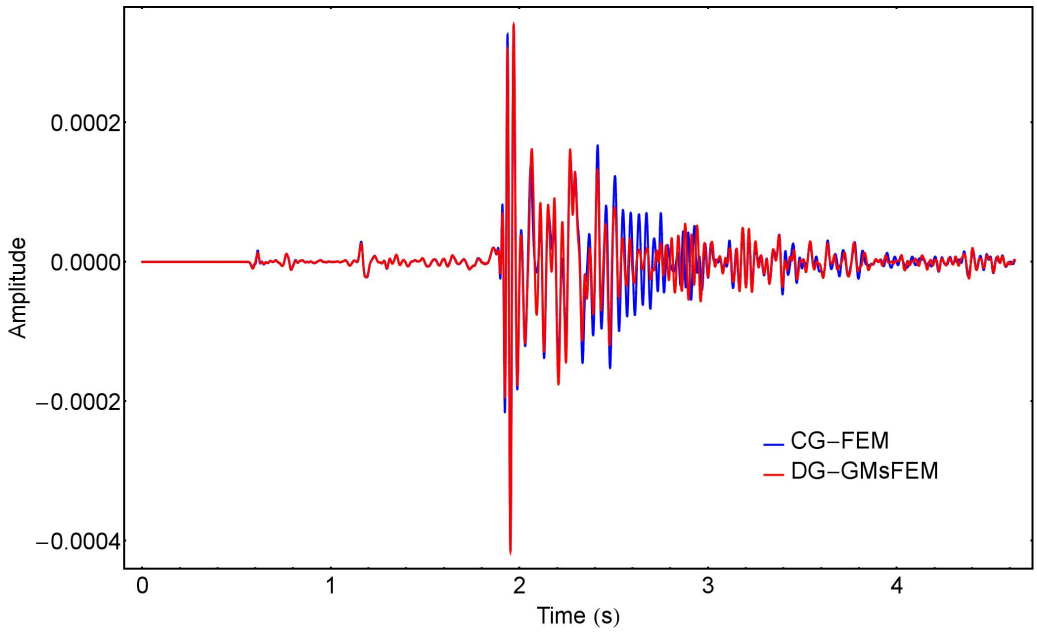


(a)

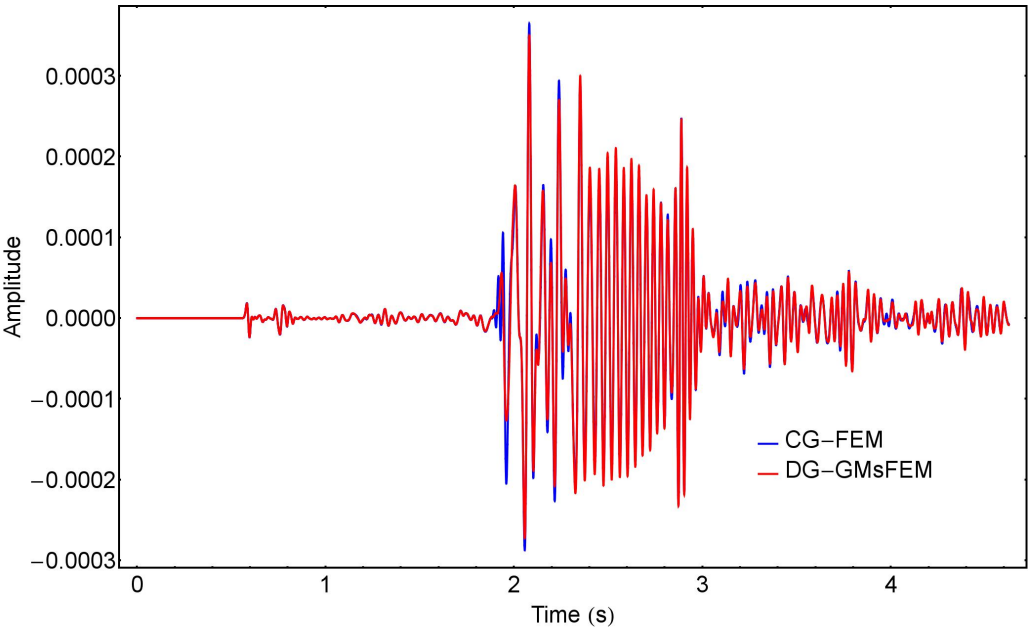


(b)

Figure 4.14: Single trace seismogram comparison of the receiver at 10 km. (a) is the $u_1$ component, (b) is the $u_3$ component.

number of basis functions assigned to each coarse element shown in Figure 4.2(b) and 4.3(b), takes about 7.6e4 s, compared with 4.0e5 s using CG-FEM, as discussed for block I. It should be noted that the computation time with CG-FEM is only related to the number of elements, however, computation time of DG-GMsFEM also depends on the number of basis functions.

Figures 4.15(a) and 4.15(b) show the $u_1$ and $u_3$ wavefield at 0.555 s, respectively. The wavefield snapshot shows complicated reflections and scatterings from the Marmousi-2 complex interface geometries and various faults. We remark that the average S-wave velocity in block II is about 930 m/s, which makes the wavelength of S-wave about 31 m, since our coarse element size is 25 m, the average wavelength is still contains less than two grids, which is difficult for conventional method to simulate. Nevertheless, we observe that there are no obvious numerical dispersion in the wavefield calculated with our DG-GMsFEM. Also, we show in Figures 4.16 and 4.17 the seismograms of $u_1$ and $u_3$ respectively, which also help to verify, that all types of waves, especially S-wave, can be modeled clearly in terms of the waveform shape.

### *4.3.3 Block III–VI*

For the rest blocks III–VI, we only show the seismogram of the receivers at a depth of 100 m, and all the other simulation parameters are same with those in block II. The average velocitys of blocks III–VI are about 1.28 km/s, 1.49 km/s, 1.89 km/s and 2.20 km/s, respectively, making the average S-wave wavelengths about 42.7 m, 49.7 m, 63.0 m and 73.3 m, respectively. Since we have utilized coarse element of size 25 m by 25 m, it could be easily seen that one wavelength contains no more than three grids in blocks III-VI, however, with the coupling mechanism provided by multiscale basis functions, we are still able to model the wavefield without obvious

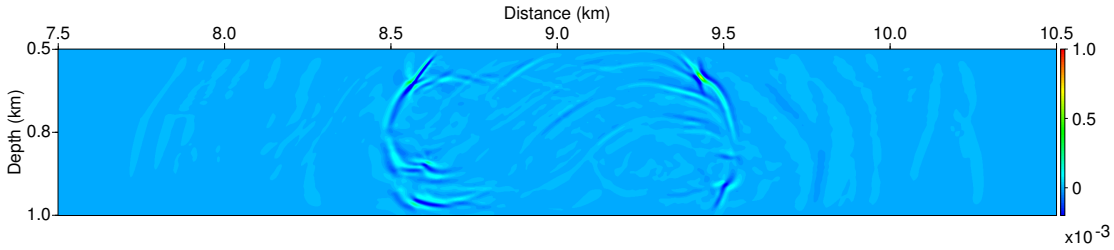


(a)

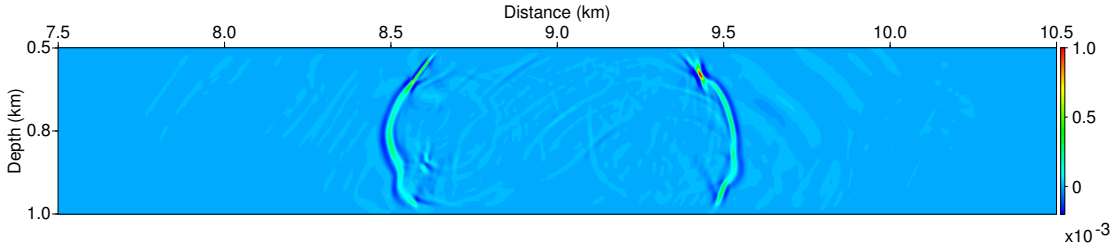


(b)

Figure 4.15: Wavefield of (a) $u_1$ and (b) $u_3$ in block II calculated with DG-GMsFEM.

numerical dispersion in S-wavefield, as can be observed in Figures 4.18(a)/4.18(b), 4.19(a)/4.19(b), 4.20(a)/4.20(b), and 4.21(a)/4.21(b) for $u_1/u_3$ component seismograms for blocks III–VI, respectively. Also, the computation time for the simulation in blocks III–VI is about 6.0e4, 5.2e4, 5.1e4, 4.3e4 s, respectively, compared with 4.0e5 s for with CG-FEM.

## 4.4 Conclusions

We have introduced a discontinuous Galerkin generalized multiscale finite-element method (DG-GMsFEM) for elastic wave propagation, and the key component of DG-GMsFEM is the construction of multiscale basis functions, which can help to capture the fine-scale information. We then apply this DG-GMsFEM to solve the elastic wave equation in the Marmousi-2 elastic model, and compare the results from continuous Galerkin finite-element method and our DG-GMsFEM, including

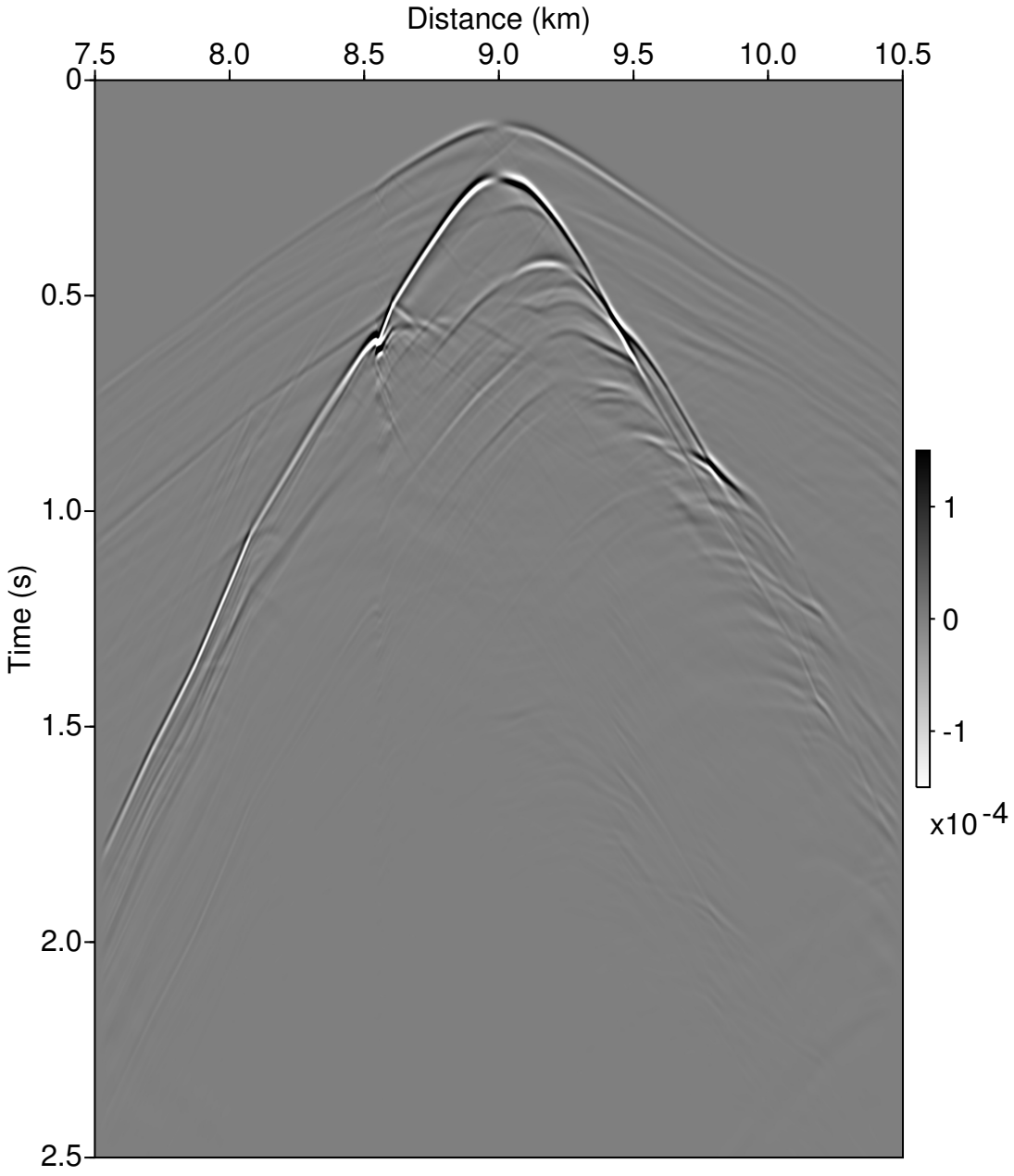


Figure 4.16: $u_1$ wavefield seismogram calculated with DG-GMsFEM for block II.

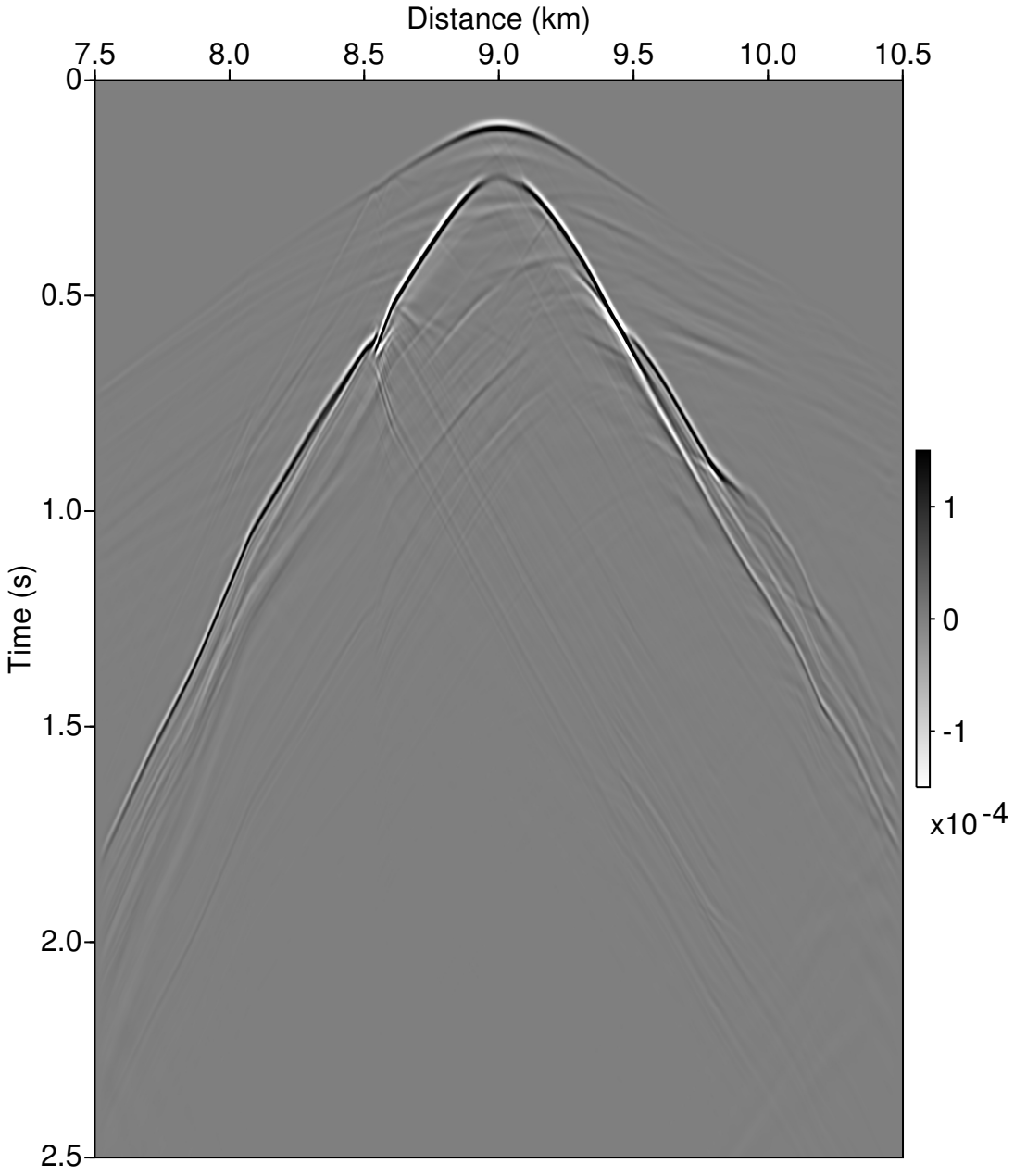


Figure 4.17: $u_3$ wavefield seismogram calculated with DG-GMsFEM for block II.

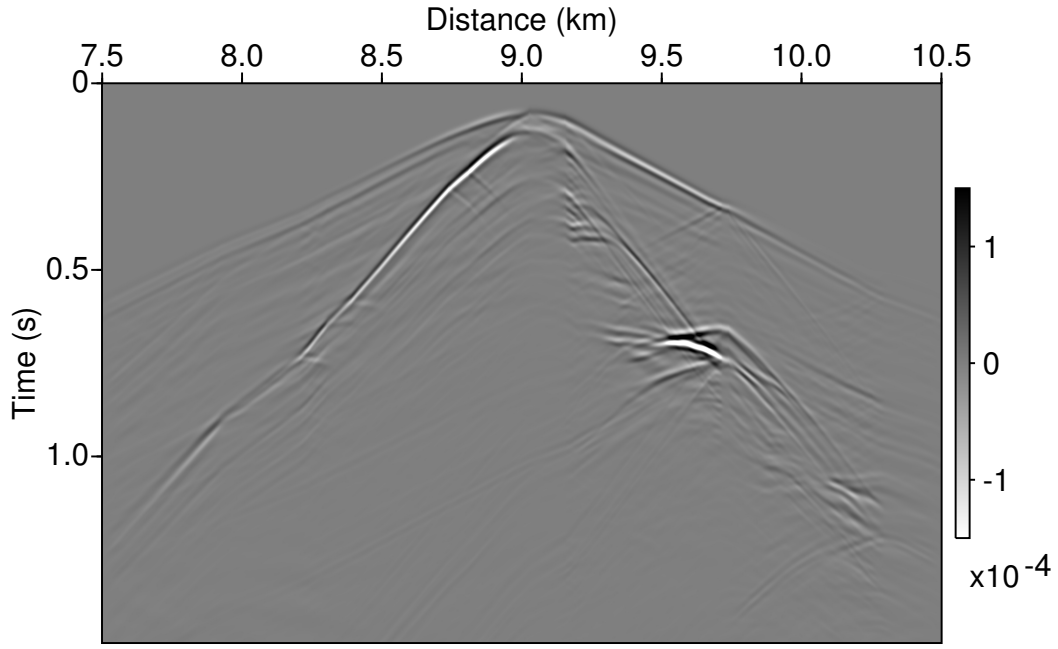


(a)

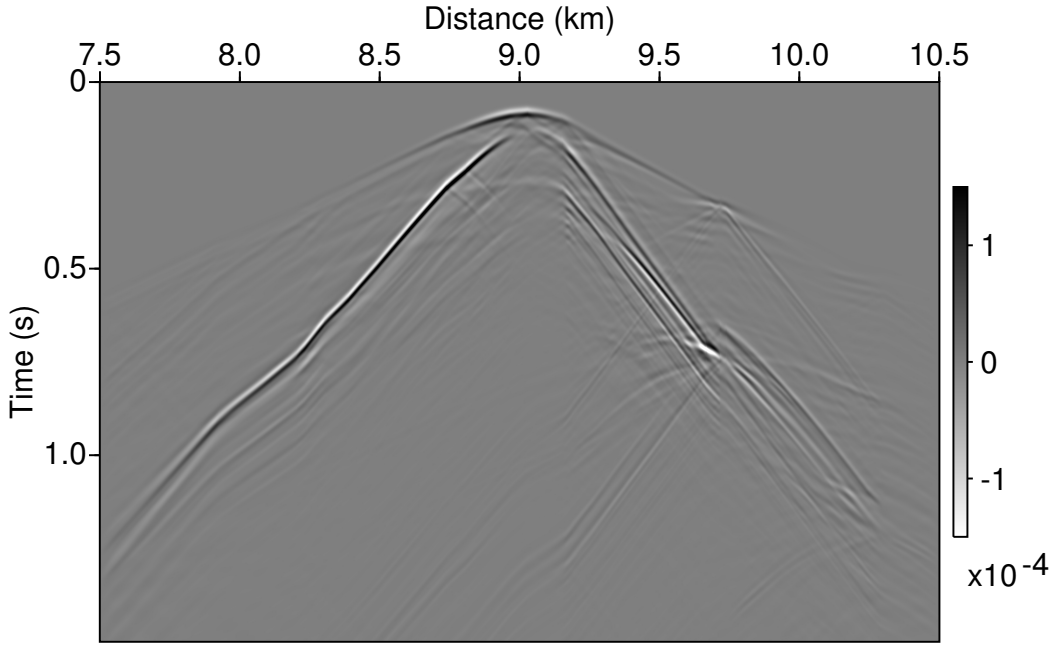


(b)

Figure 4.18: (a)$u_1$ and (b) $u_3$ wavefield seismograms calculated with DG-GMsFEM for block III.

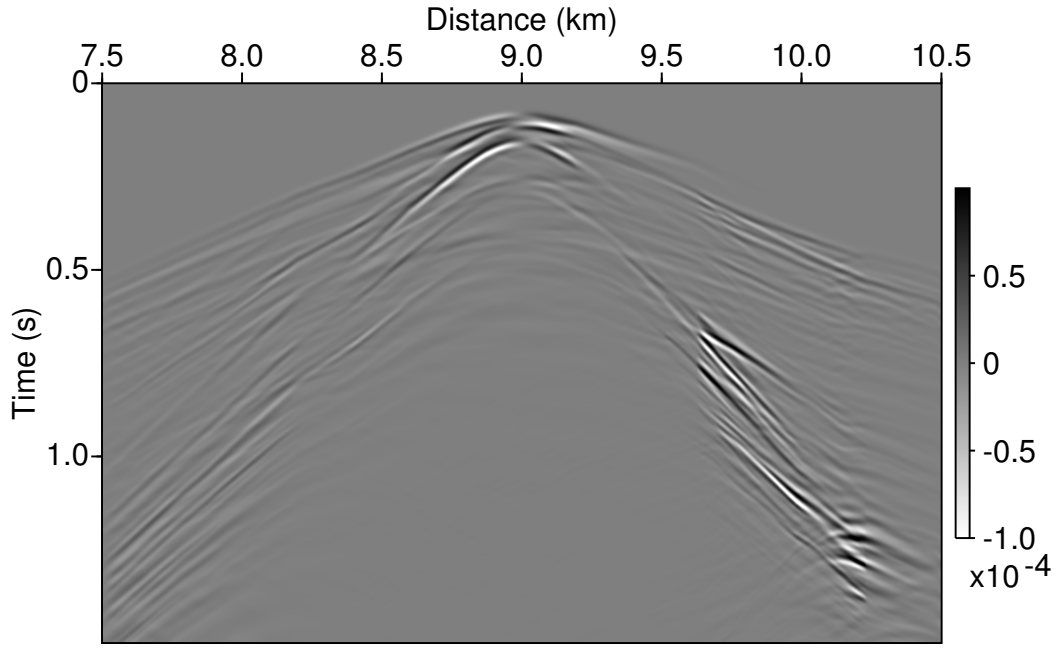


(a)

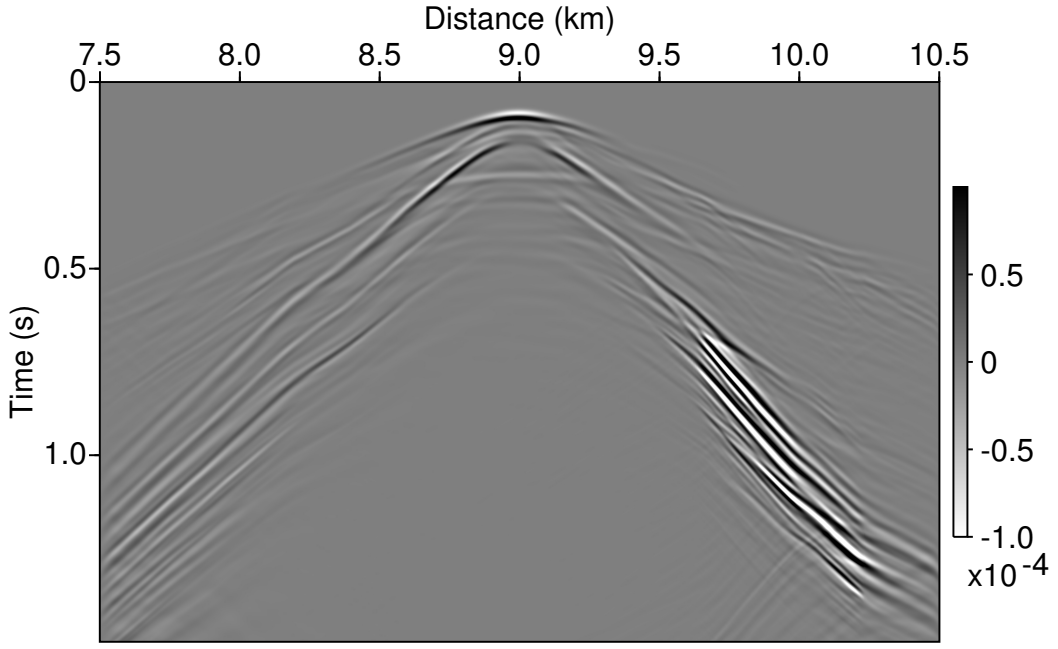


(b)

Figure 4.19: (a)$u_1$ and (b) $u_3$ wavefield seismograms calculated with DG-GMsFEM for block IV.

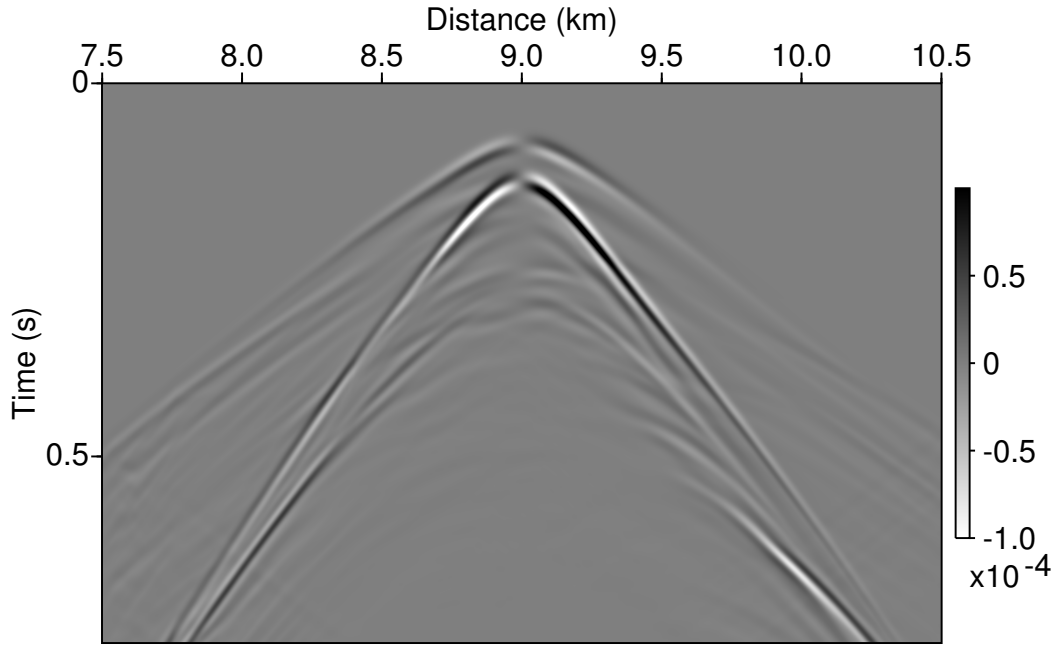


(a)

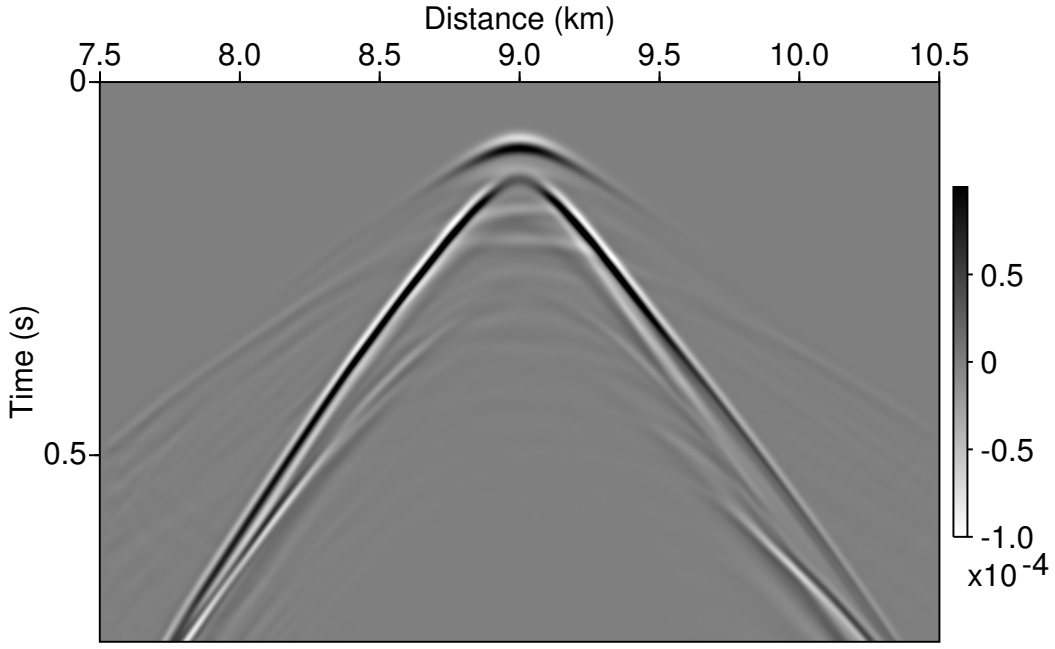


(b)

Figure 4.20: (a)$u_1$ and (b) $u_3$ wavefield seismograms calculated with DG-GMsFEM for block V.

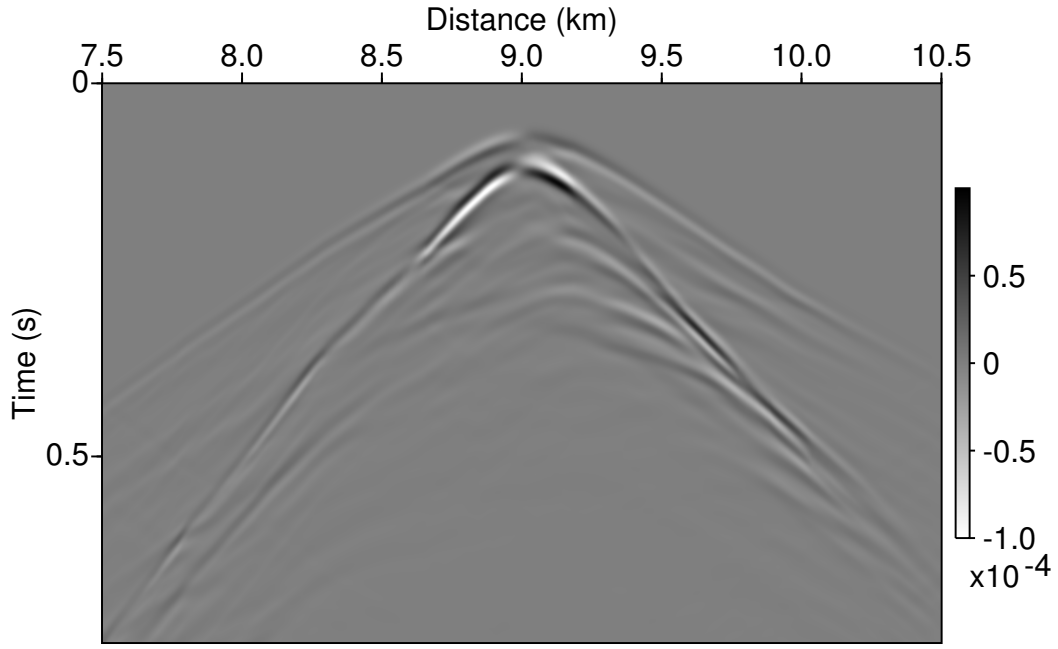


(a)

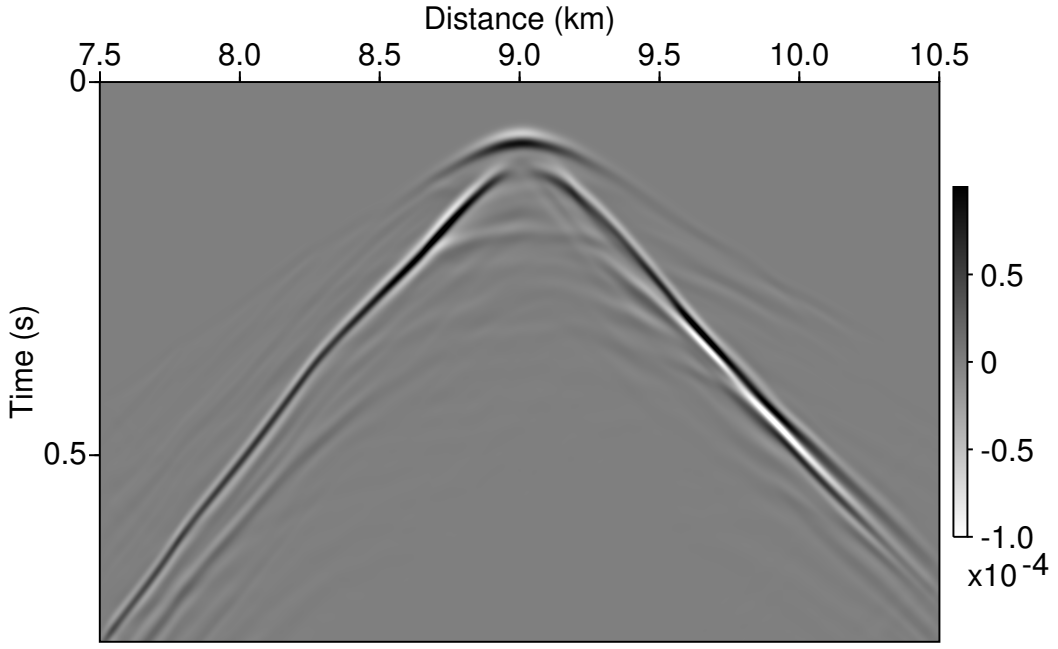


(b)

Figure 4.21: (a)$u_1$ and (b) $u_3$ wavefield seismograms calculated with DG-GMsFEM for block VI.

the wavefield snapshots, the seismograms, as well the single trace seismograms in the model. The comparison show that our DG-GMsFEM can effectively reduce the computation time of elastic wave equation simulation, while keeping the error satisfactorily small. Specially, our DG-GMsFEM can adopt coarse element size that is larger than the half of wavelength of S-wavefield, without introducing noticeable numerical dispersion, making our method attractive for wide applications in practice.

# 5. SUMMARY

## 5.1 Conclusions

In the preceding sections, I have investigated new multiscale methods for simulating elastic wave propagation in heterogeneous anisotropic media.

I first propose a numerical homogenization method for arbitrary heterogeneous anisotropic medium by using one multiscale basis function solved from an appropriately defined local problem for each coarse block in a fine discretized model, and through this numerical homogenization, I finally get a set of effective medium parameters that can approximately represent the elastic properties for each coarse block. The effectiveness of the proposed numerical homogenization method is verified with several numerical examples, and I find that the proposed approach can provide satisfactory results.

The numerical homogenization method based on the multiscale theory can be applied to reduce the computation costs by representing a coarse block with a homogeneous equivalent medium. However, the heterogeneities in the Earth medium often show multiple spatial scales, and therefore in certain circumstances such homogenization will result in serious loss of fine scale information. For this reason, I then develop the generalized multiscale finite-element method for elastic wave propagation, both in continuous Galerkin and discontinuous Galerkin formulations. The key ingredient of the GMsFEM is the definition and calculation of multiscale basis functions defined through some local spectral problems, and I provide two ways to get such multiscale basis functions to reliably incorporate the influence of fine-scale heterogeneity. I then designed four numerical examples to examine the relationship between the number of basis functions and the accuracy of the GMsFEM. I also

propose a method for determining the number of basis functions that are required to assign to each coarse block in GMsFEM by using the eikonal equation to calculate the maximum time difference in each coarse block.

To investigate the functionality of GMsFEM for realistic examples, I applied DG-GMsFEM to simulate the elastic wave propagation in Marmousi-2 elastic model in the third section. To test the current prototype code I selected a portion of the original model for simulations. These tests already show the capability of our multiscale method in reducing the computation time compared with conventional method. Specially, with our method it is possible to use a mesh with the grid size that is comparable to the wavelength of the wavefield, which makes the multiscale method an attractive tool for realistic applications.

## 5.2 Future work

There are several possible improvements that can be implemented for the GMsFEM, based on the results of the numerical experiments presented in the dissertation.

First, the current implementation of the method is in MATLAB, which favors the readability and easy maintenance of the codes. However, it is well known that MATLAB is a high-level language, and therefore will be much slower than complied languages such as C/C++ and FORTRAN. It is therefore necessary to transfer the current implementation to C/C++ or FORTRAN in the future, adding necessary optimization such as parallelization, sparse matrix manipulation technique, and so on, to make it feasible to simulate the wave propagation in realistic size models, both in 2-D and 3-D.

Second, given the current theory development on GMsFEM, it is necessary to consider the possibility of adding attenuating mechanisms to the elastic wave equation, i.e., visco-elastic wave equation, or further, two-phase mechanisms, i.e., poro-elastic

wave equations. There will be a couple of issues to be solved though for such possible extensions, such as the incorporation of quality factor $Q$ in the basis functions, or the fluid-solid interactions in the basis functions, and the corresponding mathematical analysis foundations for these complicated mechanisms.

Finally, a 3-D implementation of the GMsFEM is straightforward based on the current theory development and will be very important for practical applications. However, since in 3-D the global matrices will likely have dimensions that are much larger then 2-D problem, an efficient implementation and substantial optimization of the code should be necessary.

# REFERENCES


Abdulle, A., and M. J. Grote, 2011, Finite element heterogeneous multiscale method for the wave equation: Multiscale Modeling & Simulation, **9**, 766–792.

Alford, R., K. Kelly, and D. Boore, 1974, Accuracy of finitedifference modeling of the acoustic wave equation: Geophysics, **39**, 834–842.

Alterman, Z., and F. C. Karal, 1968, Propagation of elastic waves in layered media by finite difference methods: Bulletin of the Seismological Society of America, **58**, 367–398.

Arbogast, T., S. Minkoff, and P. Keenan, 1998, An operator-based approach to upscaling the pressure equation: Computational Methods in Water Resources XII, Computational Mechanics Publications, Southampton, UK, 405–412.

Arnold, D., F. Brezzi, B. Cockburn, and L. Marini, 2002, Unified analysis of discontinuous Galerkin methods for elliptic problems: SIAM Journal on Numerical Analysis, **39**, 1749–1779.

Backus, G. E., 1962, Long-wave elastic anisotropy produced by horizontal layering: Journal of Geophysical Research, **67**, 4427–4440.

Baysal, E., D. Kosloff, and J. Sherwood, 1983, Reverse time migration: Geophysics, **48**, 1514–1524.

Bérenger, J.-P., 1994, A perfectly matched layer for the absorption of electromagnetic waves: Journal of Computational Physics, **114**, 185 – 200.

Beydoun, W., and T. Keho, 1987, The paraxial ray method: Geophysics, **52**, 1639–1653.

Bohlen, T., and E. Saenger, 2006, Accuracy of heterogeneous staggered-grid finite-difference modeling of rayleigh waves: Geophysics, **71**, T109–T115.

Bolt, B., and W. Smith, 1976, Finite-element computation of seismic anomalies for bodies of arbitrary shape: Geophysics, **41**, 145–150.

Budiansky, B., and R. J. O'Connell, 1976, Elastic moduli of a cracked solid: International Journal of Solids and Structures, **12**, 81–97.

Capdeville, Y., L. Guillot, and J.-J. Marigo, 2010, 2-D non-periodic homogenization to upscale elastic media for P-SV waves: Geophysical Journal International, **182**, 903–922.

Carcione, J., S. Picotti, F. Cavallini, and J. Santos, 2012, Numerical test of the schoenberg-muir theory: Geophysics, **77**, C27–C35.

Carcione, J. M., 2007, Wave fields in real media: Theory and numerical simulation of wave propagation in anisotropic, anelastic, porous and electromagnetic media, 2nd ed., revised and extended ed.: Elsevier Science, Amsterdam, volume **38** *of* Handbook of Geophysical Exploration: Seismic Exploration.

Cerjan, C., D. Kosloff, R. Kosloff, and M. Reshef, 1985, A nonreflecting boundary condition for discrete acoustic and elastic wave equations: Geophysics, **50**, 705–708.

Červený, V., and F. Hron, 1980, The ray series method and dynamic ray tracing system for three-dimensional inhomogeneous media: Bulletin of the Seismological Society of America, **70**, 47–77.

Chang, W., and G. McMechan, 1987, Elastic reversetime migration: Geophysics, **52**, 1365–1375.

Chu, C., and P. Stoffa, 2012, Implicit finite-difference simulations of seismic wave propagation: Geophysics, **77**, T57–T67.

Chung, E., Y. Efendiev, and W. T. Leung, 2013a, Generalized multiscale finite element methods for wave propagation in heterogeneous media: arXiv:1307.0123.

Chung, E., and B. Engquist, 2006, Optimal discontinuous Galerkin methods for wave

propagation.: SIAM Journal on Numerical Analysis, **44**, 2131–2158.

———, 2009, Optimal discontinuous Galerkin methods for the acoustic wave equation in higher dimensions.: SIAM Journal on Numerical Analysis, **47**, 3820–3848.

Chung, E., W. Leung, Y. Efendiev, and R. Gibson Jr., 2013b, Generalized multiscale finite element modeling of acoustic wave propagation: SEG Technical Program Expanded Abstracts 2013.

Chung, E. T., Y. Efendiev, and R. L. Gibson Jr., 2011a, An energy-conserving discontinuous multiscale finite element method for the wave equation in heterogeneous media: Advances in Adaptive Data Analysis, **3**, 251–268.

———, 2011b, Multiscale finite-element modeling of acoustic wave propagation: SEG Technical Program Expanded Abstracts 2011.

Claerbout, J. F., 1985, Imaging the Earth's interior: Blackwell Scientific Publications, Inc., Cambridge, MA.

Cockburn, B., 2003, Discontinuous Galerkin methods: ZAMM - Journal of Applied Mathematics and Mechanics / Zeitschrift für Angewandte Mathematik und Mechanik, **83**, 731–754.

Cohen, G., 2002, Higher-order numerical methods for transient wave equations: Springer-Verlag, Berlin.

Cohen, G., and S. Fauqueux, 2005, Mixed spectral finite elements for the linear elasticity system in unbounded domains: SIAM journal on Scientific Computing, **26 (3)**, 864–884.

Collino, F., and C. Tsogka, 2001, Application of the perfectly matched absorbing layer model to the linear elastodynamic problem in anisotropic heterogeneous media: Geophysics, **66**, 294–307.

Dablain, M., 1986, The application of high-order differencing to the scalar wave equation: Geophysics, **51**, 54–66.

Davis, T., 2001, Multicomponent seismology—the next wave: Geophysics, **66**, 49–49.

De Basabe, J., and M. Sen, 2007, Grid dispersion and stability criteria of some common finite-element methods for acoustic and elastic wave equations: Geophysics, **72**, T81–T95.

De Basabe, J. D., M. K. Sen, and M. F. Wheeler, 2008, The interior penalty discontinuous galerkin method for elastic wave propagation: Grid dispersion: Geophysical Journal International, **175**, 83–93.

de la Puente, J., M. Dumbser, M. Käser, and H. Igel, 2008, Discontinuous Galerkin methods for wave propagation in poroelastic media: Geophysics, **73**, T77–T97.

de la Puente, J., M. Ferrer, M. Hanzich, J. Castillo, and J. Cela, 2014, Mimetic seismic wave modeling including topography on deformed staggered grids: Geophysics, **79**, T125–T141.

Drake, L. A., and B. A. Bolt, 1989, Finite element modelling of surface wave transmission across regions of subduction: Geophysical Journal International, **98**, 271–279.

Dumbser, M., and M. Käser, 2006, An arbitrary high-order discontinuous Galerkin method for elastic waves on unstructured meshes — II. The three-dimensional isotropic case: Geophysical Journal International, **167**, 319–336.

Dumbser, M., M. Käser, and E. F. Toro, 2007, An arbitrary high-order discontinuous galerkin method for elastic waves on unstructured meshes – V. Local time stepping and p-adaptivity: Geophysical Journal International, **171**, 695–717.

Dupuy, B., L. De Barros, S. Garambois, and J. Virieux, 2011, Wave propagation in heterogeneous porous media formulated in the frequency-space domain using a discontinuous Galerkin method: Geophysics, **76**, N13–N28.

E, W., and B. Engquist, 2002, The heterogeneous multi-scale methods: Communications in Mathematical Sciences, **1**, 87–132.

———, 2005, The Heterogeneous Multi-Scale Method for Homogenization Problems:

Springer, Berlin, volume **44** *of* Lecture Notes in Computational Science and Engineering.

Efendiev, Y., J. Galvis, and T. Y. Hou, 2013, Generalized multiscale finite element methods (GMsFEM): Journal of Computational Physics, **251**, 116–135.

Efendiev, Y., J. Galvis, G. Li, and M. Presho, 2013, Generalized multiscale finite element methods: Oversampling strategies: arXiv:1301.2866.

Efendiev, Y., J. Galvis, and X.-H. Wu, 2011, Multiscale finite element methods for high-contrast problems using local spectral basis functions: Journal of Computational Physics, **230**, 937 – 955.

Efendiev, Y., and T. Y. Hou, 2009, Multiscale Finite Element Methods: Theory and Applications: Springer, Berlin, volume **4** *of* Surveys and Tutorials in the Applied Mathematical Sciences.

Engquist, B., H. Holst, and O. Runborg, 2007, Multiscale methods for the wave equation: PAMM, **7**, 1140903–1140904.

———, 2011, Multi-scale methods for wave propagation in heterogeneous media: Communications in Mathematical Sciences, **9**, 33–56.

Engquist, B., and A. Majda, 1977, Absorbing boundary conditions for numerical simulation of waves: Proceedings of the National Academy of Sciences, **74**, 1765–1766.

Etgen, J., S. Gray, and Y. Zhang, 2009, An overview of depth imaging in exploration geophysics: Geophysics, **74**, WCA5–WCA17.

Fornberg, B., 1990, High-order finite differences and the pseudospectral method on staggered grids: SIAM Journal on Numerical Analysis, **27**, 904–918.

Fu, S., Y. Efendiev, K. Gao, and R. Gibson Jr., 2013, Multiscale modeling of acoustic wave propagation in 2D heterogeneous media using local spectral basis functions: SEG Technical Program Expanded Abstracts 2013, 3553–3558.

Gao, H., and J. Zhang, 2008, Implementation of perfectly matched layers in an arbitrary geometrical boundary for elastic wave modelling: Geophysical Journal International, **174**, 1029–1036.

Gao, K., R. Gibson Jr., E. Chung, Y. Efendiev, and S. Fu, 2013, A multiscale method for elastic wave equation modeling: SEG Technical Program Expanded Abstracts 2013, 3444–3448.

Gibson, R., V. Durussel, and K. Lee, 2005, Modeling and velocity analysis with a wavefront-construction algorithm for anisotropic media: Geophysics, **70**, T63–T74.

Gibson, R., K. Gao, E. Chung, and Y. Efendiev, 2014, Multiscale modeling of acoustic wave propagation in 2d media: Geophysics, **79**, T61–T75.

Givoli, D., T. Hagstrom, and I. Patlashenko, 2006, Finite element formulation with high-order absorbing boundary conditions for time-dependent waves: Computer Methods in Applied Mechanics and Engineering, **195**, 3666 – 3690.

Goff, J. A., and T. H. Jordan, 1988, Stochastic modeling of seafloor morphology: Inversion of sea beam data for second-order statistics: Journal of Geophysical Research: Solid Earth, **93**, 13589–13608.

Gray, S., and N. Bleistein, 2009, True-amplitude gaussian-beam migration: Geophysics, **74**, S11–S23.

Gray, S., and W. May, 1994, Kirchhoff migration using eikonal equation traveltimes: Geophysics, **59**, 810–817.

Grechka, V., 2003, Effective media: A forward modeling view: Geophysics, **68**, 2055–2062.

Grechka, V., and M. Kachanov, 2006, Effective elasticity of rocks with closely spaced and intersecting cracks: Geophysics, **71**, D85–D91.

Greenberg, M. L., and J. P. Castagna, 1992, Shear-wave velocity estimation in porous rocks: Theoretical formulation, preliminary verification and applications1: Geo-

physical Prospecting, **40**, 195–209.

Grote, M. J., A. Schneebeli, and D. Schötzau, 2006, Discontinuous Galerkin finite element method for the wave equation: SIAM Journal on Numerical Analysis, **44**, pp. 2408–2431.

Hagstrom, T., A. Mar-Or, and D. Givoli, 2008, High-order local absorbing conditions for the wave equation: Extensions and improvements: Journal of Computational Physics, **227**, 3322 – 3357.

Hansbo, P., and M. G. Larson, 2011, Energy norm a posteriori error estimates for discontinuous galerkin approximations of the linear elasticity problem: Computer Methods in Applied Mechanics and Engineering, **200**, 3026 – 3030.

Haskell, N. A., 1953, The dispersion of surface waves on multilayered media: Bulletin of the Seismological Society of America, **43**, 17–34.

Helbig, K., and M. Schoenberg, 1987, Anomalous polarization of elastic waves in transversely isotropic media: The Journal of the Acoustical Society of America, **81**, 1235–1245.

Higdon, R., 1991, Absorbing boundary conditions for elastic waves: Geophysics, **56**, 231–241.

Hill, N. R., 1990, Gaussian beam migration: Geophysics, **55**, 1416–1428.

Hou, T. Y., and X.-H. Wu, 1997, A multiscale finite element method for elliptic problems in composite materials and porous media: Journal of Computational Physics, **134**, 169 – 189.

Hudson, J. A., 1980, Overall properties of a cracked solid: Mathematical Proceedings of the Cambridge Philosophical Society, **88**, 371–384.

Hughes, T. J., 1987, The finite element method: linear static and dynamic finite element analysis: Dover Publications, Mineola.

Jiang, L., Y. Efendiev, and V. Ginting, 2009, Global multiscale methods for acoustic

wave equations with continuum scales. Submitted.

Kachanov, M., 1980, Continuum model of medium with cracks: Journal of the Engineering Mechanics Division, **106**, 1039–1051.

———, 1992, Effective elastic properties of cracked solids: Critical review of some basic concepts: Applied Mechanics Reviews, **45**, 304–335.

Kamath, N., and I. Tsvankin, 2013, Full-waveform inversion of multicomponent data for horizontally layered vti media: Geophysics, **78**, WC113–WC121.

Käser, M., and M. Dumbser, 2006, An arbitrary high-order discontinuous Galerkin method for elastic waves on unstructured meshes – I. The two-dimensional isotropic case with external source terms: Geophysical Journal International, **166**, 855–877.

———, 2008, A highly accurate discontinuous Galerkin method for complex interfaces between solids and moving fluids: Geophysics, **73**, T23–T35.

Käser, M., M. Dumbser, J. De La Puente, and H. Igel, 2007, An arbitrary high-order discontinuous galerkin method for elastic waves on unstructured meshes — iii. viscoelastic attenuation: Geophysical Journal International, **168**, 224–242.

Kaufmann, P., S. Martin, M. Botsch, and M. Gross, 2008, Flexible simulation of deformable models using discontinuous Galerkin FEM: Proceedings of the 2008 ACM SIGGRAPH/Eurographics Symposium on Computer Animation, Eurographics Association, 105–115.

Kelly, K., R. Ward, S. Treitel, and R. Alford, 1976, Synthetic seismograms: A finite-difference approach: Geophysics, **41**, 2–27.

Kennett, B. L. N., 1979, Theoretical reflection seismograms for elastic media: Geophysical Prospecting, **27**, 301–321.

———, 1985, Seismic wave propagation in stratified media: Cambridge University Press, Cambridge, UK. Cambridge Monographs on Mechanics.

Klimeš, L., 2002, Correlation functions of random media: Pure and Applied Geo-

physics, **159**, 1811–1831.

Komatitsch, D., C. Barnes, and J. Tromp, 2000a, Simulation of anisotropic wave propagation based upon a spectral element method: Geophysics, **65**, 1251–1260.

———, 2000b, Wave propagation near a fluid-solid interface: A spectral-element approach: Geophysics, **65**, 623–631.

Komatitsch, D., D. Göddeke, G. Erlebacher, and D. Michéa, 2010, Modeling the propagation of elastic waves using spectral elements on a cluster of 192 GPUs: Computer Science - Research and Development, **25**, no. 1, 75–82.

Komatitsch, D., and R. Martin, 2007, An unsplit convolutional perfectly matched layer improved at grazing incidence for the seismic wave equation: Geophysics, **72**, SM155–SM167.

Komatitsch, D., and J. Tromp, 1999, Introduction to the spectral element method for three-dimensional seismic wave propagation: Geophysical Journal International, **139**, 806–822.

———, 2002, Spectral-element simulations of global seismic wave propagation I. Validation: Geophysical Journal International, **149**, 390–412.

———, 2003, A perfectly matched layer absorbing boundary condition for the second-order seismic wave equation: Geophysical Journal International, **154**, 146–153.

Komatitsch, D., and J.-P. Vilotte, 1998, The spectral element method: An efficient tool to simulate the seismic response of 2D and 3D geological structures: Bulletin of the Seismological Society of America, **88**, 368–392.

Komatitsch, D., J.-P. Vilotte, R. Vai, J. M. Castillo-Covarrubias, and F. J. Sánchez-Sesma, 1999, The spectral element method for elastic wave equations—application to 2-D and 3-D seismic problems: International Journal for Numerical Methods in Engineering, **45**, 1139–1164.

Korostyshevskaya, O., and S. Minkoff, 2006, A matrix analysis of operator-based

upscaling for the wave equation: SIAM Journal on Numerical Analysis, **44**, 586–612.

Kosloff, D., and E. Baysal, 1982, Forward modeling by a fourier method: Geophysics, **47**, 1402–1412.

Kosloff, R., and D. Kosloff, 1986, Absorbing boundaries for wave propagation problems: Journal of Computational Physics, **63**, 363–376.

Larson, M. G., and F. Bengzon, 2013, The Finite Element Method: Theory, Implementation, and Applications: Springer, Berlin, volume **10** *of* Texts in Computational Science and Engineering.

Levander, A. R., 1988, Fourth-order finite-difference P-SV seismograms: Geophysics, **53**, 1425–1436.

Leveille, J., I. Jones, Z. Zhou, B. Wang, and F. Liu, 2011, Subsalt imaging for exploration, production, and development: A review: Geophysics, **76**, WB3–WB20.

Lipnikov, K., and L. Huang, 2008, A mimetic finitedifference method for acousticwave modeling on arbitrary meshes: SEG Technical Program Expanded Abstracts 2008, 2067–2071.

Liu, Y., 2013, Globally optimal finite-difference schemes based on least squares: GEOPHYSICS, **78**, T113–T132.

Liu, Y., X. Chang, D. Jin, R. He, H. Sun, and Y. Zheng, 2011, Reverse time migration of multiples for subsalt imaging: Geophysics, **76**, WB209–WB216.

Liu, Y., and M. Sen, 2010, A hybrid scheme for absorbing edge reflections in numerical modeling of wave propagation: Geophysics, **75**, A1–A6.

Liu, Y., and M. K. Sen, 2012, A absorbing boundary condition for elastic staggered-grid modelling: Geophysical Prospecting, **60**, 1114–1132.

Marfurt, K., 1984, Accuracy of finitedifference and finiteelement modeling of the scalar and elastic wave equations: Geophysics, **49**, 533–549.

Martin, G. S., R. Wiley, and K. J. Marfurt, 2006, Marmousi2: An elastic upgrade for marmousi: The Leading Edge, **25**, 156–166.

Masson, Y. J., S. R. Pride, and K. T. Nihei, 2006, Finite difference modeling of Biot's poroelastic equations at seismic frequencies: Journal of Geophysical Research: Solid Earth, **111**, B10305.

McMechan, G. A., 1983, Migration by extrapolation of time-dependent boundary values: Geophysical Prospecting, **31**, 413–420.

Meza-Fajardo, K. C., and A. S. Papagerogiou, 2008, A nonconvolutional, split-field, Perfectly Matched Layer for wave propagation in isotropic and isotropic elastic emdia: Stability analysis: Bulletin of Seismological Society of America, **98**, 1811–1836.

Mittet, R., 2002, Freesurface boundary conditions for elastic staggeredgrid modeling schemes: Geophysics, **67**, 1616–1623.

Mora, P., 1987, Nonlinear two-dimensional elastic inversion of multioffset seismic data: Geophysics, **52**, 1211–1228.

Owhadi, H., and L. Zhang, 2005, Homogenization of parabolic equations with a continuum of space and time scales.

———, 2007, Metric-based upscaling: Communications on Pure and Applied Mathematics, **60**, 675–723.

———, 2008, Numerical homogenization of the acoustic wave equations with a continuum of scales: Computer Methods in Applied Mechanics and Engineering, **198**, 397–406.

Özdenvar, T., and G. A. McMechan, 1997, Algorithms for staggered-grid computations for poroelastic, elastic, acoustic, and scalar wave equations: Geophysical Prospecting, **45**, 403–420.

Patera, A. T., 1984, A spectral element method for fluid dynamics: Laminar flow in

a channel expansion: Journal of Computational Physics, **54**, 468 – 488.

Ping, P., Y. Zhang, and Y. Xu, 2014, A multiaxial perfectly matched layer (M-PML) for the long-time simulation of elastic wave propagation in the second-order equations : Journal of Applied Geophysics, **101**, 124 – 135.

Podvin, P., and I. Lecomte, 1991, Finite difference computation of traveltimes in very contrasted velocity models: a massively parallel approach and its associated tools: Geophysical Journal International, **105**, 271–284.

Reed, W. H., and T. R. Hill, 1973, Triangular mesh methods for the neutron transport equation: Technical report, Los Alamos Scientific Laboratory Technical Report, LA-UR-73-479.

Rijpsma, G., and W. Zijl, 1998, Upscaling of Hooke's law for imperfectly layered rocks: Mathematical Geology, **30**, 943–969.

Rivière, B., 2008, Discontinuous Galerkin Methods For Solving Elliptic And Parabolic Equations: Theory and Implementation: Society for Industrial and Applied Mathematics, Philadelphia.

Rivière, B., M. Wheeler, and V. Girault, 1999, Improved energy estimates for interior penalty, constrained and discontinuous galerkin methods for elliptic problems. Part I: Computational Geosciences, **3**, 337–360.

Rivière, B., M. F. Wheeler, and V. Girault, 2001, A priori error estimates for finite element methods based on discontinuous approximation spaces for elliptic problems: SIAM Journal on Numerical Analysis, **39**, 902–931.

Robertsson, J., J. Blanch, and W. Symes, 1994, Viscoelastic finite-difference modeling: Geophysics, **59**, 1444–1456.

Robertsson, J. O. A., 1996, A numerical free-surface condition for elastic/viscoelastic finite-difference modeling in the presence of topography: Geophysics, **61**, 1921–1934.

Saenger, E., and T. Bohlen, 2004, Finite-difference modeling of viscoelastic and anisotropic wave propagation using the rotated staggered grid: Geophysics, **69**, 583–591.

Saenger, E. H., R. Ciz, O. S. Krüger, S. M. Schmalholz, B. Gurevich, and S. A. Shapiro, 2007, Finite-difference modeling of wave propagation on microscale: A snapshot of the work in progress: Geophysics, **72**, SM293–SM300.

Saenger, E. H., N. Gold, and S. A. Shapiro, 2000, Modeling the propagation of elastic waves using a modified finite-difference grid: Wave Motion, **31**, 77–92.

Sarma, G. S., K. Mallick, and V. R. Gadhinglajkar, 1998, Nonreflecting boundary condition in finite-element formulation for an elastic wave equation: Geophysics, **63**, 1006–1016.

Sayers, C., and M. Kachanov, 1991, A simple technique for finding effective elastic constants of cracked solids for arbitrary crack orientation statistics: International Journal of Solids and Structures, **27**, 671–680.

Sayers, C. M., 1996, Stress-dependent elastic wave velocities in shales: International Journal of Rock Mechanics and Mining Sciences and Geomechanics Abstracts, **33**, 72A.

———, 1999, Stress-dependent seismic anisotropy of shales: Geophysics, **64**, 93–98.

———, 2002, Stress-dependent elastic anisotropy of sandstones: Geophysical Prospecting, **50**, 85–95.

Schoenberg, M., and F. Muir, 1989, A calculus for finely layered anisotropic media: Geophysics, **54**, 581–589.

Schoenberg, M., and C. M. Sayers, 1995, Seismic anisotropy of fractured rock: Geophysics, **60**, 204–211.

Seriani, G., and E. Priolo, 1994, Spectral element method for acoustic wave simulation in heterogeneous media: Finite Elements in Analysis and Design, **16**, 337 –

348.

Sethian, J., and A. Popovici, 1999, 3-D traveltime computation using the fast marching method: Geophysics, **64**, 516–523.

Shipp, R. M., and S. C. Singh, 2002, Two-dimensional full wavefield inversion of wide-aperture marine seismic streamer data: Geophysical Journal International, **151**, 325–344.

Singh, S. C., T. A. Minshull, and G. D. Spence, 1993, Velocity structure of a gas hydrate reflector: Science, **260**, 204–207.

Symes, W., 2007, Reverse time migration with optimal checkpointing: Geophysics, **72**, SM213–SM221.

Tarantola, A., 1984, Inversion of seismic reflection data in the acoustic approximation: Geophysics, **49**, 1259–1266.

Thomson, W. T., 1950, Transmission of elastic waves through a stratified solid medium: Journal of Applied Physics, **21**, 89–93.

Tsvankin, I., J. Gaiser, V. Grechka, M. van der Baan, and L. Thomsen, 2010, Seismic anisotropy in exploration and reservoir characterization: An overview: Geophysics, **75**, 75A15–75A29.

Tsvankin, I., and V. Grechka, 2011, Seismology of azimuthally anisotropic media and seismic fracture characterization: Society of Exploration Geophysicists, Tulsa.

Vdovina, T., and S. Minkoff, 2008, An a priori error analysis of operator upscaling for the acoustic wave equation.: International Journal of Numerical Analysis and Modeling, **5**, 543–569.

Vdovina, T., S. Minkoff, and S. Griffith, 2009, A two-scale solution algorithm for the elastic wave equation: SIAM Journal on Scientific Computing, **31**, 3356–3386.

Vdovina, T., S. Minkoff, and O. Korostyshevskaya, 2005, Operator upscaling for the acoustic wave equation: SIAM Journal on Multiscale Modeling and Simulation, **4**,

1305–1338.

Versteeg, R., 1993, Sensitivity of prestack depth migration to the velocity model: Geophysics, **58**, 873–882.

Vidale, J., 1988, Finite-difference calculation of travel times: Bulletin of the Seismological Society of America, **78**, 2062–2076.

Vigh, D., K. Jiao, D. Watts, and D. Sun, 2014, Elastic full-waveform inversion application using multicomponent measurements of seismic data collection: Geophysics, **79**, R63–R77.

Virieux, J., 1986, P-SV wave propagation in heterogeneous media: Velocity-stress finite-difference method: Geophysics, **51**, 889–901.

Virieux, J., H. Calandra, and R.-É. Plessix, 2011, A review of the spectral, pseudo-spectral, finite-difference and finite-element modelling techniques for geophysical imaging: Geophysical Prospecting, **59**, 794–813.

Virieux, J., and S. Operto, 2009, An overview of full-waveform inversion in exploration geophysics: Geophysics, **74**, WCC1–WCC26.

Wheeler, M., 1978, An elliptic collocation-finite element method with interior penalties: SIAM Journal on Numerical Analysis, **15**, 152–161.

Wihler, T. P., 2006, Locking-free adaptive discontinuous Galerkin FEM for linear elasticity problems: Mathematics of Computation, **75**, pp. 1087–1102.

Wilcox, L. C., G. Stadler, C. Burstedde, and O. Ghattas, 2010, A high-order discontinuous Galerkin method for wave propagation through coupled elastic–acoustic media: Journal of Computational Physics, **229**, 9373 – 9396.

Wu, R.-S., 1994, Wide-angle elastic wave one-way propagation in heterogeneous media and an elastic wave complex-screen method: Journal of Geophysical Research: Solid Earth, **99**, 751–766.

Xia, J., R. D. Miller, and C. B. Park, 1999, Estimation of near-surface shear-wave

velocity by inversion of rayleigh waves: Geophysics, **64**, 691–700.

Yan, J., and P. Sava, 2008, Isotropic angle-domain elastic reverse-time migration: Geophysics, **73**, S229–S239.

Zhang, Y., G. Zhang, and N. Bleistein, 2005, Theory of true-amplitude one-way wave equations and true-amplitude common-shot migration: Geophysics, **70**, E1–E10.

Zhu, T., 1988, Raykirchhoff migration in inhomogeneous media: Geophysics, **53**, 760–768.

Zijl, W., M. Hendriks, and C. 't Hart, 2002, Numerical homogenization of the rigidity tensor in Hooke's law using the node-based finite element method: Mathematical Geology, **34**, 291–322.

# APPENDIX A

## LOCAL STATIC LINEAR ELASTICITY PROBLEM SOLVED WITH 2ND-ORDER FINITE-ELEMENT

The local problem in equation 2.6 with boundary conditions 2.7 can be solved with standard continuous Galerkin finite-element method (e.g., Larson and Bengzon, 2013). We present here some details to illustrate the procedure.

First, we transform equation 2.6 into the form that is more commonly used in FEM with fourth-order elasticity tensor $\mathbf{c} = c_{ijkl}$:

$$-\nabla \cdot \boldsymbol{\sigma} = \mathbf{0}, \tag{A.1a}$$

$$\boldsymbol{\sigma} = \mathbf{c} : \boldsymbol{\varepsilon}, \tag{A.1b}$$

$$\boldsymbol{\varepsilon} = \frac{1}{2}[\nabla \mathbf{u} + (\nabla \mathbf{u})^{\mathrm{T}}], \tag{A.1c}$$

where $\boldsymbol{\varepsilon}$ is the strain tensor. For the boundary conditions 2.7, it is easy to show that they are equivalent to the following Neumann boundary conditions:

$$\boldsymbol{\sigma} \cdot \mathbf{n}_1^+ = (\sigma_{11}, \sigma_{13}) = (1, 1), \tag{A.2a}$$

$$\boldsymbol{\sigma} \cdot \mathbf{n}_1^- = (-\sigma_{11}, -\sigma_{13}) = (-1, -1), \tag{A.2b}$$

$$\boldsymbol{\sigma} \cdot \mathbf{n}_3^+ = (\sigma_{13}, \sigma_{33}) = (1, 1), \tag{A.2c}$$

$$\boldsymbol{\sigma} \cdot \mathbf{n}_3^- = (-\sigma_{13}, -\sigma_{33}) = (-1, -1), \tag{A.2d}$$

where $\mathbf{n}_1^+ = (1, 0)$ is the outward pointed normal of the right vertical boundary, $\mathbf{n}_1^- = (-1, 0)$ is the outward pointed normal of the left vertical boundary, $\mathbf{n}_3^+ = (0, 1)$ is the outward pointed normal of the bottom horizontal boundary and $\mathbf{n}_3^- = (0, -1)$

is the outward pointed normal of the top horizontal boundary.

The elasticity problem must be solved in each of the four sub-rectangles within the support $K_\sigma$ for the stress variables (Figure 2.1), and we assume that each sub-rectangle is composed of $r_1 r_3$ finer elements. The elastic parameters $\mathbf{c}$ are homogeneous on a fine element but generally heterogeneous within the rectangle, and the discretization is shown in Figure A.1.

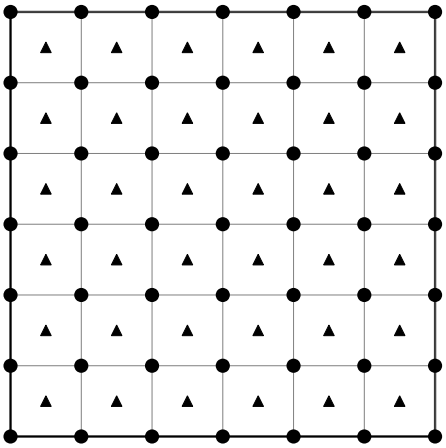

Figure A.1: A sketch of the fine mesh discretization for the local problem. To solve the local problem with FEM, we compute displacement $\mathbf{u}$ at the locations ●, and after the calculation of $\mathbf{u}$, we can obtain the stress for a fine element at the center of a fine element at locations ▲.

The above problem and discretization results in the following weak form

$$\int_K \boldsymbol{\sigma}(\mathbf{u}) : \boldsymbol{\varepsilon}(\mathbf{u}) d\mathbf{x} = \int_{\partial K} \boldsymbol{\sigma}(\mathbf{u}) \cdot \mathbf{n} ds, \tag{A.3}$$

with $\mathbf{n}$ being the outward pointed normal on each edge of $K$. We further have the discrete form

$$\mathbf{AU} = \mathbf{B}, \tag{A.4}$$

where we assemble $\mathbf{A}$ and $\mathbf{B}$ simply with 2nd-order finite-element basis functions (e.g., Larson and Bengzon, 2013). Given the analytic expressions for the basis functions and the discretization in Figure A.1, we then develop exact expressions for $\mathbf{A}$ and $\mathbf{B}$ for a fine element $K_h$ using `Mathematica` to complete the algebra:

$$\mathbf{A}_{K_h} = \begin{pmatrix} A_{11} & A_{12} & A_{13} & A_{14} & A_{15} & A_{16} & A_{17} & A_{18} \\ & A_{22} & A_{23} & A_{24} & A_{25} & A_{26} & A_{27} & A_{28} \\ & & A_{33} & A_{34} & A_{35} & A_{36} & A_{37} & A_{38} \\ & & & A_{44} & A_{45} & A_{46} & A_{47} & A_{48} \\ & & & & A_{55} & A_{56} & A_{57} & A_{58} \\ & & & & & A_{66} & A_{67} & A_{68} \\ & & & & & & A_{77} & A_{78} \\ & & & & & & & A_{88} \end{pmatrix}, \tag{A.5}$$

where

$$A_{11} = \frac{1}{6}((2C_{11}\Delta x_3)/\Delta x_1 + 3C_{15} + (2C_{55}\Delta x_1)/\Delta x_3), \tag{A.6}$$

$$A_{12} = \frac{1}{12}(3(C_{13} + C_{55}) + (4C_{35}\Delta x_1)/\Delta x_3 + (4C_{15}\Delta x_3)/\Delta x_1), \tag{A.7}$$

$$A_{13} = (C_{55}\Delta x_1)/(6\Delta x_3) - (C_{11}\Delta x_3)/(3\Delta x_1), \tag{A.8}$$

$$A_{14} = \frac{1}{12}(3C_{13} - 3C_{55} + (2C_{35}\Delta x_1)/\Delta x_3 - (4C_{15}\Delta x_3)/\Delta x_1), \tag{A.9}$$

$$A_{15} = \frac{1}{6}(-3C_{15} - (C_{55}\Delta x_1)/\Delta x_3 - (C_{11}\Delta x_3)/\Delta x_1), \tag{A.10}$$

$$A_{16} = \frac{1}{12}(-3(C_{13} + C_{55}) - (2C_{35}\Delta x_1)/\Delta x_3 - (2C_{15}\Delta x_3)/\Delta x_1), \tag{A.11}$$

$$A_{17} = -((C_{55}\Delta x_1)/(3\Delta x_3)) + (C_{11}\Delta x_3)/(6\Delta x_1), \tag{A.12}$$

$$A_{18} = \frac{1}{12}(-3C_{13} + 3C_{55} - (4C_{35}\Delta x_1)/\Delta x_3 + (2C_{15}\Delta x_3)/\Delta x_1), \tag{A.13}$$

$$A_{22} = \frac{1}{6}(3C_{35} + (2C_{33}\Delta x_1)/\Delta x_3 + (2C_{55}\Delta x_3)/\Delta x_1), \tag{A.14}$$

$$A_{23} = \frac{1}{12}(-3C_{13} + 3C_{55} + (2C_{35}\Delta x_1)/\Delta x_3 - (4C_{15}\Delta x_3)/\Delta x_1), \tag{A.15}$$

$$A_{24} = (C_{33}\Delta x_1)/(6\Delta x_3) - (C_{55}\Delta x_3)/(3\Delta x_1), \tag{A.16}$$

$$A_{25} = \frac{1}{12}(-3(C_{13} + C_{55}) - (2C_{35}\Delta x_1)/\Delta x_3 - (2C_{15}\Delta x_3)/\Delta x_1), \tag{A.17}$$

$$A_{26} = \frac{1}{6}(-3C_{35} - (C_{33}\Delta x_1)/\Delta x_3 - (C_{55}\Delta x_3)/\Delta x_1), \tag{A.18}$$

$$A_{27} = \frac{1}{12}(3C_{13} - 3C_{55} - (4C_{35}\Delta x_1)/\Delta x_3 + (2C_{15}\Delta x_3)/\Delta x_1), \tag{A.19}$$

$$A_{28} = -((C_{33}\Delta x_1)/(3\Delta x_3)) + (C_{55}\Delta x_3)/(6\Delta x_1), \tag{A.20}$$

$$A_{33} = \frac{1}{6}(-3C_{15} + (2C_{55}\Delta x_1)/\Delta x_3 + (2C_{11}\Delta x_3)/\Delta x_1), \tag{A.21}$$

$$A_{34} = \frac{1}{12}(-3(C_{13} + C_{55}) + (4C_{35}\Delta x_1)/\Delta x_3 + (4C_{15}\Delta x_3)/\Delta x_1), \tag{A.22}$$

$$A_{35} = -((C_{55}\Delta x_1)/(3\Delta x_3)) + (C_{11}\Delta x_3)/(6\Delta x_1), \tag{A.23}$$

$$A_{36} = \frac{1}{12}(3C_{13} - 3C_{55} - (4C_{35}\Delta x_1)/\Delta x_3 + (2C_{15}\Delta x_3)/\Delta x_1), \tag{A.24}$$

$$A_{37} = \frac{1}{6}(3C_{15} - (C_{55}\Delta x_1)/\Delta x_3 - (C_{11}\Delta x_3)/\Delta x_1), \tag{A.25}$$

$$A_{38} = \frac{1}{12}(3(C_{13} + C_{55}) - (2C_{35}\Delta x_1)/\Delta x_3 - (2C_{15}\Delta x_3)/\Delta x_1), \tag{A.26}$$

$$A_{44} = \frac{1}{6}(-3C_{35} + (2C_{33}\Delta x_1)/\Delta x_3 + (2C_{55}\Delta x_3)/\Delta x_1), \tag{A.27}$$

$$A_{45} = \frac{1}{12}(-3C_{13} + 3C_{55} - (4C_{35}\Delta x_1)/\Delta x_3 + (2C_{15}\Delta x_3)/\Delta x_1), \tag{A.28}$$

$$A_{46} = -((C_{33}\Delta x_1)/(3\Delta x_3)) + (C_{55}\Delta x_3)/(6\Delta x_1), \tag{A.29}$$

$$A_{47} = \frac{1}{12}(3(C_{13} + C_{55}) - (2C_{35}\Delta x_1)/\Delta x_3 - (2C_{15}\Delta x_3)/\Delta x_1), \tag{A.30}$$

$$A_{48} = \frac{1}{6}(3C_{35} - (C_{33}\Delta x_1)/\Delta x_3 - (C_{55}\Delta x_3)/\Delta x_1), \tag{A.31}$$

$$A_{55} = \frac{1}{6}(3C_{15} + (2C_{55}\Delta x_1)/\Delta x_3 + (2C_{11}\Delta x_3)/\Delta x_1), \tag{A.32}$$

$$A_{56} = \frac{1}{12}(3(C_{13} + C_{55}) + (4C_{35}\Delta x_1)/\Delta x_3 + (4C_{15}\Delta x_3)/\Delta x_1), \tag{A.33}$$

$$A_{57} = (C_{55}\Delta x_1)/(6\Delta x_3) - (C_{11}\Delta x_3)/(3\Delta x_1), \tag{A.34}$$

$$A_{58} = \frac{1}{12}(3C_{13} - 3C_{55} + (2C_{35}\Delta x_1)/\Delta x_3 - (4C_{15}\Delta x_3)/\Delta x_1), \tag{A.35}$$

$$A_{66} = \frac{1}{6}(3C_{35} + (2C_{33}\Delta x_1)/\Delta x_3 + (2C_{55}\Delta x_3)/\Delta x_1), \tag{A.36}$$

$$A_{67} = \frac{1}{12}(-3C_{13} + 3C_{55} + (2C_{35}\Delta x_1)/\Delta x_3 - (4C_{15}\Delta x_3)/\Delta x_1), \tag{A.37}$$

$$A_{68} = (C_{33}\Delta x_1)/(6\Delta x_3) - (C_{55}\Delta x_3)/(3\Delta x_1), \tag{A.38}$$

$$A_{77} = \frac{1}{6}(-3C_{15} + (2C_{55}\Delta x_1)/\Delta x_3 + (2C_{11}\Delta x_3)/\Delta x_1), \tag{A.39}$$

$$A_{78} = \frac{1}{12}(-3(C_{13} + C_{55}) + (4C_{35}\Delta x_1)/\Delta x_3 + (4C_{15}\Delta x_3)/\Delta x_1), \tag{A.40}$$

$$A_{88} = \frac{1}{6}(-3C_{35} + (2C_{33}\Delta x_1)/\Delta x_3 + (2C_{55}\Delta x_3)/\Delta x_1), \tag{A.41}$$

with $\Delta x_1$ being the fine element edge length in $x_1$ direction, and $\Delta x_3$ being the fine element edge length in $x_3$ direction, and $C_{ij}$ are elasticity constants of the element $K_h$, which is assumed to be constant within $K_h$ but generally heterogeneous in a coarse element. If using higher order finite elements, $C_{ij}$ should be interpolated with some appropriate interpolation rules. For matrix $\mathbf{B}$, which is related to the boundary conditions, we have the element matrix $\mathbf{B}_{K_h}$ for the fine element $K_h$ on left, right, top and boundaries as

$$\mathbf{B}_{K_h}|_{\text{left boundary}} = -\frac{1}{2}(\Delta x_3, \Delta x_3, 0, 0, 0, 0, \Delta x_3, \Delta x_3)^{\mathrm{T}}, \tag{A.42}$$

$$\mathbf{B}_{K_h}|_{\text{right boundary}} = \frac{1}{2}(0, 0, \Delta x_3, \Delta x_3, \Delta x_3, \Delta x_3, 0, 0)^{\mathrm{T}}, \tag{A.43}$$

$$\mathbf{B}_{K_h}|_{\text{top boundary}} = -\frac{1}{2}(\Delta x_1, \Delta x_1, \Delta x_1, \Delta x_1, 0, 0, 0, 0)^{\mathrm{T}}, \tag{A.44}$$

$$\mathbf{B}_{K_h}|_{\text{bottom boundary}} = \frac{1}{2}(0, 0, 0, 0, \Delta x_1, \Delta x_1, \Delta x_1, \Delta x_1)^{\mathrm{T}}, \tag{A.45}$$

which again are calculated with exact integration rules.

The above system has $2(r_1+1)(r_3+1)$ degrees of freedom for $\mathbf{u}$ (including $u_1$ and $u_3$). In Larson and Bengzon (2013), the stress tensors on triangular elements can be obtained with the gradients of $\mathbf{u}$ calculated using `MATLAB` built-in PDE function

`pdegrad`. Since we have used rectangular elements, we calculate the stress tensor at the center of each fine element with definition of equation A.1b using the rotated staggered-grid finite-difference scheme (Saenger et al., 2000). For example, for $\sigma_{11}$ at the $(j_1, j_3)$-th fine element, we have

$$
\begin{aligned}
&\sigma_{11}(j_1, j_3) \\
&= C_{11}(j_1, j_3)\frac{1}{2\Delta x_1}\left\{\left[u_1\left(j_1+\frac{1}{2}, j_3+\frac{1}{2}\right) - u_1\left(j_1-\frac{1}{2}, j_3-\frac{1}{2}\right)\right]\right. \\
&\qquad \left. + \left[u_1\left(j_1+\frac{1}{2}, j_3-\frac{1}{2}\right) - u_1\left(j_1-\frac{1}{2}, j_3+\frac{1}{2}\right)\right]\right\} \\
&+ C_{13}(j_1, j_3)\frac{1}{2\Delta x_3}\left\{\left[u_3\left(j_1+\frac{1}{2}, j_3+\frac{1}{2}\right) - u_3\left(j_1-\frac{1}{2}, j_3-\frac{1}{2}\right)\right]\right. \\
&\qquad \left. - \left[u_3\left(j_1+\frac{1}{2}, j_3-\frac{1}{2}\right) - u_3\left(j_1-\frac{1}{2}, j_3+\frac{1}{2}\right)\right]\right\} \\
&+ C_{15}(j_1, j_3)\frac{1}{2\Delta x_1}\left\{\left[u_3\left(j_1+\frac{1}{2}, j_3+\frac{1}{2}\right) - u_3\left(j_1-\frac{1}{2}, j_3-\frac{1}{2}\right)\right]\right. \\
&\qquad \left. + \left[u_3\left(j_1+\frac{1}{2}, j_3-\frac{1}{2}\right) - u_3\left(j_1-\frac{1}{2}, j_3+\frac{1}{2}\right)\right]\right\} \\
&+ C_{15}(j_1, j_3)\frac{1}{2\Delta x_3}\left\{\left[u_1\left(j_1+\frac{1}{2}, j_3+\frac{1}{2}\right) - u_1\left(j_1-\frac{1}{2}, j_3-\frac{1}{2}\right)\right]\right. \\
&\qquad \left. - \left[u_1\left(j_1+\frac{1}{2}, j_3-\frac{1}{2}\right) - u_1\left(j_1-\frac{1}{2}, j_3+\frac{1}{2}\right)\right]\right\}, \qquad \text{(A.46)}
\end{aligned}
$$

where $\Delta x_1$ and $\Delta x_3$ are the length of the vertical and horizontal edges of the fine element, respectively. This solution, along with the solutions in the other three blockers, is further taken as the multiscale basis function $\phi_{11}$ of stress component $\sigma_{11}$, as described in the text. Multiscale basis functions for the other stress components can be calculated in the same way.

# APPENDIX B

## NUMERICAL HOMOGENIZATION FOR 3-D HETEROGENEOUS, GENERALLY ANISOTROPIC MEDIA

For 3-D heterogeneous, anisotropic elastic media, we decompose the support of $\boldsymbol{\sigma}$ with 8 cubic blocks, and in each of the blocks, we assume similar local linear elasticity problem, i.e., equation 2.6, satisfied. We can define similar boundary conditions as those in 2-D case. If we denote the two faces of cubic block that are perpendicular with $x_i$ axis with $\mathcal{F}_i$, the boundary conditions for each stress component will be

$$\sigma_{11} = 1 \qquad \text{on} \quad \mathcal{F}_1, \tag{B.1}$$

$$\sigma_{22} = 1 \qquad \text{on} \quad \mathcal{F}_2, \tag{B.2}$$

$$\sigma_{33} = 1 \qquad \text{on} \quad \mathcal{F}_3, \tag{B.3}$$

$$\sigma_{23} = 1 \qquad \text{on} \quad \mathcal{F}_2 \quad \text{and} \quad \mathcal{F}_3, \tag{B.4}$$

$$\sigma_{13} = 1 \qquad \text{on} \quad \mathcal{F}_1 \quad \text{and} \quad \mathcal{F}_3, \tag{B.5}$$

$$\sigma_{12} = 1 \qquad \text{on} \quad \mathcal{F}_1 \quad \text{and} \quad \mathcal{F}_2. \tag{B.6}$$

This local problem can also be solved with FEM which is similar with that in Appendix A. After solving the local problems in all of the 8 cubic blocks, we join them together to form the basis functions of $\boldsymbol{\sigma}$ in $K_\sigma$.

With similar algebraic manipulations as those for 2-D case, we can finally have

the 3-D effective compliance matrix as

$$\tilde{\mathbf{S}} = \begin{pmatrix} S_{11}\phi_{11}\phi_{11} & S_{12}\phi_{22}\phi_{11} & S_{13}\phi_{33}\phi_{11} & S_{14}\phi_{23}\phi_{11} & S_{15}\phi_{13}\phi_{11} & S_{16}\phi_{12}\phi_{11} \\ S_{12}\phi_{11}\phi_{22} & S_{22}\phi_{22}\phi_{22} & S_{23}\phi_{33}\phi_{22} & S_{24}\phi_{23}\phi_{22} & S_{25}\phi_{13}\phi_{22} & S_{26}\phi_{12}\phi_{22} \\ S_{13}\phi_{11}\phi_{33} & S_{23}\phi_{22}\phi_{33} & S_{33}\phi_{33}\phi_{33} & S_{34}\phi_{23}\phi_{33} & S_{35}\phi_{13}\phi_{33} & S_{36}\phi_{12}\phi_{33} \\ S_{14}\phi_{11}\phi_{23} & S_{24}\phi_{22}\phi_{23} & S_{34}\phi_{33}\phi_{23} & S_{44}\phi_{23}\phi_{23} & S_{45}\phi_{13}\phi_{23} & S_{46}\phi_{12}\phi_{23} \\ S_{15}\phi_{11}\phi_{13} & S_{25}\phi_{22}\phi_{13} & S_{35}\phi_{33}\phi_{13} & S_{45}\phi_{23}\phi_{13} & S_{55}\phi_{13}\phi_{13} & S_{56}\phi_{12}\phi_{13} \\ S_{16}\phi_{11}\phi_{12} & S_{26}\phi_{22}\phi_{12} & S_{36}\phi_{33}\phi_{12} & S_{46}\phi_{23}\phi_{12} & S_{56}\phi_{13}\phi_{12} & S_{66}\phi_{12}\phi_{12} \end{pmatrix}, \tag{B.7}$$

where

$$S_{ij}\phi_{st}\phi_{pq} = \frac{1}{n_1 n_2 n_3} \sum_{j_1=1}^{n_1} \sum_{j_2=1}^{n_2} \sum_{j_3=1}^{n_3} S_{ij}(j_1, j_2, j_3)\phi_{st}(j_1, j_2, j_3)\phi_{pq}(j_1, j_2, j_3), \tag{B.8}$$

is a summation over all fine elements within $K_\sigma$, $n_i$ is the number of fine elements along the $i$-th axis, with $i = 1, 2, 3$, and $\phi_{ij}$ are the multiscale basis functions solved from local problem for $\sigma_{ij}$. And the effective elasticity matrix for a coarse block $K_\sigma$ is

$$\tilde{\mathbf{C}} = \tilde{\mathbf{S}}^{-1}. \tag{B.9}$$

Finally, for the density, we have

$$\tilde{\rho} = \frac{1}{n_1}\frac{1}{n_2}\frac{1}{n_3} \sum_{j_1=1}^{m_1} \sum_{j_2=1}^{n_2} \sum_{j_3=1}^{n_3} \rho(j_1, j_2, j_3). \tag{B.10}$$

# APPENDIX C

## $2L$-TH ORDER ROTATED STAGGERED-GRID FINITE-DIFFERENCE SCHEME

Throughout the numerical experiments to compare the wavefield in fine-scale media and in the effective media, we solve the anisotropic wave equation using high-order rotated staggered-grid (RSG) finite-difference method. The RSG finite-difference method for wave equations has already been discussed within many literatures (e.g., Saenger et al., 2000; Saenger and Bohlen, 2004), and here since we only provide some necessary steps.

Essentially, in RSG, the derivatives of a field variable $u$ defined at integer position $(i_1, i_3)$ are expressed as the summation or difference of the derivatives along rotated axes (Saenger et al., 2000), i.e.,

$$\partial_1 u = \frac{\Delta r}{2\Delta x_1}(D_3 u + D_1 u), \tag{C.1a}$$

$$\partial_3 u = \frac{\Delta r}{2\Delta x_3}(D_3 u - D_1 u), \tag{C.1b}$$

with the conventional staggered-grid derivatives $D_1$ and $D_3$ along rotated axes expressed as

$$D_1 = \frac{1}{\Delta r}\sum_{m=1}^{L} c_m \left[ u\left(i_1 + \frac{1}{2}m, i_3 - \frac{1}{2}m\right) - u\left(i_1 - \frac{1}{2}m, i_3 + \frac{1}{2}m\right)\right], \tag{C.2a}$$

$$D_3 = \frac{1}{\Delta r}\sum_{m=1}^{L} c_m \left[ u\left(i_1 + \frac{1}{2}m, i_3 + \frac{1}{2}m\right) - u\left(i_1 - \frac{1}{2}m, i_3 - \frac{1}{2}m\right)\right], \tag{C.2b}$$

where $\Delta r = \sqrt{\Delta x_1^2 + \Delta x_3^2}$, $L$ is half of the order of spatial accuracy, $i_1$ and $i_3$ are the

integers along the $x_1$ and $x_3$ axes, respectively, and the staggered-grid coefficients can be calculated as (Fornberg, 1990)

$$c_m = \frac{(-1)^{L+1} \prod_{n=1,n\neq m}^{L} (2n-1)^2}{(2m-1) \prod_{n=1,n\neq m}^{L} [(2m-1)^2 - (2n-1)^2]}. \tag{C.3}$$

In our numerical tests, we have used 20th-order spatial accuracy, i.e., $L = 10$, to calculate the spatial differential operators in the anisotropic elastic wave equation, and the finite-difference coefficients are listed in Table C.

| $m$ | $c_m$ |
|---|---|
| 1 | 1.241816 |
| 2 | -0.1128924 |
| 3 | 2.7094169e-2 |
| 4 | -7.4434527e-3 |
| 5 | 1.9297841e-3 |
| 6 | -4.3061300e-4 |
| 7 | 7.7077173e-5 |
| 8 | -1.0216503e-5 |
| 9 | 8.8378061e-7 |
| 10 | -3.7237577e-8 |

Table C: Coefficients of 20th order staggered-grid finite-difference scheme